





**UNIVERSIDAD REY JUAN CARLOS**  
**DEPARTAMENTO DE TEORÍA DE LA SEÑAL Y COMUNICACIONES,**  
**SISTEMAS TELEMÁTICOS Y COMPUTACIÓN**



**PhD Thesis**

**COST-EFFECTIVE AND LARGE AREA LITHOGRAPHY SYSTEM BASED  
ON ELECTRIC-ARC FOR MICRO/NANOSTRUCTURING OF GRAPHENE  
AND THIN FILM CONDUCTORS: DEVELOPMENT AND  
PHENOMENOLOGY**

**Autor:** D. Miguel García Vélez

**Directores:** Dr. D. Ángel Luis Álvarez Castillo

Dra. Dña. María del Carmen Coya Párraga

**2015**

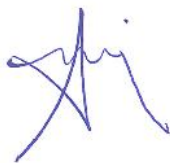


El Dr. D. Ángel Luis Álvarez Castillo y la Dra. Dña. María del Carmen Coya Párraga, profesores Titulares de Universidad del Departamento de Teoría de la Señal y Comunicaciones, Sistemas Telemáticos y Computación, directores de la Tesis Doctoral **“Cost-effective and large area lithography system based on electric-arc for micro/nanostructuring of Graphene and thin film conductors: development and phenomenology.”** realizada por el doctorando Don Miguel García Vélez.

Hacen constar:

Que esta Tesis Doctoral reúne los requisitos necesarios para su defensa y aprobación.

En Móstoles, a 10 de Abril de 2015.



Dr. D. Ángel Luis Álvarez Castillo



Dra. Dña. Mª de Carmen Coya Párraga



## AGRADECIMIENTOS

Como todo trabajo de investigación, éste ha contado con la colaboración y participación de personas e instituciones sin las cuales no hubiese sido posible su realización. A todos ellos quiero expresar mi gratitud en estas líneas.

Con este proyecto culmina un ciclo muy interesante e enriquecedor, no solo a nivel profesional sino también en lo personal. Agradezco especialmente a mis tutores, la Dra. M<sup>a</sup> del Carmen Coya Párraga y el Dr. Ángel Luis Álvarez Castillo por haberme dado la oportunidad de ingresar a su equipo de trabajo, su confianza desde el primer día, por poner a mi disposición todos los recursos físicos y económicos para el desarrollo de este proyecto, la crítica constructiva y sobre todo por la dedicación y tiempo que han tenido a lo largo de estos años.

También, agradezco a la Dra. Alicia de Andrés del Instituto de Materiales de Madrid (CSIC) por su alta implicación y colaboración en las tareas de caracterización y análisis como también en el suministro de materiales para su procesamiento, al igual que al Dr. Esteban Climent, Dra. Carmen Múnuera y Dr. Xavi Díez Betriu por sus valiosos aportes. Igualmente, al Dr. Carlos Zaldo por sus consejos e intermediación para la fabricación de las piezas según las necesidades y especificaciones en la unidad de apoyo general – taller mecánico del instituto.

Gracias a la Universidad Rey Juan Carlos por brindarme el espacio para el desarrollo de la investigación, al personal docente, en concreto al Dr. Joaquín Rams Ramos por permitirme el uso de sus equipos, al Dr. José Luis Trueba Santander y Dr. Manuel Arrayás Chazeta por sus excelentes aportes y entretenidas conversaciones. Además, quisiera hacer extensiva mi gratitud al Dr. José Luis Pau y Dr. Carlos García Núñez del Departamento de Física Aplicada de la Universidad Autónoma por su grata colaboración.

Por supuesto, a mis padres y a mi hermana que desde la distancia me acompañaron en esta aventura de forma incondicional, brindándome su apoyo. A ti Juliana, que pese a la distancia siempre estuviste presente, dándome ánimos, por ser un sustento permanente, por los buenos momentos y los que vendrán. A la familia, regada por el planeta, gracias por su buena energía. A los amigos incondicionales, por soportarme, su apoyo ha sido muy importante para la consecución de este logro.

A todos: ¡Gracias Totales!



*“Para lograr lo posible hay que intentar una y otra vez lo imposible”*

*- El abuelo Hernando -*



---

## TABLE OF CONTENTS

<b>RESUMEN EN CASTELLANO .....</b>	<b>xv</b>
<b>STATEMENT OF ORIGINALITY.....</b>	<b>xxii</b>
<b>CHAPTER 1 . RESEARCH CONTEXT: INTRODUCTION .....</b>	<b>25</b>
<b>1.1 ORGANIC ELECTRONICS CONTEXT .....</b>	<b>25</b>
1.1.1. Market size, potential and profitability: 2013 - 2023.....	27
1.1.2. Brief notes on patterning methods for high yield and large area substrates	30
<b>1.2. PRINCIPLES OF ELECTRICAL DISCHARGE MACHINING .....</b>	<b>33</b>
1.2.1. EDM Process Parameters.....	37
1.2.2. EDM Applications .....	39
1.2.2.1. Micro – EDM and Nano - EM .....	39
<b>1.3. COST EFFECTIVE LITHOGRAPHY METHOD BASED ON ARC- EROSION SYSTEM .....</b>	<b>41</b>
1.3.1. Aspects and Basic Operating Principle .....	41
1.3.2. Autoalign system.....	47
<b>1.4. GRAPHENE FOR ELECTRONIC DEVICES.....</b>	<b>49</b>
1.4.1. Graphene Synthesis Methods.....	49
1.4.1.1. Chemical Vapor Deposition (CVD) for graphene single-layer and multilayer. ....	49
1.4.1.2. Graphene Oxide .....	50
1.4.1.3. Arc – Discharge graphite evaporation.....	51
1.4.1.4. Other Methods.....	51
1.4.2. Graphene Patterning Methods: state of the art.....	52
1.4.2.1. Group 1: Lithography.....	53
1.4.2.2. Group 2: Soft lithography .....	55

---

1.4.2.3. Group 3: Maskless Lithography or Direct Writing .....	58
<b>1.5. REFERENCES .....</b>	<b>64</b>
<b>CHAPTER 2 . OBJECTIVES .....</b>	<b>76</b>
2.1. GENERAL OBJECTIVE .....	76
2.2. SPECIFIC OBJECTIVES .....	76
<b>CHAPTER 3 . ELECTROEROSION MACHINE DEVELOPMENT, METHODS AND TECHNIQUES .....</b>	<b>78</b>
3.1 COMERCIAL PART SELECTION.....	78
3.1.1. Piezoelectric stages.....	78
3.1.2. Dino - Lite AD4113ZT4 Digital Microscope.....	80
3.1.3. Antivibration System: PLM Pneumatic Mount.....	81
3.1.4. Commercial Arc Erosion Tip Types.....	81
3.2 DESIGNED PARTS .....	83
3.2.1. Nano and micrometric stages Stands.....	83
3.2.2. Tip Attachment Mechanism .....	84
3.3 ELECTRICAL MEASUREMENTS.....	87
3.4 FINITE ELEMENT ANALYSIS MODEL .....	88
3.4.1. Glass-ITO Model.....	90
3.5 OPTICAL AND MORPHOLOGICAL PATTERN CHARACTERIZATION .....	91
3.5.1. Optical Images.....	91
3.5.2. Contact Profilometer .....	92
3.5.3. Micro-Raman analysis.....	92
3.5.4. Atomic Force Microscopy .....	98
3.6 REFERENCES.....	100

---

<b>CHAPTER 4 . EXPERIMENTAL RESULTS.....</b>	<b>103</b>
<b>4.1 ELECTRO EROSION ON INDIUM-TIN OXIDE (ITO)</b>	
<b>THIN FILMS .....</b>	<b>103</b>
4.1.1. ITO on Polyethylene Terephthalate (PET/ITO) .....	112
<b>4.2 ELECTRICAL EROSION ON ALUMINUM DOPED ZINC OXIDE</b>	
<b>(AZO).....</b>	<b>114</b>
4.2.1. Example of device application: Organic Solar Cells on AZO.....	116
<b>4.3 ELECTRICAL EROSION ON ZINC NITRIDE .....</b>	<b>118</b>
<b>4.4 ELECTROEROSION ON GOLD.....</b>	<b>125</b>
4.4.1. PET/ITO/GOLD .....	132
<b>4.5 DISCHARGE TRANSIENT ANALYSIS.....</b>	<b>135</b>
<b>4.6 FINITE ELEMENT ANALYSIS FOR PHYSICAL SYSTEM</b>	
<b>SIMULATION .....</b>	<b>145</b>
4.6.1. Influence of the tip sharpness, separation tip-sample, and doping of the	
target layer on the electrostatic properties .....	146
4.6.2. Simulation of electrostatic magnitudes in case of contact between tip	
and sample, for different crater radius and layer thicknesses. ....	152
<b>4.7 REFERENCES.....</b>	<b>160</b>
<b>CHAPTER 5 . ARC-EROSION PATTERNING IN GRAPHENE AND</b>	
<b>RELATED MATERIALS.....</b>	<b>163</b>
<b>5.1 GRAPHENE OXIDE PATTERNING .....</b>	<b>163</b>
<b>5.2 REDUCED GRAPHENE OXIDE PATTERNING .....</b>	<b>170</b>
<b>5.3 SINGLE-LAYER GRAPHENE PATTERNING.....</b>	<b>173</b>
5.3.1. Grooves in graphene .....	174
5.3.2. Spots or craters in graphene.....	189
5.3.3. Nano-flakes in graphene .....	197
5.3.4. Discussion on the mechanisms .....	201

---

---

<b>5.4 REFERENCES.....</b>	<b>205</b>
<b>CHAPTER 6 . CONCLUSIONS .....</b>	<b>208</b>
<b>APPENDIX A.....</b>	<b>215</b>
<b>APPENDIX B.....</b>	<b>227</b>

---

## RESUMEN EN CASTELLANO

Este trabajo presenta el diseño y la implementación de un sistema de litografía de bajo coste para láminas delgadas de materiales conductores, directa y ecológica al no requerir el uso de fotoresinas ni disolventes, así como el estudio detallado del fenómeno físico asociado al proceso. Esta técnica está basada en erosión por arco voltaico, descargas eléctricas localizadas en el orden de  $\mu\text{s}$ , permitiendo velocidades de operación de  $\text{cm/s}$  perfectamente compatibles con el procesamiento en gran área.

El efecto de la técnica litográfica presentada en este trabajo se ha estudiado en profundidad sobre semiconductores como el  $\text{In}_2\text{O}_3: \text{Sn}$  (ITO),  $\text{ZnO}: \text{Al}$  (AZO) o Nitruro de Zinc ( $\text{Zn}_3\text{N}_2$ ), así como en el oro, conductor metálico por excelencia. Además, debido a la apertura de posibilidades de desarrollo en el campo de la ciencia y tecnología de materiales por a la irrupción del grafeno, se ha estudiado extensivamente el efecto de esta técnica litográfica sobre dicho material. Esta investigación pretende aportar una solución ecológica, eficiente y escalable que responda al reto actual que supone el procesado de gran área.

En el Capítulo 1 se evalúa el potencial de esta tecnología, repasando el estado actual de los métodos de litografía para luego centrarse en los retos y avances en esta materia. Una vez establecido el contexto en el cual se desarrolla este trabajo, se revisan los principios básicos del mecanizado por electroerosión, el cual podría considerarse el antecedente lógico del trabajo aquí presentado (EDM por sus siglas en inglés), haciendo un recorrido generalizado por aspectos de procesamiento, parametrización y aplicaciones en la escala micro y nanométrica, señalando las diferencias con la técnica aquí presentada. Adicionalmente, se realiza una revisión bibliográfica relacionada con el estado actual de la litografía sobre grafeno como material prometedor para dispositivos electrónicos.

A continuación, en el Capítulo 2, se establecen de forma específica los objetivos de esta tesis doctoral. En el Capítulo 3 se realiza una detallada descripción del sistema diseñado e implementado para la litografía por arco voltaico. Se detallan las partes comerciales que posibilitan el desempeño de esta tarea, especificando aspectos técnicos y una diversidad de características de los componentes involucrados. También se hace especial énfasis en el diseño propio de una serie de piezas fundamentales para su correcto funcionamiento, soportado adecuadamente con los planos realizados para su

---

fabricación. Además, se establece un protocolo de actuación para el procedimiento de erosión y la mención de una serie de actividades previas con el objetivo de garantizar un resultado satisfactorio. El prototipo está basado en dos nano-posicionadores (XY y Z) acoplados a tres micro-estaciones lineales (X, Y, Z) para cubrir distancias de trabajo desde micras a centímetros. El modo de funcionamiento consiste en una sonda muelle, sometida a una tensión DC (0-100 V) respecto a la superficie conductora a erosionar, la cual está conectada a tierra. Esta sonda se “desliza” sobre la superficie conductora permitiendo una monitorización eléctrica continua del proceso y por tanto la posibilidad de corregir la inclinación inherente de los sustratos en tiempo real vía software. La sonda va dejando una región aislada a su paso, limitada por el tamaño de las puntas utilizadas, que puede diseñarse como si de un plotter se tratara. El principio físico se basa en la autolimitación natural de las descargas eléctricas generadas debido a este aislamiento o eliminación del material conductor. Por otro lado, se introduce un modelo de elementos finitos basados en el software COMSOL Multiphysics, en donde se establecen las condiciones para la simulación del fenómeno, de cara a abordar otro de los objetivos de este trabajo que consiste en encontrar una explicación al fenómeno físico de la descarga.

Los capítulos 4 y 5 se dedican a investigar exhaustivamente el efecto de estas micro-descargas sobre distintos materiales, así como demostrar su aplicación mediante diversos ejemplos. La investigación tiene un doble objetivo: por un lado obtener las condiciones adecuadas para un correcto procesamiento de cada material especificando voltajes umbral, rangos de voltaje idóneos para la obtención de patrones de buena calidad: condiciones de velocidad y aceleración utilizados en la parametrización de la máquina, presión y tipo de punta utilizada, entre otros. Por otro lado, estudiar el fenómeno físico que por el cual se produce la erosión por arco-voltaico. Para lo primero, se han diseñado experimentos que implican la realización de patrones (líneas y cuadrados) en distintas condiciones, de cuyo estudio hemos podido obtener las condiciones óptimas de procesado. Para el segundo objetivo, es más conveniente la realización de otro tipo de patrones, cráteres en este caso, a distintas tensiones, presiones o condiciones de humedad (dependiendo del material). El estudio de las descargas eléctricas registradas con estas experiencias nos ha permitido proponer un modelo circuital que explica el comportamiento fenomenológico de la dinámica de la erosión eléctrica del material. Por último, utilizando métodos de elementos finitos y con la experiencia sobre todos los materiales estudiados, se propone un modelo

---

comprendido de la distribución de líneas de campo en el sistema sonda-muestra que explica la progresión del proceso de erosión.

### **Óxido de Indio-Estaño (ITO)**

Dado el interés y de su gran importancia para la electrónica orgánica actual, las primeras pruebas efectuadas con esta técnica litográfica se hacen sobre ITO, consiguiendo patrones de muy buena calidad al trabajar en un rango de voltajes entre 11 y 15 V, obteniendo aislamiento eléctrico tanto con polaridad positiva como negativa de la sonda con respecto a la muestra. La utilización de la polaridad negativa en el procedimiento genera una mayor cantidad de residuo, siendo necesario el uso de un ataque químico, mientras que con polaridad positiva sucede lo opuesto, siendo retirados con una mayor facilidad. Sin embargo, se observa un mayor desgaste en la punta utilizada para el proceso. Por otro lado, también fue posible el procesamiento de este material en sustratos flexibles, mediante la utilización de puntas geoméricamente más pequeñas. Con este tipo de puntas, se pueden procesar patrones más estrechos, con unidades de micra de separación, obteniendo micro-hilos de óxido de indio-estaño con un ancho en promedio de  $\sim 7 \mu\text{m}$ , separadas de 3 a 4  $\mu\text{m}$ .

### **Óxido de Zinc: Aluminio (AZO)**

Como una alternativa al ITO, también se desarrollan pruebas con óxido de zinc dopado con aluminio. Se obtienen patrones de muy buena calidad, utilizando un rango entre -30 V y -45 V. Aunque la erosión es efectiva con voltajes superiores a ese rango, no se recomienda su uso, el resultado final de los patrones no es el adecuado en términos de calidad. Por su parte, el uso de voltajes inferiores a -30 V no son los idóneos para garantizar un completo aislamiento. A modo de aplicación y con éxito, se han integrado estas capas procesadas en células solares orgánicas de heterounión.

### **Nitruro de Zinc- $\text{Zn}_3\text{N}_2$**

Mediante una colaboración con la Universidad Autónoma de Madrid, el nitruro de zinc también fue objeto de pruebas con esta técnica litográfica de bajo coste. Se elimina material utilizando voltajes desde -15 hasta -16 V, con un voltaje umbral establecido en -14 V, insuficiente para el proceso de erosión. Estudios posteriores han revelado la

---

presencia de esferas ricas en zinc en los bordes de los patrones debido al proceso de sublimación del material, como también de estructuras blandas submicrónicas justo en el centro del patrón, producto de los altos cambios composicionales inducidos por el tratamiento eléctrico. Estas propiedades hacen de esta técnica una herramienta muy útil para el aislamiento de transistores de lámina delgada en arquitectura 2D o la fabricación de nanoestructuras de óxido de zinc para aplicaciones en optoelectrónica.

### **Oro: Au**

También se realizan experiencias sobre Au, conductor ampliamente utilizado en electrónica. Para estas pruebas, se prepararon una serie de muestras con espesores distintos (100 nm, 52 nm y 15 nm) y se trabajó con un rango de voltaje bastante amplio, con polaridad negativa, con el fin de establecer el valor adecuado para su procesamiento. Para todos los casos, hay una situación común: si se trabaja a partir de 16 V hasta 20 V e independiente del espesor de la capa delgada, los patrones presentan irregularidades bastante notorias en sus bordes, dejando entrever una baja calidad de definición. Los rangos de voltaje utilizados para el procesamiento de las muestras según el espesor de la capa son: para 15 nm (3 – 14 V), 52 nm (4 – 12 V) y 100 nm (8 – 12 V) respectivamente, resaltando la alta calidad obtenida en las muestras de menor espesor. Los resultados muestran una relación directa entre el espesor de la capa delgada y el voltaje de procesamiento, haciéndose más pequeño a medida que el espesor disminuye dando como resultado la posibilidad de procesar el material en un rango de voltajes más diverso.

A su vez, se observa claramente una peculiaridad común a todos los materiales procesados: la existencia de un reborde, producto de la acumulación de material durante el procesamiento y también por la cantidad de material. El efecto de estos rebordes en dispositivos optoelectrónicos es perjudicial, en términos generales, para su correcto funcionamiento, por lo cual es necesario retirarlos o reducirlos en altura. Para ello, se ha buscado un método de ataque químico adecuado en el caso del ITO o alternativamente para el caso del Au, hemos implementado un algoritmo en el que la punta se desempeña simplemente como una herramienta de barrido que va recorriendo los patrones ya procesados, retirando esta acumulación de material, sin necesidad de ataque químico.

---

## **Grafeno y materiales 2D relacionados: óxido de grafeno y óxido de grafeno reducido)**

El Capítulo 5 de este trabajo, recoge los resultados obtenidos con el grafeno y materiales 2D relacionados. Gracias a la colaboración con el Instituto de Materiales de Madrid (ICMM – CSIC) fue posible llevar a cabo pruebas de erosión eléctrica en óxido de grafeno depositado por métodos a partir de disolución y óxido de grafeno reducido. Asimismo, se ha estudiado la técnica propuesta sobre grafeno comercial sobre SiO<sub>2</sub>/Si y sobre cuarzo. Se ha evaluado el efecto de las condiciones de erosión: presión, humedad y movimiento de la punta determinan la parcial o completa eliminación del grafeno, como la transformación a óxido de grafeno o incluso la obtención de dominios de nanografeno de muy buena calidad. Es en materiales 2D donde la técnica propuesta de erosión por arco voltaico adquiere su mayor potencialidad debido a la no presencia de residuos. Gracias a este hecho se han podido realizar microhilos de grafeno con una relación 1200:1.

En óxido de grafeno, los resultados finales muestran que en condiciones de aire seco se da una erosión incompleta, por interacción mecánica sin la aplicación de voltaje, incluso la espectroscopia Raman muestra que una pequeña cantidad de material es removida por este mecanismo. Cuando se aplica voltaje, la calidad de los patrones mejora considerablemente pero el resultado no es inmune a la generación y acumulación de residuos en los bordes como también en el interior del patrón. Los mejores resultados bajo estas condiciones se dan a un voltaje de -60 V en el que casi todo el material es eliminado satisfactoriamente, según las medidas efectuadas por espectroscopia Raman. También, se han desarrollado ensayos alternativos en condiciones de humedad para contrarrestar la baja conductividad eléctrica y rigidez del óxido de grafeno. Para ello, se prepararon disoluciones con diferentes grados de acidez, en donde se observan diferencias claras entre los patrones procesados en seco y con humedad: todos los residuos en los bordes y dentro de los patrones observados previamente, desaparecen por la interacción del agua, además de la completa remoción del material para todo el rango de voltajes. Por otro lado, se obtienen los mismos resultados independientemente de la concentración de ácido, en donde se resalta una excelente definición y calidad.

Gracias al método de reducción de óxido de grafeno utilizado en colaboración con el Instituto de Materiales de Madrid (ICMM – CSIC) fue posible probar la técnica de litografía con este tipo de muestras. El proceso de fabricación de estas capas es igual hasta la fase de recocido, en donde dos etapas adicionales son necesarias para reducir el

---

material. Debido a la consistencia blanda de las capas reducidas y su insuficiente conductividad, no se observa ningún tipo de diferencia o cambio desde -10 V hasta -20 V, como tampoco indicios de un progreso lateral en cada uno de los patrones, de hecho, el ancho final de cada uno de los patrones realizados corresponde al diámetro de la punta. Aun así, el óxido de grafeno reducido es retirado, incluso sin un voltaje aplicado.

Finalmente, las pruebas con grafeno se desarrollan con productos comerciales fabricados y distribuidos por empresas del sector. Graphene Supermarket distribuye grafeno sobre una capa intermedia de 90 nanómetros de óxido de silicio y un sustrato de silicio. Además, gracias a la colaboración con el Instituto de Materiales de Madrid (ICMM – CSIC) fue posible probar la técnica en grafeno sobre sustratos de cuarzo, distribuido por Graphenea. Ambos tipos de grafeno se fabricaron por el método de deposición química de vapor, proceso utilizado frecuentemente para fabricar materiales en fase sólida con una alta pureza en la industria de semiconductores.

Las principales pruebas de electroerosión fueron realizadas en grafeno sobre sustratos de silicio. Los resultados indican que la remoción del grafeno es satisfactoria mediante la combinación adecuada de dos factores: el voltaje aplicado y el rayado mecánico, siendo el voltaje el parámetro principal que rige el procedimiento. No obstante, el rayado mecánico sin aplicación de voltaje no es suficiente para la eliminación del material, como tampoco el incremento de presión en la superficie: no se aprecian cambios aparentes en todo el rango de compresión utilizado (0.3 – 10  $\mu\text{m}$ ). El grafeno restante está claramente roto en escala nanoscópica.

Un voltaje aplicado de -10 V no es suficiente para una correcta erosión del grafeno, los patrones obtenidos son muy similares a los procesados sin voltaje. Por el contrario, la ausencia de grafeno es extensiva cuando se incrementa el voltaje a -20 V. En términos de calidad y definición, la electroerosión del grafeno mejora sustancialmente mediante la utilización de un voltaje aplicado de -30 V, al igual que su eliminación: casi total. Adicionalmente, los resultados muestran que a partir de -40 V se obtienen patrones más irregulares, empeorando su calidad; en donde la remoción del grafeno vuelve a ser incompleta, presentando rasgos en forma de lóbulos muy cerca de los bordes, cuya densidad aumenta a medida que el voltaje se incrementa hasta -60 V. No existen señales de grafeno dentro de estos lóbulos, sugiriendo una completa remoción del material. Un efecto adicional es la aparición de escamas de grafeno con un tamaño de 7 nm aproximadamente, mediante la utilización de voltajes inferiores a -20 V.

---

Por otro lado, también se desarrollan experimentos relacionados con descargas eléctricas en regiones localizadas debajo de la punta, con el fin de estudiar los mecanismos físicos que rigen el procedimiento de la electroerosión. La descarga eléctrica se produce durante la aproximación vertical a la superficie de la muestra, presumiblemente justo antes del toque. Para ello, se diseña un modo especial de trabajo que evita los efectos del rayado mecánico y permite una mejor apreciación de estos mecanismos mediante toques sucesivos, creando patrones de puntos con diferentes parámetros de operación. Estos experimentos se llevan a cabo en diferentes sustratos e inicialmente en condiciones de baja humedad relativa. Adicionalmente, se incluyen experimentos variando en aumento la humedad relativa, con el fin de identificar su rol en este fenómeno.

---

## STATEMENT OF ORIGINALITY

This thesis is an account of work carried out by the author in Departamento de Teoría de la Señal y Comunicaciones, Sistemas Telemáticos y Computación at Universidad Rey Juan Carlos, under the supervision of Dra. M<sup>a</sup> Del Carmen Coya Párraga and Dr. Ángel Luis Álvarez Castillo. Where the work of others has been drawn upon this is duly acknowledged in the text, and a list of references is presented at the end of each chapter. No part of this thesis has been submitted towards the completion of another degree at Universidad Rey Juan Carlos or elsewhere.

Parts of the thesis have been submitted to or published in the following scientific journals or conference presentations.

### **Journal articles:**

Miguel García-Vélez, Ángel Luis Álvarez and Carmen Coya “Development of electrical-erosion instrument for direct write micro-patterning on large area conductive thin films”. *Review of Scientific Instruments* 2015, Submitted.

Esteban Climent-Pascual, Miguel García-Vélez, Ángel Luis Álvarez, Carmen Coya, Carmen Munuera, Xavier Díez-Betriu, Mar García-Hernández and Alicia de Andrés. “Large area graphene and graphene oxide patterning and nanographene fabrication by one-step lithography”. *Carbon* 2015, DOI: 10.1016/j.carbon.2015.04.018, in press.

Carmen Coya, Ángel Luis Álvarez, Miguel García-Vélez, Pablo Martín-Ramos, Manuela Ramos-Silva, Carlos Zaldo, Pedro Chamorro-Posada and Jesús Martín-Gil. “NIR-OLED (1.54  $\mu\text{m}$ ) emitting electroluminescent diode arrays based on Er-complexes manufactured by cost-effective methods”. *Opt. Pura Apl.* 46 (3) 257-263 (2013).

C. García Núñez, J. Jiménez-Trillo, M. García-Vélez, J. Piqueras, J.L. Pau, C. Coya, A.L. Álvarez. “Sub-micron ZnO: N particles fabricated by low voltage electrical discharge lithography on Zn<sub>3</sub>N<sub>2</sub> sputtered films”. *Applied Surface Science* 285P, pp. 783-788 (2013).

---

## Conference proceedings:

M. García-Vélez, A.L. Álvarez, C. Coya, G. Alvarado, X. Díez-Betriu, A. de Andrés. “Direct-write patterning of metals and graphene oxide electrodes by arc erosion for organic device manufacturing”. *IEEE Proc. Of the 2013 Spanish Conference on Electron Devices*, pp. 2013.

## Conference Contributions:

M. García-Vélez, A.L. Álvarez, C. Coya, G. Alvarado, X. Díez-Betriu, A. de Andrés. “Direct-write patterning of metals and graphene oxide electrodes by arc erosion for organic device manufacturing”. Spanish Conference on Electron Devices; February 12-14, Valladolid - Spain, 2013.

R. Mallavia, A. L. Álvarez, C. Coya, J. Jiménez-Trillo, M. García-Vélez, G. Alvarado “Proposal of a low-cost, mask-less procedure for patterning electrodes of organic devices at nanoscale using electrodischarges”. 13th Trends in Nanotechnology International Conference (TNT2012), Symposium: Nanofabrication tools & nanoscale integration. September 10 - 14, Madrid – Spain, 2012.

Miguel García-Vélez, Carmen Coya, Ángel Luis Álvarez, Xavier Díez-Betriu, Alicia de Andrés. “Cost effective pre – patterned alternative anode for bulk heterojunction organic solar cells”, 5th International Symposium on Flexible Organic Electronics. July 2 – 5, Thessaloniki – Greece, 2012.

Xavier Díez-Betriu, Miguel García-Vélez, Carmen Coya, Ángel Luis Álvarez, Alicia de Andrés. “Polymer-fullerene organic solar cells on amorphous-nanocrystalline Al doped ZnO transparent conducting thin films” 8th International Conference on Organic Electronics. June 25 – 27, Tarragona – Spain, 2012.

A. L. Álvarez, J. Jiménez-Trillo, G. Alvarado, M. García-Vélez, C. Coya. “Development of organic microdisplays and field-effect transistors by a low-cost, mask-less procedure using electrodischarges”. The 8th International Conference on Organic Electronics. June 25 – 27, Tarragona – Spain, 2012.

A.L. Álvarez, C. Coya, J. Jiménez-Trillo, M. García Vélez, G. Alvarado, C. García, J. L. Pau. “Development of organic micro-device arrays using a new low-

---

cost, large area lithographic technique based on arc erosion”. E-MRS Spring Meeting 2012, Symposium Q: Novel Materials and fabrication methods for new emerging devices. May 14 –17, Strasbourg – France, de 2012.

## CHAPTER 1 . RESEARCH CONTEXT: INTRODUCTION

### 1.1 ORGANIC ELECTRONICS CONTEXT

The research carried out in this Thesis is mainly framed within the field of Organic Electronics. Although not restricted to this field, the lithography technique here proposed finds straightforward application on those materials, thin films, active layers and electrodes used in Organic Electronics, whenever they exhibit certain conductivity. At the same time, its main characteristics, such as scalability and good accuracy and precision, are notably suitable for large area operation, a key point for organic electronics.

It is worth remembering that the synthesis of some organic molecules and polymers with electrical behavior [1], paved the way to a new class of electronics, Organic and Large Area Electronics (OLAE), with currently huge market potential in four key application areas: displays; lighting; photovoltaics and integrated smart systems (radio-frequency identifications tags, RFID, for example). More importantly, it is predicted that over the course of the next decade the market will gain an annual value of several hundred billion Euros [2, 3]. Organic materials provide electronic devices with certain unique properties out of reach for materials used in conventional Microelectronics (silicon, III-V or II-VI materials). These properties include chemical sensing, biocompatibility, flexibility, large area applications and low-cost processing.

Low-cost manufacturing methods and compatibility with flexible substrates are two of the most exciting chances of plastic electronics. These attributes have enabled

new outstanding applications such as: chip RFID tags made from interconnected organic field-effect transistors (OFETs), large-area photovoltaic cells (PVs) on flexible substrates or painted on building roofs (which may be economically replaced every year to match color preferences of homeowners), bright and high resolution flat screen displays made from organic light emitting diodes (OLEDs), see for instance [4, 5].

The success of organic active materials lies in the ease of tuning electronic and processing properties by chemical design from the synthesis stage, as well as mechanical flexibility and chance of low cost processing at low temperature. These characteristics changed the manufacturing paradigm in favor of the Roll to Roll (R2R) technology, and those compatible printing methods. R2R is currently accepted as the more promising processing technology for high throughput of this kind of devices [6].

In general, the main drawback of organic materials for electronic applications comes from their amorphous structure, which eventually reduces charge carrier mobility and makes them not suitable for high speed electronics. Degradation of the properties, variability and lack of reproducibility during certain manufacturing steps also ballast the progress of Organic Electronics. However, the astonishing properties of graphene [7, 8], which, show a good compatibility with the previous paradigms, creates new expectations and paves the way to new added value applications, overcoming current economic and environmental drawbacks.

In any case, a real take off of this promising market will demand novel methods focused in achieving high production yields. This is the context in which this Thesis work has been realized, trying to develop a novel patterning technique that meets high yield, environmental and cost requirements. In this context, we have focused our efforts in developing a one-step and dry lithography method for thin film conducting electrodes on a variety of materials. This Thesis proposes a novel, cost-effective approach based on the erosion effect associated to electrical discharges.

In this chapter, the market around the field of Organic Electronics is reviewed and updated. Some brief notes on patterning methods for high yield and large area substrates are also commented. Next, the state of the art of an industrial technique focused on electrical discharges (EDM) to conform metal pieces, in which our prototype was firstly inspired, is described in detail. In the last subsections, basic principles driving the operation of our electric-arc lithography system, together with current advances on lithography of graphene, are discussed. Chapter 2 lists briefly the main objectives of this work, and in chapter 3 our specific home-made prototype is presented, as well as the

experimental techniques and methods used for carrying out this research. In chapter 4, the principles of arc erosion, together with the results obtained for patterning of conventional electrodes, based on Indium Tin oxide, ITO ( $\text{In}_2\text{O}_3: \text{Sn}$ ), Gold, Aluminum, ZnO:Al (AZO), or other novel semiconductors such as  $\text{Zn}_3\text{N}_2$  are discussed. Encouraged by the high expectations of graphene and related materials, chapter 5 is devoted to the study of lithography on graphene, graphene oxide and reduced graphene oxide. A circuital model is proposed for the arc erosion physical mechanism. Finally, the conclusions are exposed on chapter 6.

### 1.1.1. Market size, potential and profitability: 2013 - 2023

Market predictions state that Organic Light Emitting Displays (OLEDs) is outlined with the highest market participation (approximately 65%) for Organic Electronics, followed by conductive inks used for a wide range of applications and finally, thin film photovoltaics. This market is divided into displays and lighting submarkets. Today OLED displays can be found in many small mobile devices like smartphones, music players, cameras as well as in TVs, in contrast to the OLED lighting submarket, which has yet to take off (just a few and expensive commercial white OLED-based lamps are available). But both exhibit very good growth expectations [9].

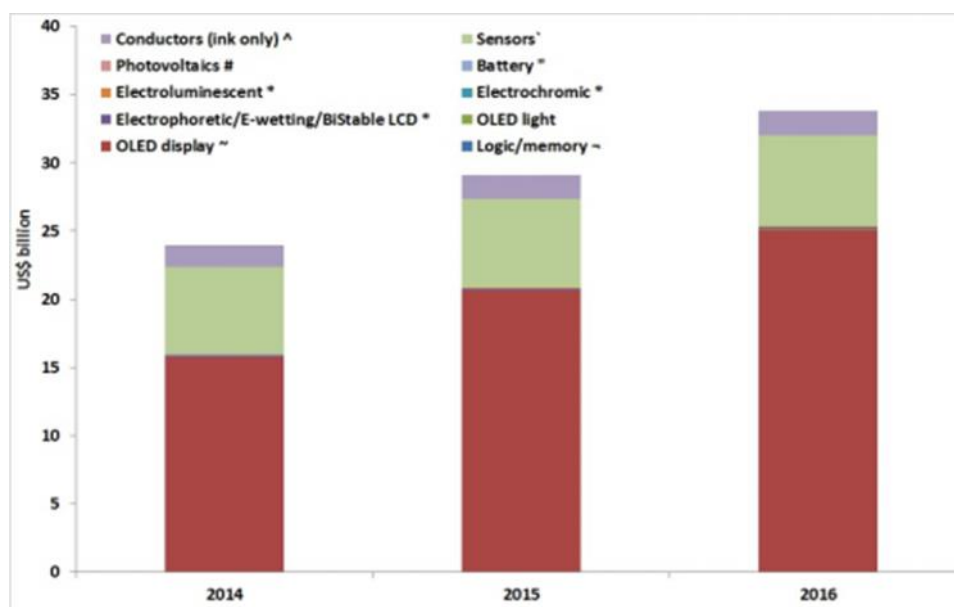


Figure 1.1: Market forecast by component type (US\$) [9]

On the other hand, stretchable electronics, logic and memory, and thin film sensors are much smaller segments, its participation in the market being more balanced,

but with a huge growth potential. Figure 1.1 shows a graphical summary of the actual market by components in terms of US\$ billions for the coming years (2014 - 2016).

According to consulting companies (IDTechEx), the total market for printed, flexible and organic electronics is expected to grow from \$16.04 billion in 2013 to \$76.79 billion in 2023. OLED display (printed) will cover the 85% of the global market. Conductive ink, thin film photovoltaics and others would have a more discrete participation but even so is expected to experience a huge growth. Figure 1.2 shows the market share prediction for 2023. In addition, Table 1.1 summarizes the total current market size and profitability of each sector.

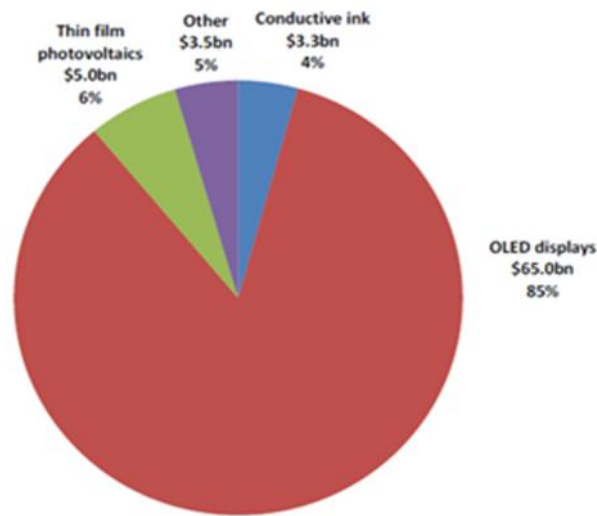


Figure 1.2: Printed Electronics market by 2023 [9].

For the sake of clarify a useful comparison can be made: global demand for antibiotics is expected to reach \$44.68 billion by 2016. The market has been expanding with an average annual growth of 6.6% between 2005 and 2011, and its expansion is expected to slow to 4.6% in recent and coming years, from 2012 onwards [10]. If this annual growth rate is maintained until 2023, antibiotics demand will be in \$61.21 billion, \$15.58 billion less than the prognostics for printed, flexible and organic electronics market by 2023. This example shows the importance of this market and their economic impact.

Printing will impact many different markets from displacing existing technologies, such as conventional displays and tentatively some silicon based photovoltaics, creating new markets, such as ultra-low cost “disposable electronics” on retail packaging, and large area sensors among others. There is a large amount of organizations working on the topic as academic institutes as well as companies with equally market share.

Component Type	2013 Market for incumbent technology	Printed. Organic, Flexible electronics Technology	Development Time	2013 Market size, \$ millions	Technology status 2013	Profitable? And IDTechEx Comment
<b>Displays</b>	\$120 billion (mainly LCD displays)	OLED Displays	20 years	10,000 – includes front plane and TFT backplane i.e. OLED module	Organics for active layers, not printed	Yes, with rapid growth
		Electrophoretic	14 years	270 – front plane value only	Printing type process to make the film.	Yes, but market is in decline
		Electroluminescent	20 + years	120	Inorganic materials	Yes, but market is in decline
		Electrochromic	12 years	2	Inorganic Materials, printed	No, the technology is too early to be commercially successful.
<b>Lighting</b>	\$ 75 billion (fluorescent, incandescent, LED)	OLED Lighting	7 years	15	Organic materials for active layers, not printed	No, but increase in investment and products.
<b>Photovoltaics</b>	\$ 30 Billion (mainly silicon)	OPV, DSSC	10 years	< 2	Organic materials for active layers, some printed	No, the technology is too early to be commercially successful.
		CIGs	15 years	2,860	Inorganic materials, majority not printed	Break-eve-due to PV commercial climate, the entire PV industry is barely breakeven.
<b>System Components</b>	\$ 200 Billion (Silicon)	Logic and Memory	12 years	3	Organic and inorganic materials, some printed	No, no mainstream successful commercial applications yet.
	\$ 30 Billion	Thin Film Batteries	15 years	4	Some printed	No, only one main application which has now stopped. Other projects in pilot.
	>\$ 20 Billion	Sensor and Actuators	10 + years	160	Mostly printed, organic and inorganic materials	Yes, highlight is healthcare electrodes/glucose test strips.
		Conductive Ink	15 + years	2,660	Mostly inorganic materials, all printed	Yes, for PV bus bars but the market has shrunk since 2012 due to the reduction in the PV market. Short term grown.

Table 1.1 Current opportunity: market size and profitability [9].

### 1.1.2. Brief notes on patterning methods for high yield and large area substrates

A wide range of large area deposition and patterning techniques can be used for organic device manufacturing. Some of them add material over a substrate (additive techniques), other remove undesired materials to achieve desired features (subtractive) and other are hybrid. Additive techniques are varieties of printing procedures: inkjet-printing, rotogravure and flexography (Figure 1.3), well used in graphic arts industry, together with processes such offset printing, screen printing and soft lithography [11]. In contrast, those etching techniques such as Rapid Ion Etching (RIE) performed through masks, and laser ablation are typical subtractive techniques. Most of them make possible the so called “Printed Electronics”, where high throughput at low cost, while preserving quality of patterns, is the main concern.

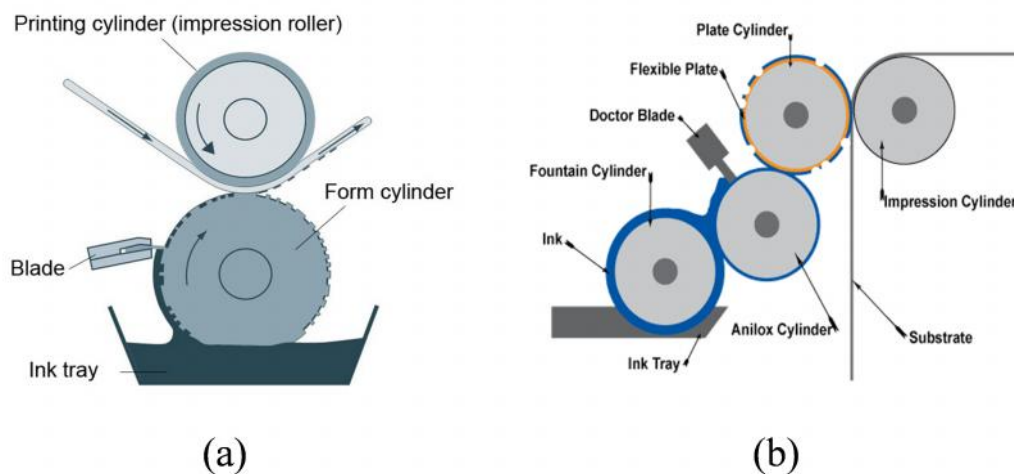


Figure 1.3: (a) Rotogravure [12] and (b) flexographic [13] scheme processes.

Regarding additive techniques, the printing procedures can have enormous throughput and low production cost. The challenges and critical printing parameters can be summarized as follows [1]:

- Printing accuracy and resolution. For example, a resolution of a few micrometers with  $\pm 5 \mu\text{m}$  position accuracy will be required for most of the smart phone or tablets displays. Multilayer printing accuracy is also a key factor.
- Wetting control and interface formation, which are key steps during manufacturing.
- Uniformity and flatness, especially critical in large panel displays. This is an issue also affected by the design of ink composition, and drying process.

- Compatibility of inks with printing components such as rollers, masks, doctor blades, and inkjet heads, with significant effect on the yield and quality in mass production.
- Throughput and cost considerations: reproducibility maintained for hundreds of printings.

In general, the smallest feature that can be printed (lateral resolution) in commercial prototypes typically ranges 10 to 100  $\mu\text{m}$ , depending on process, throughput, substrate and ink properties. Film thickness can range from under 1  $\mu\text{m}$  to tens of  $\mu\text{m}$ . Comparison of characteristics for different printing methods are summarized in Table 1.2.

Printing method	Ink viscosity (cP)	Line width ( $\mu\text{m}$ )	Line thickness ( $\mu\text{m}$ )	Speed (m/min)	Other feature
Inkjet	10–20 (electrostatic inkjet: Approx. 1,000)	30–50 (electrostatic inkjet: Approx. 1)	Approx. 1	Slow (rotary screen: 10 m/s)	Surface tension: 20–40 dyn/cm On demand Noncontact
Offset	100–10,000	Approx. 10	Several–10	Middle—fast Approx. 1,000	
Gravure	100–1,000	10–50	Approx. 1	Fast Approx. 1,000	
Flexo	50–500	45–100	<1	Fast Approx. 500	
Screen	500–5,000	30–50	5–100	Middle Approx. 70	
Dispense $\mu\text{CP}$	1,000–10 <sup>6</sup> –	Approx. 10 Approx. 0.1	50–100 Approx. 1	Middle Slow	Single stroke
Nanoimprint	–	Approx. 0.01	Approx. 0.1	Slow	

Table 1.2: Comparison of characteristics for different printing methods [14].

In additive techniques, resolution, reproducibility, ink formulation and post print processing are the main challenges to overcome. On the other hand, feature distortion caused by the way the fluid is deposited over a surface is likely the main concern. Most inks need to be annealed / sintered after printing, and this can affect the substrate used and other layers deposited on the substrate. It also adds time and/or cost.

Among all the additive techniques, it is worth giving some brief notes about inkjet printing. This technique has aroused much interest to deposit functional materials, avoiding many lithographic steps, and saving a large amount of active material [15]. Here, a printing cylinder or plate is not necessary and can thus better correct in-line distortion issues. It is used to provide successful results also in combination with pre-

patterned substrates. Print heads have been successfully reduced, achieving features in the order of one micron in laboratory. Throughput of this kind of machines is not very high, but it is beginning to increase due to the implementation of several types of heads in a single machine. There are two interesting variants that have begun to generate great expectations: aerosol and super inkjet printing. The second one has claimed for the ability to manage micron features without pre-patterning the substrate.

With reference to subtractive techniques, the one proposed in this thesis work, based in the concept of electrical erosion, must be considered within this group because it performs material removal using electrical discharges. Later on, it will be shown its ability of drawing patterns with specific dimensions and purposes on conductive materials. In this line, it is worth commenting briefly other typical subtractive technique, laser ablation, which may act as a competitor in the field of micro- nano-patterning extended to large areas. In laser ablation, material is removed in the volume where the energy of a single laser pulse is absorbed. It obviously depends on the material optical properties and the laser wavelength (for a review of applications of laser ablation see this “Special Issue on Laser Processing” [16]).

Among the advantages of laser ablation it can be cited that laser pulses may be very fast (from ms to fs) and can be precisely controlled. Thus, material can be removed so quickly that very little heat is transmitted to the surrounding, so it can be performed on delicate or heat-sensitive materials. Moreover, no solvents are used, so it is environmentally friendly. Eventually, although the setup requires a high initial investment, the running costs are low. The main advantage of this technique over electrical erosion is performance on dielectric semi-transparent materials (quartz, sapphire, methacrylate, etc.) where our electrical technique is almost useless (it requires conductive materials) or would require very high voltages.

Among the disadvantages: resolution is dependent on the focusing system, and is usually limited to the beam waist diameter for the used wavelength. Large area operation, where a small tilt is present and then flatness is difficult to maintain, implies a continuous laser beam focus correction, which makes difficult the implementation. Otherwise, size and feature resolution could be jeopardized along the sample. Changing the target material uses to require changing wavelength (ultimately, changing the laser equipment, which may not be available for the specified wavelength). In thin films, where the absorbing volume is very small, it is not always easy to find an appropriate laser, and in many cases, the layer below is also ablated, which jeopardizes subsequent

uses. In addition, irregular edges in the patterns are often provoked. This can be critical, for example, with graphene. Many of these drawbacks are resolved with the electrical erosion system. Moreover, working with electrical signals allows operating in ‘read-mode’, a way of monitoring and feedback the process ‘on-line’ during operation, something out of reach for laser working.

A comparison between throughput and feature size of several processes above mentioned is shown in Figure 1.4, including our arc-erosion technique highlighted by the red dashed rectangle. There are no single standard processes in existence today: the final choice depends on the specific requirements of the device.

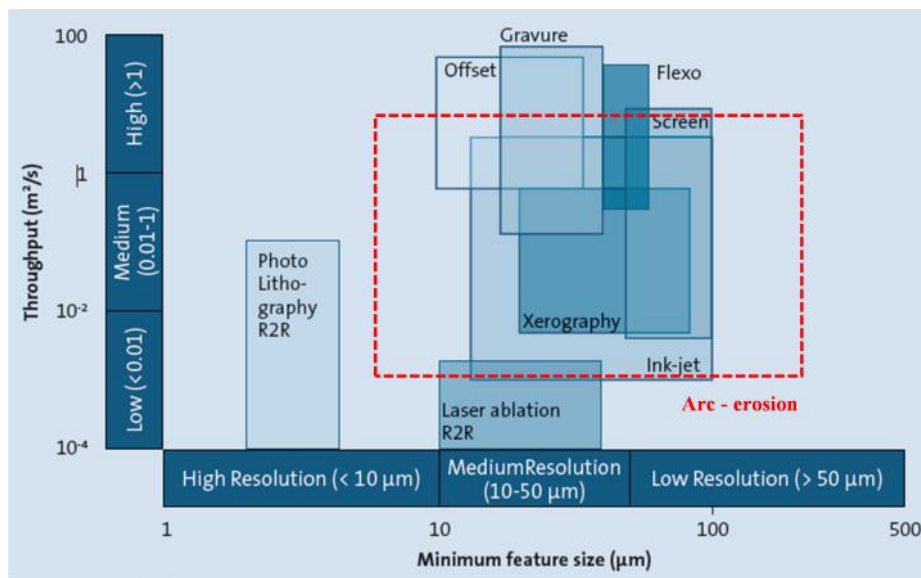


Figure 1.4: Throughput versus feature size for a range of typical production processes [17], where we have included our prototype for electrical discharge lithography (red dashed rectangle).

## 1.2. PRINCIPLES OF ELECTRICAL DISCHARGE MACHINING

One of the industrial techniques which most resemble the one proposed in this Thesis work is electro-discharge machining (EDM). Actually conventional EDM is performed in conditions very far from those used in our prototype, but it shares a similar basic principle, namely, to take advantage of the huge energy supplied by a localized electrical discharge to remove material. EDM uses high voltage pulses, typically from hundreds to kV with duration of  $\mu\text{s}$ , and with mediation of a dielectric fluid between tip and sample in order to remove residues. In contrast, our technique is allowed to operate with DC low voltage in room conditions. In section 1.3, the reasons for this difference will be explained. Next, a detailed introduction on how to manage electrical discharges to machine metal blocks is presented.

The erosive effect of electrical discharges was discovered by the English scientist Joseph Priestley in 1770. But it was not until 1943, 173 years later during World War II, when scientists B.R. and N.I. Lazarenko began using the destructive effect of such discharges for machining new developed metals which were very difficult to process with conventional methods. The Lazarenko's machine consisted in a first order RC (Resistance – Capacitance) relaxation circuit, one of the most basic in electronics, shown in Figure 1.5: it stores energy for certain time and then discharges that energy through a resistance. The purpose of this circuit is to apply an amount of energy in terms of joule heating enough to remove material in a given area and in a very short time [18].

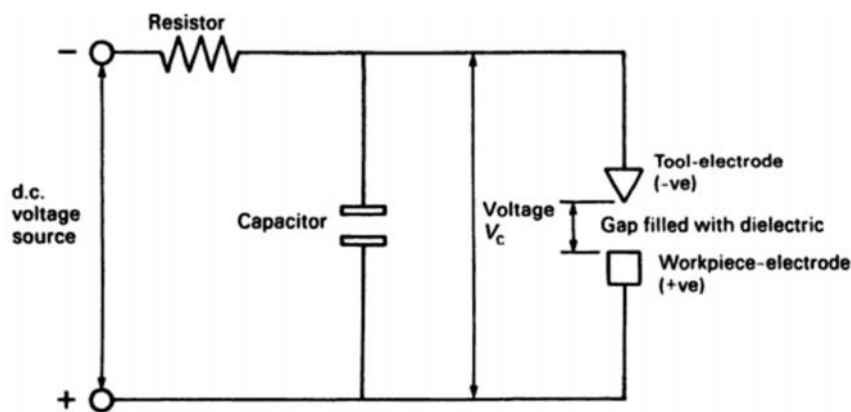


Figure 1.5: Lazarenko's RC Circuit [19, 20]

In 1950s this relaxation circuit was industrially introduced, being the basis of subsequent developments in EDM technology. Until that time, the only known EDM process was Conventional EDM, and its applicability in industry and market was widely accepted. At the beginning of 1970s, driven by the great advances in electronics, Wire EDM machines (WEDM) appeared, where discharges were accomplished between a wire and the metal piece, a technique suitable to cut blocks. But the breakthrough came in 1980s with the introduction of power transistors and Computer Numerical Control (CNC) giving a boost to this technique, improving the efficiency of the machining operation. These improvements led to more stable and easy control machines and eventually to better defined and finished parts.

EDM is a subtractive material technique which is performed by a successive unidirectional high energy pulsed current in a dielectric medium (usually a liquid) between an electrode and a work piece. Material removal is obtained by a succession of sparks separated in time which, according to the thermoelectric theory results from a

sudden conversion of electrical energy into thermal energy. There is not mechanical energy intervention, so properties as toughness, hardness and strength of the material are only indirectly related to the material removal procedure [20, 21].

In EDM the work piece is immersed in a dielectric fluid. The insulating effect of this dielectric fluid is important to avoid electrolysis of the electrodes during the process [2]. The main functions of the dielectric fluid are: to act as insulator until the potential reaches a threshold value, as a flushing medium to remove any debris between electrodes, and to serve as a cooling mechanism. The most common dielectric mediums used are hydrocarbon oils such as Kerosene [22]. Transparent and low viscosity fluids are also used, although are more expensive but makes the work piece cleaning more easily. These machines are provided with a circulation and filtration system to purify the dielectric fluid and reuse it [21].

The first main condition for processing any material with this technique is that it must be conductive. The melting point and latent fusion heat are also important physical properties in determining the volume of metal removed per discharge. The elimination volume per discharge is typically between  $10^{-6}$  to  $10^{-4}$  mm<sup>3</sup> [21].

With reference to composition of the probe electrode, graphite, copper, tungsten and tungsten carbide are the most used [22]. Mechanical wear of the probe is a very important factor because directly affects the dimensional accuracy and geometry of features, and it is related with the material's fusion point: the smaller the greater is the wear rate. For this reason graphite is considered an adequate material due to its maximum wear resistance [21]. Research is being done on many new materials including composites, for example a ZrB<sub>2</sub>-Cu tool, showing higher material removal rate (MRR) and lesser tool wear (TWR) as compared to copper, but had some shortcomings in terms of average surface roughness and over-cut [22].

All new developments in this technology follow the main objective established years ago: machining of extremely stiff and hard materials, i.e., high strength and temperature resistive (HSTR) conductors (like tungsten carbide) with complicated geometry and profiles.

Currently, there are two types of EDM modalities widely used in industry: Conventional EDM and Wire EDM or WEDM (Figure 1.6). Both modalities are used to drill circular and non-circular holes, generate profiles and make complex shaped dies of both macro and micro sizes [22]. In Conventional EDM, the work piece can be formed

either by replication of a shaped tool electrode, or by a three dimensional movement of a simple electrode, or the combination of both methods. Numerical controls take care of synchronization of the gap conditions, axes and pulse generators [23].

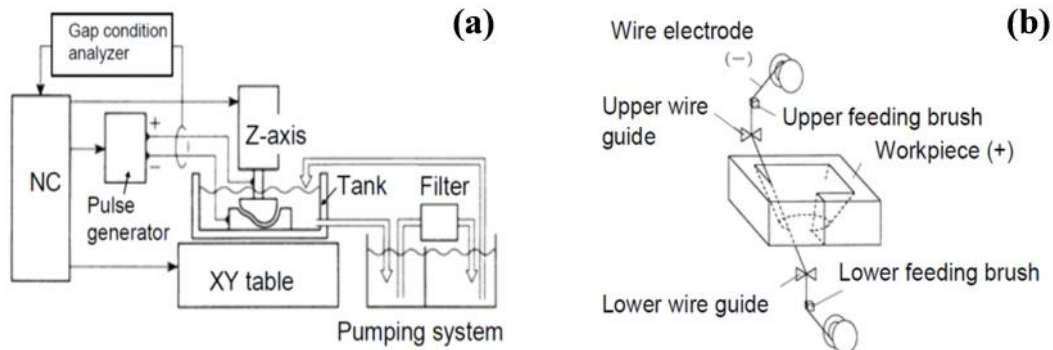


Figure 1.6: Sketches of the most widely used EDM modalities; (a) Conventional EDM and (b) Wire EDM [23].

Below, in Figure 1.7 are shown some examples manufactured with Conventional EDM. The accuracy is limited by the geometry of the electrode and also by the manufacturing conditions like involved current, which plays a crucial role for surface finishing. Due to the constant development in this area, through new mechanical and electronic designs, more complex geometries can be manufactured. As an example, Makino [24] Company offers a model with interesting technical aspects, highlighting its capacity of producing corner radius of 0.005 mm and surface finish quality of 0.6 micron (maximum height roughness -  $R_y$ ).

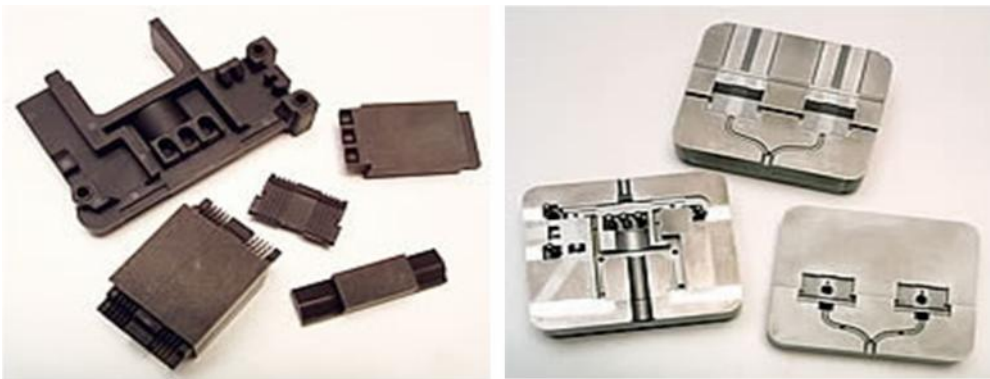


Figure 1.7: Conventional EDM part examples (y mm o um typical minimum feature) [25].

Wire EDM, is a Conventional EDM variation, a major recent development. This modality, consist of a wire which moves slowly describing a predetermined path cutting the work piece. This process is used for cutting plates up to 300 mm thick, fabrication of hard metal tools, punches and dies. Moreover, it is also used for cutting intricate components for electronics industry.

Wire is usually made of brass, copper or tungsten, also coated by zinc or brass with several layers. Its diameter is typically 0.3 mm for roughing and 0.2 mm for finishing cuts. Relevant physical properties as tensile strength and fracture toughness must be suitably chosen, as well as a high electrical conductivity. The system should guarantee the ability to drag the waste generated in the process. Concerning the manufacturing speed it is common to use values between 0.15 – 9 m/min [21]. In Figure 1.8 can be seen two images corresponding to a processing stage used and a finished part.

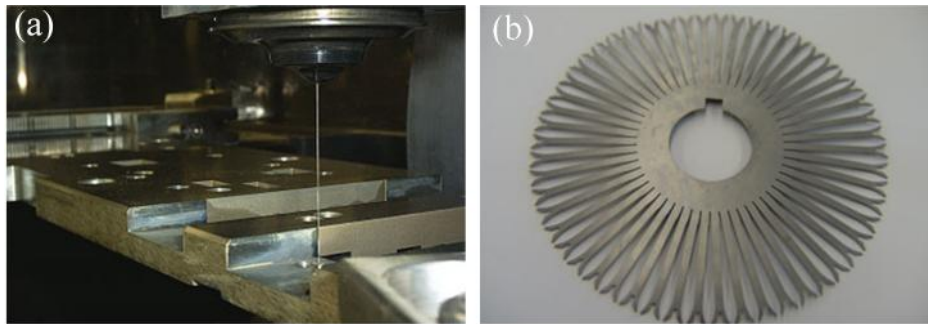


Figure 1.8: (a) WEDM processing stage and (b) final processed example part [26].

All the effort and interest, academic and/or industrial, focuses in to develop improvements to these variations with the aim to combine processes already used with WEDM, hybrid machining processes (HMP) leveraging the combine advantages.

### 1.2.1. EDM Process Parameters

It is considered of relevance to discuss the most important processing parameters for an efficient and fast processing, regardless of the EDM type used. These are summarized in this section:

- a) Discharge voltage. In EDM, this parameter is fixed in view of the spark gap and breakdown strength of the dielectric medium. Potential difference begins to increase until an ionization path appears through the dielectric. Once the current begin to flow this potential difference drops and stabilizes [20].

The properties of flushing and debris drag can be improved by increasing the gap between electrode and work piece, but this inevitably leads to work with higher discharge voltage. Variables like removal rate (MRR) and tool wear (TWR) also increase, what could result in a high surface roughness [23] and for this reason a compromise must be assumed.

b) Peak current. This is the most important parameter in EDM technology, because, it governs the power delivered to the target during the process. This value is established as function of the cut area and the performing operation.

If the current is incremented to a higher level, MRR improves but the surface finishing and tool's wear are jeopardized. This in turn will reduce accuracy. Using graphite for these purposes reduces this issue in a considerable way [20, 23].

c) Pulse Duration (On-Time) and Interval (Off-Time). Both parameters are typically fixed in microseconds. Material removal depends on the applied energy during on-time pulse and that is why duration of these pulses and the number of cycles per second are important [23]. The longer duration, the wider and deeper the crater will be, so the surface finishing is greatly affected by these parameters. Long on-time pulse duration will cause that MRR has a considerable slowing rate because of the residue recast phenomenon associated with the impact produced by the electric arc. Off-time interval directly affects the cut stability and operation speed. Slower time to make the operation faster may cause the dielectric fluid to not perform satisfactorily the debris flushing and cleaning. It could not also be well deionized making the next sparks unstable.

d) Pulse Waveform. Commonly, generators use rectangular pulse shape. To facilitate ignition sometimes transient high peak voltage pulses are introduced before the main pulse.

e) Polarity. In general, is determined by experimentations and depends on tool material, target material, and pulse length combinations [20]. In general, negative polarity (probe negative biased with respect to the target material) means that electrons impinge on the material during dielectric breakdown and otherwise with positive polarity. That is why negative polarity uses to be more efficient for etching materials.

f) Electrode gap. As mentioned above, this is a very important parameter for an efficient working of EDM. To guarantee an excellent stability and

performance of the system two important requirements are necessary: high reaction speed in order to respond to short circuits and a gap stability of the system during operation.

### 1.2.2. EDM Applications

This section talks about some EDM applications commonly found in the industry. Topics related to micro and nano - EDM will be discussed separately because of its mayor interest in this Thesis work

#### 1.2.2.1. Micro – EDM and Nano - EM

Reducing cost and increasing reliability is closely linked to miniaturizing electronic devices. Due to the high precision and surface quality, EDM is a potentially important technique. Numerous developments in EDM have focused on the production of micro–tools, micro-components and components with micro-features [27].

Micro – EDM is similar to conventional EDM, the significant difference between micro and macro EDM is the plasma channel radius. By controlling the amount of energy released, it is possible to machine micro-features on electrically conductive materials [23]. Good repeatability has made micro – EDM the best process for achieving high accuracy in micro-features [27].

Pham *et al*, have categorized the micro-EDM technology for manufacturing micro-features in four groups:

- Conventional micro-EDM. A micro-featured electrode is used to reproduce its mirror image in a work piece.
- Micro - Wire EDM, where 0.02 mm wires are used for cutting conductive work pieces.
- Micro – EDM drilling, where 5 – 10  $\mu\text{m}$  diameter electrodes are used to drill micro holes in the work piece.
- Micro – EDM milling, where 5 – 10  $\mu\text{m}$  diameter electrodes used to machine three- dimensional micro – cavities, adopting types of movements similar to the ones used in conventional milling.

As mentioned above, trends towards the miniaturization have rapidly increased to such an extent of modifying the existing EDM machines [23].

Process mechanism, surface integrity, sensing and control, tooling and tool wear continue to be an important topic of research. The boiling and the melting point of an electrode material are major physical properties to take into account. Tungsten with its high melting point and tensile strength is the predominant material in micro – EDM technology [22]. Tool's wear is taken and important role as the measurement scale is reduced. In this line, suggested wear compensation techniques are already reported [22, 28, 29, 30].

There are a few reports describing a novel nano electro-machining process based on a scanning tunneling microscope (STM) platform in atmospheric air, capable of fabricating nano-features of 10 nm and also an array of nano-features in programmed way with repeatability. The volume of material removal increases almost linearly with increasing number of features machined. In Figure 1.9, there is a schematic presentation of the dry Nano-EM setup proposed by Jahan et al. [31]. Authors state that one of the major challenges in nanofabrication using dry nano-EM is the roughness of the surface, which should be in the angstrom level in order to ensure that all the nano-features are machined properly. In consequence, this technique is not valid for large scale applications.

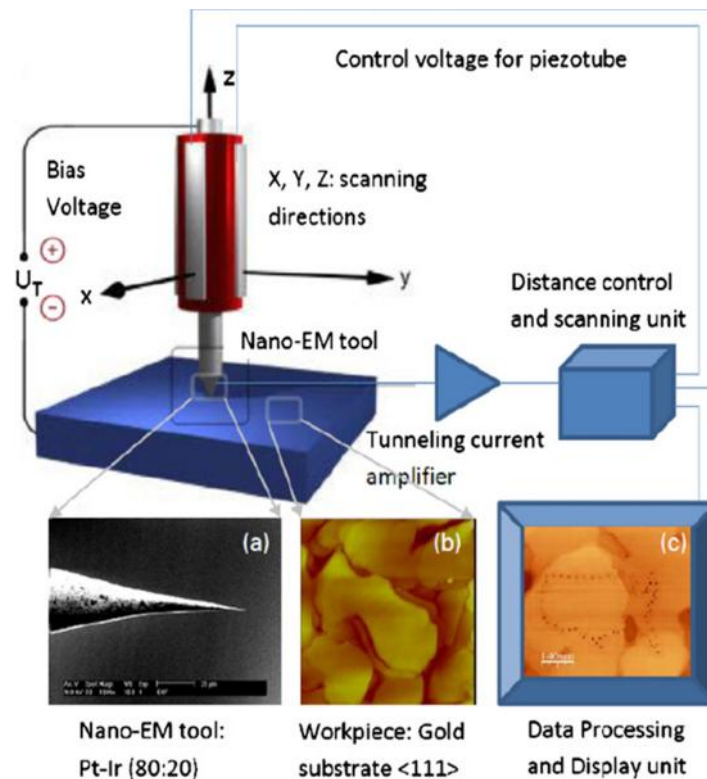


Figure 1.9: Dry Nano-EM setup proposed by [31].

### 1.3. COST EFFECTIVE LITHOGRAPHY METHOD BASED ON ARC-EROSION SYSTEM

Cost effective and environmentally friendly procedures are currently a great challenge for the industrialization of future devices and applications in a wide variety of areas. This Thesis faces the challenging problem of implementing a low-cost and large area patterning procedure compatible with roll-to-roll production lines. We propose a novel approach taking advantage of arc-erosion effect [32]. Operating principles and basic aspects directly related to this technique are discussed throughout this section.

#### 1.3.1. Aspects and Basic Operating Principle

The study of electrical discharges on conductive materials is performed using a conventional needle-to-plane electrode configuration according to the scheme shown in Figure 1.10, where the plane represents the sample to be patterned. This arrangement is suitable to affect at once small material regions of the order of the tip diameter. Since these discharges are transient phenomena involving a wide range of currents depending on the measurement configuration, I will adopt the general term *spark* when speaking about the short electrical trace measured by the oscilloscope during this discharge.

In our case, commercial spring-probes (made of beryllium copper), are used to damp the contact between tip and sample. The spring constant is  $300 \text{ N/m} \pm 20\%$ , which, as far as we have observed, prevents mechanical erosion of layers for those spring compressions below  $1 \mu\text{m}$ . The most used probes are cone-shaped with apex angle between  $45^\circ$  and  $60^\circ$ , and average tip radius from  $10$  to  $20 \mu\text{m}$ . Alternatively, we have also used acupuncture needles (described in Chapter 3, Figure 3.10), with very good tip sharpness although not having a spring to damp contact with the sample. More details on these probes are given in section 3.1.4 (Chapter 3).

The probe is *negatively* biased with a DC voltage ( $0 - 100 \text{ V}$ ) respect to ground, which is located on the material surface by an array of silver paint dots. The probe is driven by means of a home-made XYZ setup, controlled by computer using specific software. The spark current is continuously monitored by a high sampling rate digital oscilloscope (Yokogawa DL6154, at  $1.5 \text{ GHz}$ ) as explained below.

Sparks are generated by gradually approaching the probe to the material at speeds in the range  $0.1 \text{ mm/s}$  to  $10 \text{ mm/s}$ . The tip contact point on the surface ( $z = 0$ ) is previously determined by recording the current response between probe and sample at

very low DC voltages ( $< 0.1$  V). In general, the contour of the working area is previously mapped to determine the tilt of the sample plane. Thus, our system does not need to eliminate the real tilt, but just “living with it” by recalculating the scheduled positions via software.

In order to measure the electrical characteristics of discharges we have arranged a circuit as shown in Figure 1.10. Current across the tip-sample gap is monitored with an oscilloscope in terms of voltage changes  $V_t = V_{Ch2} - V_{Ch1}$ , in a series resistor,  $R_t$ .

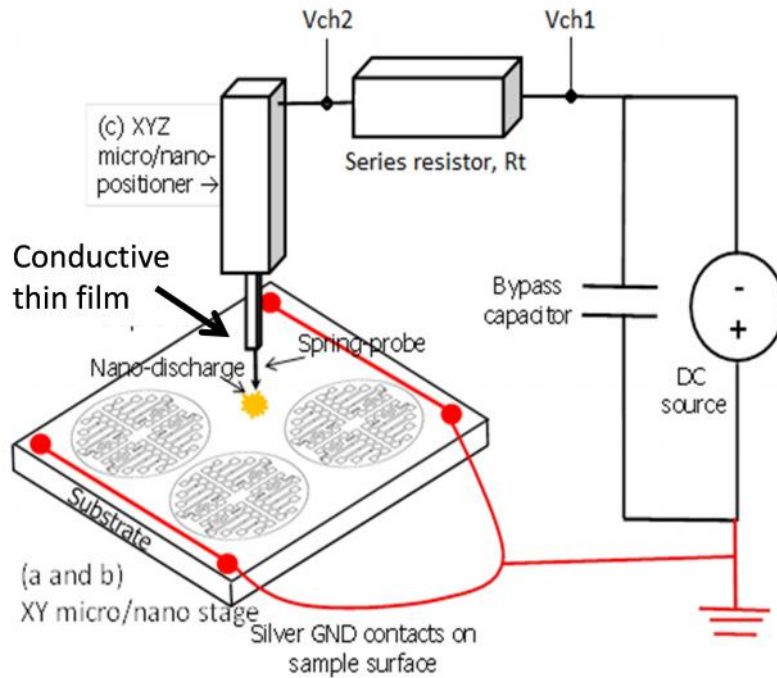


Figure 1.10: Schematic of homemade arc erosion system.

As the metal probe approaches the conductive layer, a capacitor is created by the tip-plane electrode configuration. The dependence of this capacitance on the gap distance will be carefully studied in Chapter 4. It has been experimentally estimated during operation to be about few tens pF, as explained in Chapter 4 and Chapter 5.

During the tip-sample approach at room conditions, a sharp current pulse (spark) between probe and material surface is detected at distances well below 100 nm. These sparks must be considered to appear within the regime of the ‘modified Paschen’s law’ [33], namely, a situation in which tip-surface gaps are so narrow that conditions of the atmospheric gas below the tip are insufficient to generate an electron avalanche, although field effect emission may assist the process. Indeed the mentioned distances should be sufficiently narrow to induce electron tunneling across the metal-air potential barrier by the expected local electric fields induced by the external voltage, which

should be of the order of  $10^9$  V/m [34]. This current, where electrons are pulled out the tip metal and impinge the material surface (according to the negative polarity), effectively short-circuits the tip-conducting sample capacitor, so the expected singularity in the capacitance at zero gap is never reached.

A relevant and well known feature is that the current produced by field effect emission is presumably able to damage the material surface. In case of very thin layers, this damage may lead even to complete material removal. In other cases, material is not entirely removed but cracked up to achieve conductance degradation. As far as we know, the detailed mechanisms responsible for this degradation are roughly described in the literature.

In any case, owed to this material damage, the current may be naturally interrupted without the need of controlling the voltage pulse duration. In this work, the interesting point is that material removal due to the spark current creates a crater below the probe. Eventually this leads the tip to settle on an insulating region of the surface, preserving a capacitive effect between tip and sample. Thus, the process may be triggered again if the tip moves horizontally on the surface and approaches the boundary with the pristine material because, at a distance sufficiently close to the boundary, a new electro-discharge may be produced. And so on. Eventually it leaves an insulating path beneath the tip as it slides on the material surface.

With the correct movement algorithm, the probe can draw patterns over samples at a great speed (tens mm/s), aided by the small spark duration, typically a few  $\mu$ s. Thus, similar or even faster operation than that offered by other commercial printing technologies, is achieved. The obtained accuracy is determined by the used tip's diameter and could be near to the micron.

This technique is fast and dry, useful to work on any substrate (curved, plastic, etc) as long as the target material shows a significant conductivity, and could be considered compatible with R2R technology.

Arc electric processing is a complex procedure, involving a few important machine parameters, as well as relevant material's characteristics. It is important to know what material we are working on, taking into account properties such as thickness, substrate type, tip size and geometry. Also room conditions (especially relative humidity) may play an important role, as it will be shown in Chapter 5.

With reference to operational parameters, the applied voltage together with its polarity, probe speed and pressure exerted by the tip on the surface are the main factors to be considered:

a) Applied voltage. In previous works it was observed that there is a threshold voltage ( $V_{th}$ ) below which electrical insulation is not achieved despite some material damage is created. In this case, optical inspection usually confirms that material has been removed or affected only partially during the discharge, but still a path for conduction remains after the tip has landed on the surface. This conduction is easily detected in the oscilloscope. In other words, below the threshold voltage, physical damage of the sample surface still remains, but not enough to interrupt conduction, so  $V_{th}$  depends on the material to be processed, tip geometry and layer thickness.

This novel technique has been already successfully proven to pattern different conductive materials like ITO or metals [35]. In Table 1.3, a list of threshold voltages for layers of 100 nm of various common electrodes we have been working on, over two kinds of substrates (glass and PET), and using a 40  $\mu\text{m}$  diameter probe, is shown.

Material/Substrate	Voltage Value [V]
ITO(100 nm)/Glass	10
ITO(100 nm)/PET	3-4
Au (100 nm)/Glass	4
Au (100 nm)/PET	3
Al (100 nm)/Glass	3
Al (100 nm)/PET	1-2

Table 1.3: Commonly used materials and threshold voltage for complete arc-erosion process [35].

These different values of threshold voltages for the same material on different substrates are partially due to the different techniques used to grow the material, but also to the thermal conductivity of the substrates and the different ability to dissipate heat. For instance, ITO on glass, whose thermal conductivity is  $1 \text{ Wm}^{-1}\text{K}^{-1}$ , gives rise to material removal at voltages above 10 V while ITO on PET, with  $0.15\text{-}0.24 \text{ Wm}^{-1}\text{K}^{-1}$  allows the electric ablation at lower voltage, above 4 V.

This characteristic is very important because allows the selective removal of stacked layers, as long as the threshold voltage to pattern the top layer was lower than that for the bottom one. Thus, vertical arrangements of stacked layers can be selectively processed [35]. An example is shown in Figure 1.11, where the top layers consisting of

Al/polymer are removed at an operating voltage of 3 V without affecting the ITO layer below (whose threshold voltage is about 10 V). It is relevant to note that this is very difficult to achieve with other subtractive techniques, like laser ablation.

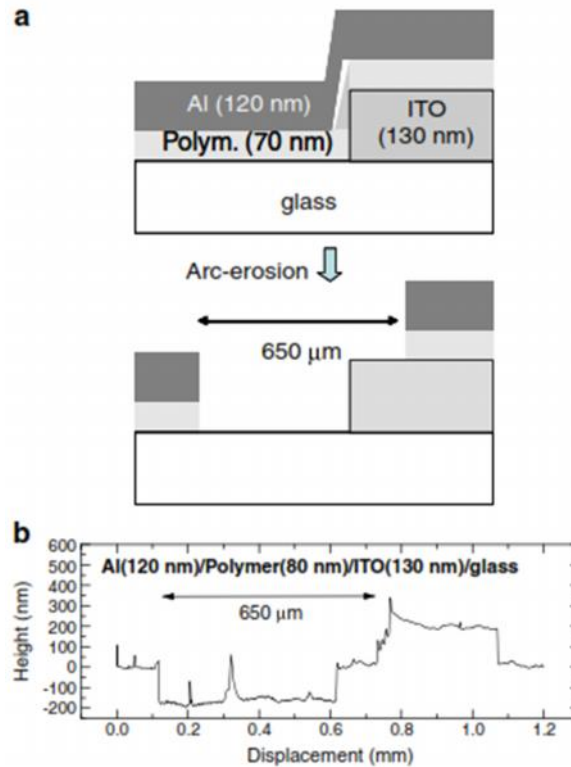


Figure 1.11: Patterning of an Al(120 nm)/Polymer(70 nm) bilayer deposited on top of a step of ITO (130 nm thick) on glass: (a) sketches the layer structure before and after Al erosion; (b) Shows a cross section recorded by contact profilometry [35].

On the other hand, when the operating voltage is well above the threshold, the erosion (crater diameter) progresses and gets larger. The mechanisms governing this progress are vaguely described in the literature, are not well understood and will be the subject of study in Chapters 4 and 5. In general, using too high voltages leads to creation of more residues, and more irregular features. So the experience suggests working at voltages above but close to the threshold one.

b) Pressure applied by the tip on the material's surface. The spring probe mounted in our system (300 N/m spring constant) is a way of avoiding the slow and expensive force feedback systems used in nanoscopic techniques like AFM or STM. It is likely the slowness of the force feedback systems what prevents real scaling of AFM and STM to long distances of the order of mm or cm.

With our system it is possible to establish the contact point on the surface ( $z = 0$ ) with 0.1 μm vertical accuracy. Despite the high precision of the mounted piezo-steppers, the limitation comes mainly from vibrations of the whole structure, not

entirely rejected by the pneumatic mount (described in section 3.1.3, of Chapter 3). In these conditions, the pressure exerted by our conventional tips when the spring is compressed  $< 1 \mu\text{m}$  (0.3 mN force) is  $< 0.5 \text{ MPa}$ , similar to that of a contact profilometer, and sufficiently low to consider mechanical damage as negligible. This spring compression is generally used in our experiments. However, even these characteristics may be excessive for smaller tips with diameters  $< 1 \mu\text{m}$ . In this case, a slight deformation of the tip could be produced. This is an issue that should be solved in order to reach submicron and nano scales.

When working with soft materials, for example, polymers or evaporated metals in thin layers ( $< 100 \text{ nm}$ ), one can resort to increase the tip pressure in order to make patterns just by mechanical scratching without any applied voltage. This method is not able to remove material suitably, so care must be taken to avoid short circuits caused by shavings, especially when working with metals. As a consequence, several runs are usually necessary to achieve an adequate electrical insulation between tracks. In Figure 1.12, some alphanumeric displays using a conjugated polymer (MDMO-PPV) as active layer, with different  $7 \times 5$  pixel configurations, were performed by OOG members at CLIQ Group (UPM) facilities (2007). Here, aluminum cathode has been patterned by scratching [36].

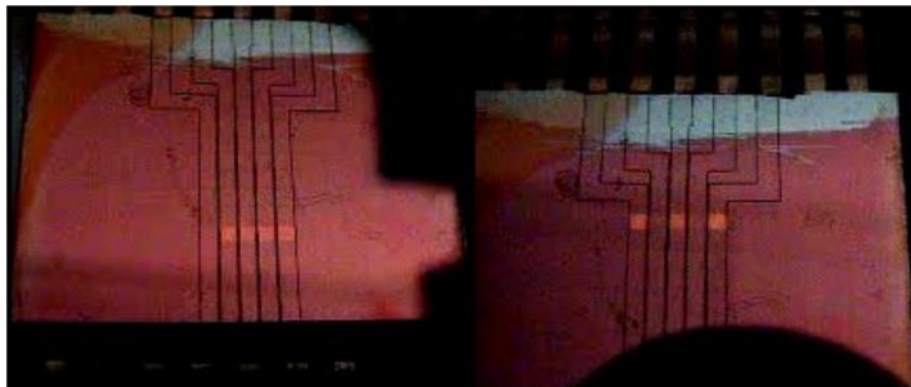


Figure 1.12: MDMO-PPV based alphanumeric display with different  $7 \times 5$  pixel configurations, performed in the OOG (2007). Here, aluminium cathode has been patterned by scratching.

In this line, some features have been patterned by scratching graphene multilayers with an AFM probe at pressures around 200-400 MPa, but the edge quality is far from being optimum [37].

c) Processing speed is a reference parameter in terms of scalability. When the tip is running across the material surface, the maximum speed is determined by two independent factors: capacitor recharging time and the diameter of the eroded zone

surrounding the tip, influenced by the operating voltage. Both factors have to allow the capacitor to recharge before the tip reaches a new conductive zone. In case of metals, low combined voltages with high operating speeds may cause casting instead of evaporation, harming the process itself. In this case the material sticks onto the tip and spoils the whole process in terms of accuracy.

d) The polarity of the tip is another parameter to be taken into account. It is always negative in relation to the material, so the electron flux is towards the sample. When polarity is inverted (probe positive), our experience is that a significant wear of the tip appears during operation, which eventually is able to interrupt the process. In Figure 1.13, a tip biased at +25 V just patterns a short ITO segment before interrupting, whereas the tip polarized at -12 V keeps working properly for long distances, according to the trajectory sketched in Figure 1.13a.

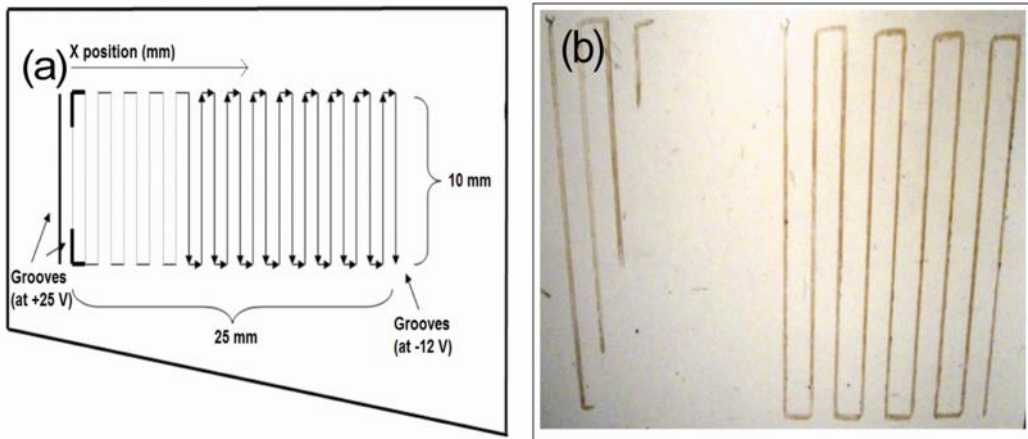


Figure 1.13: (a) sketch of the path followed by the probe at two different operating voltages, +25 and -12 V. (b) Image where the brown line corresponds to the probe trajectory with a width estimated around 150  $\mu\text{m}$  [32].

Experimental trials have been done and the main conclusion is that effects associated to the spark produce a sort of impacts on the tip surface contributing to the tool's wear. However, it is necessary a detailed comprehension of the physical mechanism involved in the process, in order to increase patterning accuracy.

### 1.3.2. Autoalign system

As stated before, one of the main objectives of this Thesis is to involve this technique into an organic device fabrication line. During device manufacturing, for example an OLED passive matrix, it is very common to use our lithography prototype to make some patterns over a sample and then take it out to deposit another layer over

the one previously processed, for subsequent patterning. The alignment of the sample for the second patterning must be exact, if we want the OLED pixels to work properly.

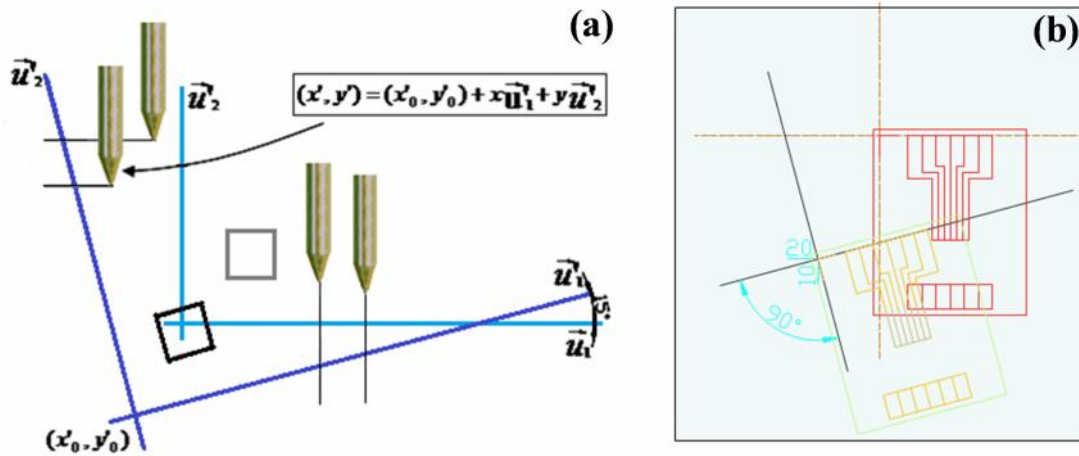


Figure 1.14: (a) Graphical description of the realignment procedure for any sample: light blue lines represent the initial coordinate axes used for the first processing stage. Once the sample has been relocated on the processing platform, this initial reference has changed and the current position is represented by the dark blue coordinate axes. There are four points necessary to perform this operation recognized in read mode: two pairs are taken by vertical movements  $(X_1, Y_1) - (X_2, Y_2)$ . The other pair  $(X_4, Y_4) - (X_3, Y_3)$  using horizontally movements and (b) illustrative example for the alphanumeric display mentioned above.

For that purpose we have implemented a method, already operative, that takes advantage of the control system precision and the electrical monitoring along the whole procedure. This procedure corrects the angle variations and displacements in relation to the beginning position by means of software, after the sample was re-placed (Figure 1.14). This routine works in background recalculating the coordinates of the second pattern to adapt them to the new position. For that purpose, it is necessary to pattern some guide marks on the samples surface e.g. in the corners. They consist of perpendicular insulated lines traced parallel to the coordinate axis of the system, close to the external frame of the sample. Once the sample is replaced, the position of these lines must be detected. The way how the system recognizes these traces is working in read mode, namely, at low voltage and high impedance, to avoid erosion of the layer.

In this way, there is not erosion but just a touching - no touching mode, monitored in terms of conduction response in the oscilloscope. This can be done with an accuracy of  $0.1 \mu\text{m}$ , the precision of the long-trip electromechanical steppers. It is just necessary to detect two points per line in order to re-calculate the new coordinate axes. Once found, the data are recorded and the software recalculates in background the positions of the new pattern.

## 1.4. GRAPHENE FOR ELECTRONIC DEVICES

Hanns Peter Boem is considered a pioneer of graphene research, who described single-layer carbon foils in 1962 [3]. Since that, graphene has been extensively studied in last years but it was only isolated for first time in 2004 by Andrey Geim and Konstantin Novoselov, who won the 2010 Nobel Prize in Physics for their work with graphene [8, 39].

The main inconvenience of graphene is the availability for developmental research, industrial and commercial uses. The high prices and complex processes to obtain high quality graphene sheets ballast its application. Also, it was difficult to grown graphene layers on a large scale using crystalline epitaxy or anything other than a metallic substrate. This severely limited its use in electronics as it is necessary to separate graphene layers from its metallic substrate without damaging the graphene (transfer process). In 2012, studies have found the way to separate graphene from the metallic substrate by the studies of its interfacial adhesive energy. The obtained quality of this graphene was enough for its use in electronic devices [40].

The commonly used method for graphene synthesis can be outlined below as well as an up to date patterning procedure art status on this material.

### 1.4.1. Graphene Synthesis Methods

#### 1.4.1.1. Chemical Vapor Deposition (CVD) for graphene single-layer and multilayer.

CVD is so far the most popular synthesis procedure because of its simplicity. The appropriate variable control as for example: gas volume, pressure, substrate and chamber temperature and time may assure a high quality output. In this method a substrate is exposed to gas molecules (methane and hydrogen [41]) within a reaction chamber, which is typically set at ambient temperature. When the combined gases come into contact with the copper substrate, a reaction occurs creating a material film on the substrate surface. When procedure has ended all waste gases are evacuated by a pumping system.

Recently, there has been demonstrated a 30 inch (76.2 cm) diagonal measure long graphene sheet compatible with R2R process [42]. Graphene was grown on cooper substrate using CVD and a Polyethylene Terephthalate (PET) layer was attached behind

the graphene face. Then copper is retired by chemical etching, leaving the graphene layer transferred to PET. Measured sheet resistance was  $125 \Omega$  for one layer. The procedure was again performed, but at this time four graphene layers were transferred to PET. At this time, measure sheet resistance was  $30 \Omega \text{ sq}^{-1}$ , comparable to that of ITO layers ( $\sim 20\text{-}100 \Omega \text{ sq}^{-1}$ ) currently present in flat panel displays and touch screens [39].

There are other good reasons to prefer CVD to other methods: final high purity, finer grained, permeability and increased hardness of the final sample, enough to justify its common use in semiconductor and also in optoelectronics industry. Additionally, it is worth noting the low procedure costs. The disadvantages of this procedure, or in other words, important concerns in terms of graphene production may be summarized: first, to find the most suitable substrate to grown the layers, and second, to develop an effective way to remove them without any damage.

#### 1.4.1.2. Graphene Oxide

Another widely used method to obtain multilayer graphene is via reduction of graphene oxide (GO). GO has two important characteristics: (1) it can be produced using inexpensive graphite as raw material by cost-effective chemical methods with a high yield, and (2) it is highly hydrophilic and can form stable aqueous colloids to facilitate the assembly of macroscopic structures by simple and cheap solution processes, both of which are important to the large-scale uses of graphene. It is the most cost effective method used so far although the final product shows poorer properties than pristine graphene.

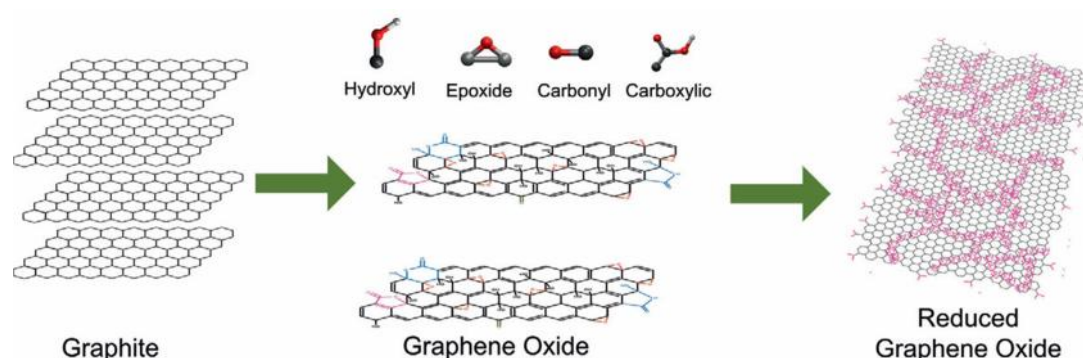


Figure 1.15: GO synthesis and reduction [43].

Graphene oxide (GO) is produced by the transformation of graphite (Figure 1.15). A redox reaction takes place between graphite and sulfuric acid or potassium permanganate. The polar O and OH groups formed during the oxidation process render

graphite oxide hydrophilic and it can be chemically exfoliated in several solvents, including water [39], using an ultrasonic bath or stirring. The GO flakes can be deposited by spin coating on a substrate. A key topic in the research and applications of GO is the reduction, which partly restores the structure and properties of graphene. Different reduction processes result in different properties of reduced GO (rGO), which in turn affect the final performance of materials or devices composed of rGO. The main reduction methods include chemical, thermal or electrochemical processes and can be reviewed in [44].

#### **1.4.1.3. Arc – Discharge graphite evaporation**

This technique is basically two electrodes facing each other, confined in a steel pressurized chamber, surrounded by gas atmosphere and cooled by water. The graphite evaporation takes place inside of this chamber.

Discharge is induced by approaching the rods to certain position, 1 to 2 mm separated. Plasma is generated and the anode begins to consume. It is necessary to correct the distance between them in order to maintain the electric arc, so cathode needs to be in a translation mode to compensate the distance between both electrodes. The favorable conditions for obtain graphene in the inner walls are by currents above 100 A, an open circuit voltage > 50 V and a H<sub>2</sub> pressure above 200 Torr. Final achieved thicknesses ranges from 0.7 to 1 nm; it means 2 to 4 graphene layers. There are also another test that involved other mixed gases e.g. H<sub>2</sub> – B<sub>2</sub>H<sub>6</sub> and H<sub>2</sub> – pyridine with achieved thicknesses of 2-3 graphene layers [45].

Other author has reported another mixing atmosphere, using e.g. He and NH<sub>3</sub>, obtaining N-doped graphene, multi-layered with thicknesses between 100 and 200 nm (2-6 layers) [4]. In other report, from 2 to 10 synthesized by air graphene nanosheets were achieved, strongly dependent of the initial pressure [47].

#### **1.4.1.4. Other Methods**

There are other procedures to get graphene sheets. The mechanical exfoliation procedure that gave Novoselov and Geim the Nobel Prize in 2010, also called the “Scotch Method” [8]. The authors used highly oriented pyrolytic graphite (HOPG) as a precursor and a scotch tape to peel flakes of graphite again and again. Then, the scotch tape was dropped into acetone to release these peeled flakes and then capture on the

surface of a Si/SiO<sub>2</sub> wafer. Unfortunately, this procedure cannot be easily scaled for mass industrial production, and just used only for academic purposes.

Thermal Decomposition of SiC is a wafer-scale graphene technique. The working principle is to decompose the silicon carbide substrate by silicon sublimation, using high temperatures (ranges between 1000 and 1500 °C). The final product is a high quality graphitic layer. There are a few non controlled aspects in this method, e.g. number of layers produced, large areas repeatability and issues concerning interface behavior that need more research [39].

Qingkai *et al* report an approach to synthesize high quality graphene by surface segregation and substrate transfer. The experiment is based in cooling rates from 20 to 0.1 °C/s of annealed foils in H<sub>2</sub> and the exposed to a CH<sub>4</sub>-Ar-H<sub>2</sub> atmosphere heated to 1000 °C for 20 minutes. Different cooling rates led to different segregation behaviors, strongly affecting the thickness and quality of the graphene films [48].

Zhang *et al* describes other technique capable to produce large-area graphene based on a thermal cracker enhanced gas source molecular beam. High quality and large graphene area is produced with temperatures reaching 800 °C onto a nickel substrate [49].

#### **1.4.2. Graphene Patterning Methods: state of the art**

Today, graphene has attracted a lot of attention thanks to its fascinating physical properties, in general terms: extremely high mobility, elasticity, electromechanical modulation and a zero but easily tunable band gap. Due to its superior mobility (200.000 cm<sup>2</sup> V<sup>-1</sup> s<sup>-1</sup> in absence of external perturbations), it becomes attractive for applications in electronics and optoelectronics field. The successful implementation in these areas directly depends on its processing and patterning capacity at appropriate resolutions.

Until now, graphene device fabrication is based in a simple variety of physical and chemical techniques capable to reach micrometer and sub-micrometer scale, included in three main groups: lithography, soft lithography and direct writing, where the main differences lie in the tools used for processing. In the current context, it is worth focusing in the efforts carried out on cost-effective processes, compatible with mass production lines over flexible substrates, which save as many steps as possible (for

example, mask alignment), as those procedures related with direct writing over a substrate.

The aim of this section is to make a quick and widespread tour through these three groups mentioned above, in order to know the actual status in graphene patterning and the used technology for this purpose. Before discussing each of these groups, Table 1.4 summarizes the advantages in terms of characteristic properties.

	Group	Advantages: main characteristics
1	Lithography	High resolution and accuracy.
2	Soft Lithography	Experimental simplicity, flexibility, compatibility and low cost.
3	Direct Writing	Reliability, scalability and low cost.

Table 1.4: Principal characteristics between patterning groups.

#### 1.4.2.1. Group 1: Lithography

Lithography techniques are probably the most frequently used today for graphene patterning. This benefits from the impetus given by the Microelectronics industry. However, there is a high concern around regular photolithography and its main drawback: the generated photoresist residues that spoil graphene properties, impacting negatively on device performance. Fortunately, because regular photolithography is considered one of the most extended ways for graphene patterning at resolutions down to 1  $\mu\text{m}$ , specific procedures has been developed to optimally remove these contaminants [50, 51, 52].

Within this group, there is a variety of alternatives which find applications in different fields (nanotechnology, etc): Colloidal lithography, electrodeposition-assisted lithography, and photo-coupled chemistry lithography. I will add some brief notes about them.

Nano-sphere lithography (also known as Colloidal Lithography) has been successfully used for patterning graphene. It is an emerging technique used for patterning at the nanoscale: surfaces can be achieved with controlled heights and diameters, varying the covered area and the feature size. The main idea is to use nano-particles (nano-spheres) as a shadow mask by spreading them along the material surface and then, etch the layer away around the nano-spheres using Reacting Ion Etching. This technique is compatible with large patterned surface areas.

Cong *et al* had successfully fabricated nano-disk arrays using this combined technique. In Figure 1.16 a graphical procedure scheme for the attainment of such structures is shown [53].

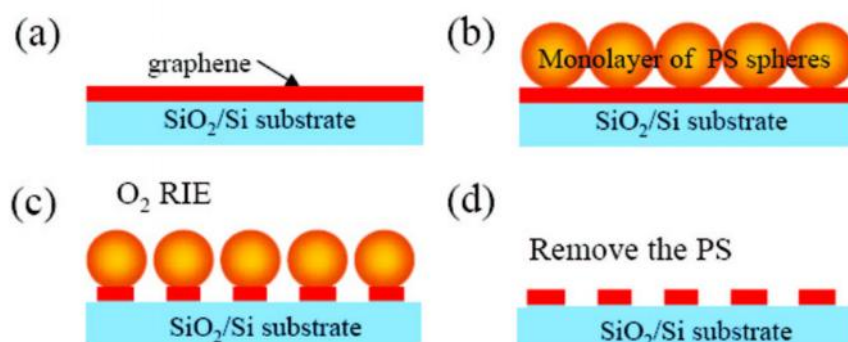


Figure 1.16: Nano-sphere lithography scheme for Nano-disk fabrication process. (a) Initial stage, graphene transfer to a SiO<sub>2</sub> substrate. (b) PS nano-spheres distribution to work as a shadow mask, (c) Reaction Ion Etching procedure to etch a portion of the Graphene sheets and (d) nano-sphere removal and final patterned surface [53].

Once graphene has been transferred to the final Si/SiO<sub>2</sub> substrate, polystyrene (PS) nano-spheres monolayer was self-assembled using a technique already reported [54]. Then, an O<sub>2</sub>-based Reactive Ion Etching was carried out over the sample, influencing directly over the unprotected zones by the nano-spheres. Finally, this nano-sphere monolayer was removed by sonication in chloroform, resulting in a periodic graphene patterning.

Another interesting technique is attributed to Pernites *et al*, in which an alternative route for GO and polymer nano-composites patterning is described on electrode surfaces like Indium - Tin Oxide (ITO). It is an electrodeposition assisted technique which can be performed at room temperature without sophisticated equipment. Novelty here is the accuracy control claimed for 2D array preparation, varying the colloidal size template and involved electrodeposition parameters [55].

Photocoupling chemistry is another alternative to obtain patterned graphene sheets. Starting from a graphene flake suspension in o-dichlorobenzene (DCB), deposited by spin-coating or dip-coating onto previously prepared silicon wafers and glass slides substrates, the sample is treated with a functionalized perfluorophenylazide (PFPA). Final pattern is obtained after subjecting the substrates to a vacuum drying, then to a UV irradiation using a photomask and finally to a two-step washing procedure and a Nitrogen drying. Some final results obtained by Liu *et al* are shown in Figure 1.17 [56].

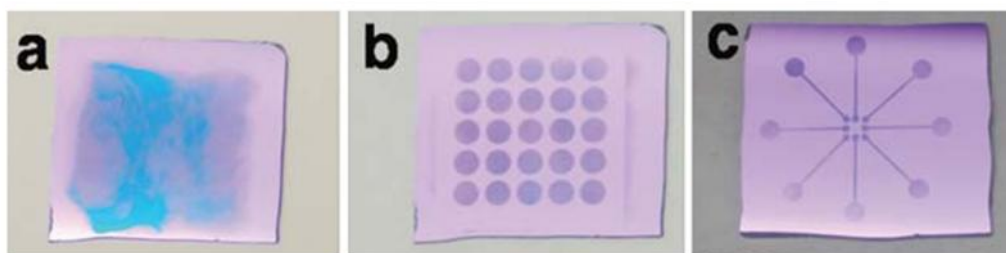


Figure 1.17: Some results obtained by Liu *et al* [56]: (a) Final layers before Photocoupling Lithography; (b) and (c) various pattern types.

#### 1.4.2.2. Group 2: Soft lithography

It receives the forename “soft” owing to the characteristic materials used to fabricate the elastomeric stamps, molds or conformable photomasks for any structure fabrication or replication activity at the micro and nanoscale.

For this purpose, Polydimethylsiloxane (PDMS) is the most used material. It is an organosilicon commonly referred as silicone, optically clear, inert, non-toxic and non-flammable. In any case, any other material having elastomeric behavior could be useful for this application.

In terms of advantages, the use of photo-reactive substances is omitted, offering experimental simplicity and low costs compared with traditional lithography methods. This technique is widely used in applications related to biotechnology, plastic electronics and other applications involving large or no planar surfaces.

Since 2007, graphene related experiences have been reported using soft lithography techniques. Microcontact Printing ( $\mu$ CP), Microtransfer Molding ( $\mu$ TM), Transfer Printing, Solvent-assisted Micromolding (SAMIM) and Micromolding in Capillaries (MIMIC) are some interesting options for graphene patterning. Below, some of these reports will be mentioned as examples for this technical field.

Within this group, the most adequate technique for large areas ( $> \text{cm}^2$ ) is the Microcontact Printing ( $\mu$ CP), which resembles the action of stamping. It is recognized as a simple, versatile and efficient method for graphene patterning [57]. PDMS patterns are used as stamps previously impregnated with ink and then deposited by contact on the target substrate. Some aspects should be taken into account to get a proper result, specifically concerning the physical stamp deformation by the stretch or compression forces, or the stamp shrinkage and swelling by improper solvent use.

Kim *et al* have developed an easily applicable process in graphene sheets through an elastomeric functionalized PDMS stamp. The proposed procedure is sketched in Figure 1.18.

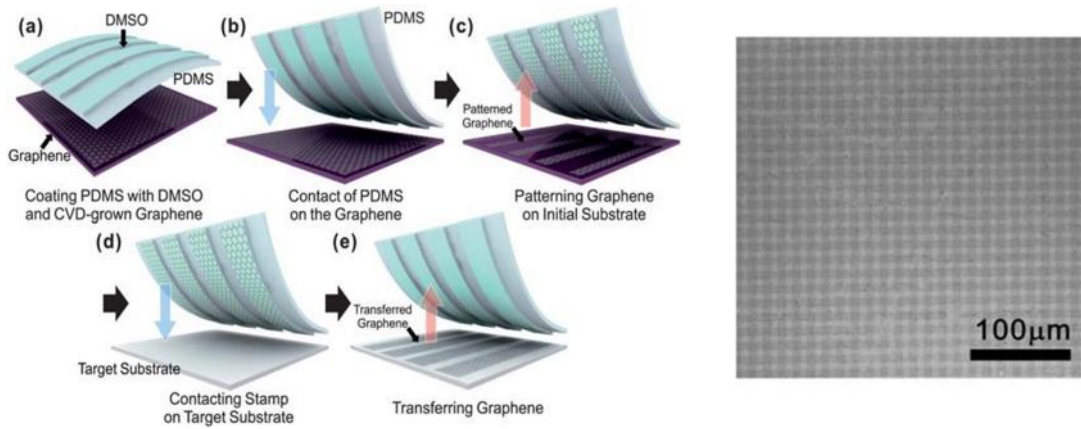


Figure 1.18: Five step Microcontact Printing procedure [58]: (left) graphical procedure and (right) final patterning sample.

The authors propose the use of a dimethyl sulfoxide (DMSO) layer to enhance the interfacial adhesive force between the stamp and the graphene layer. With this procedure it was possible to obtain patterns with a  $3\mu\text{m}$  width array resolution and successfully implemented in graphene-based capacitors with a dielectric constant of about  $\sim 4.8$  at 1 kHz [58]. Other progresses in transfer printing have been reported several years ago [59, 60, 61]. Another reported application uses the DMSO-coated PDMS stamp to shape graphene electrodes with a  $5\mu\text{m}$  line width resolution, and used in a TFT application [62].

Other soft lithography related technique is the so called Microtransfer Molding ( $\mu\text{TM}$ ). It is considered a rapid and suitable method for a wide material range and also large area, typically used to form complex three-dimensional isolated or interconnected microstructures of organic polymers. These microstructures are formed by filling microchannels on the surface of a PDMS mold with a liquid precursor [63], and then put it into contact with a planar or contoured substrate. Then the mold is peeled out, leaving the final microstructures on the target surface.

A variant of this technique is reported by Kim *et al* where periodic assemblies were created on a substrate by controlling solvent evaporation, obtaining self-organized rGO patterns over a large area. The procedure begins with an aqueous suspension deposited in a microscopic gap between two surfaces: a curved one (silica lens) and a planar target surface. The final pattern, size and distribution are geometry-dependent: spherical silica glass is used to achieve circles or rings and cylindrical silica glass for

stripes. Parameters such as solvent evaporation, suspension concentration and target surface treatment determine the pattern final result [5]. Figure 1.19 shows the three step solvent-assisted procedure.

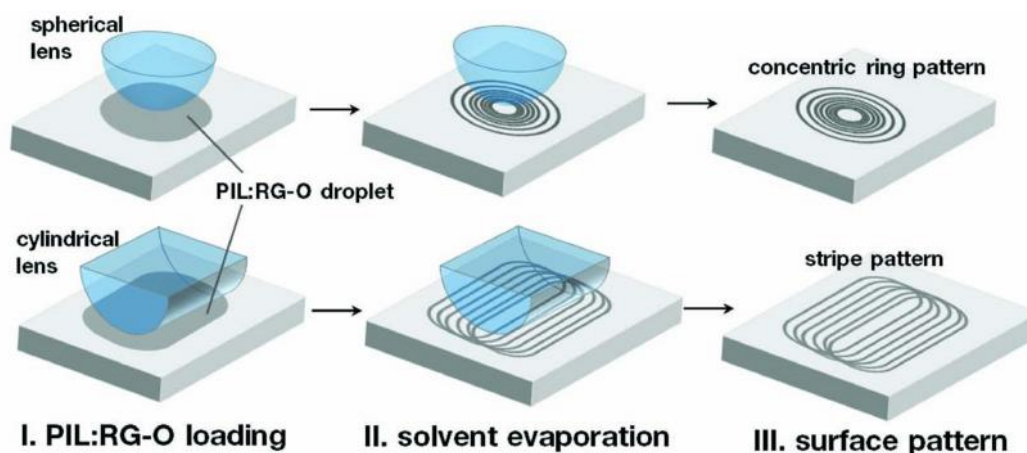


Figure 1.19: Three step solvent-assisted procedure. (Above) spherical lens is used to achieve circles or rings and cylindrical silica lens for stripes (bottom) [64].

Another way to mold microstructures is by capillarity, also known as Micromolding in Capillaries or MIMIC. The capillary network is created by the contact between a PDMS stamp and a target substrate. The material for patterning is in liquid phase and is deposited to fill the capillary network cavities, as shown in Figure 1.20. Experimentally, this technique is very simple and capable to mold structures with a feature size of  $2\ \mu\text{m}$  but at a very slow rate, due to its high viscosity [65].

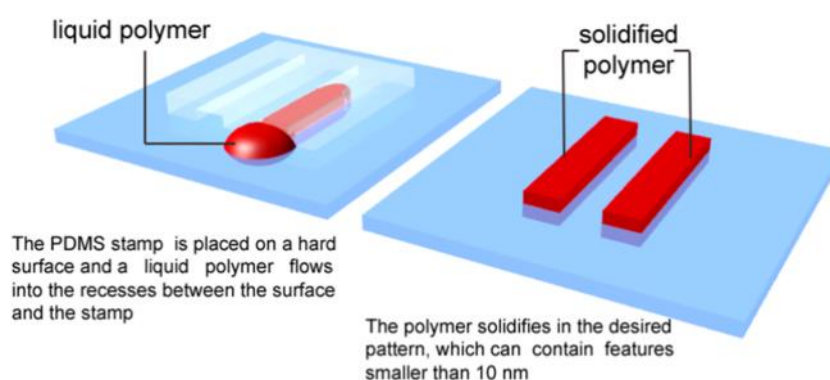


Figure 1.20: Micromolding in Capillaries procedure scheme [66].

Current applications implementing Micromolding in Capillaries cover two different technical areas: flexible electronics and biotechnology. Xue *et al* have developed a flexible super-capacitor, where reduced graphene oxide (rGO) is used as electrode for final nanorods growth [67]. Also in biotechnology, rGO patterns are used as a biointerface for the investigation of human embryonic cell adhesion. These rGO

patterns have micro-scale dimensions and are subsequently obtained via an environmentally-friendly reduction procedure [68].

### 1.4.2.3. Group 3: Maskless Lithography or Direct Writing.

In general terms, this group includes all methods where photoresist and shadow masks are not required, grouped in five main common topics: subtractive techniques like electron beam lithography, direct laser writing, focused ion beam and scanning probe lithography, as well as additive techniques like inkjet printing, or those techniques restricted to oxidize graphene. The purpose of this section is to show the relevance of each technique emphasizing aspects related to their applications.

Electron beam lithography [69, 70, 71] (EBL) and laser writing [72, 73, 74, 75] are the most commonly subtracting methods used for graphene and 2D related materials patterning. EBL is especially chosen for submicron resolution. Thiele *et al* show an electron-beam-induced oxidation alternative being able to pattern with resolution, better than 20 nm [76]. Also, Zhang *et al* uses a 1 nm electron probe to “write and draw” onto graphene sheets [77] and the use of a neutral beam etching to fabricate low-defect nanoribbon arrays [78]. Image examples are shown in Figure 1.21.

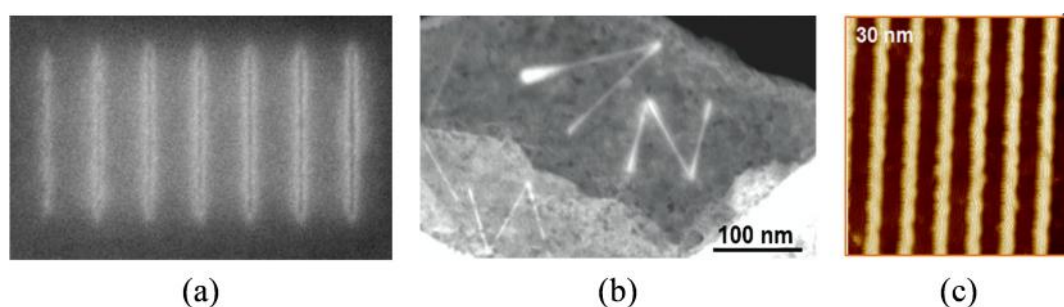


Figure 1.21: Graphical examples for Graphene patterning by electron beam technique: (a) Electron-beam-induced direct etching of graphene [76]; (b) “Write and Draw” onto graphene sheets [77] and (c) 30 nm features by neutral beam etching [78].

There is an intensive effort on the use of lasers of different energies, from the infrared to the ultraviolet and different time scales, from continuous to femto-second lasers [79] to pattern graphene and graphene oxide materials [80, 81, 82]. A fair amount of related contributions have been reported, some of the latest are listed below. Perhaps, one of the most relevant and interesting is that related to a laser-induced transfer method proposed for both graphene transferring and patterning in one step. Random patterns can be positioned and also precisely aligned to pre-existing structures on demand, wet-

chemical steps are not necessary and all procedures can be performed at room conditions [83].

In Figure 1.22a, the suspended graphene/PMMA layer structure is attached on a target substrate by a vapor treatment, the surface tension driving a self-flattening effect. Femtosecond laser ablation is performed to define graphene/PMMA patterns that are simultaneously transferred to the target substrate (Figure 1.22b). The final pattern remains on substrate after detachment because there is a non-physical link between it and the suspended structure, this final step is shown in Figure 1.22c.

Another versatile technique is proposed by Teoh *et al* to create a three dimensional graphene oxide (GO)/reduced GO (rGO) stacked-layer structure with the added attribute that micropatterns could be defined in each layer involving a focused laser beam. The final patterns are made on a previously GO spin-coated preheated substrate. Final scanned region (rGO) or pristine GO can be preferentially removed by ultrasonication by tuning the laser power and the temperature of the GO during the patterning process [73].

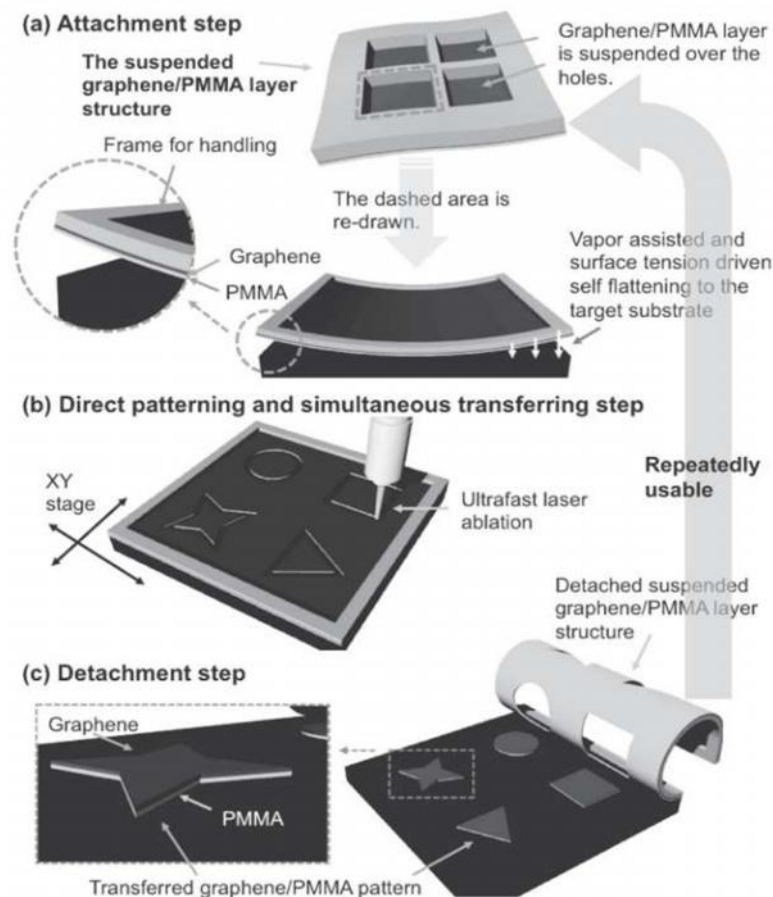


Figure 1.22: Three method flow of laser-induced pattern transfer (LIPT) [83].

Advances in biosensors have been also reported. Lorenzoni *et al* have developed a single shot laser ablation technique for graphene processing, obtaining transparent conductive patterns with micrometer lateral resolution. Figure 1.23 shows a primary embryonic neuron array grown directly onto the substrate, capable to mimic the previously patterned design [84].

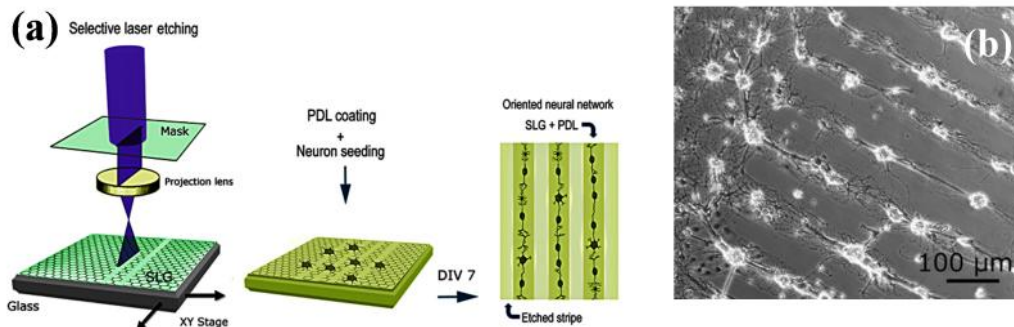


Figure 1.23: (a) Schematic procedure for neural ordered network creation. (b) Cultured embryonic cell arrangement, mimicking the pattern previously processed [84].

Focused ion beam is another technique used for graphene patterning [71, 85]. Due to the ability to sputter, the focused ion beam works as a micro and nano machining tool. The smallest milled features are somewhat larger than 10–15 nm, mainly beam size-dependent and on the interactions with the sample being milled. Zhang *et al* has achieved patterning of epitaxial graphene on SiC into an array of graphene nanoribbons, as narrow as 15 nm, with only the optimization of crucial ion beam parameters [86]. It is important to highlight that electron or ion beams allow graphene and related materials to be patterned in the smallest scales but are limited to small areas. Ultimately, undesirable defects on the surface may occur due to the high energy processes involved in the procedure [87].

There are also advances by using helium beam [88, 89, 90, 91], which is inherently less harmful than gallium ions, obtaining sub-10 nm patterns. Kalhor *et al* use a combination of electron beam lithography and a direct milling with the sub-nanometer focused helium ion beam generated by a helium ion microscope, in order to fabricate graphene quantum dot devices [92].

Special consideration deserve scanning probe techniques, like AFM and STM, which other than acting as sensors can also work as actuators. Nanoscale patterning with atomic force microscopy (AFM) is usually mediated by localized oxidation of graphene by adsorbed water layers, following the same chemical reactions proposed for tunneling microscopy (STM) in graphite more than 20 years ago [93, 94]. More

information is also found in these reviews [87, 95]. Nevertheless, the observation of a different behavior in ultra-high vacuum led to propose a different mechanism based in the sublimation of carbon from graphite [96]. But in general, humidity dependent electrochemical processes are proposed for any AFM patterning including the reduction of graphene oxide films [97]. The use of other adsorbed molecules was proposed to lower the imprint size down to 3 nm [98]. Recently a correlation between the work function of graphene oxide and relative humidity has been demonstrated [99]. Otherwise, the use of the AFM tip as a knife without applied voltage (the scratching already commented in section 1.3.1), is not effective for graphene on SiO<sub>2</sub>/Si because its tendency to fold [100]. Complex systems to increase the patterned area are being proposed as an array of five nano-tips allowing scales up to 500 μm [101], but the approaching mechanism based in force-feedback is too slow and ultimately restrict their application to millimeter areas. Although the nano-size of the patterned areas prevents their Raman characterization, the oxidation of submicron islands on graphite with AFM has been evidenced indeed by Raman [102]. Many physycal aspects, as the relevance of the sign of the applied voltage to the tip with apparently contradictory results [103, 104, 105] are still under discussion.

On the other hand, Martínez *et al* have developed an instrument for parallel oxidation nanolithography, capable to pattern nanoscale silicon oxide motives on 1 cm<sup>2</sup> regions through the control of the exerted pressure and lateral positioning of the stamp on the sample [106], an interesting alternative, besides AFM, for semiconductor, metallic and organic surfaces local oxidation.

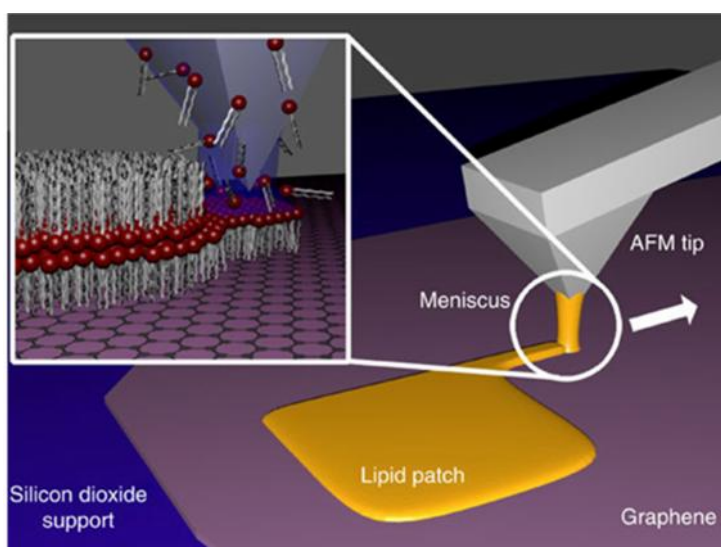


Figure 1.24: General scheme of the Dip Pen Nanolithography writing process [109].

Dip Pen Nanolithography (DPN) is also an AFM based lithography method coming in an upward trend [107, 108]. Herein, the tip is used to pattern directly onto a certain surface; mainly used in biosensor functionalization, nanoscale sensor fabrication and nanoscale protein chip applications. Hirtz *et al* reported in 2013, an application in sensor devices showing the direct writing of tailored phospholipid membranes on graphene using dip-pen nanolithography (Figure 1.24), allowing a multiplexed assembly of these membranes in a close proximity [109].

Furthermore and finally, Inkjet Printing (IJP) has been extensively investigated as an alternative tool for the line patterning of graphene, but conductive inks must meet specific and exigent conditions in terms of solubility, viscosity and surface tension [110, 111, 112]. Jang *et al* achieved an IJP method in 2011 for graphene patterning over flexible substrates (PET) with high resolution. Here, the patterned graphene flakes could also be controlled by varying the GO ink concentration and the number of print runs [113].

More recent attempts in this topic have been reported by Torrisi *et al.*, which have prepared a low cost graphene-based ink by liquid phase exfoliation of graphite in *n*-methylpyrrolidone (NMP) for thin film transistors printing [114]. One of the concerns of this technique is the right election of the solvent where graphene flakes are suspended.

Li *et al* proposed an efficient inkjet printing alternative, using a ‘distillation-assisted solvent exchange’ technique to prepare high-concentration graphene dispersions. The aim of this last step is to convert the toxic NMP and dimethylformamide (DMF) into an environmentally-friendly and high viscosity solvent [115].

One of the most interesting and recent reports is related to a simultaneous synthesis and patterning of graphene electrodes. The author calls it Reactive Inkjet Process (RIP). Here, the graphene oxide ink and the reducing agent are printed separately using individual nozzles onto the same spot, as schematically shown in Figure 1.25. These two inks mix each other, reacting and producing final reduced graphene oxide patterns on the target substrate. Final patterns showed moderate conductivity and transmittance. The effectiveness of this technique and the conductive properties of the reactive inkjet-printed rGO pattern were verified by the fabrication of a LED circuit and demonstrated in [116].

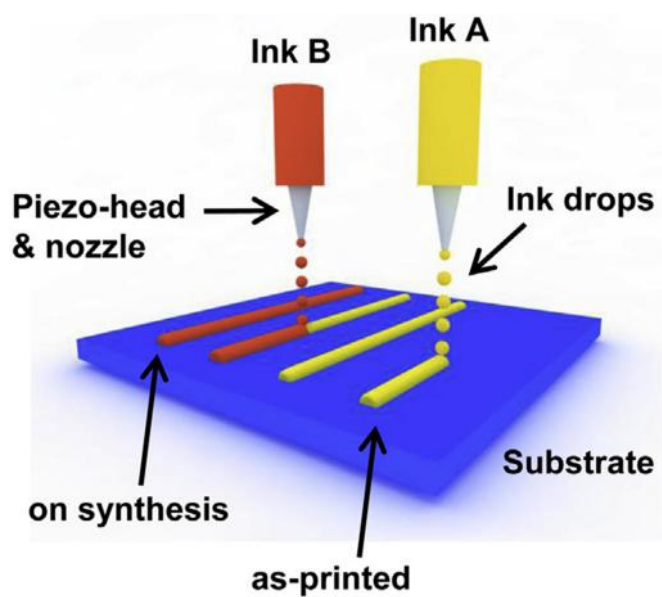


Figure 1.25: Scheme description of the RIP process. After ink A is printed first, ink B is printed in the same pattern for chemical reaction with ink A on a substrate [6].

## 1.5. REFERENCES

- [1] H. Akamatu, H. Inokuchi and Y. Matsunaga, "Electrical Conductivity of the Perylene-Bromide Complex," *Nature*, vol. 173, no. 4395, pp. 168-169, 1954.
- [2] "Organic & Large Area Electronics (OLAE) - An Overview of OLAE Innovation," 2011.
- [3] E. Commission, "CORDIS - Community Research and Development Information Service," [Online]. Available: [http://cordis.europa.eu/fp7/ict/photonics/home\\_en.html](http://cordis.europa.eu/fp7/ict/photonics/home_en.html).
- [4] H. Klauk, *Organic Electronics: Materials, Manufacturing and Applications*, Wiley, 2006.
- [5] H. Klauk, *Organic Electronics II: More Materials and Applications*, Wiley, 2012.
- [6] J. Willmann, D. Stocker and E. Dörsam, "Characteristics and evaluation criteria of substrate-based manufacturing. Is roll-to-roll the best solution for printed electronics?," *Org. Electron.*, vol. 15, no. 7, pp. 1631-1640, 2014.
- [7] A. Geim and K. Novoselov, "The Rise of Graphene," *Nature Materials*, vol. 6, no. 3, pp. 183-191, 2007.
- [8] K. Novoselov, A. Geim, S. Morosov, D. Jiang, Y. Zhang, S. Dubonos, I. Grigorieva and A. Firsov, "Electric Field Effect in Atomically Thin Carbon Films," *Science*, vol. 306, no. 5296, pp. 666-669, 2004.
- [9] IDTechEx, "Printed, Organic and Flexible Electronics forecasts, players and opportunities 2013-2023," 2013.
- [10] "World Antibiotics Market to Reach 34.1 Billion Euros in 2016 according to Global Research and Data Services," 09 September 2012. [Online]. Available: <http://www.prweb.com/releases/2012/9/prweb9878949.htm>. [Accessed 13 April 2013].
- [11] B. Mitchel, A. Bernard, A. Bietsch, E. Delamarche, M. Geissler, D. Juncker, H.

- Kind, J. Renault, H. Rothuizen, H. Schmid, P. Schmidt-Winkel, R. Stutz and H. Wolf, "Printing meets Lithography: Soft approaches to high-resolution patterning," *IBM J. Res. & Dev.*, vol. 45, no. 5, pp. 697-719, 2001.
- [12] Siemens, "Gravure Printing Machine," [Online]. Available: <http://w3.siemens.com/mcems/mc-solutions/en/mechanical-engineering/printing-machines/gravure-printing-machine/pages/gravure-printing-machine.aspx>.
- [13] "American Label Group Inc - Flexigraphic Machine," 2011. [Online]. Available: [www.americanlabel.com/algweb/exp\\_flexo.asp](http://www.americanlabel.com/algweb/exp_flexo.asp).
- [14] K. Suganuma, *Introduction to Printed Electronics*, New York: Springer, 2014.
- [15] M. Singh, H. Haverinen, P. Dhagat and G. Jabbour, "Inkjet Printing - Process and Its Applications," *Adv. Mater.*, vol. 22, no. 6, pp. 673-685, 2010.
- [16] "Special Issue on Laser processing," *Appl. Phys. A*, vol. 101, no. 2, Nov. 2010.
- [17] OE-A, "Organic and Printed Electronics Applications Technologies and Suppliers," 2013.
- [18] K. H. a. S. Newman, "State of the art electrical discharge machining (EDM)," *Journal of Machine Tools and Manufacture*, vol. 43, pp. pp. 1287-1300, 2003.
- [19] J. McGeough, *Advanced Methods of Machining*, Springer Science & Business Media, 1988.
- [20] S. Kumar, R. Singh, T. Singh and B. Sethi, "Surface modification by electrical discharge machining: a review," *Journal of Materials Processing Technology*, vol. 209, pp. 3675-3687, 2009.
- [21] S. Kalpakjian and S. R. Schmid, *Manufacturing Engineering and Technology*, Prentice Hall, 2000.
- [22] K. Rajurkar, M. Sundaram and A. Malshe, "Review o Electrochemical and Electrodischarge Machining," *Procedia CIRP*, vol. 6, pp. 13-26, 2013.
- [23] S. Mahendran, R. Devarajan, T. Nagarajan and A. Majdi, "A Review of Micro - EDM," *Proceedings of The International Multi conference of Engineers and*

*Computer Scientist*, vol. II, 2010.

- [24] "Makino," 2014. [Online]. Available: <http://www.makino.com/ram-edm/edac1/>.
- [25] "Leech Industries," [Online]. Available: <http://www.leechind.com/edm.html>.
- [26] "Steadman Tool and Die Inc," [Online]. Available: <http://steadmantool.com/wireedm.html>.
- [27] D. Pham, S. Dimov, S. Bigot, A. Ivanov and K. Popov, "Micro-EDM recent developments and research issues," *Journal of Materials Processing Technology*, vol. 149, pp. 50-57, (2004).
- [28] J. Narasimhan, Z. Yu and K. Rajurkar, "Tool wear compensation and path generation in Micro and Macro EDM," *Transaction of NAMRI/SME*, vol. 32, pp. 151-158, 2004.
- [29] P. Bleys, J. Kruth, B. Lauwers, A. Zryd, R. Delpretti and C. Tricarico, "Real-time tool wear compensation in milling EDM," *Annals of the CIRP*, vol. 5, no. 1, pp. 157-160, 2002.
- [30] Z. Yu, T. Masuzawa and M. Fujino, "Micro-EDM for three-dimensional cavities - Development of uniform wear method," *Annals of the CIRP*, vol. 47, no. 1, pp. 169-172, 1998.
- [31] M. P. Jahan, A. P. Malshe and K. Rakunjar, "Experimental investigation and characterization of nano-scale dry electro-machining," *Journal of Manufacturing Processes*, vol. 14, pp. 443-451, 2012.
- [32] J. Jiménez-Trillo, *Nueva técnica litográfica de bajo coste basada en micro-erosión por arco compatible con el procesado sobre gran área de dispositivos orgánicos flexibles*, Madrid: Universidad Rey Juan Carlos, 2011.
- [33] D. Go y D. Pohlman, «A mathematical model of the modified Paschen's curve for breakdown in microscale gaps,» *J. Appl. Phys*, vol. 107, nº 103303, 2010.
- [34] H. Timko, F. Djurabekova, K. Nordlund, L. Costelle, K. Matyash, R. Schneider, A. Toerklep, G. Arnau-Izquierdo, A. Descoedres, S. Calatroni, M. Taborelli and W. Wuensch, "Mechanism of surface modification in the plasma-surface

- interaction in electrical arcs,” *Phys. rev. B*, vol. 81, no. 184109, 2010.
- [35] J. Jimenez-Trillo, A. Álvarez, C. Coya, E. Céspedes and A. Espinosa, "The use of arc-erosion as a patterning technique for transparent conductive materials," *Thin Solid Films*, vol. 520, no. 4, p. 1318, 2011.
- [36] B. Arrendondo Conchillo, *PhD Thesis. Fabrication, Characterization and Modelling of Organic Electroluminescent Diodes with Blue Emission. Application to the Design and Manufacturing of Organic Displays.*, Madrid - Móstoles, 2008.
- [37] R. Suda, T. Saito, A. Tseng y J. Shirakashi, «Nanoscale Mechanical Scratching of Graphene using Scanning Probe Microscopy,» *IEEE Proc. 5th Int Nanoelectron. Conf.*, vol. 287, 2013.
- [38] H.-P. Boem, “Graphen - wie eine Laborkuriosität plötzlich äusserst interessant wurde,” *Angewandte Chemie*, vol. 122, no. 49, pp. 9520-9523, (2010).
- [39] D. R. Cooper, B. D'Anjou, N. Ghattamaneni, B. Harack, M. Hilke, A. Horth, N. Majlis, M. Massicotte, L. Vandsbuger, E. Whiteway and V. Yu, “Experimental Review of Graphene,” *ISRN Condensed Mater Physiss*, vol. 2012, no. 501686, 2012.
- [40] J. De la Fuente, “Graphenea,” 2013. [Online]. Available: <http://www.graphenea.com/pages/graphene-publications>.
- [41] X. Li, W. Cai, J. An, S. Kim, J. Nah, D. Yang, R. Piner, A. Velamakanni, I. Jung, E. Tutuc, S. Banerjee, L. Colombo and R. Ruoff, "Large-area synthesis of high-quality and uniform Graphene films on copper foils," *Science*, vol. 324, no. 5932, pp. 1312-1314, 2009.
- [42] S. Bae, H. Kim, Y. Lee, X. Xu, J.-S. Park, Y. Zheng, J. Balakrishnan, T. Lei, H. R. Kim, Y. I. Song, Y.-J. Kim, K. S. Kim, B. Özyilmaz, J.-H. Ahn, B. H. Hong and S. Iijima, “Roll to Roll production of 30-inch graphene films for transparent electrodes,” *Nature Nanotechnology*, vol. 5, no. 8, pp. 574-578, 2010.
- [43] F. Bonaccorso, A. Lombardo, T. Hasan, Z. Sun, L. Colombo and A. C. Ferrari, “Production and processing of graphene and 2D crystals,” *Materials Today*, vol.

- 15, no. 12, pp. 564-589, (2012).
- [44] S. Pei and H.-M. Cheng, "The reduction of graphene oxide," *Carbon*, vol. 50, no. 9, p. 3210–3228, 2012.
- [45] K. Subrahmanyam, L. Pachankarla and A. a. R. C. Govindaraj, "Simple method of preparing graphene flakes by an arc-discharge method," *The Journal of Physical Chemistry C Letters*, vol. 113, pp. pp. 4257-4259, 2009.
- [46] N. Li, Z. Wang, K. Zhao, Z. Shi and Z. a. X. S. Gu, "Large Scale synthesis of N-doped multi-layered graphene sheets by simple arc-discharge method," *Carbon*, vol. 48, no. 1, pp. 255-259, 2010.
- [47] N. Li, Z. Wang, K. Zhao, Z. Shi and Z. a. X. S. Gu, "Synthesis of single-wall carbon nanohorns by arc-discharge in air and their formation mechanism," *Carbon*, vol. 48, no. 5, pp. 1580-1585, 2010.
- [48] Q. Yu, J. Lian, S. Siriponglert, H. Li and Y. a. P. S. Chen, "Graphene segregated on Ni surfaces and transferred to insulators," *Applied Physics Letters*, vol. 113103, 2008.
- [49] N. Zhang, M. Olmedo and G. a. L. J. Wang, "Layer-by-layer synthesis of large-area graphene films by thermal cracker enhance gas source molecular beam epitaxy," *Carbon*, vol. 49, no. 6, pp. 2046-2052, 2011.
- [50] Y. Dan, N. J. Kybert and A. C. Johnson, "Intrinsic response of graphene vapor sensors," *Nano Lett*, vol. 9, no. 4, pp. 1472-1475, 2009.
- [51] R. Shi, H. Xu, B. Chen, Z. Zhang and L.-M. Peng, "Scalable fabrication of graphene devices through photolithography," *Appl Phys Lett*, vol. 102, no. 113102, 2013.
- [52] W. Li, Y. Liang, D. Yu, L. Peng, K. P. Pernstich, T. Shen, A. R. H. Walker, G. Cheng, C. A. Hacker, C. A. Richter, Q. Li, D. J. Gundlach and X. Liang, "UV/Ozone treatment to reduce metal-graphene contact resistance," *Appl Phys Lett*, vol. 102, no. 183110, 2013.
- [53] C. Cong, T. Yu, Z. Ni, L. Lui and Z. a. H. W. Shen, "Fabrication of graphene

- nanodisk arrays using nanosphere lithography,” *J. Phys. Chem. C*, vol. 113, pp. 6529-6532, 2009.
- [54] J. Rybczynski, U. Ebels and M. Giersig, “Large-scale, 2D arrays of magnetic nanoparticles,” *Colloid Surf, A*, vol. 219, no. 1, pp. 1-6, 2003.
- [55] R. Pernites, A. Vergara, A. Yago and K. a. A. R. Cui, “Facile approach to graphene oxide and poly(N-vinylcarbazole) electro-patterned films,” *Chem Commun*, vol. 47, pp. pp. 9810-9812, 2011.
- [56] L.-H. Liu, G. Zorn, D. G. Castner, R. Solanki and M. M. a. Y. M. Lerner, “A simple and scalable route to wafer-sie patterned graphene,” *Mater Chem*, vol. 20, pp. 5041-5046, 2010.
- [57] J.-Y. Hong and J. Jang, “Micropatterning of graphene sheets: recent advances in techniques and applications,” *J. Mater Chem*, vol. 22, pp. 8179-8191, 2012.
- [58] H. Kim, M.-W. Jung, S. Myung, D. Jung, S. S. Lee, K.-J. Kong, J. Lim, J.-H. Lee, C. Y. Park and K.-S. An, “Soft lithography of graphene sheets via surface energy modification,” *J. Mater Chem C*, vol. 1, pp. 1076-1079, 2013.
- [59] X. Liang, Z. Fu and S. Y. Chou, “Graphene transistors fabricated via transfer-printing in device active-areas on large wafer,” *Nano Lett*, vol. 7, no. 12, pp. 3840-3844, 2007.
- [60] L. Song, L. Ci, W. Gao and P. M. Ajayan, “Transfer printing of graphene using gold films,” *ACS Nano*, vol. 3, no. 6, pp. 1353-1356, 2009.
- [61] M. J. Allen, V. C. Tung, L. Gomez, Z. Xu, L.-M. Chen, K. S. Nelson, C. Zhou, R. B. Kaner and Y. Yang, "Soft transfer printing of chemically converted graphene," *Adv Materials*, vol. 21, no. 20, pp. 2098-2102, 2009.
- [62] S. Jeong, M.-W. jung, J.-Y. Lee, H. Kim, J. Lim, K.-S. An, Y. Choia and S. S. Lee, “Graphene electrodes transfer-printed with a surface energy-mediated wet PDMS stamp: impact of Au doped-graphene for high performance solubleoxide thin-film transistors,” *J. Mater Chem*, no. 1, pp. 5635-5637, 2013.
- [63] F. Li, M. Xue, X. Ma, M. Zhang and T. Cao, “Facile patterning of reduced

- graphene oxide film into microelectrode array for highly sensitive sensing,” *Analy Chem*, vol. 83, no. 16, pp. 6426-6430, 2011.
- [64] T. Y. Kim, S. W. Kwon, S. J. Park, D. H. Yoon, K. S. Suh and W. S. Yang, “Self-organized graphene patterns,” *Adv Materials*, vol. 23, no. 24, pp. 2734-2738, 2011.
- [65] X.-M. Zhao, Y. Xia and G. M. Whitesides, “Fabrication of three-dimensional micro-structures: microtransfer molding,” *Adv Materials*, vol. 8, no. 10, pp. 837-840, 1996.
- [66] D. a. B. P. de Leeuw, “Max Planck Institute for Polymer Research,” 2013. [Online]. Available: <http://www.mpip-mainz.mpg.de/148087/Micro-Patterning>.
- [67] F. L. J. Z. H. S. M. Z. a. T. C. Mianqi Xue, “Structure-based enhanced capacitance: in situ growth of highly ordered polyaniline nanorods on reduced graphene oxide patterns,” *Adv Funct Mater*, vol. 22, no. 6, pp. 1284-1290, 2012.
- [68] L. E. Delle, R. Lanche, J. Ka-Yan Law, M. Weil, X. Thang Vu, P. Wagner and S. and Ingebrandt, “Reduced graphene oxide micropatterns as an interface for adherent cells,” *Physica Status Solidi a*, vol. 210, pp. 975-982, 2013.
- [69] J. Q. Zhengqing, J. A. Rodríguez-Manzo, S. J. Hong, Y. W. Park, E. A. Stach, M. Drndić and A. Johnson, “Direct electron beam patterning of sub-5nm monolayer graphene interconnects,” *Proceedings of SPIE, Alternative Lithographic Technologies V*, p. 86802F, 2013.
- [70] J. Gardener and J. and Golovchenko, “Ice-assisted electron beam lithography of graphene,” *Nanotechnology*, vol. 23, no. 18, p. 185302, 2013.
- [71] M. C. Lemme, D. C. Bell, J. R. Williams, L. A. Stern, B. W. Baugher, P. Jarillo-Herrero and C. M. and Marcus, “Etching of graphene devices with helium ion beam,” *ACS Nano*, vol. 3, no. 9, pp. 2674-2676, 2009.
- [72] D. Weia, J. I. Mitchella, C. Tansarawiputb, W. Nama, M. Qib, P. D. Yeb and X. and Xua, “Laser direct synthesis of graphene on quartz,” *Carbon*, vol. 53, pp. 374-379, 2013.

- [73] H. F. Teoh, Y. Tao, E. S. Tok, G. Wei and C. H. Sow, "Direct laser-enabled graphene oxide-reduced graphene oxide layered structures with micropatterning," *J. Appl Phys*, vol. 112, p. 064309, 2012.
- [74] V. Strong, S. Dubin, M. El-Kady, A. Lech, Y. Wang and B. a. K. R. Weiller, "Patterning and electronic tuning of laser scribed graphene for flexible all-carbon devices," *ACS Nano*, vol. 6, no. 2, pp. 1395-1403, 2012.
- [75] R. Stöhr, R. Kolesov, K. Xia and J. and Wrachtrup, "All-optical high-resolution nanopatterning and 3D suspending of graphene," *ACS Nano*, vol. 5, no. 6, pp. 5141 - 5150, 2012.
- [76] C. Thiele, A. Felten, T. Echtermeyer, A. Ferrari, C. Casiraghi, H. v. Löhneysen and R. and Krupke, "Electron-beam-induced direct etching of graphene," *Carbon*, vol. 64, pp. 84-91, 2013.
- [77] W. Zhang, Q. Zhang, M.-Q. Zhao and L. T. and Kuhn, "Direct writing on graphene paper by manipulating electrons as invisible ink," *Nanotechnology*, vol. 24, p. 275301, 2013.
- [78] C.-H. Huang, C.-Y. Su, T. Okada, L.-J. Li, K.-I. Ho, P.-W. Li, I.-H. Chen, C. Chou, C.-S. Lai and S. and Samukawab, "Ultra-low-edge-defect graphene nanoribbons patterned by neutral beam," *Carbon*, vol. 61, pp. 229-235, 2013.
- [79] R. Trusovas, K. Ratautas, G. Ra iukaitis, J. Barkauskas, I. Stankevi ien , G. Niaura and R. Mažeikien , "Reduction of graphite oxide to graphene with laser irradiation," *Carbon*, vol. 52, p. 574–582, 2013.
- [80] Y. Zhou, Q. Bao, B. Varghese, L. A. L. Tang, C. K. Tan, C.-H. Sow and K. P. Loh, "Microstructuring of Graphene Oxide Nanosheets Using Direct Laser Writing," *Advanced Materials*, vol. 22, no. 1, pp. 67-71, 2010.
- [81] E. Ghadim, N. Rashidi, S. Kimiagar, O. Akhavan, F. Manouchehri and E. Ghaderi, "Pulsed laser irradiation for environment friendly reduction of graphene oxide suspensions," *Applied Surface Science*, vol. 301, p. 183–188, 2014.

- [82] X. Zheng, B. Jia, X. Chen and M. Gu, "In Situ Third-Order Non-linear Responses During Laser Reduction of Graphene Oxide Thin Films Towards On-Chip Non-linear Photonic Devices," *Advanced Materials*, vol. 26, no. 17, p. 2699–2703, 2014.
- [83] J.-H. Yoo, J. B. Park, S. Ahn and C. P. and Grigoropoulos, "Laser-Induced direct graphene patterning and simultaneous transferring method for graphene sensor platform," *Small*, vol. 9, no. 24, pp. 4269-4275, 2013.
- [84] M. Lorenzoni, F. Brandi, S. Dante, A. Giugni and B. and Torre, "Simple and effective graphene laser processing for neutron patterning application," *Scientific Reports*, vol. 3, p. 1954, 2013.
- [85] D. Bell, M. Lemme, L. Stern, J. Williams and C. Marcus, "Precision cutting and patterning of graphene with helium ions," *Nanotechnology*, vol. 20, p. 455301, 2009.
- [86] Y. Zhang, C. Hui, R. Sun, K. Li, K. He, X. Ma and F. and Liu, "A large-area 15 nm graphene nanoribbon array patterned by a focused ion beam," *Nanotechnology*, vol. 25, no. 13, p. 135301, 2014.
- [87] J. Feng, W. Li, X. Qian and J. Qi, "Patterning of graphene," *Nanoscale*, vol. 4, no. 16, pp. 4883-4899, 2012.
- [88] Y. Wang, M. Abb, S. A. Boden, J. Aizpurua, C. de Groot and O. L. and Muskens, "Ultrafast nonlinear control of progressively loaded, single plasmonic nanoantennas fabricated using helium ion milling," *Nano Letters*, vol. 13, no. 11, pp. 5647-5653, 2013.
- [89] D. Fox, Y. Zhou, A. O'Neill, S. Kumar, J. Wang, J. Coleman, G. Duesberg, J. Donegan and H. and Zhang, "Helium ion microscopy of graphene: beam damage, image quality and edge contrast," *Nanotechnology*, vol. 24, no. 33, p. 335702, 2013.
- [90] M. Melli, A. Polyakov, D. Gargas, C. Huynh, L. Scipioni, W. Bao, D. Ogletree, P. Schuck, S. Cabrini and A. and Weber-Bargioni, "Reaching the theoretical resonance quality factor limit in coaxial plasmonic nanoresonators fabricated by

- helium ion lithography," *Nano Letters*, vol. 13, no. 6, pp. 2687-2691, 2013.
- [91] S. Nakaharai, T. Iijima, S. Ogawa, S. Suzuki, S.-L. Li, K. Tsukagoshi, S. Sato and N. and Yokoyama, "Conduction tuning on graphene based on defect-induced localization," *ACS Nano*, vol. 7, no. 7, pp. 5694-5700, 2013.
- [92] N. Kalhor, S. Boden and H. and Mizuta, "Sub-10 nm patterning by focused He-ion beam milling for fabrication of downscaled graphene nano devices," *Microelectronics Engineering*, vol. 144, pp. 70-77, 2014.
- [93] L. Biró, P. Nemes-Incze and P. Lambin, "Graphene: nanoscale processing and recent applications," *Nanoscale*, vol. 4, no. 6, pp. 1824-1829, 2012.
- [94] R. McCarley, S. Hendricks and A. Bard, "Controlled nanofabrication of highly oriented pyrolytic graphite with the scanning tunneling microscope," *J. Phys. Chem.*, vol. 96, no. 25, p. 10089–10092, 1992.
- [95] L. Biró and P. Lambin, "Nanopatterning of graphene with crystallographic orientation control," *Carbon*, vol. 48, no. 10, pp. 2677-2689, 2010.
- [96] S. Kondo, M. Lutwyche and Y. Wada, "Nanofabrication of layered materials with the scanning tunneling microscope," *Applied Surface Science*, vol. 75, no. 1-4, pp. 39-44, 1994.
- [97] J. M. Mativetsky, E. Treossi, E. Orgiu, M. Melucci, G. Veronese, P. Samorì and V. Palermo, "Local current mapping and patterning of reduced graphene oxide," *J. Am. Chem. Soc.*, vol. 132, no. 40, p. 14130–14136, 2010.
- [98] J. Park, K. Kim, J.-Y. Park, T. Choi and Y. Seo, "Graphite patterning in a controlled gas environment," *Nanotechnology*, vol. 22, no. 33, p. 335304, 2011.
- [99] C. W. Lee, B. J. Min, S. I. Kim and H. K. Jeongb, "Stacking of water molecules in hydrophilic graphene oxides characterized by Kelvin probe force microscopy," *Carbon*, vol. 54, p. 353–358, 2013.
- [100] Y. He, H. Dong, T. Li, C. Wang, W. Shao, Y. Zhang, L. Jiang and W. Hu, "Graphene and graphene oxide nanogap electrodes fabricated by atomic force microscopy nanolithography," *Appl. Phys. Lett.*, vol. 97, no. 133301, 2010.

- [101] K. Carroll, X. Lu, S. Kim, Y. Gao, H. Kim, S. Somnath, L. Polloni, R. Sordan, W. King, J. Curtis and E. Riedo, "Parallelization of thermochemical nanolithography," *Nanoscale*, vol. 6, no. 3, pp. 1299-1304, 2014.
- [102] N. Kurra, G. Prakash, S. Basavaraja, T. Fisher, G. Kulkarni and R. Reifenger, "Charge storage in mesoscopic graphitic islands fabricated using AFM bias lithography," *Nanotechnology*, vol. 22, no. 24, p. 245302, 2011.
- [103] J. G. Park, C. Zhang, R. Liang and B. Wang, "Nano-machining of highly oriented pyrolytic graphite using conductive atomic force microscope tips and carbon nanotubes," *Nanotechnology*, vol. 18, no. 40, p. 405306, 2007.
- [104] I.-S. Byun, D. Yoon, J. S. Choi, I. Hwang, D. H. Lee, M. J. Lee, T. Kawai, Y.-W. Son, Q. Jia, H. Cheong and B. H. Park, "Nanoscale lithography on monolayer graphene using hydrogenation and oxidation," *ACS Nano*, vol. 5, no. 8, p. 6417–6424, 2011.
- [105] S. Masubuchi, M. Arai and T. Machida, "Atomic force microscopy based tunable local anodic oxidation of graphene," *Nano Lett.*, vol. 11, no. 11, p. 4542–4546, 2011.
- [106] J. Martínez, N. S. Losilla, F. Biscarini, G. Schmidt, T. Borzenko, L. W. Molenkamp and R. Garcia, "Development of a parallel local oxidation nanolithography instrument," *Review of scientific Instruments*, vol. 77, no. 086106, 2006.
- [107] K. Salaita, Y. Wang and C. A. Mirkin, "Applications of dip-pen nanolithography," *Nature Nanotechnology*, vol. 2, pp. 145-155, 2007.
- [108] W. M. Wang, N. Stander, R. M. Stoltenberg, D. Goldhaber-Gordon and Z. Bao, "Dip-pen nanolithography of electrical contacts to single graphene flakes.," *ACS Nano*, vol. 4, no. 11, pp. 6409-6416, 2010.
- [109] M. Hirtz, A. Oikonomou, T. Georgiou, H. Fuchs and A. and Vijayaraghavan, "Multiplexed biometric lipid membranes on graphene by dip-pen nanolithography," *Nature Communications*, vol. 4, p. 2591, 2013.

- [110] J. Cho, K. Shin and J. Jang, "Micropatterning of conducting polymer tracks on plasma treated flexible substrate using vapor phase polymerization-mediated inkjet printing," *Synth Met*, vol. 160, p. 1119, 2010.
- [111] J. Cho, K. Shin and J. Jang, "Polyaniline micropattern onto flexible substrate by vapor deposition polymerization-mediated inkjet printing," *Thin Solid Films*, vol. 518, pp. 5060-5070, 2010.
- [112] J. Jang, J. Ha and J. and Cho, "Fabrication of water-dispersible polyaniline-poly(4-styrenesulfonate) nanoparticles for inkjet-printed chemical-sensor applications," *Adv Materials*, vol. 19, p. 1772, 2007.
- [113] K. Shin, J. Hong and J. and Jang, "Micropatterning of graphene sheets by inkjet printing and its wideband dipole-antenna application," *Adv Materials*, vol. 23, no. 18, pp. 2113-2118, 2011.
- [114] F. Torrisci, T. Hasan, W. Wu, Z. Sun, A. Lombardo, T. Kulmala, G. Hsieh, S. Jung, F. Bonaccorso, P. Paul, D. Chu and A. and Ferrari, "Inkjet-printed graphene electronics," *ACS Nano*, vol. 6, no. 4, pp. 2992-3006, 2012.
- [115] J. Li, F. Ye, S. Vaziri, M. Muhammed, M. Lemme and M. and Östling, "Efficient inkjet printing graphene," *Adv Materials*, vol. 25, no. 29, pp. 3985-3992, 2013.
- [116] Kukjoo Jim; Sung Il Ahn; and Kyung Cheol choi, "Simultaneous synthesis and patterning of graphene electrodes by reactive inkjet printing," *Carbon*, vol. 66, pp. 172-177, 2014.

## CHAPTER 2 . OBJECTIVES

### 2.1. GENERAL OBJECTIVE

The main objective of this thesis dissertation is to settle down the basic principles of a novel one-step lithography method for micro/nano patterning of thin film conducting materials, based on the electrical discharge principles. This objective requires the design, assemble, calibration and optimization of a specific purpose machine, and a thorough study of the electrical erosion effects on different conducting materials: from Indium Tin Oxide, ITO ( $\text{In}_2\text{O}_3$ : Sn), Gold, Aluminum, or ZnO: Al (AZO), to novel semiconductors such as  $\text{Zn}_3\text{N}_2$  and finally, a deep study of the electric-arc lithography process on the promising graphene, graphene oxide and reduced graphene oxide.

### 2.2. SPECIFIC OBJECTIVES

- Design, fabrication and implementation of an arc-erosion specific purpose machine ready to work from nano- to millimeter scales.
- Development of an electrical erosion lithography protocol, independent of the material and substrate characteristics, highlighting the relevance of movement characteristics and tilt correction for an optimal patterning.

- Study the effects of electrical discharges on thin films of different conducting materials for two purposes:
  - Obtaining the proper conditions for a well-defined and high quality micro/nano patterning in the case of relevant materials like ITO ( $\text{In}_2\text{O}_3: \text{Sn}$ ), Gold and Aluminum, AZO,  $\text{Zn}_3\text{N}_2$ , and graphene and related materials.
  - Obtaining a comprehensive model of the physical phenomena involved in the patterning process, according to the following steps:
    - To systematically analyze the electric-arc physical mechanism by means of experiments with different probes and different operating conditions.
    - To implement a finite element based model in order to simulate and clarify the involved electrostatic properties and other physical mechanisms, through the use of the COMSOL Multiphysics software.
    - To propose a circuital model for the electrical erosion mechanism that fits to the obtained experimental results.

## **CHAPTER 3 . ELECTROEROSION MACHINE DEVELOPMENT, METHODS AND TECHNIQUES**

In this chapter, the specific purpose machine that has been developed in this thesis work aimed to perform dry and direct nano/micro patterning using the electro erosion concept is described. Also the different experimental equipment and techniques used to characterize the patterned surfaces, as well as the simulation procedure and the software used to simulate the physics phenomenology associated to the process are briefly described.

### **3.1 COMERCIAL PART SELECTION**

Each commercial or home-designed component of the final assembly is described in the following sections. The final drawings of manufactured parts together with the technical data of the components can be consulted at Appendix A and B.

#### **3.1.1. Piezoelectric stages**

Basically, the system consist in two independent piezo electrical actuators attached to long trip electromechanical steppers (high precision PLS-85 PI linear stages micro positioners [1]): a XY piezo-positioners (PIHera P-621.2CD, Figure 3.1a) and a Z linear actuator (LISA P753.31C, Figure 3.1b), The trip is up to 3 cm in vertical

direction, and 10 cm in horizontal direction, both with  $0.1 \mu\text{m}$  resolution and  $1 \mu\text{m}$  reproducibility. The piezo-stages guarantee a precision motion with resolution of  $0.05 \text{ nm}$  and vertical trip of  $38 \mu\text{m}$ , and resolution of  $0.4 \text{ nm}$  for a horizontal trip of  $100 \mu\text{m}$ . The micro positioners are moved by a 2-phase stepper motor and a closed loop system that improves accuracy and are driven by a SMC Corvus ECO controller, connected to PC via RS-232 or USB interface which is programmed with specific software. All these devices from Physik Instrumente GmbH were supplied by PIMicos Ibérica. Technical information of both piezoelectric devices is available in Appendix A.1 and A.2 respectively.



Figure 3.1: Commercial piezo stages for prototype upgrade: (a) PI Hera nanopositioner family and (b) PI LISA linear actuator family [2].

A modular controller (Figure 3.2a) is used to operate both piezoelectric sensors. Consist of a 48 centimeter chassis (PI reference E-500) where it contains the amplifier modules (E-505), sensor/servo-control modules (E-509) one for each channel (X, Y and Z). There is also a piezo controller operational module (interface/display module E-517) allowing functions as data recording or wave generation for any of the three channels.

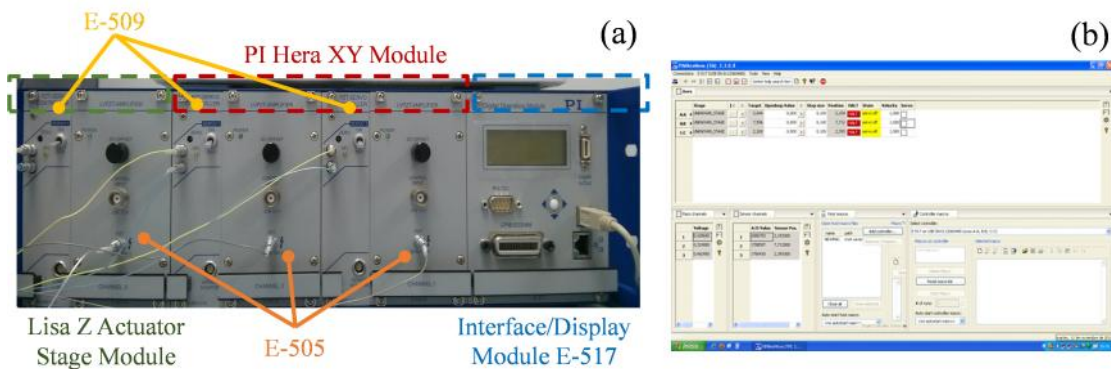


Figure 3.2: (a) Piezoelectric Modular controller and (b) PIMikroMove Software print screen.

All this hardware came with Windows XP operating system based control software (Figure 3.2b) easy to install and operate. It provides the ability to drive the piezoelectric sensors in two ways: open loop (bias control) and close loop (distance control) switching from one mode to the other instantly. It also could receive specific instructions through text files, written in a simple language being able to process any pattern continually.

The controller is very versatile; a self-made design software could be used to control all the main features of the piezoelectric sensor in tandem with the PSL-85 stages; this will prevent the use of two different software interfaces joining all movement actions into one and more complete software. Graphic software as LabView for example, has a quick integration with this type of positioning systems and also text-based programs as Matlab, C, C++, Python and others.

### 3.1.2. Dino - Lite AD4113ZT4 Digital Microscope

A Dino-Lite AD4113ZT4 digital microscope (Figure 3.3a) is used for visual inspection. The magnification of 400 ~ 470x allows us to locate the tip over the sample tens nanometers above. This ensures safety when working with rigid tips and thinner samples (Figure 3.3b). The microscope is easily PC controlled via USB 2.0 and is equipped with a calibration system. It has a resolution 1.3M pixels (SXGA), up to 30 frames per second (fps) of refresh rate [3].

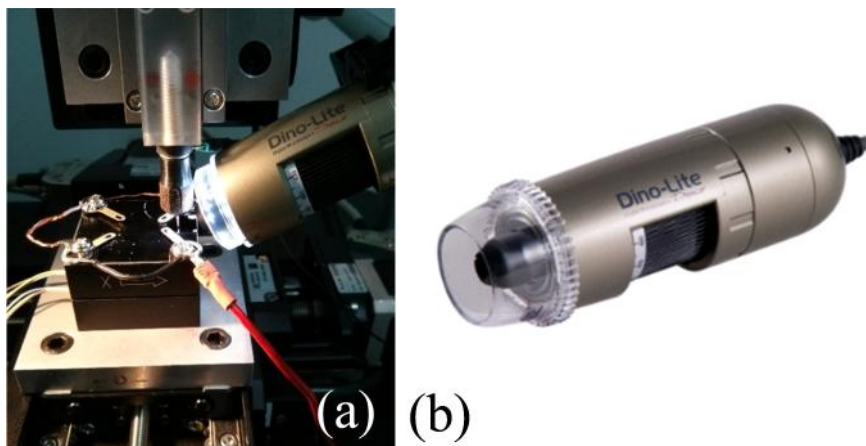


Figure 3.3: (a) Sample processing- microscope positioning and (b).Dino - Lite AD4113ZT4 –Microscope detail

### 3.1.3. Antivibration System: PLM Pneumatic Mount

The machine was insulated with four pneumatic mounts. Vibrations and shocks are harmful for accurate results. These kinds of accessories provide both: attenuation of disturbing vibrations and shocks. Also serves as a levelling tool.

In particular, this mounts provide significant reduction of vibration occurring at frequencies above 5.0 Hz. Supplied with a tank valve, the isolators are inflated and levelled manually using a hand pump or air chuck connected to an air supply [4]. Table 3.1 shows dimension characteristics of the selected model for this purpose.

DIMENSIONS [mm]										
Model	A	B	C	D	E	F	G	H	I	Max. Load
PLM 1	76.2	60.4	6.9	UNC-2B	11.9	73.2	25.4	63.5	3.2	45 kg

The technical drawing shows two views of the pneumatic mount. The top view is a square with side length A, containing a central circular hole with diameter D and a smaller hole with diameter E. The bottom view shows the side profile of the mount with dimensions B (width), C (height of the top flange), F (total height), G (height of the top flange), H (total height including the base), and I (height of the base). The working height is labeled as H.

A photograph showing three pneumatic mounts of different sizes. The largest one is on the left, a medium-sized one in the center, and a smaller one on the right. They are all black with a silver-colored base plate.

Table 3.1: PLM Pneumatic Mount – Model PLM 1 main dimensions [4].

### 3.1.4. Commercial Arc Erosion Tip Types

Commercial spring-probes (made of beryllium copper) by Chi Shing Ltd., are used to damp the contact between tip and sample, with a spring constant of 300 N/m  $\pm$  20%. Most of performed tests were done with the same type of tip (Figure 3.4): a three part probe (plunger, spring and barrel) generally used in contact mode. Tip diameter ranges between 20 and 40  $\mu$ m. The spring material is tempered high-carbon steel also known as “spring wire” (SWP). At full stroke, this spring provides 100 gram-force resulting in a spring constant of 300 N/m  $\pm$  20%. For further information, general tip datasheet is available in Appendix A, section A.3. Plunger is made of SK4 steel alloy Rhodium plated and the barrel material is phosphor bronze plated gold [5].

The advantage of this kind of tip is the capability to control the applied force on the material. It should be noted that the electro-erosion process is performed in contact mode at very low spring compressions, in the range between 0.3 and 10  $\mu\text{m}$  which correspond to applied forces from 0.1 to 3.3 mN, according to Hooke' Law expression. This guarantees working pressures similar to those employed in contact profilometry, avoiding damage of the sample. We did not observe mechanical damage on the samples below 1  $\mu\text{m}$  tip compression.



Figure 3.4: Commercial Spring Probe for arc erosion process [datasheet in Appendix A, section A.3]

Other tests were performed using a Dong Bang acupuncture needle (Figure 3.5a); reference DB102; with a vertex diameter of 5 – 6  $\mu\text{m}$  (Figure 3.5b). Acupuncture needles used for this purpose were split, separating the manipulation spring from the needle itself, allowing a stronger attachment to the machine. Besides, this rigid tip can be damaged during the approach method and do not include an integrated shock absorber mechanism, so they are used either directly or bended to form a home-made cantilever, as shown in Figure 3.5c.

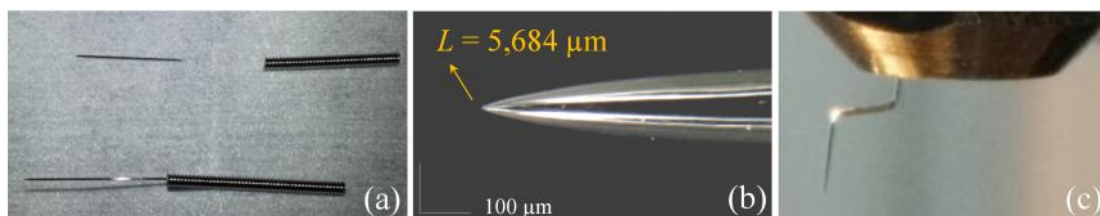


Figure 3.5: Dong Bang commercial acupuncture needle details: (a) sectional cut for assembly (b) needle tip vertex: between 5 and 6  $\mu\text{m}$  diameter and (c) home-made cantilever fabricated with this acupuncture needles.

Materials for this type of needles are surgical grade stainless steel with 12-20% of Chromium, 0.2 – 3% Molybdenum and 8 – 12 % of Nickel. The presence of Chromium increases wear and corrosion resistance, Molybdenum gives high strength and edge sharpness and Nickel a smooth polished finish. With these components, this tip is suitable for this application.

## **3.2 DESIGNED PARTS**

New parts were designed in order to assemble the final prototype. The parts were manufactured at Instituto de Ciencia de Materiales de Madrid in the Mechanical Workshop subdivision, according to our design and specifications.

### **3.2.1. Nano and micrometric stages Stands**

The prototype is mounted on a Newport board (750 x 450 millimeters with M6 holes arranged in a 25 millimeters grid). The manufactured stands are made from aluminum and duly planarized. The parallelism between faces varies from 0 to 15  $\mu\text{m}$  along 72 - 75 mm. However, a method has been implemented to correct the tilt by an automatic correction algorithm. Additional information is given in Appendix A (section A.4), regarding general aspects for the arc erosion procedure, the tip approaching protocol and the tilt correction method previously mentioned.

The final subassembly for the XY and Z units is showed in Figure 3.6 (drawing details for related parts are available in Appendix B, sections B.1., B.2, and B.3.). M4 (For PI Hera Figure 3.6a) and M2.5 (For LISA, Figure 3.6b) screws were used to attach each piezoelectric to its stand. Using screws makes the system easy to assemble or disassemble and adds stiffness to the whole set. Maintenance is also easier and faster. The final assembly for the XY unit is capable to reach a wide range of working distance (mm to tens of nm).

The micrometric arm stage for Z-axis is a variant of the PLS - 85 micrometric stage used in the XY unit, with a few modifications related to the way how it is coupled. Its main frame is an “L” shaped plate part that holds the step by step motor and the mechanism needed for axial movement. Also it has less travel than XY unit and its position could be modified directly in the main frame. More details are given in the following section.

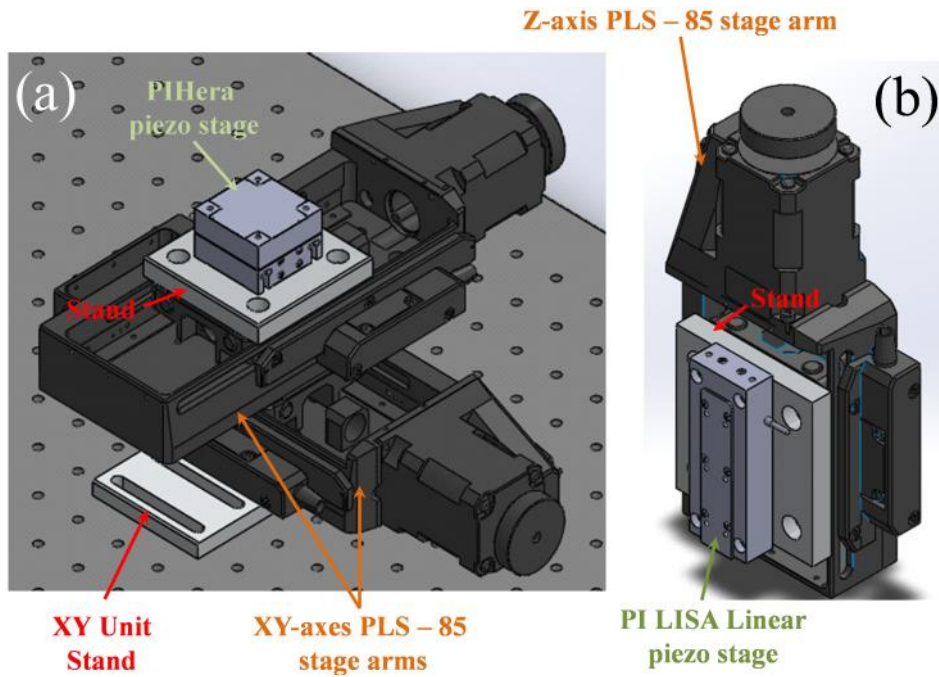


Figure 3.6: XY-axes and Z-axis subsystems separate assembly details: (a) micrometric – nanometric XY unit with manufactured stands (red) and (b) micrometric – nanometric Z unit.

### 3.2.2. Tip Attachment Mechanism

The tip attachment mechanism was designed in order to operate with a wide range of tips. The external screw which hosts the collet is similar to that used in Dremel motorized tools, allowing the adaptation of a commercial Dremel fixation kit. The reference of this accessory is 4485 and is shown in Figure 3.7.



Figure 3.7: Dremel commercial accessory used as attachment mechanism. (Left) Detail of a external screw of a Dremel tool. (Right) Comercial Dremel kit ref 4485 [6].

Figure 3.8 shows the final screw bolt with two different diameters (M6 / 0.280" - 40UNS-2), self-designed to adapt the commercial Dremel kit, made from brass, good electrical conductor, excellent machinability, highly resistance to corrosion and cheaper

than aluminum, make it a suitable material for this purpose (Drawing information is given in Appendix B, B.4.)

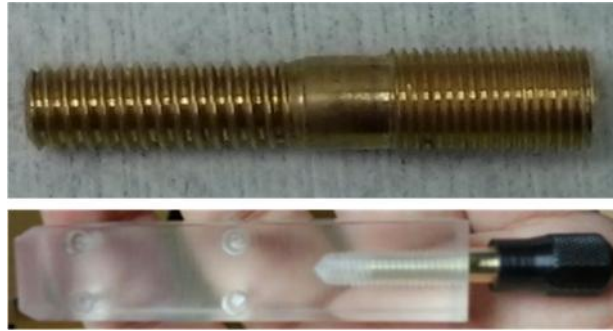


Figure 3.8: Final tip attachment mechanism two-screw bolt (top) and tip attaching assembling (down).

The way in which the screw bolt is adapted to the Z-axis piezoelectric is through a self-designed poly (methyl methacrylate) part (details given in Appendix B – B.5.). This material was chosen because of its main properties: great ease of machining, excellent insulator, similar hardness to aluminum, high impact resistance and lighter than any other metal. Piezoelectric sensors are very weight sensitive, especially when hung vertically. Reduce its weight is the main objective: the sensor would operate more accurately. Final assembly of the tip attaching mechanism is also shown in Figure 3.8 (down). With this last component, Z-axis unit is completed and final disposition of the components are shown in Figure 3.9, including CAD design and final assembly.

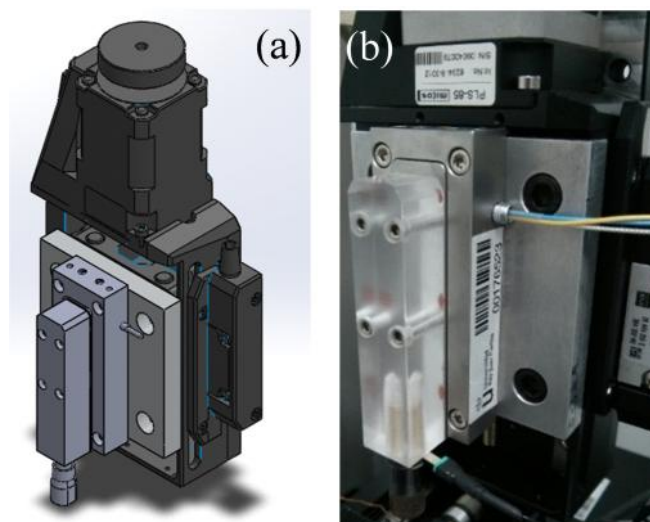


Figure 3.9: (a) Z-Axis unit CAD modelling, final design and (b) final assembly, Z- Axis current status.

Once Z-axis subsystem is assembled, it is directly attached to a 250 mm beam, which is supported by two 500 mm height columns, see Figure 3.10. The Z-axis subsystem height can be varied through this beam, moving it up and down as needed to a required height, being secured by means with four fasten press thread accessories. With this clamping main frame a high degree of robustness and verticality was achieved. This structure was originally previously conceived before the changes outlined above.

Final assembly is done by the joint of these three subsystems, making this task easier and faster. Full machine prototype is shown in Figure 3.11 (left) after Z- unit (PI Lisa Linear actuator and PSL - 85 modified stage) was attached to the supporting main frame, directly above of the XY unit (PI Hera piezo stage and XY PSL-85 micrometric arms). A structured table was made to wear only the arc-erosion machine on mentioned anti-vibratory supports, locating corresponding controllers, power sources, other instruments and accessories in a separated place, in order to avoid unwanted vibrations and shocks that may arise from handling or operation, see Figure 3.11 (right). Additionally, this prototype is located in a 10000 class clean room, adequate place to perform the proposed arc-erosion tasks.

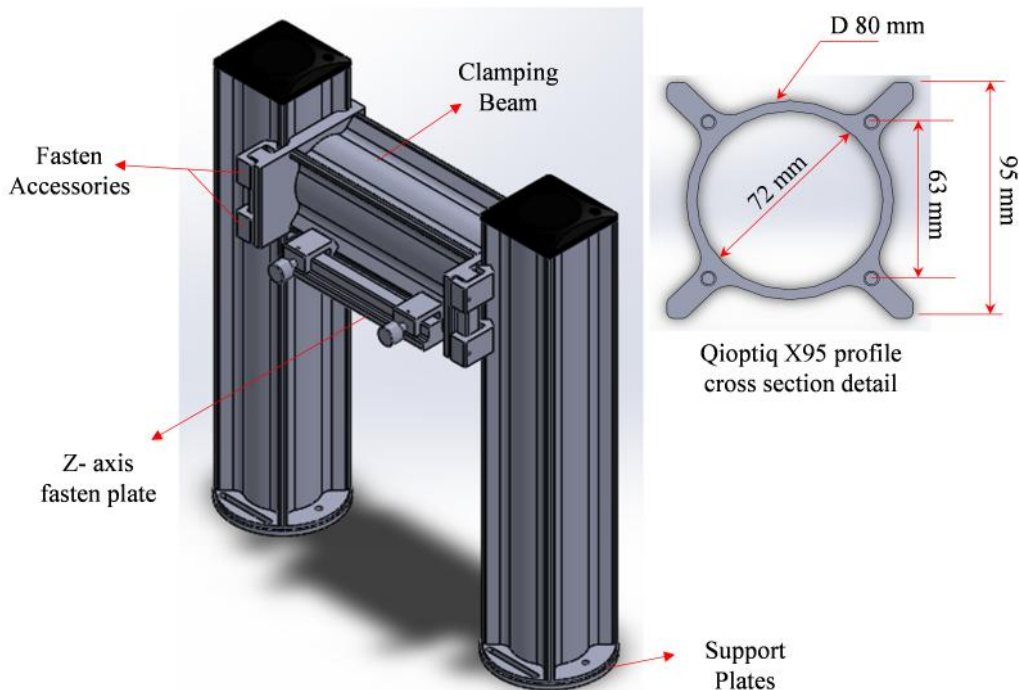


Figure 3.10: CAD assembly for main frame design. Inset: Qioptiq X95 profile cross section detail.



Figure 3.11: Final machine assembly over self-made structured table (left) and complete arc-erosion system, including all the supporting equipment for the proposed tasks (right).

### 3.3 ELECTRICAL MEASUREMENTS

The probe is negatively biased with a DC voltage (0 – 100 V) respect to ground, which is located on the sample surface by silver paint dots. The power supply used is a Promax FAC-662B (Figure 3.12a). Consist of two independent sources that can provide an output voltage between 0 and 30 V and also allowing using them in tracking function: reaching 60 V, expanding it voltage output at twice. Current values for each mode are from 0 to 2 A (0 – 30 V) and 0 to 1 V (0 – 60 V) with a limiting protective knob. A 220  $\mu$ F bypass capacitor at the output of the DC Source supplies the necessary current even although the protective current-limitation stage is active.



Figure 3.12: Support Equipment: (a) Promax FAC – 662B, (b) Yokogawa DL 6154 Oscilloscope and (c) Yokogawa Digital Multimeter Model 7562

A Yokogawa 1.5 GHz and 10 GS/s oscilloscope DL 6000-DL 6154 Figure 3.12b) is used to motorize de current y a load resistor. Finally, a Yokogawa digital multimeter

model 7562 (Figure 3.12c) is also used for current and resistance measurements. The final electro erosion scheme can be shown in Figure 3.13.

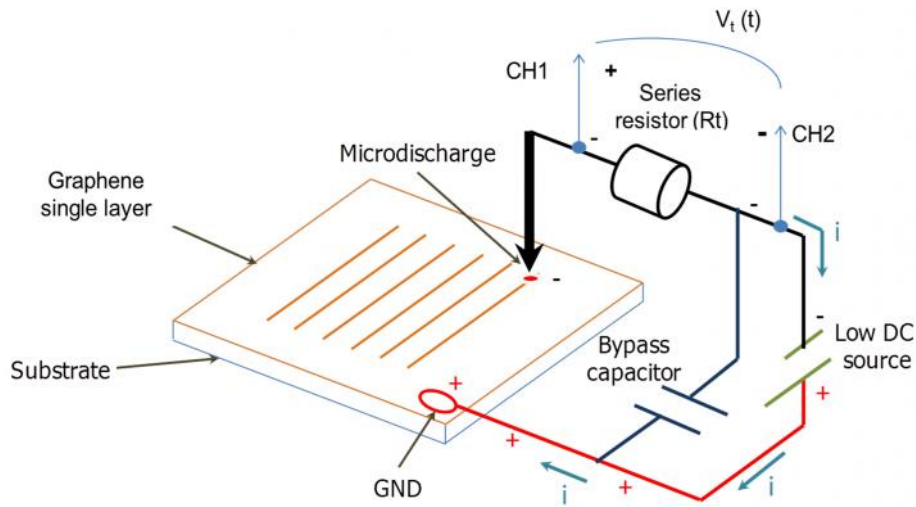


Figure 3.13: Electro erosion circuit scheme.

In order to measure the electrical characteristics of this phenomenon we have arranged a circuit as shown in Figure 3.13, where current across the tip-sample junction is monitored with an oscilloscope in terms of voltage changes ( $V_t$ ) in a series resistor ( $R_t$ ). Both, a broad tip to increase capacitance, and a high series resistance  $R_t$ , have been chosen in order to favor measurability of the experiment. Otherwise, the signal is obscured within the electrical noise, something that complicates its observation in experiments with nano-probes (STM, AFM) owed to their low capacitance. The sample-to-tip contact point ( $z = 0$ ) is previously determined by recording the electrical response between probe and sample at very low DC voltages ( $< 0.1$  V).

### 3.4 FINITE ELEMENT ANALYSIS MODEL

In order to elucidate the physical phenomena, a finite element analysis solver and simulation software package had been used. This software is known as COMSOL Multiphysics: a modular set of predefined user interfaces with associated tools for modelling common applications [7], very useful in physical and engineering applications.

One of the specific modules available and the most used in this thesis work is the semiconductor module, allowing a detailed study of our own semiconductor application at the fundamental level. The semiconductor module used for all the simulations solves

Poisson's Equation in conjunction with the continuity equations for charge carriers, solving carrier concentrations (electrons and holes) explicitly [8].

Usually for finite element analysis, model geometry is crucial; boundary conditions directly depend on it, while it is simplest the probability to obtain a solution in short processing period increases. Unfortunately, this processing period also depends directly on system resources; a lot of data is handled, filling up a great amount of system memory. This reinforces the idea of ensuring model simplicity for final simulations. Our original model is a solid of revolution; taking into account the above items, for simplification; the model can be represented by an axisymmetric geometry i.e. symmetry around an axis. Moreover, some physical problems related with field theory, continuous media or quantum theory can be "easily" solved when data involved obey to this type of symmetry, reducing spatial coordinates from three to two.

Figure 3.14 shows model's geometry for simulation procedures. There are five zones of interest, demarcated by letters: (a) is the surrounding space corresponding to air; (b) is the solid substrate; (c) half spring probe tip; (d) silver ground contact and (e) showed in the detailed inset, correspond to the thin layer.

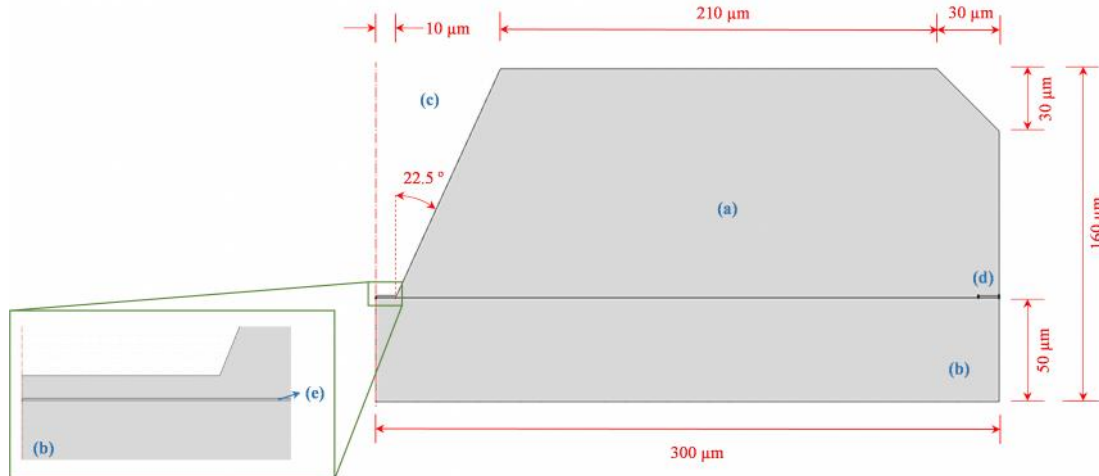


Figure 3.14: Established geometry for finite element analysis.

In this thesis are included two types of models where substrate (b) and thin film (e) change depending on the case, keeping the same geometry. The main difference between each case is basically the assigned materials. Both models will be described below.

### 3.4.1. Glass-ITO Model

For this model, the substrate considered glass (b) and a 100 nm  $\text{In}_2\text{O}_3$ :  $\text{SnO}_2$ , typically 90%  $\text{In}_2\text{O}_3$ , 10%  $\text{SnO}_2$  by weight (ITO) thin film (e). The absence of ITO as a standard material in Comsol library has required its creation with the characteristic values found in the bibliography. Table 3.2 shows the final ITO properties used for simulation purposes. On the other hand, for glass substrate and the silver ground contact, all used properties were the available at Comsol material library. It is necessary to highlight that Comsol has the characteristic to edit these default properties, allowing the user to change any or all of the properties for any material available, it may be the case that a property does not match or is not the appropriate one, being able to change it for a more realistic value.

Once all materials properties were set and assigned to previously modelled geometry, semiconductor physics module is added. According to the geometry, Figure 3.15 shows the assigned boundary contact conditions for final modelling. As these properties are assigned some features are also defined e.g. voltage value at tip's Schottky contact and a zero voltage for ground at the silver contact.

Relative permittivity	~ 9	[9]
Band Gap	3.75 eV	
Electron Affinity	4.7 eV	[10]
Conduction Band	$4.137 \times 10^{24} \text{ m}^{-3}$	[11, 12]
Electron Mobility	$50 \text{ cm}^2/(\text{V s})$	[12]

Table 3.2: Properties used for ITO model simulation.

Furthermore, another important parameter for the adequate simulation is the doping implementation for ITO thin film. Khusayfan *et al* [13] and Chowdhury *et al* [14] have demonstrated that the doping for ITO is maintained in the range from  $1 \times 10^{19}$  to  $1 \times 10^{20} \text{ cm}^{-3}$  ( $1 \times 10^{25} - 1 \times 10^{26} \text{ m}^{-3}$ ).

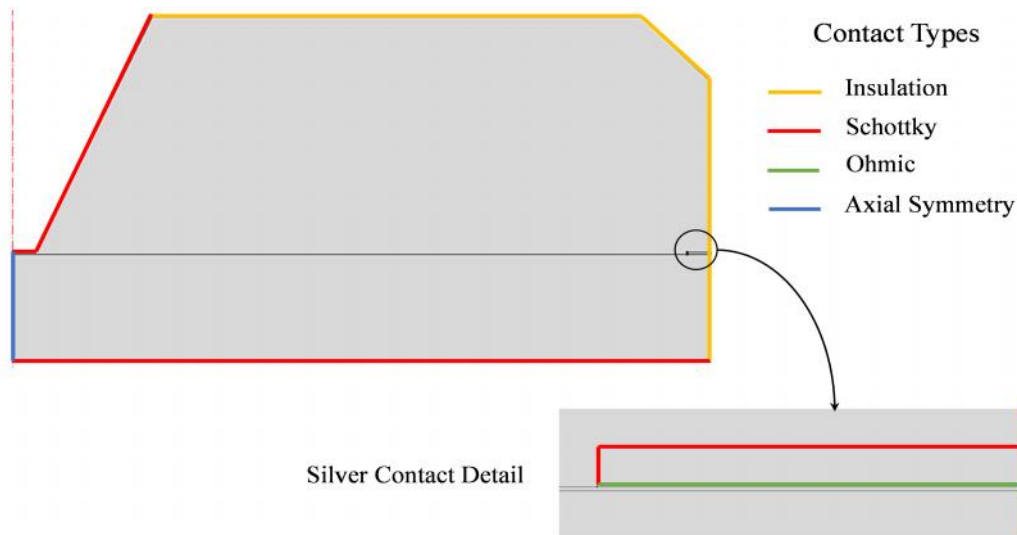


Figure 3.15: Glass – ITO Finite Element Model: semiconductor module contact assignment.

The last step prior to model compilation is the mesh construction, an important feature for finite element analysis. Being a 2D model, the adequate meshing option is the use of triangles or quadrilaterals: the simplest type of mesh, quick and easy to build. This procedure is done automatically by COMSOL using the physic-controlled mesh option, allowing mesh density selection, in this case extremely fine mesh density is selected in order to obtain a more accurate result. It is possible to manipulate the mesh element size requiring more system resources.

### 3.5 OPTICAL AND MORPHOLOGICAL PATTERN CHARACTERIZATION

#### 3.5.1. Optical Images

Optical images have been acquired with a SMZ - 168 Stereo zoom microscope from Motic [15] with a 5.0 Megapixel coupled Digital microscope camera reference Moticam 2500 [16]. All images were processed by the Motic Images Plus 2.0 software, developed by the same manufacturer.

### 3.5.2. Contact Profilometer

Inspections on final patterns were held in a KLA – Tencor AlphaStep D120 Stylus profiler (Figure 3.16). This equipment has 55 mm scan length, Z sensor range up to 1.2 mm; with a 200 mm motorized sample positioning stage and a force control in a range between 0.03 mg to 10 mg. Resolution is given by the tip size, in this case, the stylus profiler is equipped with a 20 micron tip. It also incorporates a 4X motorized camera for sample visualization [17].



Figure 3.16: AlphaStep D120 profiler for pattern characterization.

### 3.5.3. Micro-Raman analysis

Due to the extreme transparency property of graphene Raman spectroscopy has become a powerful technique to univocally characterize graphene, graphite [18] and more recently graphene oxide [19]. In fact, Raman spectroscopy is an integral part of graphene research. It is used to determine the number and orientation of layers, the quality and types of edge, the effects of perturbations: such as electric and magnetic fields, strain, doping, disorder and functional groups. This, in turn, provides insight into all  $sp^2$ -bonded carbon allotropes, because graphene is their fundamental building block.

Raman scattering or the Raman Effect is the inelastic scattering of a photon. When photons are scattered from an atom or molecule after irradiate a material with certain frequency, most photons are elastically scattered (Rayleigh scattering), such that the scattered photons have the same energy (frequency and wavelength) as the incident

photons. A small fraction of the scattered photons (with a much lower probability) are scattered by an excitation, with the scattered photons having a frequency different from, and usually lower than that of the incident photons. The photon can exit the sample with lower energy (Stokes process - S) or with higher energy (Anti-Stokes process - AS). Since the sample has to return to the stationary state, the lost or gained energy must correspond to the phonon energy.

The general case for most of the materials the Raman scattering is known to be *non-resonant*, as the scattered energy does not match an electronic state. If this is not the case and the excitation or scattered energies coincide with an electronic transition, the process is called *resonant* increasing by orders of magnitude the Raman intensity. But the absence of a band-gap in graphene makes all wavelengths of incident radiation resonant and, thus the corresponding spectrum displays a high intensity giving us a powerful tool to characterize the patterned areas in graphene.

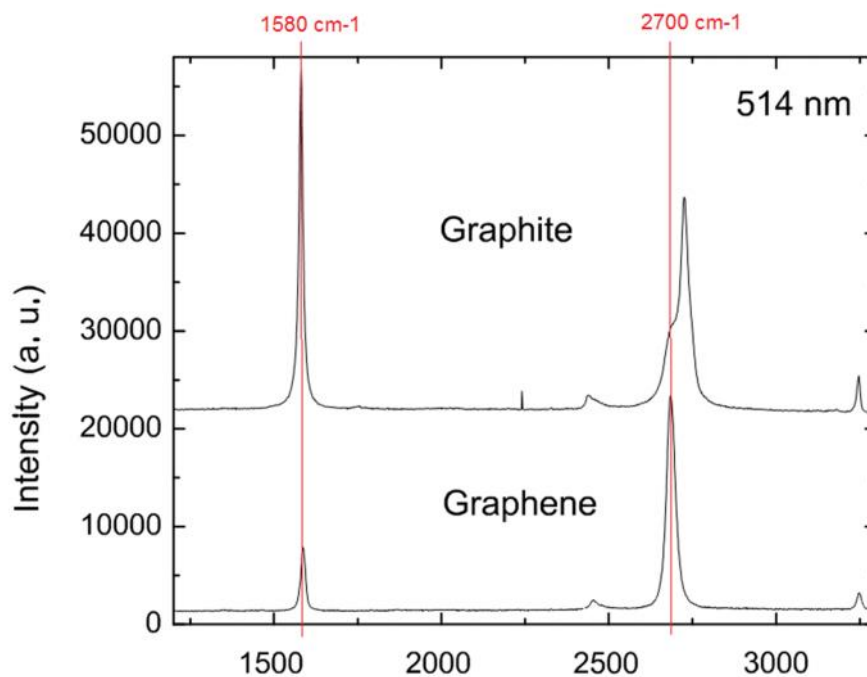


Figure 3.17: Raman Spectrum for monolayer Graphene, a comparison with Graphite [20].

The Raman spectra of a single layer graphene (SLG) and of highly ordered graphite are plotted in Figure 3.17. Two main peaks called G and 2D are considered. The origin of the G peak at around  $1580 \text{ cm}^{-1}$  is directly related to the stretching mode of  $\text{sp}^2$  bonds. At around  $2700 \text{ cm}^{-1}$  Raman shift, the 2D peak originates from a process with two phonons involved with opposite wave vectors. There are several two phonon peaks

observable but the 2D is the most intense and relevant. The frequency of the 2D peak is determined by the energy of the incident laser since the induced electronic transition determines the phonon wave vector. For visible laser excitation (2-3 eV) the wave vector is close to the K point. Its intensity and width changes as a function of the number of carbon layers because the resonant Raman mechanism implied it is closely linked to the electronic structure. As showed in Figure 3.17, a large amount of stacked graphene sheets, i.e. graphite, shows a different Raman spectrum. For the graphite case the intensity ratio of 2D to G peaks is lower, around 0.5, compared to the SLG case where the ratio is almost 4. Also the shape and frequency of the 2D peak differ significantly. The Raman spectra of 2, 3 and 4 graphene layers are distinguishable so Raman spectroscopy is a straightforward technique to determine the number of layers (up to 4-5 layers) as well as whether they are stacked as in graphite or not [19]. The main features of Graphene Raman spectrum are referred to the 2D band: 25  $\text{cm}^{-1}$  narrower and its intensity is four times higher than the G band.

When Graphene monolayer contains defects, two additional bands appear at 1350 and 1620  $\text{cm}^{-1}$ , named as D and D'. Graphene oxide and reduced graphene oxide can be considered as highly disordered forms of graphene with different degrees. The most important feature of the Raman spectra for this kind of compounds (Figure 3.18) is the D peak around 1350  $\text{cm}^{-1}$  D Raman Shift ( $\text{cm}^{-1}$ ) usually referred as *defects peak*. The D peak can be viewed as a breathing mode of the six-fold aromatic ring. This mode is forbidden in perfect graphite and only becomes active in the presence of defects in the lattice. Its intensity is related to  $\text{sp}^2$  clusters size because it is produced only in small regions of the crystallite like the edges or near a defect. This way, smaller crystallites with more edges will show a higher D peak. Disorder in the edges of the lattice may arise from structural and topological defects (vacancies, dislocations...). Chemical modifications of the structure like its oxidation may appear as defects in the edges but also in the interior of the crystallite. Nevertheless, since D peak is related to the C  $\text{sp}^2$  rings, C=C chains do not present this vibration. Also, it is an indication of the formation of new rings in the reduction processes of graphene/graphite oxide.

So, for our purposes, Raman spectrum could be considered as a characteristically “finger print”. Figure 3.18 shows based measured spectrum for commercial Graphene samples used along this thesis work [21] and this spectrum has been used for comparison. As an example, following figures will show a set of different type of

obtained spectra. These plots depict what could be found as a result according to the pattern process, discussing some key features to understand further results. In Figure 3.19, plot A (red) belongs to a pristine Graphene monolayer, same spectrum as showed previously, taken as base spectrum. Plot B (blue) is an example for broken Graphene in grain size form but without its removal: key features here at first instance are: the G peak still remains comparing both which means that Graphene have not been removed, and the 2D peak decreases comparing it with pristine monolayer, resulting in a low quality Graphene. There is also noticeable that D and D' have appear implying that there are added defects in the Graphene monolayer.

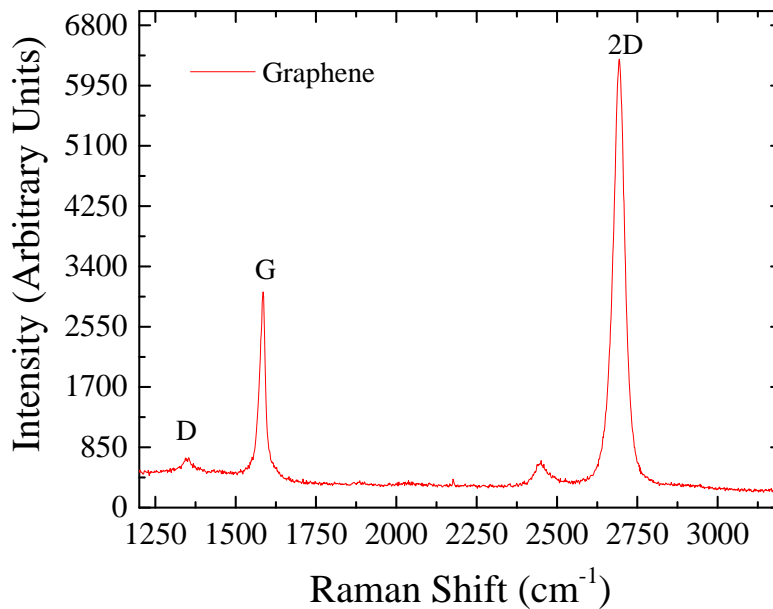


Figure 3.18: Micro Raman spectrum of commercial pristine Graphene from Graphene Supermarket.

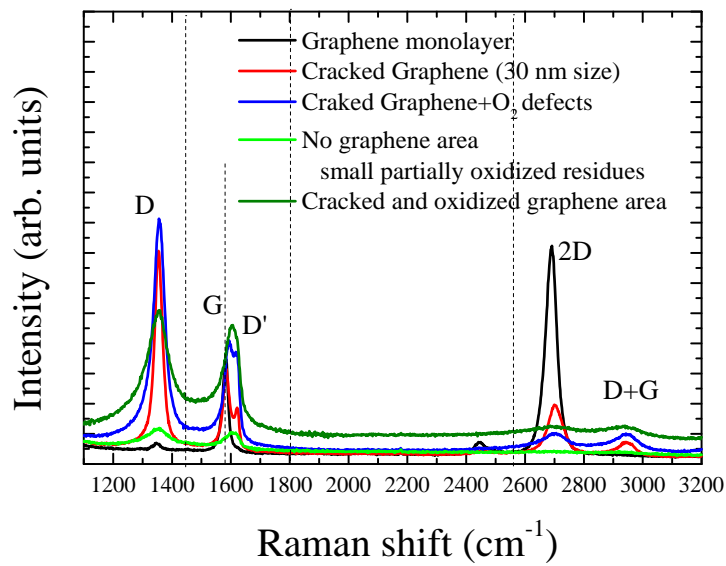


Figure 3.19: Micro-Raman spectra showing different effects of the electro erosion process at different conditions on Graphene.

Plot C (green) is another example found in the tests here gathered. Plot C (green) and plot B (blue) have some notable differences. In terms of intensity, peak D and D' are bigger and slightly wider. Peak 2D in plot C (green) is even smaller. Formerly, it was said that plot B (blue) corresponds to broken Graphene in a grain type size. In the case of plot C (green) Graphene is also broken but in smaller pieces. The way how the grain size is known [22], is through equation (3) expressed as follows:

$$L_a(n) = (2.4 \times 10^{-1}) \cdot \lambda_{li}^4 \cdot \left(\frac{I_D}{I_G}\right)^{-1} \quad (3)$$

Where:

- $I_D$  and  $I_G$ : is the D and G peak intensity.
- $\lambda$ : Laser wavelength

In Figure 3.19, there is another interesting spectrum: plot D (magenta). Graphene has not been removed and is probably oxidized due to the material's substrate arc erosion. Perhaps, it is one of the most easy to distinguish because peaks D and G have the peculiarity of being almost equal in intensity. Moreover, peak D' has been engulfed by G and 2D has practically disappeared.

Last case is showed in Figure 3.20, plot E (cyan). It corresponds to a particular area where Graphene has been removed; G peak has been reduced enough in comparison with plot A, a pristine area. Even though, this case is similar to plot D in relation to the difference between peaks D and G, very similar in terms of intensity, this means that the slightly remaining Graphene can be partially oxidized and very small in size.

The Raman spectroscopy experimental set up consists in an Ar laser, using the 488nm laser line in a range of power between 22 - 120mW with a Jobin Yvon HR-460 monochromator. The scattered light was analyzed with a Jobin Yvon HR-460 monochromator coupled to a Peltier cooled Synapse CCD. The incident beam is focused with an Olympus BX60M microscope with x4, x20 and x100 objectives. A Holographic filter Kaiser Super-Notch-Plus was used to remove the Rayleigh signal. The minimum laser spot size, diffraction limited, is  $1.22 \lambda / NA = 630 \text{ nm}$  for 488 nm and  $NA = 0.95$ . The theoretical diffraction limited spatial resolution achievable using an optical microscope is  $0.61 \lambda / NA$ , which is around 350 nm for optical images but clearly above this value for Raman. It is consider that the Raman spatial resolution is around  $0.7 \mu\text{m}$ . Experimental setup is shown in Figure 3.21.

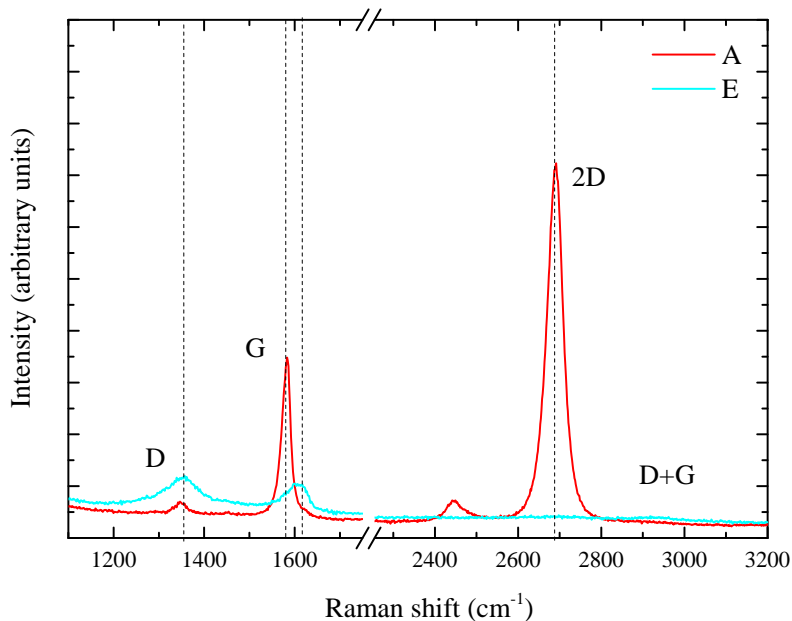


Figure 3.20: Pristine Graphene area (red) vs Graphene removed area (cyan).



Figure 3.21: Experimental setup for Raman Spectroscopy, courtesy of Instituto de Ciencia de Materiales de Madrid (CSIC).

#### 3.5.4. Atomic Force Microscopy

The Atomic Forces Microscopy (AFM) is a characterization technique belonging to the family of Scanning Probe Microscopies (SPM). These techniques are characterized by using a physical probe to scan surfaces. Specifically, AFM uses a cantilever with a sharp tip at its end that is used to scan the surface. A laser beam is focused over the tip's surface in such a way its reflection is collected by a photodiode. The deflection suffered by the tip in contact with the surface is then recorded by the photodiode. The technique allows resolutions in the Z component in the order of the tenths of an angstrom.

Several measure modes can be performed according the tip motion. Contact mode is a measure mode where the tip is dragged across the surface of the sample and the deflection of the cantilever is kept constant. This mode is more aggressive and damages the sample but allows overcoming ambient humidity and other liquids surface interactions. Non-contact mode is another way to measure based in a scan of the surface while the tip is oscillated at the resonance frequency and the amplitude of the oscillation is kept constant. The goal of this mode is to not damage the sample but water interactions are its main drawback. Tapping mode is an intermediate mode where

oscillation amplitude is kept around the 50% of the free amplitude. Tapping mode provides higher resolution with minimum sample damage.

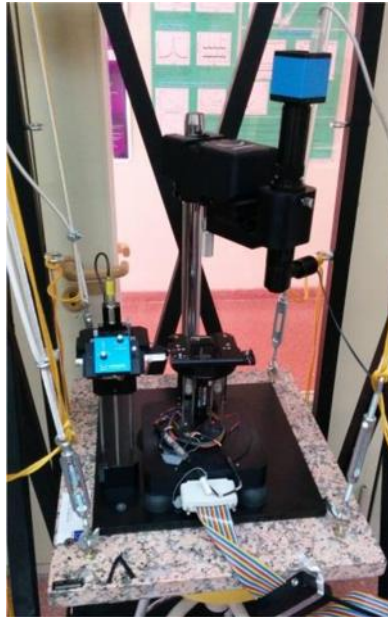


Figure 3.22: (a) Scanning probe microscope used for AFM measures, courtesy of Instituto de Ciencia de Materiales de Madrid (CSIC).

In this case, AFM images were made with a Nanotec microscope. The software used was WSxM [23] from Nanotec Company. The measurements were made under ambient conditions. The images have been acquired in tapping mode using commercial silicon tips Nanosensors PPP-QNCHR with a 20-30 nm tip diameter. AFM setup is shown in Figure 3.22.

### 3.6 REFERENCES

- [1] Physik Instrumente (PI) GmbH & Co, “PLS - 85 Linear Stages Product Detail,” [Online]. Available: <http://www.physikinstrumente.com/product-detail-page/pls-85-601301.html>. [Accessed 2012].
- [2] “Physik Instrumente - Motion and Movement Products: Motorized and Positioning Systems for large travel ranges and Piezo Positioning System for nanometer resolution travel range,” [Online]. Available: <http://www.physikinstrumente.com/>. [Accessed 2012].
- [3] Dino-Lite, Digital Microscope, “AM4113ZT4 Dino-Lite Premier,” 2014. [Online]. Available: <http://www.dino-lite.com/web/AM4113ZT4.html>. [Accessed 2013].
- [4] “Fabreeka Vibration and Shock Control,” [Online]. Available: <http://www.fabreeka.com/Products&productId=29>. [Accessed 2013].
- [5] , Chi Shing Meter Cable Manufacturing, «Supplier: RS Amidata,» [En línea]. Available: <http://es.rs-online.com/web/>. [Último acceso: 2011].
- [6] Dremel, «Collets (3.2 mm) Including a Collet Nut (4485),» 2014. [En línea]. Available: <http://www.dremeleurope.com/gb/en/collets-3-2mm-includingacolletnut-214-ocs-p/>. [Último acceso: 2012].
- [7] “Comsol Multiphysics - General Finite Element Analysis Software Suite Description,” [Online]. Available: <http://www.comsol.com/products>. [Accessed 2013].
- [8] “Comsol Multiphysics Software - Semiconductor Module Description Overview,” [Online]. Available: <http://www.comsol.com/semiconductormodule#overview>. [Accessed 2013].
- [9] W. G. Van Sark, L. Korte and F. Roca, Physics and Technology of Amorphous - Crystalline Heterostructure Silicon Solar Cells. Chapter 9: Deposition and

- Properties of TCOs by Florian Ruske, pp. 301-330, Table 9.1, Springer, 2012.
- [10] G. G. Pethuraja, W. Roger E., A. K. Sood, C. Lee, N. J. Alexander, H. Efstathiadis, P. Haldar and J. L. Harvey, "Current-Voltage Characteristics of ITO/p-Si and ITO/n-Si," *Advances in Materials Physics and Chemistry*, vol. 2, no. 59-62, 2012.
- [11] C. Kittel, *Introduction to Solid State Physics - 8th Edition*, Wiley, 2004, p. 704.
- [12] K. Ellmer and R. Mientusb, "Carrier transport in polycrystalline transparent conductive oxides: A comparative study of zinc oxide and indium oxide," *Thin Solid Films*, vol. 516, no. 14, pp. 4620-4627, 2008.
- [13] N. Khusayfan and M. El-Nahass, "Study of Structure and Electro-Optical Characteristics of Indium Tin Oxide Thin Films," *Adv Cond Matter Physics*, p. 408182, 2013.
- [14] F. Chowdhury, S. Chowdhury, F. Hasan and T. Begum, "Optical properties of Undoped and Indium-doped Tin Oxide Thin Films," *Journal of Bangladesh Academy of Sciences*, vol. 35, no. 11, pp. 99-111, 2011.
- [15] M. E. «SMZ168 Series Versatile Stereo Microscope solution,» [En línea]. Available: <http://www.moticeurope.com/accessories/accessories-stands/boom-stands-1/smz168-series/>.
- [16] R. A. «Digital microscope camera Moticam 2500 Datasheet,» [En línea]. Available: [http://www.ryfag.ch/sites/default/files/docs/digital\\_mikroskopkamera\\_moticam\\_2500-en.pdf](http://www.ryfag.ch/sites/default/files/docs/digital_mikroskopkamera_moticam_2500-en.pdf).
- [17] "KLA Tencor - Surface Profiling Alpha Step D120," [Online]. Available: <http://www.kla-tencor.com/surface-profiling/alpha-step-d-600.html>. [Accessed 2013].
- [18] C. Ferrari and D. Basko, "Raman Spectroscopy as a versatile tool for studying the

- properties of graphene,” *Nat. Nanotechnology*, vol. 8, pp. 235-246, 2013.
- [19] X. Díez-Betriu, S. Álvarez-García, C. Botas, P. Álvarez, J. Sánchez-Marcos, C. Prieto, R. Menéndez and A. de Andrés, “Raman spectroscopy for the study of reduction mechanisms and optimization of conductivity in graphene oxide films,” *J. Mater. Chem C*, vol. 1, pp. 6905-6912, 2013.
- [20] C. Ferrari, J. Meyer, V. Scardaci, C. Casiraghi, M. Lazzeri, F. Mauri, S. Piscanec, D. Jiang, K. Novoselov, S. Roth and A. Geim, “Raman Spectrum of Graphene and Graphene Layers,” *Phys. Rev. Lett.*, vol. 97, p. 187401, 2006.
- [21] “Graphene Supermarket - Single/Double layer Graphene on 90 nm Silicon Dioxide Wafer - 10 pack,” [Online]. Available: <http://graphene-supermarket.com>. [Accessed 2013].
- [22] L. Cancado, K. Takai, T. Enoki, M. Endo, Y. Kim, H. Mizusaki, A. Jorio, L. Coelho, R. Magalhaes-Paniago and M. Pimienta, “General Equation for the determination of the crystallite size  $L_a$  of nanographite by Raman spectroscopy,” *Appl. Phys. Lett.*, vol. 88, p. 163106, 2006.
- [23] I. Horcas, R. Fernández, M. Gómez-Rodríguez, J. Colchero, J. Gómez-Herrero and A. Baro, “A software for scanning probe microscopy and a tool for nanotechnology,” *Re. Sci. Instrum.*, vol. 78, p. 013705, 2007.

## CHAPTER 4 . EXPERIMENTAL RESULTS

In this chapter the study of the electrical arc effect on different conducting materials is presented: from semiconductors like indium tin oxide (ITO or  $\text{In}_2\text{O}_3: \text{Sn}$ ), ZnO: Al (AZO) or Zinc Nitride ( $\text{Zn}_3\text{N}_2$ ) to conducting materials as aluminum or gold. First, the work is aimed to establish the appropriate conditions that lead to well resolved patterns for each material, highlighting threshold operating voltages. Then, a phenomenological discussion of the electrical erosion process will be carried out using finite element method simulation tools.

All these experiments have been done following the experimental setup diagram shown in Figure 3.13 (Chapter 3), which corresponds to the use of negative polarity unless otherwise indicated.

### 4.1 ELECTRO EROSION ON INDIUM-TIN OXIDE (ITO) THIN FILMS

Previous attempts of electric arc erosion on ITO are described in [1], obtaining a threshold voltage for operation on ITO/glass of -11 V. Below this voltage, fails increase dramatically, but it should be noted that the influence of the polarity on the arc-erosion

process had not been studied in detail. This section focuses on the effect of the polarity<sup>1</sup> (positive or negative) of the spring probe with respect to the glass/ITO sample. The operating conditions are summarized in Table 4.1.

Variable	Value
Travel speed (v)	0,1 mm/s
Test Resistance (R)	0,5
Travel acceleration (a)	100 mm/s <sup>2</sup>
Tip Compression	10 $\mu$ m
Tip diameter	40-50 $\mu$ m

Table 4.1: Processing values during test.

- **Groove patterns at different voltages and polarities.**

Electrical erosion on ITO layers (100 nm) on glass substrate was performed for applied voltages from  $\pm 11$  V to  $\pm 20$  V according to the pattern shown in Figure 4.1. In this figure we can observe optical images of the obtained grooves, (a) and (c), and their measured profiles, (b) and (d), before any etching treatment.

From the optical images, we can verify that negative polarization induced grooves with more optical contrast, what suggests better resolved patterns. From -11 V to -13 V, the edges are clearly defined through all the length of the groove. From -15 V we can observe that an effect of waving edge appears and increases with applied bias. These results are related with the nature of the arc-erosion process that has been preliminary exposed in Chapter 1, and will be discussed later in the phenomenological discussion of this chapter. The widths of the grooves increase with applied voltage, Figure 4.1(e), with a linear relation up to 15 V.

For positive polarity performed patterns, lower contrast is observed in the optical images and also the mentioned wave-edge effect is less evident. The groove width

<sup>1</sup> Positive polarization corresponds with inverse situation for applied  $V_{DC}$  in Figure 3.18 in Chapter 3, that is, negative terminal grounded

increases with applied voltage, in the same way as negative polarization, but it is also noticeable that these grooves are wider than those made using negative polarity, as it can be checked in Figure 4.1(e). A drawback is that an increased wear of the probe with positive polarity is observed.

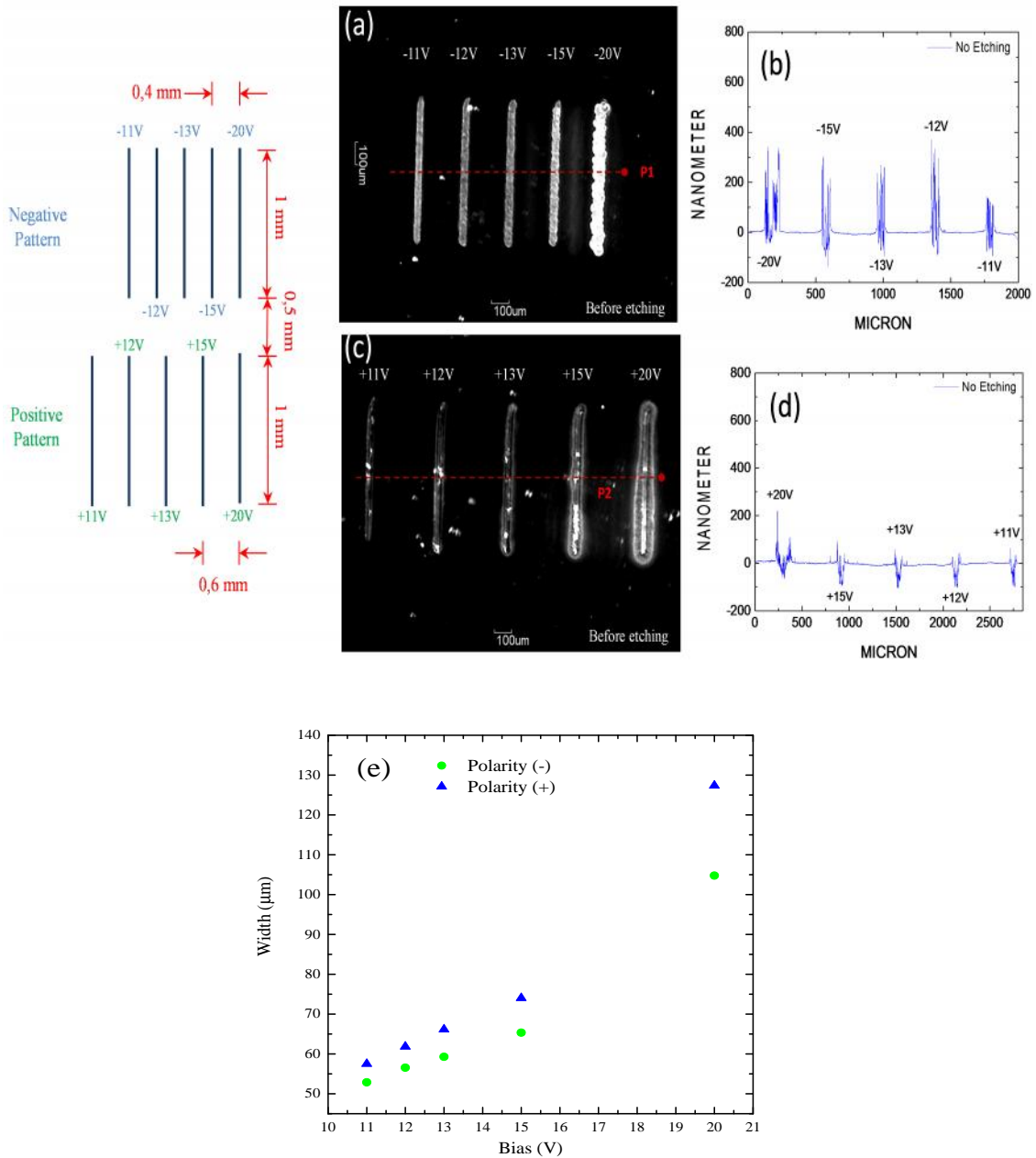


Figure 4.1: Dimensions and layout (left) and final pattern results for negative and positive polarities: optical images grooves (a,c) and (b,d) profilometry; (e) width variation of the electrical eroded grooves.

The profilometry measurements (Figure 4.1b and d), reveal that the electro erosion process generates particles or “waste” material accumulated at the edges of the

grooves. For negative bias the effect is more dramatic. In the profile image, we can observe peaks with a height  $> 200$  nm. These particles become troublesome on final optoelectronic devices and they have to be eliminated, because they induce electrical short cuts in active layers with typical thickness about 100-200 nm or less. For positive polarity, over heights are reduced considerably, slightly over 50 nm. But even so, this remaining material accumulation is still harmful for performance of optoelectronic devices, leading to leakage currents, shunt resistances and eventually in device short circuit. Usually, an appropriate chemical etching has to be carried out in order to remove this material waste, discussed later in this section.

Micrographs of extended areas eroded by performing many runs are shown in Figure 4.2, where this procedure was done at two different voltages, 10 V (close to the threshold for erosion) and 20 V (well above). The different textures suggest that a phase transition may occur or a change in the proportion of the oxides present. However, X-ray diffraction studies revealed no changes in the oxide phases, but just an increase of the material amorphization with increasing voltage. This degree of amorphization becomes a critical feature for the success of the subsequent chemical etching in order to remove affected ITO. A high degree of amorphization was observed to prevent the suitable operation of the etching. This aspect is analyzed in the following subsections.

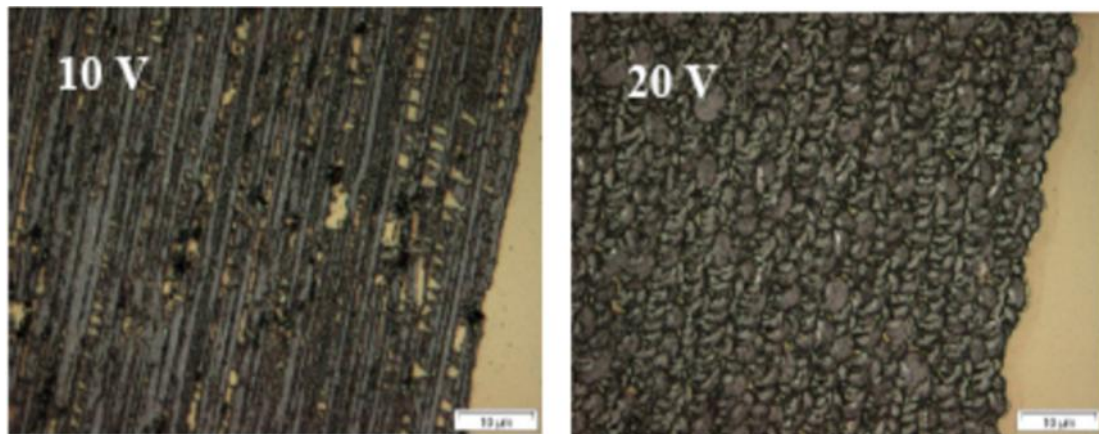


Figure 4.2: Microphotographs ( $73 \mu\text{m} \times 55 \mu\text{m}$  area) of eroded ITO at -10 V and -20 V.

- **Square patterns using  $\pm 12$  V to test electrical isolation**

To check the electrical isolation of the electro erosion lithography process, the current and resistance were measured from inside to outside of a closed square pattern and then compared to the values for same ITO points after arc-erosion. This measure is made using a digital multimeter in series to the main electrical circuit, and thus using

the proper tip to close the circuit. In view of our previous results, it was selected an intermediate processing voltage value ( $\pm 12$  V) to process the patterns. Five squares of one-millimeter side, and 500 microns spaced were performed maintaining the conditions summarized in Table 4.1. The final results are shown in Figure 4.3, where (a) are the squares performed using negative polarity and (b) for positive polarity.

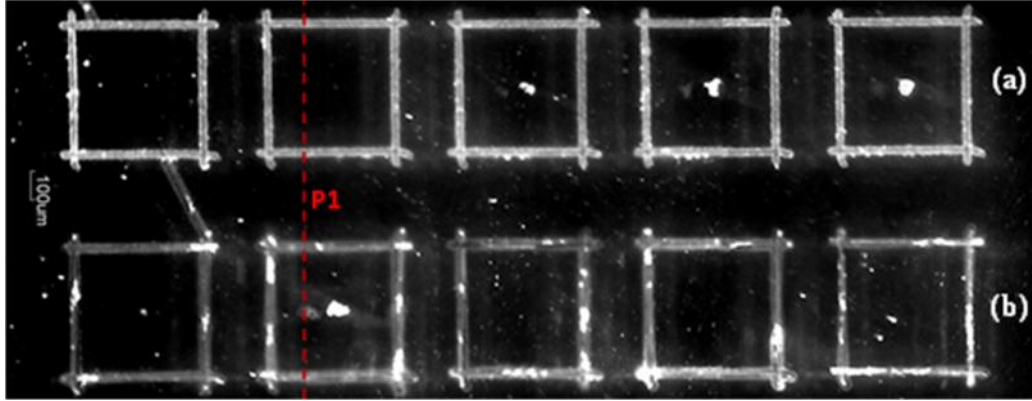


Figure 4.3: Final square patterns using a constant voltage and varying polarity: (a) -12V and (b) +12V. The red dotted line (P1), indicate the region where profilometry is taken.

-12 V Arc-Erosion						
Square	$V_b$ [V]	$I_b$ [A]	$R_b$ [ $\Omega$ ]	$R_a$ [M $\Omega$ ]	$I_a$ [A]	$V_a$ [V]
1	2,3	8,36E-02	27,51	3,19	7,20E-07	2,3
2	2,3	7,17E-02	32,08	3,71	6,20E-07	2,3
3	2,2	8,02E-02	27,43	2,34	9,40E-07	2,2
4	2,3	8,25E-02	27,88	1,11	2,07E-06	2,3
5	2,3	8,44E-02	27,25	2,16	1,02E-06	2,2
+12 V Arc-Erosion						
Square	$V_b$ [V]	$I_b$ [A]	$R_b$ [ $\Omega$ ]	$R_a$ [M $\Omega$ ]	$I_a$ [A]	$V_a$ [V]
1	2,2	7,85E-02	28,03	0,83	2,64E-06	2,2
2	2,2	7,75E-02	28,41	3,10	7,42E-07	2,3
3	2,3	8,12E-02	28,31	1,96	1,02E-06	2,0
4	2,4	7,84E-02	30,61	1,56	1,47E-06	2,3
5	2,3	8,48E-02	27,12	3,57	5,60E-06	2,0

Table 4.2: Arc-erosion square electrical isolation test results.

The isolation results are summarized below in Table 4.2. The measured resistance of the ITO thin film ( $R_b$ ) before arc-erosion is 30  $\Omega$ . When negative polarity is applied for processing, this resulted value increases six orders of magnitude above the initial

value i.e. order of mega ohms ( $M \Omega$ ), and consequently the leakage current is reduced from 4 to 5 orders of magnitude. For positive polarity, the data shows the same behavior as negative polarity, resistance after arc-erosion reaches mega ohm ( $M \Omega$ ) and also the measured current after arc-erosion decreases in the same way as negative polarity. Thus, electrical isolation in ITO thin films can indeed be successfully achieved for both polarities.

- **Waste elimination: chemical etching process**

As mentioned above, the produced waste during the electrical erosion results in failures and undesirable effects on the final device. Typically, chemical etching methods are used to eliminate these residues. Despite the fact that there are a variety of etching methods [2, 3], in this Thesis I have selected a soft chemical etching able to directly affect such material accumulation at the edges without jeopardizing the electrical properties of the non-eroded ITO.

The basic procedure for the chemical etching referred here was taken from Hohnholz *et al* [4] and modified to adapt to room conditions and make it less aggressive. Using a solution (1:1) of distilled water and hydrochloric acid (37%), samples are exposed to a 10 seconds etching bath at 20 °C and then rinsed with distilled water. By electrical measurements it has been checked that the etching rate on pristine ITO is below 1 Å/s.

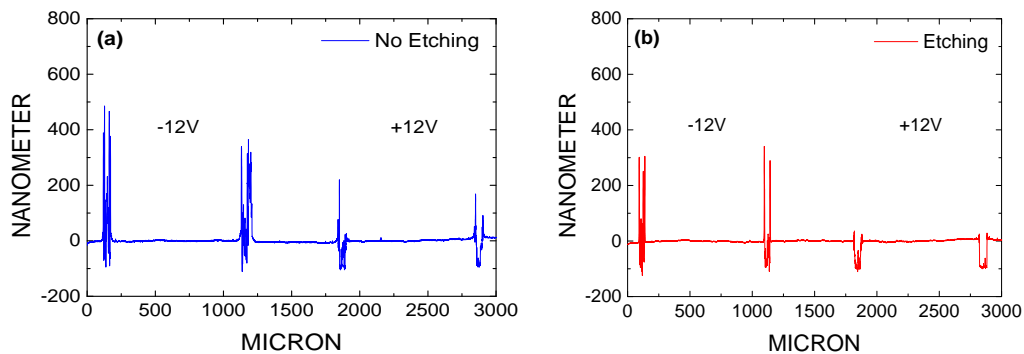


Figure 4.4: profilometry for closed pattern arc-erosion: (a) before and (b) after wet etching.

Figure 4.4 shows the obtained profilometry measurements on two of the previous square patterns performed at  $\pm 12$  V, after (a) and before (b) the chemical etching. The wet etching process is more effective for positive polarization: residues within the grooves disappeared almost completely. However, for negative polarity, the amount of

waste within the groove has decreased but has not completely disappeared and the heights associated to material at the edges remain quite similar once wet etching has been made. Apparently, a strong amorphization in the features performed at negative polarity prevents the correct work of the etching. This effect could be related to the n-character of the ITO semiconductor under the spark process. The bombardment of electrons on the layer at negative polarity could result in a higher degree of amorphization of the ITO thin film preventing the correct operation. For positive polarity the only drawback is that tip degrades faster than with negative bias.

To summarize the effect of the arc-erosion on ITO/glass, it has been demonstrated ITO patterning, obtaining isolated regions using both polarities. It has been observed that negative polarity induces more critical effects as waste production or wave-edge effect, to be taken in to account in order to avoid short current in final devices.

- **Spot patterns at different voltages and polarities**

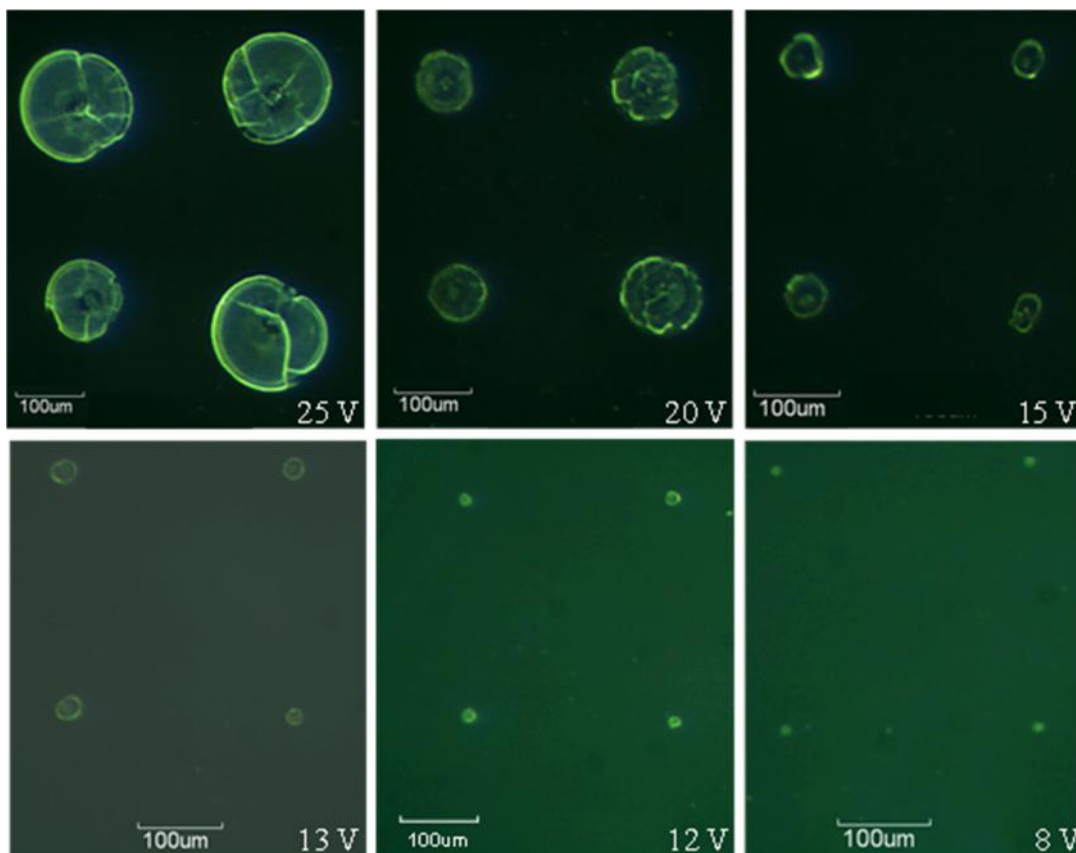


Figure 4.5: four spot sets results due a successively touch method on ITO (100 nm) / glass substrates using a voltage range from -5 V to -25 V and negative polarity.

Besides grooves, electrical erosion on ITO (100 nm)/glass substrates was also performed. In this case, a four spot arrangement through successive ‘touches’ in which the operating voltage was increased from -5 V until -25 V was performed. For low voltages, in particular between -5 V and -7 V, no representative features are seen on the working area. Figure 4.5 shows some of the obtained results from -8 V to -25 V. Small spots begin to be noticed from -8 V, its appearance and geometry are similar up to -10 V. Henceforth, from about -12 V, the spot lateral progress is notorious as the applied voltage is increased. The voltage at which progress of the crater radius is observed will be considered a sort of threshold voltage.

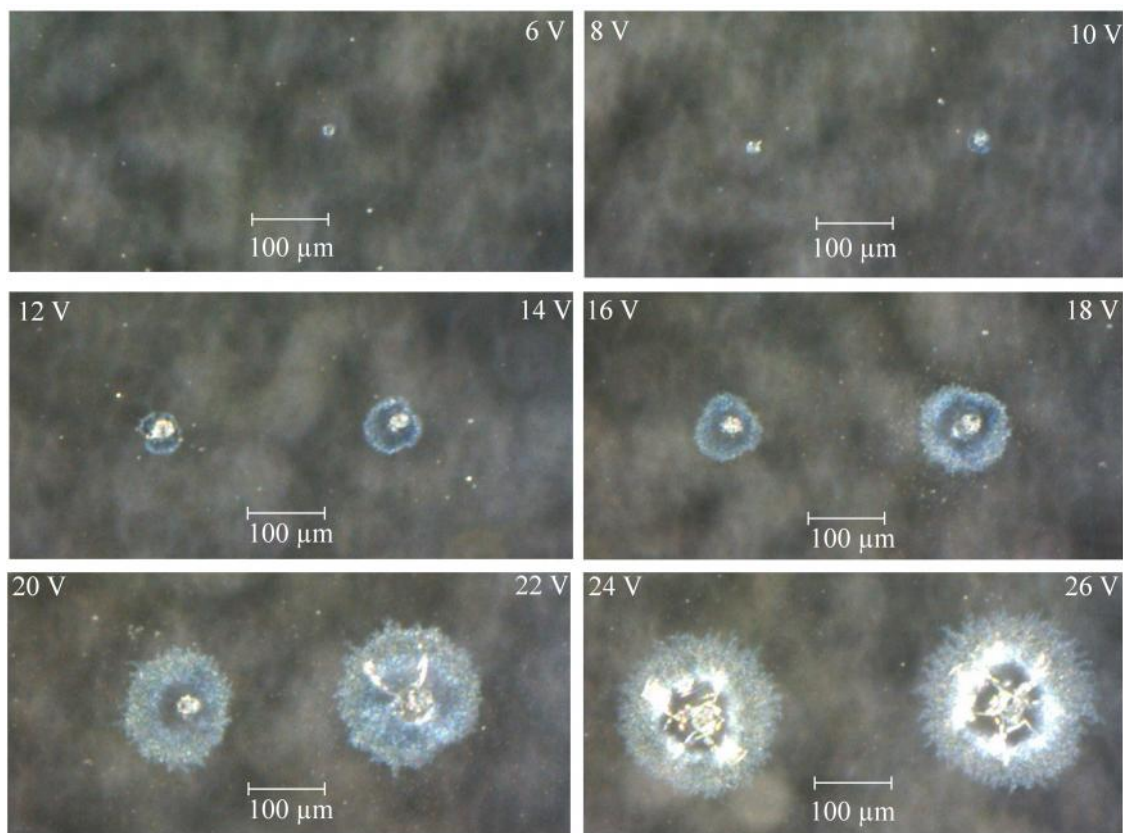


Figure 4.6: positive polarity electrical erosion examples in the voltage range from +6 V to +26 V on ITO/glass substrates.

Similar experiment was also carried out using positive polarity. Another four spot pattern, with a 300  $\mu\text{m}$  separation between spots, was performed using a voltage range from +6 V to +26 V. One of the main differences observed by changing the polarity is the appearance of features already for operating voltages as low as +6 V, unlike electric erosion with negative polarity which started at higher absolute values (-8 V). Final spots performed with low voltages do not exhibit evident changes in terms of aspect and geometry until the voltage is increased to +10 V, slightly before than the case of

working with negative polarity. Henceforth, significant diameter changes begin to be noticed. Figure 4.6 displays some of the obtained features, where the spot evolution can be observed as increasing voltage.

The most interesting feature concerns the final spot aspect. It consists of a shining central core (shining optically means roughness), surrounded by a uniform larger area with poor optical contrast (less roughness). The size of the central core progresses slowly with voltage, and is not distinguished until 18 V. However, the surrounding crowns extend to large areas than those observed in craters with negative polarity, although their surface quality is smoother (poor optical contrast). Perhaps, this is the most noticeable difference between the spots in Figure 4.5 (negative) and Figure 4.6 (positive), inferring that the electric discharge effect may be driven in a different way. Negative polarity (electrons impinging on sample) seems to be more aggressive with the surface. Positive polarity leaves a smoother surface, but progresses at larger distances. Probably the n-doped character of the ITO is directly related to this effect. But also the room atmosphere seems to play a role. Figure 4.7 plots the evolution of radius of the total affected region as function of applied voltage. Initially, the radius keeps constant until a certain  $V_{th}$  (-8 V for positive polarization and -10V for negative polarization). From  $V_{th}$  onwards, the radius grows quasi-linearly. In section 4.5 this behavior will be analyzed in detail.

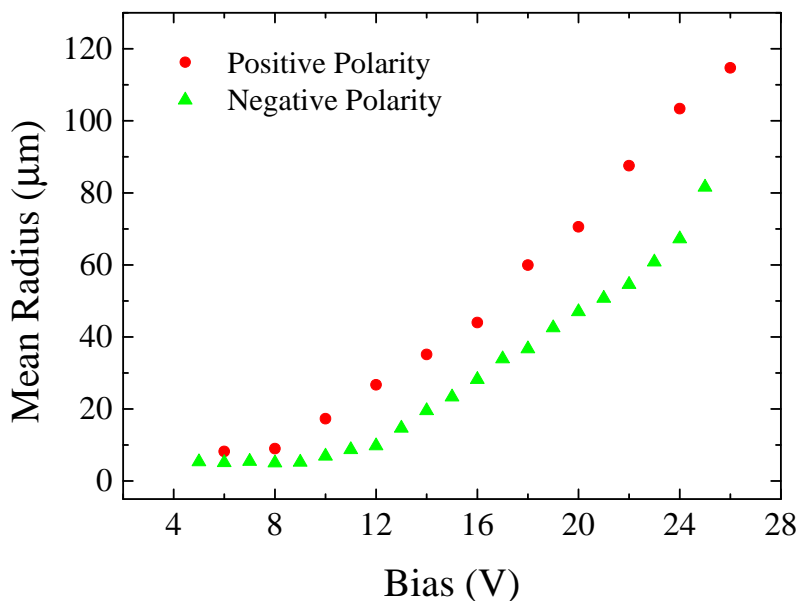


Figure 4.7: Voltage polarity comparison on performed ITO/Glass spots.

#### 4.1.1. ITO on Polyethylene Terephthalate (PET/ITO)

Since the groove width is limited by the tip diameter, very sharp tungsten tips were also considered (vertex  $< 5 \mu\text{m}$ ), seeking for ITO features as small as possible. This motivated the use of rigid acupuncture needles, described in Chapter 3, with tip vertex between  $2.5$  and  $3 \mu\text{m}$ .

In case of soft substrates like PET, one can work with rigid needles as long as the position of the surface is accurately determined. Otherwise, the mechanical pressure flattens the tip due to wear, as shown in Figure 4.8. This induces different widths along the groove.

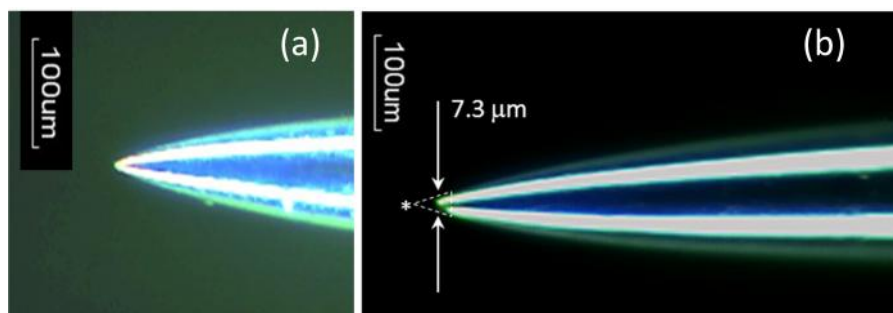


Figure 4.8: Comparison between: (a) new acupuncture tip and another (b) worn by working cycles.

The wear in the tip is originated by unwanted shocks during the approximation procedure. In addition, X and Y movements can also increase wear by friction affecting its geometry. This situation is avoided by a slow and a safe approach using smooth movements, managing slowest speeds and shorter distance steps and using probes in form of cantilevers.

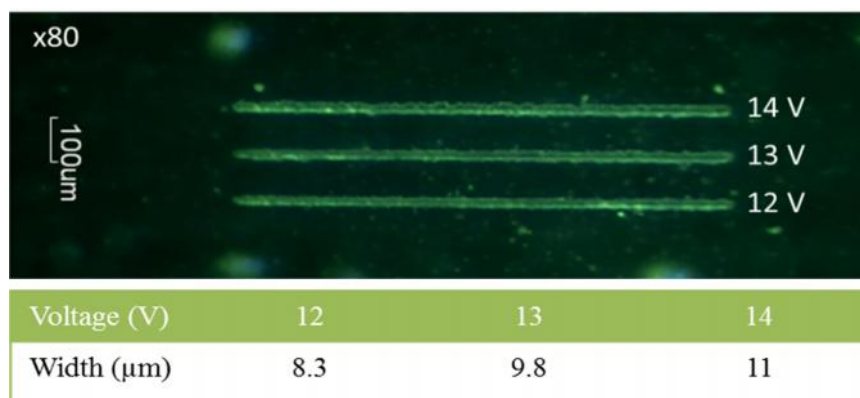


Figure 4.9: Final groove width for PET/ITO patterning for 12, 13 and 14V.

One millimeter long and 100  $\mu\text{m}$  separated lines were patterned on an ITO/PET sample at voltages from -12 V to -14 V. The obtained grooves and their widths, measured with the camera software (Motic Images Plus 2.0), are shown in Figure 4.9.

Figure 4.10a, shows a microphotograph of an area of 250 x 100  $\mu\text{m}$  with a pattern on ITO exhibiting groove width average of 7  $\mu\text{m}$ . These patterns were made with 9  $\mu\text{m}$  distance between centers. A more detailed image is shown in Figure 4.10b. AFM image is shown in Figure 4.11, accompanied by the respective measured profile for two specific areas, highlighted in Figure 4.11a (red) and Figure 4.11b (green) respectively. According to these data, the obtained groove width ranges from 2.5 to 3  $\mu\text{m}$ , matching up with the diameter of the tip aforementioned.

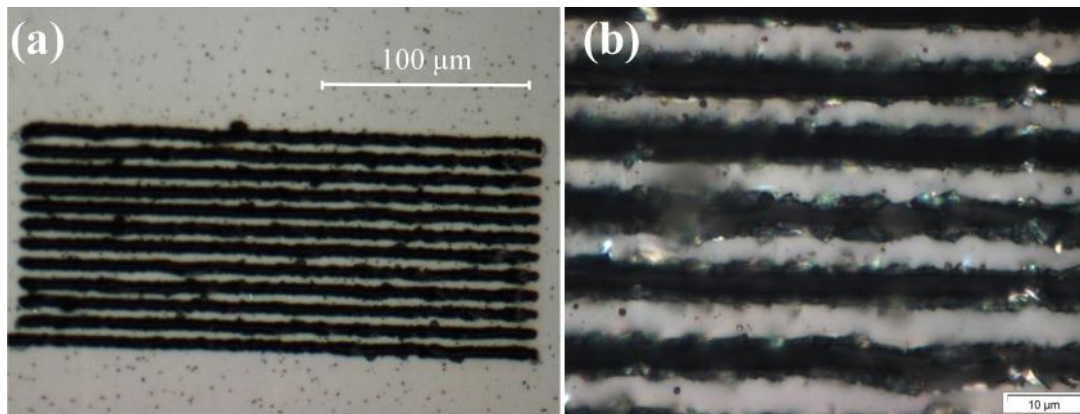


Figure 4.10: Final groove patterns at 12 V as working bias; (a) ITO 250 x 100  $\mu\text{m}$  full patterned area and (b) Final result for 9  $\mu\text{m}$  distance between centres.

Waste material is also observed in the AFM profiles, with protrusions greater than 400 nm, already observed in previous ITO/glass patterns that could be very harmful for the final device performance. In this case, the use of a plastic substrate makes difficult to find a method to remove waste without affecting the PET substrate.

As a conclusion, an ITO micro-ribbon pattern with 2.5-3  $\mu\text{m}$  in width and 7  $\mu\text{m}$  spaced (250 x 100  $\mu\text{m}$ ) were obtained on PET using -12 V as applied bias and a rigid acupuncture needle. Despite the magnificent result in patterning terms, the problem is now focused on finding a suitable etching method to remove the residual waste on edges without affecting the plastic substrate, in order to avoid background problems in manufacturing and further testing of optoelectronic devices, the adequate active layers

must have greater thicknesses ( $> 400$  nm) in the hypothetical case of an immediate implementation of this technique.

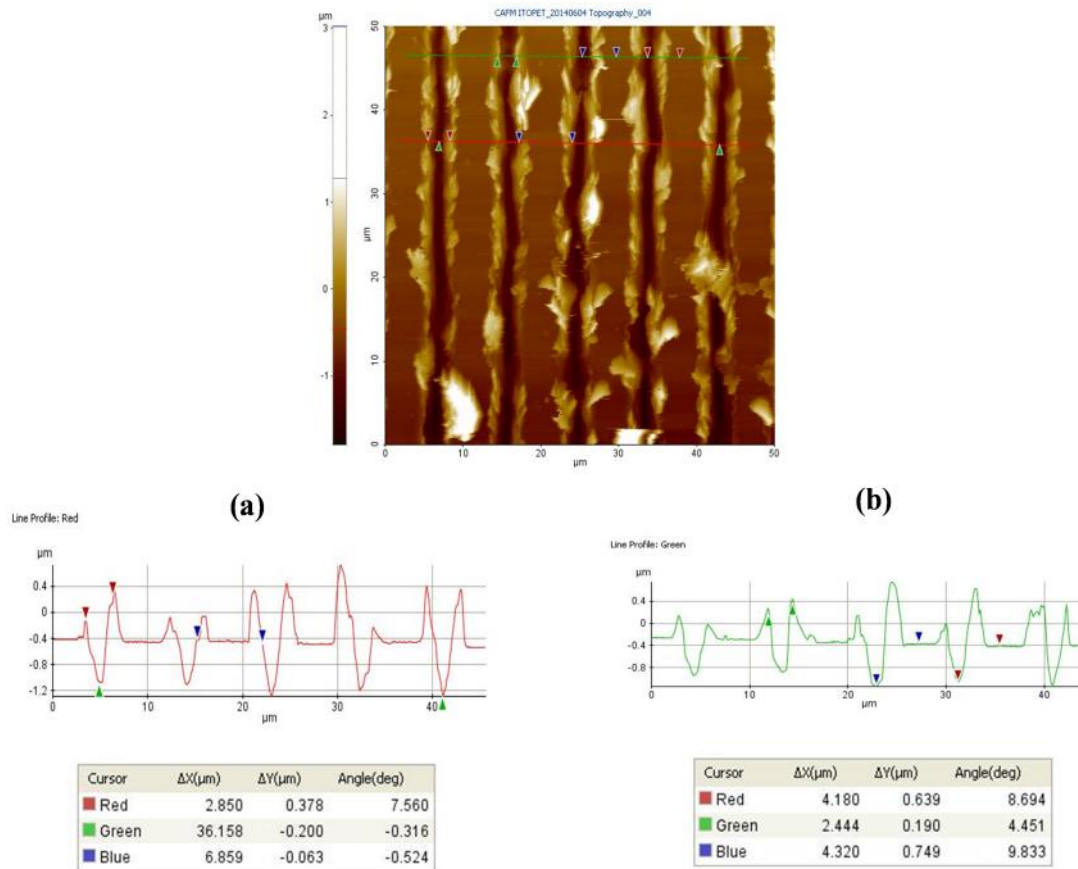


Figure 4.11: AFM image for PET/ITO pattern,  $\sim 7$   $\mu\text{m}$  width micro-ribbons: (a) red line and (b) green profilometry.

## 4.2 ELECTRICAL EROSION ON ALUMINUM DOPED ZINC OXIDE (AZO)

In this section it will be shown the electrical erosion effect on ZnO: Al (AZO) thin films. Zinc Oxide (ZnO) is an n-type direct semiconductor with a wide band gap (3.37 eV at room temperature) and a wide resistivity range ( $10^{-4} - 10^{12}$  cm). ZnO is transparent in the visible light range, making it an interesting material for applications in transparent electronics, with other properties of application in optoelectronics and spintronic devices [5]. To increase ZnO conductivity, a dopant ion is introduced to modify its electronics properties. This dopant needs to be incorporated into the crystal structure of the host material. In the case of AZO, an  $\text{Al}^{3+}$  ion occupies a  $\text{Zn}^{2+}$  lattice sites in order to provide a free electron and enhance the conductivity of the ZnO [6].

Currently, AZO layers are used as transparent electrodes for optoelectronic devices. Its metal components (Zn and Al), are cheaper and less toxic compared to the most used material for this purpose: Indium – Tin Oxide. There is also a great concern about the Indium world availability, driving the research and development of new alternative materials and composites for its replacement.

The samples have been supplied by our collaborators at Instituto de Materiales de Madrid (CSIC). Al doped ZnO layers were prepared by RF sputtering from a target with a composition of 97 wt% ZnO and 3 wt% Al<sub>2</sub>O<sub>3</sub>, deposited at room temperature and grown under Argon atmosphere. Samples were annealed under high vacuum conditions in order to avoid air and oxygen effects on their electrical and structural properties. More detailed experimental information is given in [7].

The sheet resistance of this AZO is close to 1 k  $\Omega$ /sq, so conduction properties are far to be ideal. In consequence, the operating voltage needed for an optimal patterning is high compared to those used on ITO and conventional metals. Electrical erosion on AZO thin films was performed for voltages in the range 20 - 60 V using a slow speed of 0.05 mm/s for horizontal movements (X & Y-axes). The optical images of the final grooves, with their widths can be seen in Figure 4.12. The optical inspection reveals three regimes: a) for voltages < 35 V, the grooves are not completed or uniform in width, b) voltages between 35-45 V seem to be suitable to obtain uniform and well defined grooves and c) above 45 V, (Figure 4.12) a significant granular texture (optical dark spots) begin to appear inside of the groove, becoming more visible at 50 V and 55 V. However, the edge aspect still remains similar. This dark contrast could be attributed to an exothermic process which is carried out during the electrical arc erosion. Material residues produced during the process are melted instantly due to the joule heating associated to the high voltages. For applied voltages > 60 V, edge irregularities predominate along and also inside of the patterned groove. In this case, the erosion mechanism has changed and progress of the craters as the tip advances is evident. A similar effect was observed in ITO including the broadening of the patterned grooves with increasing voltages (from 15 V). This effect will be discussed later in this chapter.

As a conclusion, adequate processing voltages for AZO in order to obtain well defined grooves are found from -30 V to -45 V. These values are higher than the ones for ITO samples due to the higher resistivity of AZO thin films.

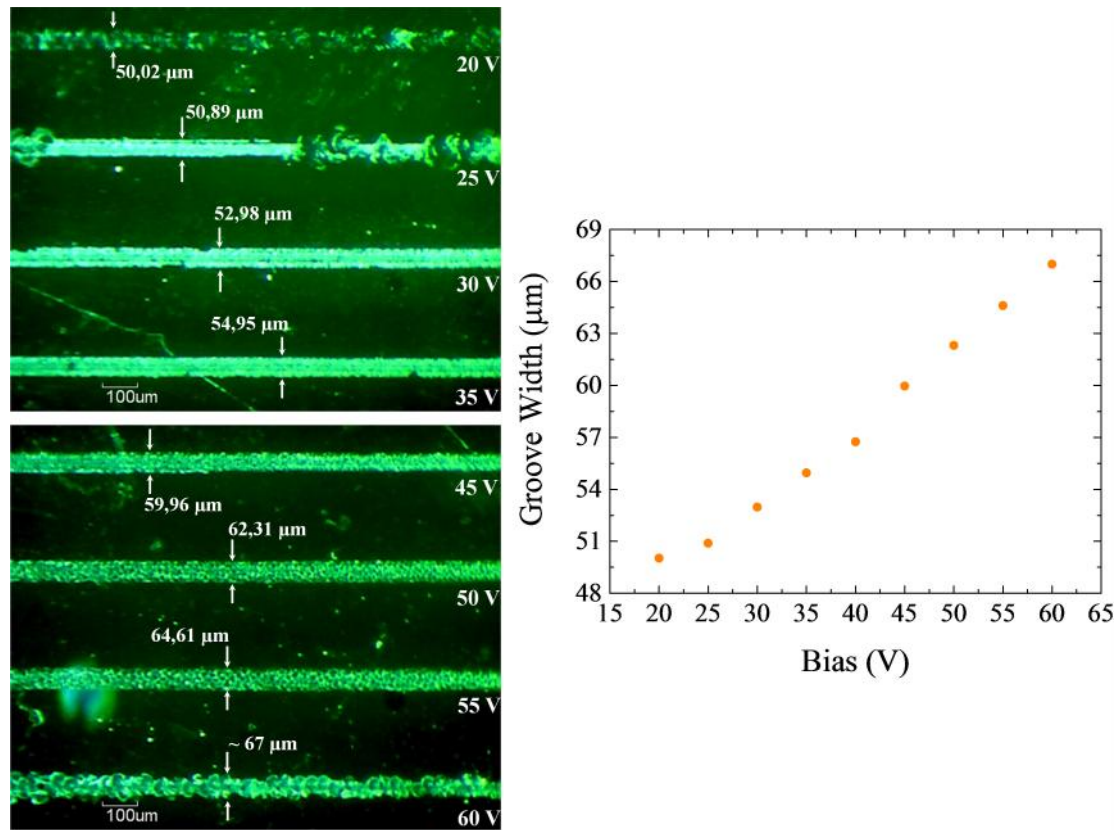


Figure 4.12: Arc eroded grooves on glass/AZO and their measured widths.

#### 4.2.1. Example of device application: Organic Solar Cells on AZO

Taking advantage of previous experience, simple structure organic solar cell devices were fabricated by solution processing methods with the following layer structure: AZO/PEDOT:PSS/Active Layer/Ca/Al. This stack is shown graphically in Figure 4.13, for a better understanding.

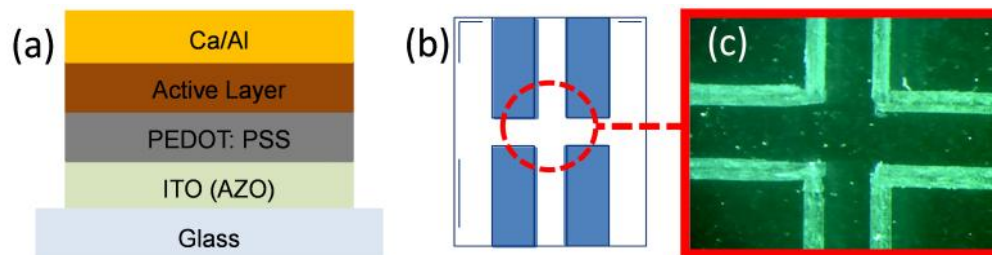


Figure 4.13: (a) AZO based solar cell layer structure. (b) The AZO anode is defined by electrical erosion on 30 x 25 mm samples; isolating the four electrodes (blue rectangles, 14.5 x 6 mm) and (c) a detail of the isolation pads are shown.

The active layer is a mixture in chlorobenzene of two well-known materials for these applications: P3HT and PCBM in a 1:1 ratio at 2.5 wt%, under appropriate filtering and deposit conditions. Aluminum (Al) and Calcium (Ca) layers were deposited by metal evaporation, using a bench-top Emitech K975X turbo-pumped thermal evaporator. All fabrication process was carried out in an inert atmosphere glove box ( $< 0.1$  ppm  $O_2$  and  $H_2O$ ).

Characterization of the final I-V device response is shown in Figure 4.14a. This device exhibits a significant slope at 0 V attributed to a leakage current and a dynamic resistance 2.5 times larger than an ITO-based device at high voltage. The former feature implies an inefficient recombination path for photogenerated carriers.

On the other hand, although not related to the lithography procedure, it is worth mentioning our specific experiments concerning the UV radiation effects on the AZO layers. In order to evaluate the effect of the usual substrate cleaning by UV-Ozone methods [8], the exposure time has been varied before organic layer deposition. It has been demonstrated that the OPV performance is greatly affected and is directly dependent on the exposure time to the ozone: 15 minutes (Figure 4.14a), 60 minutes (Figure 4.14b) and 120 minutes (Figure 4.14c). A drastic performance decrease is evidenced after 120 minutes. The serial resistance increases as the exposure time is larger. The exposure to ozone atmosphere has been reported to reduce the oxygen vacancies concentration and to increase the material work function [9] explaining the conductivity reduction. Also there is a current density drop even more evident after 120 minutes of exposure. As a summary, final characterization results are shown in Table 4.3.

UV-Ozone [exposure time]	15 minutes	60 minutes	120 minutes
$V_{oc}$	0.5 V	0.45 V	0.38 V
$J_{sc}$	-2.33 mA/cm <sup>2</sup>	-2.48 mA/cm <sup>2</sup>	-0.04 mA/cm <sup>2</sup>
$R_s$	460 $\Omega$	2 k $\Omega$	6.7 k $\Omega$
FF	38 %	29.3%	49.8%
PCE	0.44 %	0.36 %	0.01 %

Table 4.3: Characterization data in function of UV – Ozone exposure time

Highly amorphous AZO layers have been integrated in a bulk heterojunction organic solar cell, instead of ITO, using electrical erosion as lithography method to

define the anode electrodes. The fabrication conditions and specially the ozone treatment are critical for charge injection, efficiency and the overall device performance due to the nature of this material.

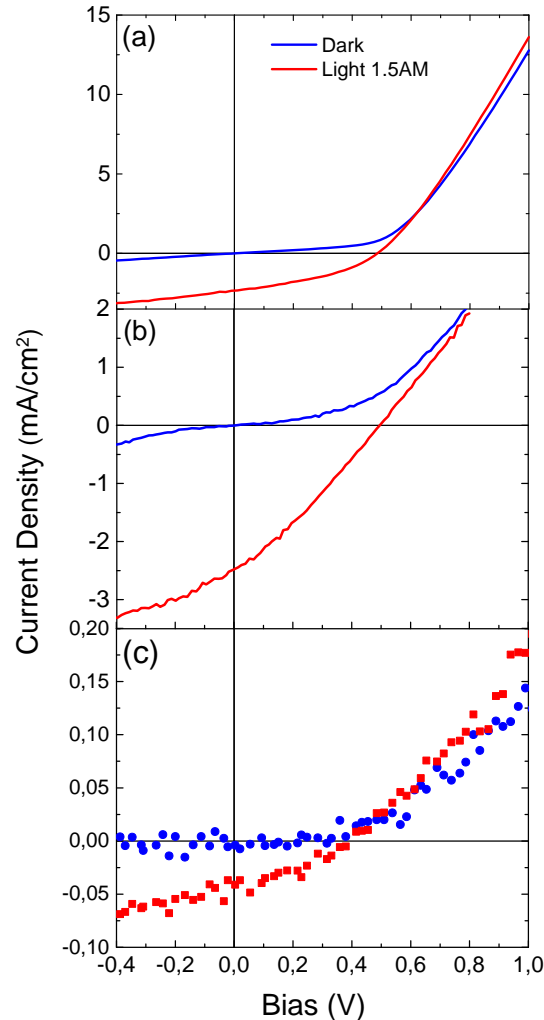


Figure 4.14: I-V curves at 1.5 AM calibrated illumination and darkness of AZO Organic Solar Cell characterization after UV - Ozone exposure: (a) 15 minutes, (b) 60 minutes and (c) 120 minutes.

### 4.3 ELECTRICAL EROSION ON ZINC NITRIDE

In this section we investigate the effects of the electric arcs on semiconducting Zn<sub>3</sub>N<sub>2</sub> films deposited by magnetron sputtering. Zinc Nitride is considered a promising semiconductor to use in electronic and optoelectronic applications (photovoltaic, sensors, TFTs and so on) owing to low cost and ecological friendliness. The high availability of its composing materials is also appealing [10]. It exhibits good electrical properties, as Hall mobility values up to 156 cm<sup>2</sup>/Vs and low resistivity ( $\sim 10^{-3}$  cm),

approaching those of polycrystalline silicon [11]. Its properties, n or p-like character, are very dependent on the production method. A big effort have been made trying to synthesize the Zinc Nitride in a reproducible way [12], promoting its use henceforth in research terms.

The samples have been prepared by collaborators from the Microelectronic Laboratory at Physical Department of the Autónoma University of Madrid. Polycrystalline nitride layers (1.5  $\mu\text{m}$  thickness layer) were prepared by radio-frequency magnetron sputtering from a pristine Zinc (Zn) target on glass or Si substrates using  $\text{N}_2$  as working gas. For more details it can be seen in reference [10].

Arc-erosion procedure was developed at room temperature, using a spring probe tip with a diameter of 40 – 50  $\mu\text{m}$ , already described in Chapter 3. The speed (0.1 mm/s) and acceleration (100  $\text{mm/s}^2$ ) for axes movements were set constant for the tests carried out. A range of voltages from 0 to 20 V was tested, using negative polarization.

Figure 4.15 shows grooves performed on  $\text{Zn}_3\text{N}_2$ , together with their profiles. Figure 4.15a exhibits the measured profilometry of the grooves. It can be deduced a threshold voltage of 15 V as apparently, the  $\text{Zn}_3\text{N}_2$  layer is not affected for voltages below this value. However, from the optical image of the grooves (Figure 4.15b), a first contact is evidenced at 14 V (spark on the top dotted red square), although the progress of the pattern seems to be interrupted, leaving this voltage as not enough to break the material (no erosion is observed in the corresponding profilometry measurements). The observed slight trace in the red dotted box is caused by mechanical friction due to the tip displacement, and could be associated to the native oxide removal on top of the nitride layer. Good quality and defined grooves are observed in the optical images when voltage is raised from 15 to 16 V, being the suitable values to work with  $\text{Zn}_3\text{N}_2$ . The appearance and quality of the groove begin to spoil when arc-erosion is carried out at 17 V. A characteristically wavy pattern begins to be clearly observed for 18 V, reducing the edge quality.

After overcoming the threshold voltage, the electric arc phenomenon induces modifications of the layer properties. In particular, profilometry results indicate that the arc discharge yields a deep trench in the scanned areas whose width increases with the bias voltage (Figure 4.16). The trench, whose depth is about 1.1  $\mu\text{m}$  quite independently of the bias voltage, is the result of the partial sublimation of the nitride layer. The sharp

upward edges obtained in the profilometry scan (Figure 4.15a) again suggests that residues of the process accumulate at the borders of the scanned area as we have observed for other materials.

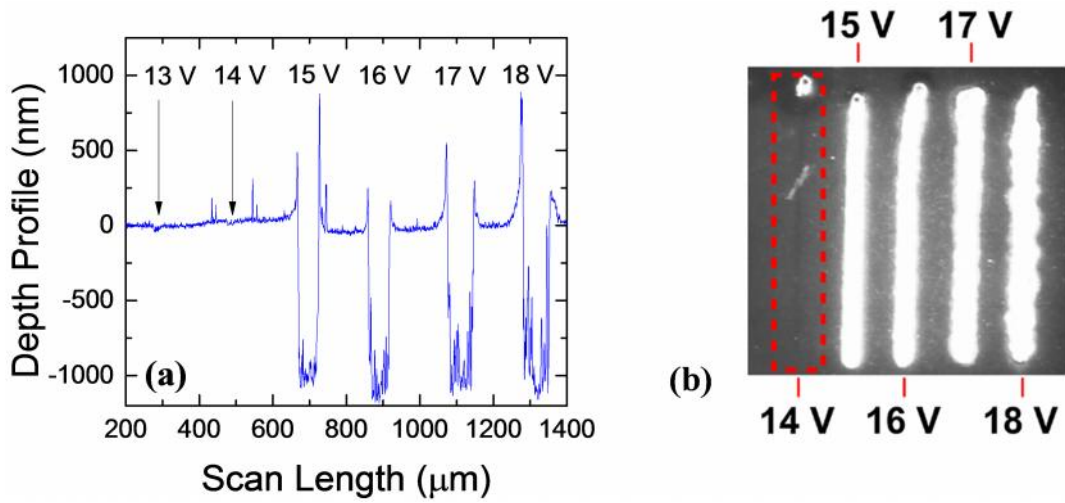


Figure 4.15: (a) Zn<sub>3</sub>N<sub>2</sub> on Si substrates patterning profilometry and (b) optical images of the patterned grooves on Zinc Nitride [7].

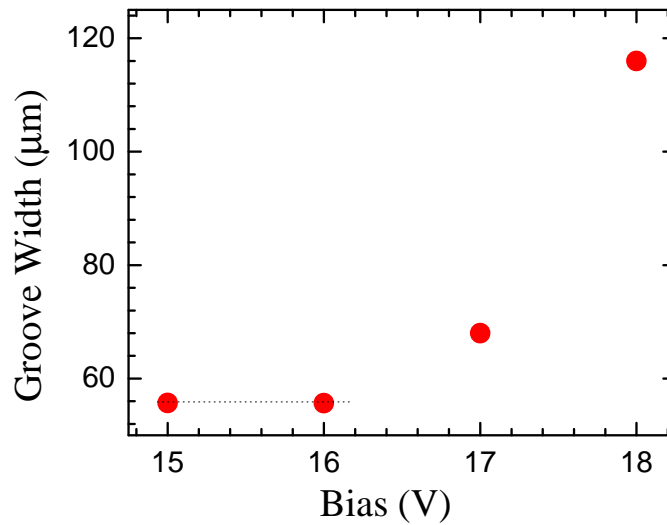


Figure 4.16: Grooves width-applied voltage relationship

As mentioned above, at values below the threshold voltages, the scan produces a shallow fingerprint on the sample surface. This fingerprint is attributed to the native oxide removal on top of the nitride layer. As this oxide usually presents higher resistivity than the nitride layer, its removal should lead to a reduction of the resistivity

of the scanned area. To investigate this point, four-probe resistivity measurements were performed in  $1 \times 3 \text{ mm}^2$  areas scanned at voltages between 0 and 15 V on  $\text{Zn}_3\text{N}_2/\text{glass}$  substrates (Figure 4.17). The result shows that resistivity diminishes from  $7.3 \times 10^{-3} \text{ cm}$  down to  $5.9 \times 10^{-3} \text{ cm}$  as the bias voltage increases from 0 to 4 V. These values are among the best values obtained for this material. It is worth noticing that resistivity at zero volts is near the value found in non-scanned Zn areas. The resistivity reduction is attributed to the joule local heating produced by the discharge current through the tip toward the nitride layer once in contact with the surface, which induces the electrical breakdown of the oxide layer on top of the nitride. This heating effect at low voltages would explain the resistivity improvement as voltage increases. On the other hand, since electric arc does not occur at these voltages, the tip pressure on the surface during the scan could cause a mechanical polishing/planarization of the native oxide.

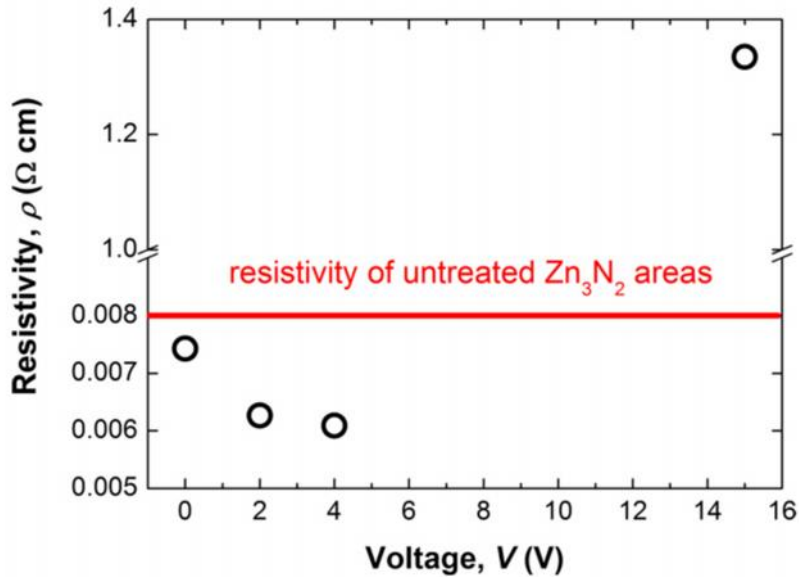


Figure 4.17: Electrical resistivity as a function of tip voltages measured in  $500 \times 500 \mu\text{m}$  scanned areas of  $1.5 \mu\text{m}$  thick  $\text{Zn}_3\text{N}_2$  films deposited on glass substrates.

Above the threshold voltage for inducing electric arc on the material, the resistivity measured in scanned areas increases drastically. At 15 V, it becomes at least two orders of magnitude higher than those values found at low voltages. Further increase of the bias voltage leads to higher resistivity than the maximum limit of the setup measurable range ( $10^5 \text{ cm}$ ). Thus, electrical erosion based lithography would allow electrical insulation of TFTs fabricated on  $\text{Zn}_3\text{N}_2$  layers with a channel length and resolution that would be determined by the tip size. At intermediate voltages (4–15 V),

the surface becomes too rough with peak-to-valley amplitudes larger than  $1\ \mu\text{m}$ , hindering the measurement of the resistivity due to the poor current uniformity. SEM observations indicate that the material tends to lift-off in sheets parallel to the scan line, keeping a separation between them of  $15\text{--}20\ \mu\text{m}$ .

Figure 4.18 shows SEM pictures taken at the edge of the scanned area under arc discharge. The images show a well-defined border between treated and untreated regions over large distances (Figure 4.18a and b). In addition, ordered arrangements of micro-droplets are observed around the trench with a linear density of  $0.23\ \mu\text{m}^{-1}$ . This density seems scarcely dependent on the substrate, scan speed and bias voltage used. Droplet size uniformity improves with the scan rate.

Compositional studies carried out by energy dispersive X-ray spectroscopy<sup>2</sup> indicate that the droplets are mainly formed by Zn. A close view of the droplet surface reveals circular areas likely related to its partial oxidation (Figure 4.18c). These Zn-rich droplets are residues of the process, which have their origin in the decomposition of Zn. Whereas N leaves the structure in molecular form during material sublimation, part of the Zn remains at the edges. The high density and order of micro-droplets along the contour of the trench suggest a potential method to synthesize seeds for the growth of Zn-based nanostructures such as ZnO nanowires (NWs).

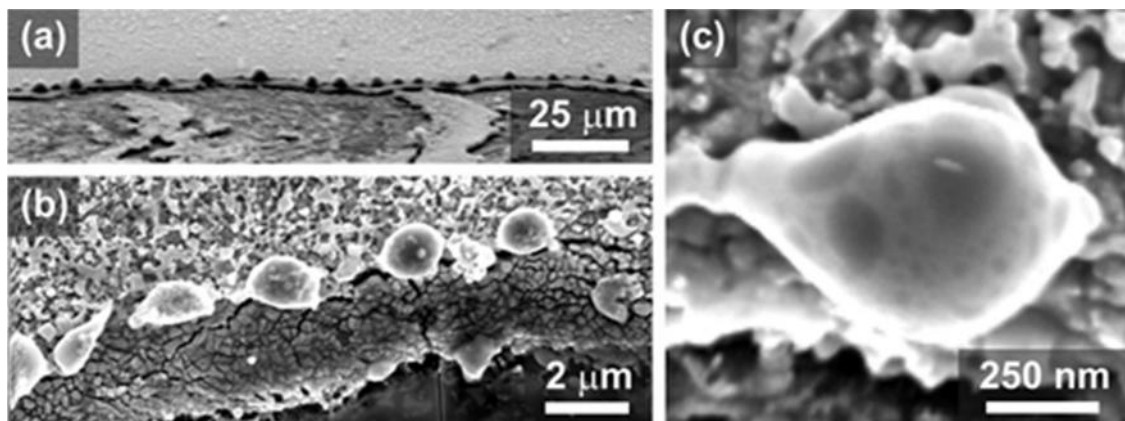


Figure 4.18:  $\text{Zn}_3\text{N}_2$  SEM images after electrical arc lithography. (a) Obtained scan edge at 15 V and 3 mm/s processing speed on a glass substrate (b) Drop shaped forms arrangement of a 16 V groove at 0.1 mm/s processing speed on a silicon substrate. (c) Drop shaped form detailed zoom in [10].

The central region of the scan presents a different morphology as a result of the arc discharge. Figure 4.19 compares the surface of the as-grown films with the surface

<sup>2</sup> Measurements carried out by the Microelectronic Laboratory Group at UAM Physics Department.

of the regions under electrical arc process. As the voltage increases, a characteristic structure formed by small faceted crystallites with sizes between 50 and 500 nm shows up. These crystallites account for the 30% volume of the layer that it is not sublimated and it is recorded at the bottom part of the groove in the profilometry study. The surface density of these crystallites on the silicon substrate is in good agreement with the typical grain density in polycrystalline  $\text{Zn}_3\text{N}_2$  grown at 473 K, as shown in Figure 4.19a–c. Grains become more separated as the tip voltage increases and tend to show marked facets. These results remind us the mentioned effect of amorphization of ITO with increasing voltages. In the case of Zinc Nitride, more reactive than ITO, a reasonable explanation for the formation of these crystals could be a recrystallization process induced by the high temperatures reached in the presence of a plasma which, fed by ambient air, is rich in oxygen active species that can easily trigger the oxidation of the nitride grains.

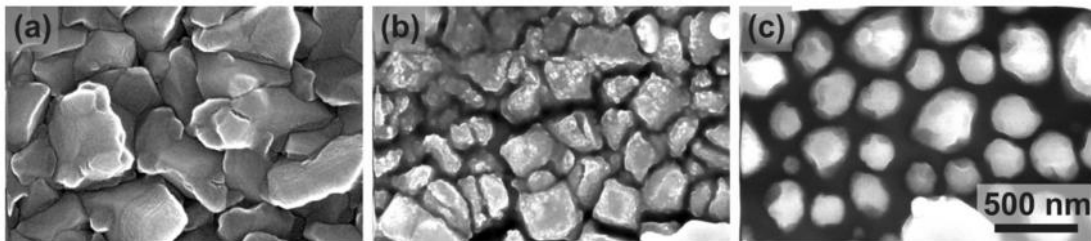


Figure 4.19: SEM viewgraphs of (a) the as-grown  $\text{Zn}_3\text{N}_2$  film on Si, and two areas underneath the probe after arc discharge treatment carried out at (b) 17 V and (c) 18 V.

In order to study this possibility, compositional studies are carried out using RBS, non-RBS and NRA<sup>3</sup> techniques. Figure 4.20 shows the RBS, non-RBS (a) and NRA (b) patterns extracted at 3.045 and 3.7 MeV, respectively, from  $\text{Zn}_3\text{N}_2$  treated at different tip and the resulting molar fractions (c) of Zn, N and calculated by RBS, non-RBS and NRA for different applied voltages (0, 15 and 20 V) on a  $\text{Zn}_3\text{N}_2$ /glass sample. The figure also shown the fitting spectra obtained from SIMNRA software. The simulation model comprises a  $\text{Zn}_x\text{N}_y\text{O}_z$  layer (x, y and z are Zn, N and O molar fractions, respectively) on top of a glass substrate.

Obtained molar fractions (Figure 4.20b), concluded that O molar fraction increases with the bias voltage from 0.03 (at 0 V) to 0.48 (at 20 V), whereas the N molar fraction decreases from 0.39 (at 0 V) to 0.02 (at 20 V). The resultant Zn molar

<sup>3</sup> Measurements at Centro de Micro-Análisis de Materiales (CMAM/UAM) by Microelectronic Lab Group (UAM).

fraction obtained from the RBS fitting shifts from values near the stoichiometric molar fraction in  $\text{Zn}_3\text{N}_2$  ( $x = 0.60$ ) to stoichiometric values in  $\text{ZnO}$  ( $x = 0.50$ ), confirming the transformation of  $\text{Zn}_3\text{N}_2$  into  $\text{ZnO}$  submicron crystals under arc discharge treatment.

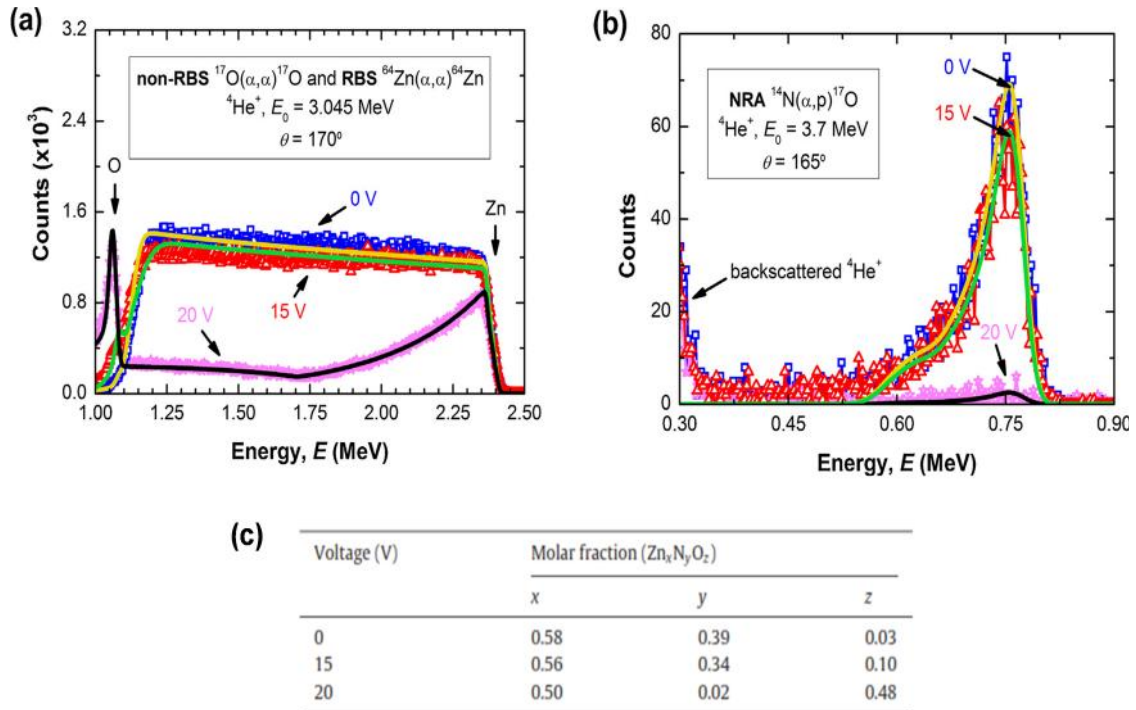


Figure 4.20: (a) RBS, non-RBS and (b) NRA patterns extracted at 3.045 and 3.7 MeV, respectively, from  $\text{Zn}_3\text{N}_2$  treated at different tip; (c) Zn, N and O molar fractions calculated by RBS, non-RBS and NRA for different applied voltages (0, 15 and 20 V) [10].

As a conclusion, we have found several interesting effects of the electrical arc on  $\text{Zn}_3\text{N}_2$ . At low voltages ( $< 15\text{V}$ ), the eroded areas present a lower resistivity due to the removal of the native oxide. At larger voltages (15 V-17 V), the electric arc discharge produces high electrical resistance properties that allows their use as lithography method. At the same time, Zn-rich micro-droplets are obtained at the scan edges as residues of the sublimation process. The electric arc process also induces strong compositional changes at the central part of the scan, yielding  $\text{ZnO}:\text{N}$  submicron structures from the Zn crystal grains.

These properties make the technique a useful tool for the reduction of the contact resistivity in  $\text{Zn}_3\text{N}_2$  surfaces, the insulation of  $\text{Zn}_3\text{N}_2$  TFTs in two-dimensional arrays, and its use in the preparation of advanced  $\text{ZnO}$  nanostructures for optoelectronic applications. From the optical point of view, the transformation process is also attractive as optical data storage technique since it enables the definition of visible transparent  $\text{ZnO}$  windows in opaque  $\text{Zn}_3\text{N}_2$  layers.

#### 4.4 ELECTROEROSION ON GOLD

Thanks to previous works a suitable voltage range for gold layer processing is known, setting it from -2 V to -16 V [1]. Gold (Au) samples were deposited by RF sputtering at the ICM (CSIC) on 10 mm x 10 mm glass substrates. A 5 nm thickness Chromium (Cr) layer was first deposited to improve the Au adhesion. Layers with different thicknesses:  $100 \pm 2$  nm,  $52 \pm 2$  nm and  $15 \pm 2$  nm were prepared in order to evaluate the electrical erosion process. In this case a spring probe was used, with spring compression of 4  $\mu$ m. Variables as acceleration and speed are set constant as 100 mm/s<sup>2</sup> and 1 mm/s respectively for all X and Y movements. The tip approximation to the surface was carried out in the way explained in Appendix A.4.2. One millimeter length grooves, 200  $\mu$ m spaced, using negative polarization, from -3V to -20 V were performed on these samples.

For the  $100 \pm 2$  nm thickness Au layer, below -6 V, no evidence of erosion is detected. Arc-erosion is successfully achieved from -8 V onwards (Figure 4.21a). So  $V_{th} = -8V$  is considered the threshold voltage for the procedure. Shining flanges are characteristic of the Au patterns performed with this technique, revealing protruding edges. Wave-like edges are observed almost from the beginning although are notorious from -12 V. From -16 V to -20 V, edges are very irregular and appeared to be “*peeled-off*”.

Below -7 V, electrical erosion may take place but only partially. Images show the groove existence but with certain different characteristics than those obtained from -8 V onwards. Grooves are not well-completed. The measured profilometry (Figure 4.22a) shows a clear step in these grooves having a width that corresponds with tip size 31  $\mu$ m, considerably smaller than for example, 50  $\mu$ m width of the pattern realized at -8 V. These observed grooves for voltages  $< 8$  V are attributed to mechanical erosion.

Adequate arc-erosion on 100 nm Au layers take place in a voltage range between -8 V and -12V. In terms of well-quality and edge finishing is recommended to establish the threshold voltage (-8 V) as the working value for final material processing.

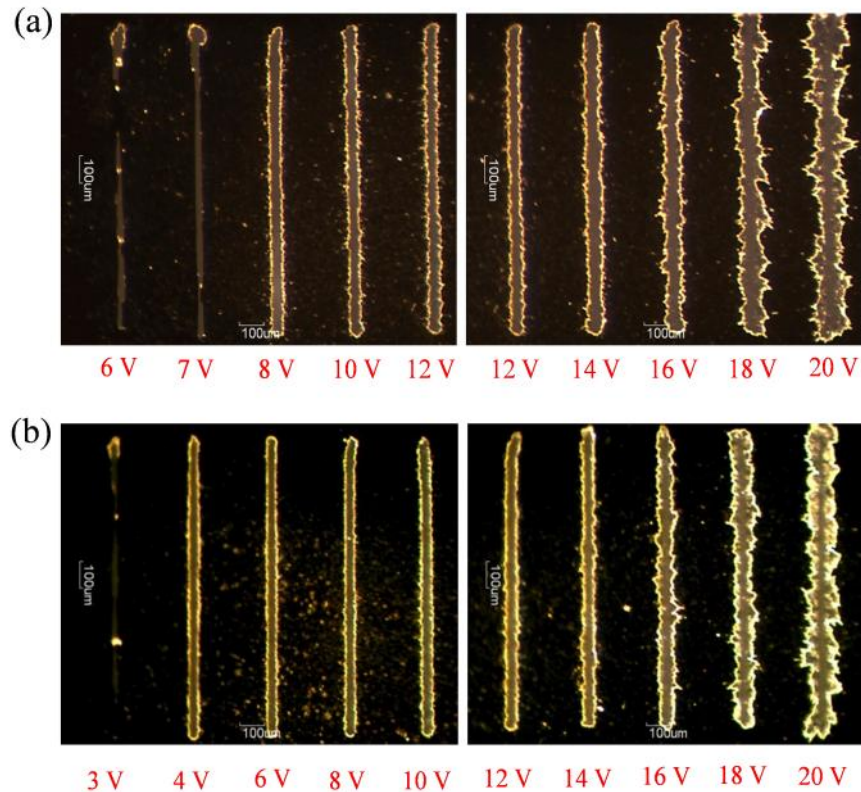


Figure 4.21: (a) 100 nm Au layer final patterning, voltage range from -6 V to -20 V and (b) 52 nm Au layer final patterning.

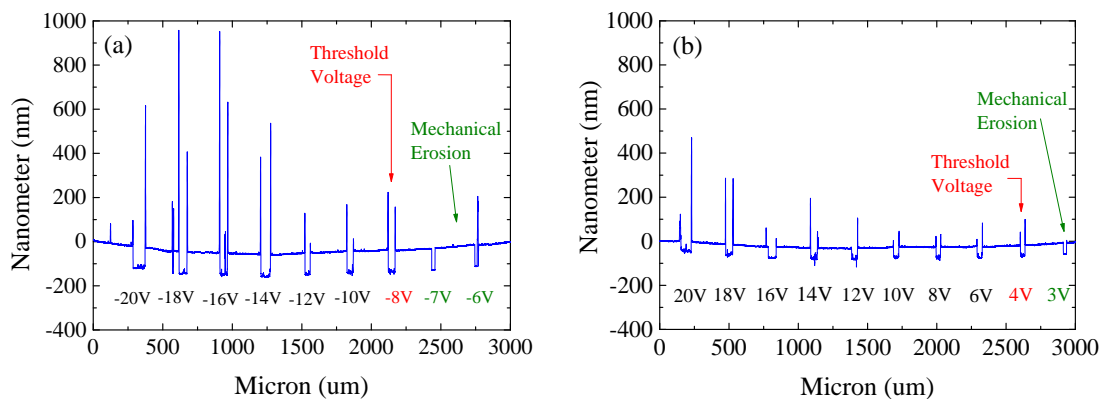


Figure 4.22: (a) 100 nm and (b) 52 nm Au layer profiles corresponding to the patterns of Figure 4.21.

For 52 nm thickness Au layer, Figure 4.21b shows the obtained grooves from -3 V to -20 V. The observed threshold voltage is for this case -4 V and the voltage range from -4 V to -8 V assures a good groove quality and edge definition. We observe the same behavior as for the 100 nm thickness layer, with wave-like edges and *peeled off* regions for high voltages. Figure 4.22b

shows a long profilometry image for all patterned grooves. Mechanical erosion also takes place; the green arrow in the image indicating the obtained trench for a voltage value of -3 V, insufficient for electrical erosion.

For a 15 nm thin Au layer, excellent results have been obtained. These grooves are the better defined so far. Resulting images are shown in Figure 4.23 in a voltage range from -2 V to -20 V. Threshold voltage is found at -3 V, and good quality electrical erosion can be performed in a wider voltage range (-3 to -14 V) compared to above tests. Pure mechanical erosion takes place at -2 V.

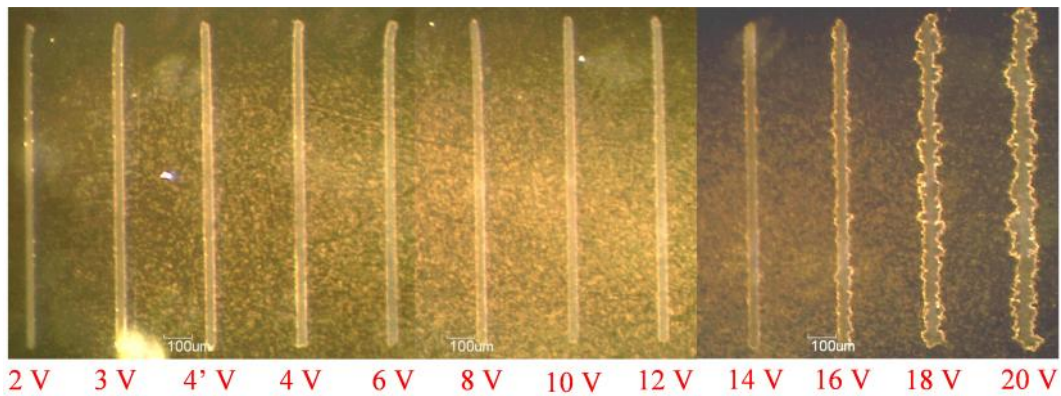


Figure 4.23: 15±2 nm Au layer final patterning.

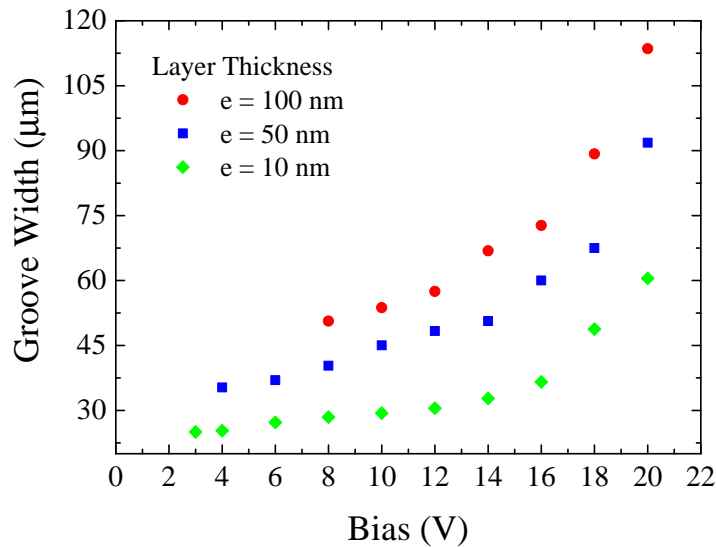


Figure 4.24: Groove width evolution as voltage increase for different Au layer thickness.

In Figure 4.25 an array of grooves 15 μm width (dark stripes) were patterned on a 15 nm thick gold layer at -5 V, using a home-made cantilever previously shown in

Figure 3.5c. Inset shows a zoom corresponding to the dashed white rectangle to verify grooves quality.

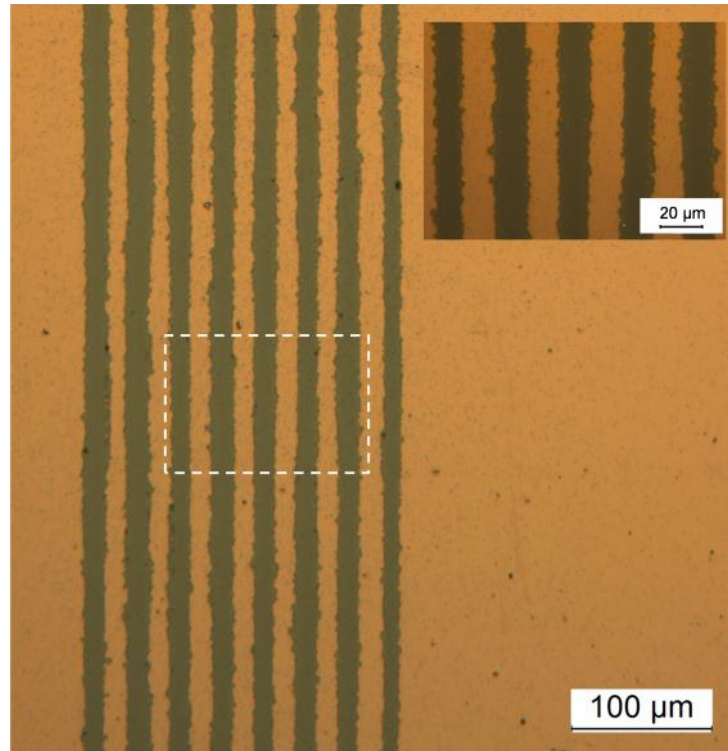


Figure 4.25: 15  $\mu\text{m}$  stripes (dark bands) patterned on a 15 nm gold layer at -5 V performed with home-made very narrow cantilevers.

Once described the above results, common and repetitive situations have been found:

- As expected, the threshold voltage decreases with the layer thickness, as also the material amount to be removed.
- Shining flanges accompany all performed features, revealing protruding edges.
- Patterns done using the voltage range from -16 to -20 V have irregular finished edges far from a correctly straight pattern.
- In order to achieve the optimal quality in terms of edge definition and lower waste on Au/Cr samples it is recommended to work near the threshold voltage, especially for thick layers, say 50 nm to greater thicknesses. In case of thin Au/Cr layers (15 nm), the margin for suitable arc-erosion is wider.

The groove width evolution with increasing voltage is shown in Figure 4.24 for each of the thicknesses studied. In contrast to the tendency observed when performing spots, where an initial flat region was observed, here the slope grows monotonically

from the beginning, although initially this tendency is slow and is subsequently enhanced from -14 V onwards.

Figure 4.26 shows profilometry measurements for each thickness at three selected voltages, -20 V, -14 V and -8 V. Material accumulation at the edges during the electrical erosion process is observed in all cases.

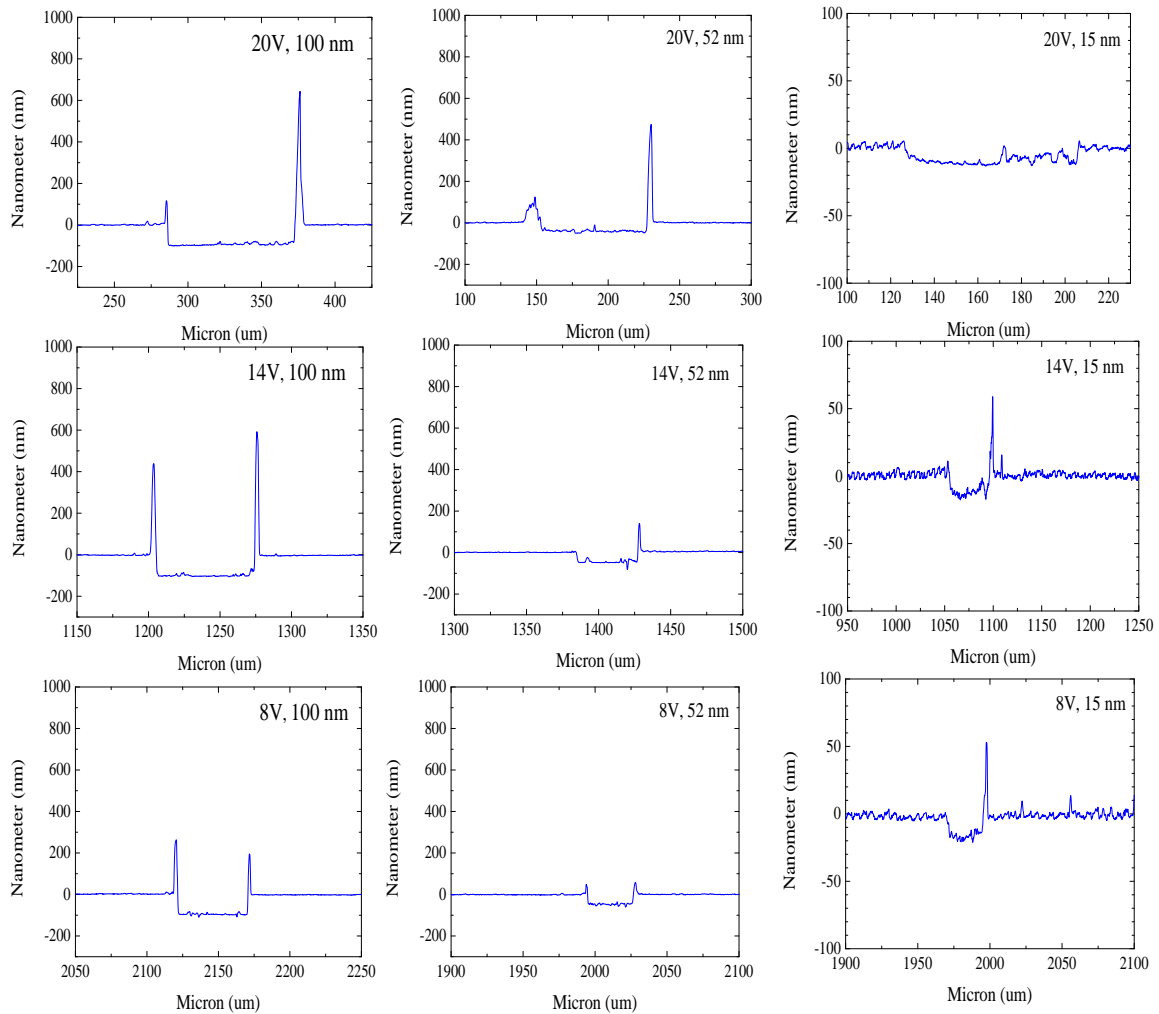


Figure 4.26: Profilometry example for -20 V, -14 V and -8 V, in 100 nm thick (left column), 52 nm thick (central column) and 15 nm thick (right column), edge standing out feature progression.

To solve this issue, a specific procedure to smooth edges was designed, wherein the tip behaves as a sweeping tool. Sweep algorithm is written to perform 0 V additional patterns over the edge features at a low speed (0.01 mm/s) in order to remove material excess. Once properly calibration was achieved the sweep method was successful. In Figure 4.27 an example for a straight pattern before and after the process is shown. There is a clear visual difference between both lines; all bright edges have disappeared,

turning into a dark stripe frontier (red arrows indicators in Figure 4.27a). Profilometry shows a great reduction of this accumulated material (almost complete), but still remaining a small amount (Figure 4.27b).

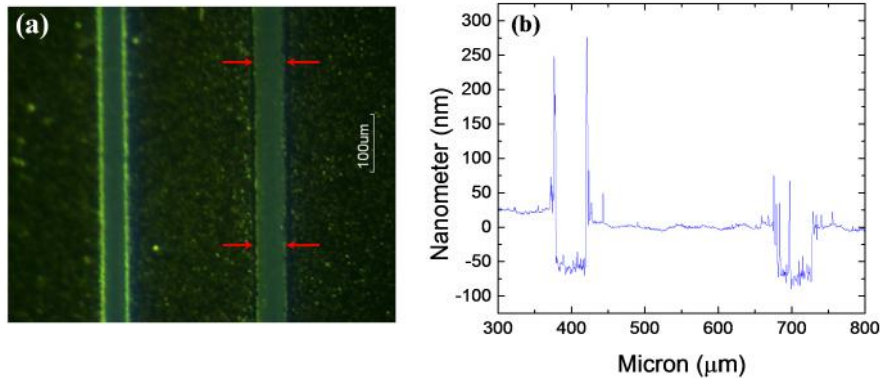


Figure 4.27: Sweep edge method for straight patterns: (a) optical image and (b) profilometry.

A great reduction of the protruding features at the edge from hundreds to tens nanometers has been achieved by using a “superficial” method without the intervention of other procedures e.g. chemicals. It is also demonstrated that the accumulated material is not melted or adhered to the surface, increasing the possibility to remove it through repetitive movement cycles, making the respective algorithm modifications. It is important to consider that this sweep method only works for well-defined grooves, which guarantees a final straight edge.

- **Spot patterns on Au 52 nm layers**

Another type of patterning was also tested on  $52 \text{ nm} \pm 2$  Au samples, varying the operating voltage and polarity. Four spot vertical arrangements were performed for each voltage, from  $\pm 3 \text{ V}$  to  $\pm 16 \text{ V}$ . Final electrical erosion results are shown in Figure 4.28 for both, positive and negative voltage polarity.

Comparing both images, some differences can be observed. In the low voltage range (from 3 to 5 V) electrical erosion begins at +5 V when positive polarity is used. Small features can be observed at +4 V, but this voltage is not enough to obtain a full material removal. In contrast, for negative polarity, electrical erosion begins at -3 V and it is maintained throughout the test range. According to this, electrical erosion using negative polarity allows the operation at smaller voltages, while positive polarity limits the electrical erosion operation to above +5 V. By contrast, electrical erosion using high

voltage positive values (+16 V) seems to be less chaotic than its negative counterpart, the spot widening is more regular and fingering (irregular edges) is not so evident. This behavior is similar to that found in ITO spots.

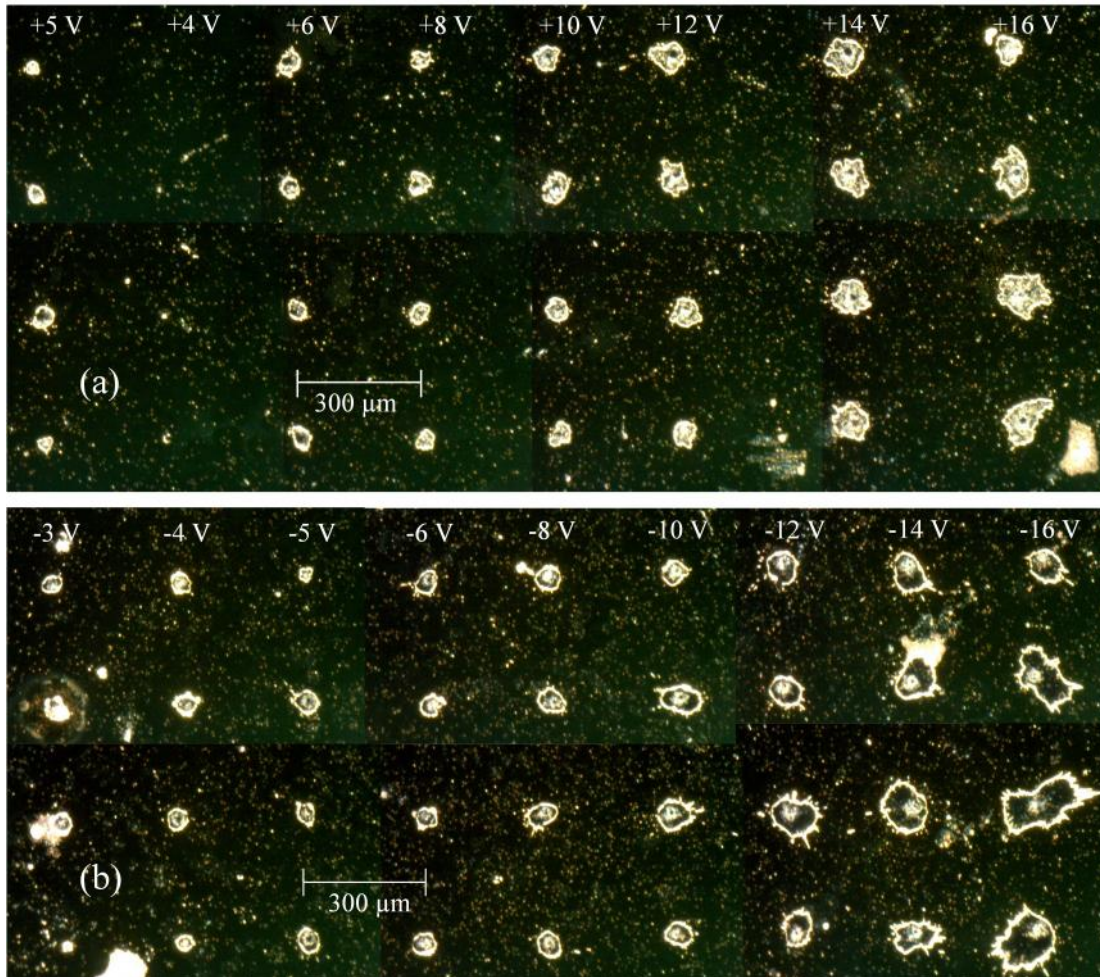


Figure 4.28: final spot arrangements: for (a) positive and (b) negative polarity.

On the other hand, in Figure 4.29 the spot size widening as voltage increases has been plotted for both polarities. In contrast to the observations in ITO, here it is observed clearly that spots performed with negative polarity are quite larger than the positive ones. On the other hand, the overall behavior shows the initial flat region until a threshold voltage  $V_{th}$  is achieved, and a subsequent monotonic increase of the radius (rather linear) with increasing voltage.

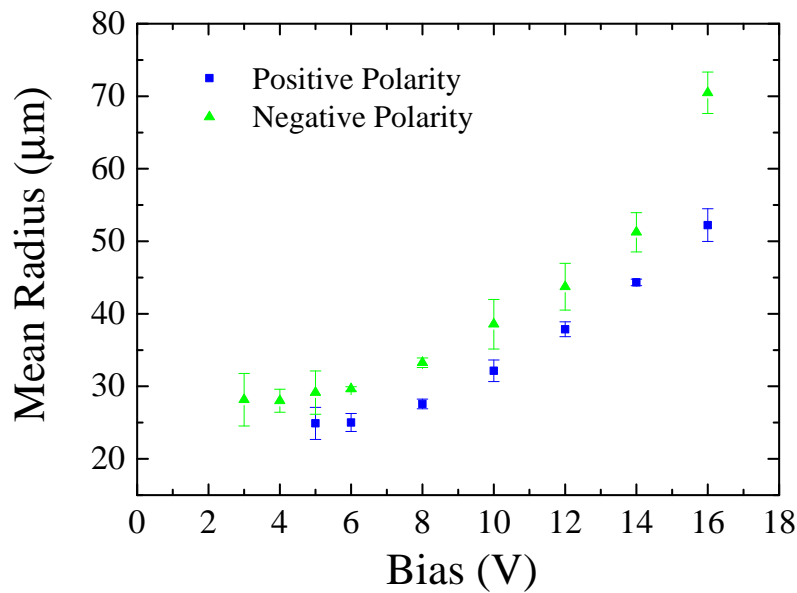


Figure 4.29: Polarity spot comparison for a bias range from  $\pm 3$  V to  $\pm 16$  V.

#### 4.4.1. PET/ITO/GOLD

In view of the successful patterning experience on ITO/PET, previously discussed in section 4.1.1, and with the idea of getting features as small as possible, it is decided to perform some test on gold samples. For this task an acupuncture needle is again used, like with ITO/PET experiments. In terms of sample preparation, gold was deposited by thermal evaporation and then deposited on PET substrates. Conductive paint droplets are then placed in each corner in order to set the ground contact and homogenize potential.

Through the combination of both implemented movement subsystems and an inherent functionality from the digital piezo stage controller module, a new processing way in tapping mode is introduced to perform the arc-erosion experiments in this section. This functionality is a wave generator tool, which allows the Z-axis piezo stage being set in a controlled oscillating mode. This module is parametrized by software, where wave type, amplitude (V) among other variables can be set as needed.

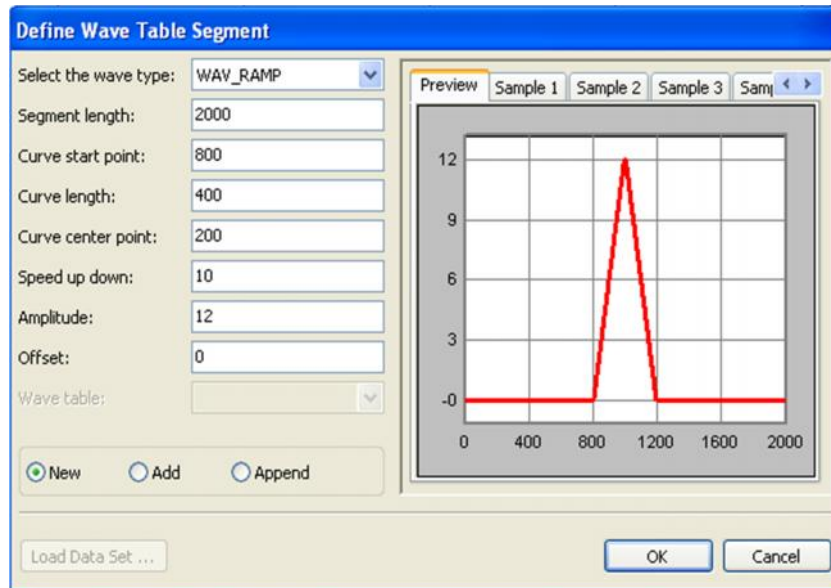


Figure 4.30: Initial wave settings PIMikroMove Software window for wave generator module parametrization.

By properly adjusting the tip height above the sample we can arrange the work in tapping mode. This mode should reduce abrasion between the tip and the sample. Figure 4.30 shows the wave data, used for tapping mode. It is necessary to emphasize that the wave generator functionality works only with piezo stages in open-loop mode, i.e. by controlling or setting a voltage value in order to obtain a specific movement. In this case, PI Lisa piezo stage is subjected to this triangular wave, whereas PI Hera XY piezo stage continues working in closed-loop.

Examples of groove patterning on this type of samples are shown in Figure 4.31. One millimeter long grooves, with a 200  $\mu\text{m}$  separation were successfully achieved using a rigid needle, at 0.01 mm/s for X and Y speed movements. Note that tapping mode requires a lower displacement speed. This pattern was developed in a voltage range from 1 to 6 V. In these samples, which were deposited on a plastic substrate without prior Cr adhesion layer, a threshold voltage  $V_{\text{th}} = 2 \text{ V}$  was found. Arc-erosion is unsuccessful using 1 V, and the brightness in the optical image denotes not removed remaining material. In general terms, this voltage range (from 2 V onwards) can be considered for processing these samples using this type of tips, but for a successful outcome in terms of quality and edge definition it is recommended to work between 2 and 3 V, respectively. At these voltages, grooves do not present, in most of its length, any defect on its edges, or at least, it is less noticeable when compared to those at higher voltages. Moreover, wavy edges appear with increasing operation voltage.

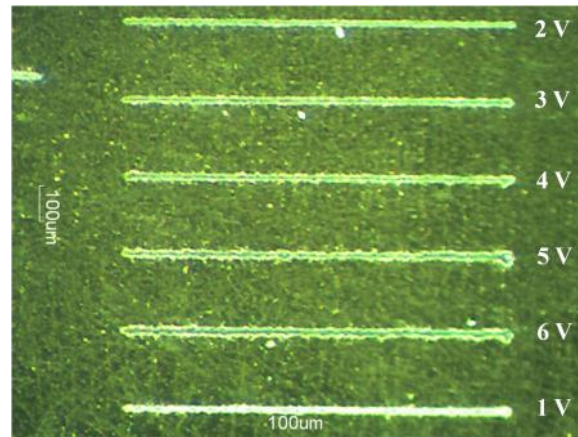


Figure 4.31: Final patterning on PET/ITO/Gold samples using an acupuncture needle, voltage bias range from 1 to 6 V and tapping mode. Movement speed was set in 0.01 mm/s.

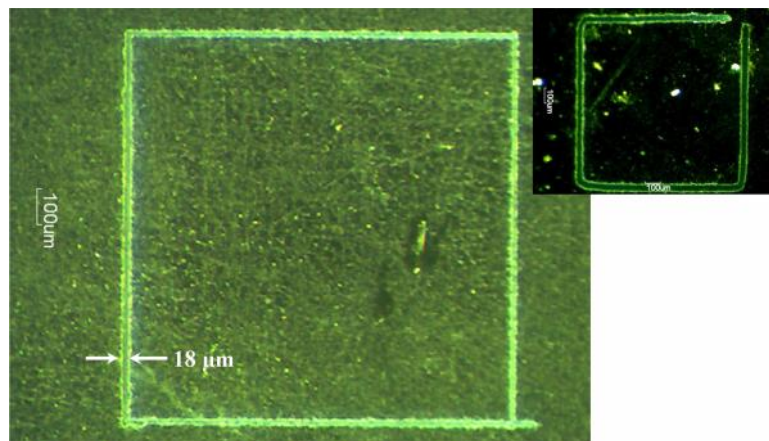


Figure 4.32: Final closed pattern obtained using tapping arc-erosion mode. Inset: one millimeter side square pattern by standard arc-erosion mode.

More encouraging results are obtained when tapping mode is implemented to perform closed patterns. Figure 4.32 shows a one millimeter side square performed on PET/ITO/Gold samples. The voltage used was 2 V and the same process speed (0.01 mm/s) was set to perform this experiment. A high quality closed pattern is successfully obtained, with well-defined 90 degrees corner intersections, compared with the feature at the inset, which was performed with a commercial spring probe. Moreover, thanks to the meticulous four-point map for tilt correction, a quality closed pattern is ensured. Another key feature for this result was the rigid tip attachment. Using spring probes, a problem stems from the two body assembly concentricity (spring and jacket) due to the gap between these two elements. This effect use to be negligible for very large patterns but noticeable for micron and nano scales. By using acupuncture needles this problem in solved immediately because basically the gap from concentricity disappears.

In conclusion, conditions for correct arc-erosion lithography on materials used in optoelectronic devices like ITO, AZO and Au have been obtained. It has been remarkable as a general result that mechanical erosion is not enough for quality performance, an applied bias and a tip compression combination is needed to achieve and adequate arc-erosion lithography. Also, it is observed an increase in the pattern width for higher operating voltages, which adds a new control parameter to the system. A wavy edge at higher operating voltages, more pronounced depending on the material, is also observed. This phenomenon is directly related to the physical process that takes places in the electrical erosion, however further studies are necessary to solve the unanswered questions. COMSOL Multiphysics software for finite element analysis has been used in order to simulate the physical system, discussed in the next section. Excellent results have also been obtained in flexible substrates using rigid tips (acupuncture type) as well as homemade cantilever probes. It has been proposed a new working mode tapping-like, by an inherent functionality implementation from the piezo stage controller.

#### 4.5 DISCHARGE TRANSIENT ANALYSIS

A more in depth study of the physical phenomena involved in the crater formation by electrical discharges is carried out by analyzing the electrical traces recorded during the process.

Figure 4.33 shows oscilloscope traces  $V_i(t)$  of sparks measured at the test resistor  $R_t$  during the tip to surface approach. They have been recorded from different target layers (gold and graphene), using a range of applied voltages (above threshold for electrical erosion) and different test resistors ( $R_t = 10$  ohm for gold and  $R_t = 1$  kohm for graphene). The duration of the spark for the samples examined appears to be in the order of  $1 \mu s$ . By doing tests on gold samples of different thicknesses, we have observed a correlation between spark duration and layer thickness. For a fixed operating voltage, the thicker the layer the longer duration, what makes sense if we understand the spark as a phenomenon of digging material. The inset in Figure 4.33 shows a trace plotted in logarithmic scale to highlight the linear behavior of specific intervals, which is an indication of conventional charge-discharge effects of capacitances through resistances.

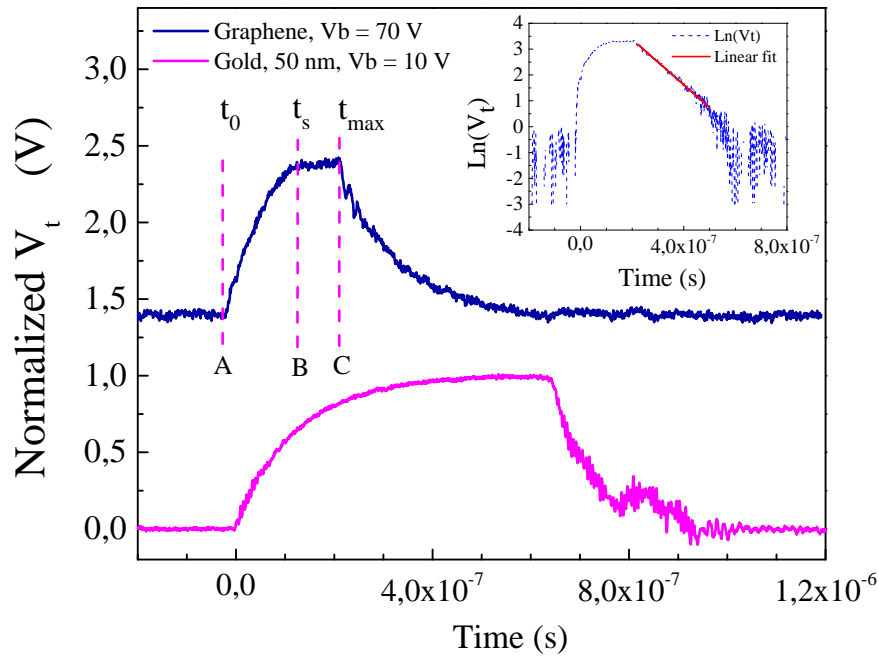


Figure 4.33: Oscilloscope traces  $V_t(t)$  of sparks measured at the test resistor  $R_t$  during the tip to surface approach.

It was experimentally found that the trace exhibits a general shape consisting of three regions: an initial raising slope from  $t = 0$  to  $t_s$  (region A, in Figure 4.33), which corresponds to the breakdown of the tip-layer capacitor,  $C_b$ , and its concomitant discharge. A saturation region from  $t_s$  to  $t_{\max}$  (region B), where the current attains a maximum and roughly steady value until the discharge quenching. This saturation is only observed for sufficiently high voltages (above the threshold for crater expansion), and when a single spark dominates the process, what not always happens. At low voltages, the ascending slope is usually interrupted before attaining this saturation, resulting in a characteristic sawtooth shape. At high voltages, the discharge occurs in many cases by a sequence of multiple sparks (Figure 4.34). This contributes undoubtedly to irregularities in the crater front. In any case, the spark quenching (process interruption) gives rise to a descending slope from  $t_{\max}$  onwards (region C in Figure 4.33), corresponding to the recharge of the new tip-plane capacitor after crater formation. Note that while  $t_0$  and  $t_{\max}$  are well defined times because they imply a clear slope change,  $t_s$  is not, and remains just as an indication to distinguish B and C regions.

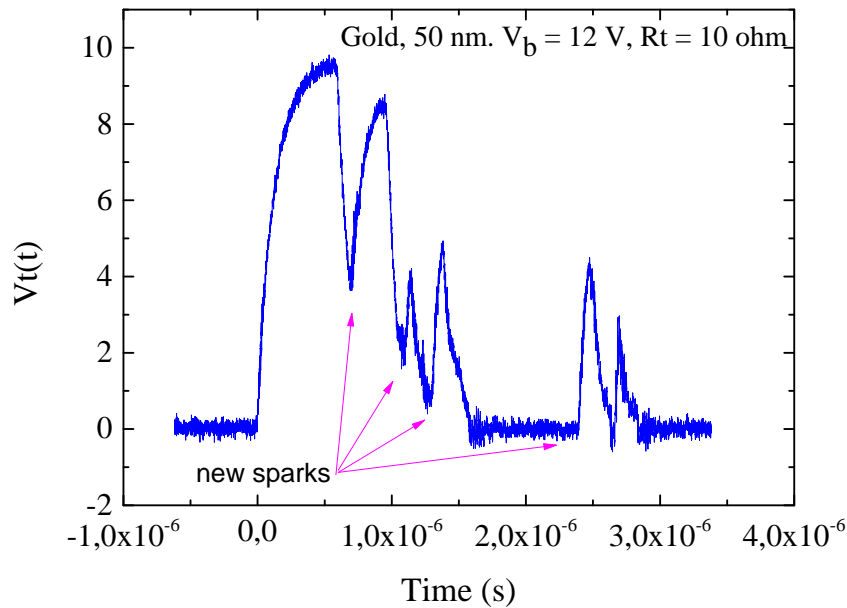


Figure 4.34: Example of multiple sparks recorded in a series resistor of 10  $\Omega$  during creation of a crater performed at 12 V on a 50 nm gold layer.

In this system several parameters are unknown and will be the subject to search:

- The initial tip-plane capacitor,  $C_b$ , which can be assumed constant because the distance covered during the spark lifetime, is very short, about 1 nm.
- The internal resistance of the target material during discharge,  $R_g$ . This involves the material resistance in the path from the tip to the external contacts during the discharge short-circuit.
- The final capacitor  $C_f$ , once the spark is extinguished.
- Any other circuital component driving the initial discharge, for example, inductive effects associated to plasma creation.

The objective of this subsection is to propose a circuital model based in the aforementioned components, able to explain the voltage traces measured at the oscilloscope. At this point it is worth mentioning that there is a variety of circuital models in the literature describing with greater or lesser extent the discharge between conductors. Depending on the nature of the considered discharge (whether it involves plasmas or field effect currents in vacuum, whether the discharge is a sustained arc or a non-equilibrium transient spark, whether the target is a semiconductor, a metal or a dielectric barrier) the processes involve different physical phenomena, including oscillations [13], time dependent resistances or inductances [14], delayed currents for

different charge species (electrons and ions) [15] space charge diffusion and accumulation [16, 17], in such a way that complex circuital models are proposed to take into account these effects. In Figure 4.35 examples of different complex models used in refs [13] and [14] are shown.

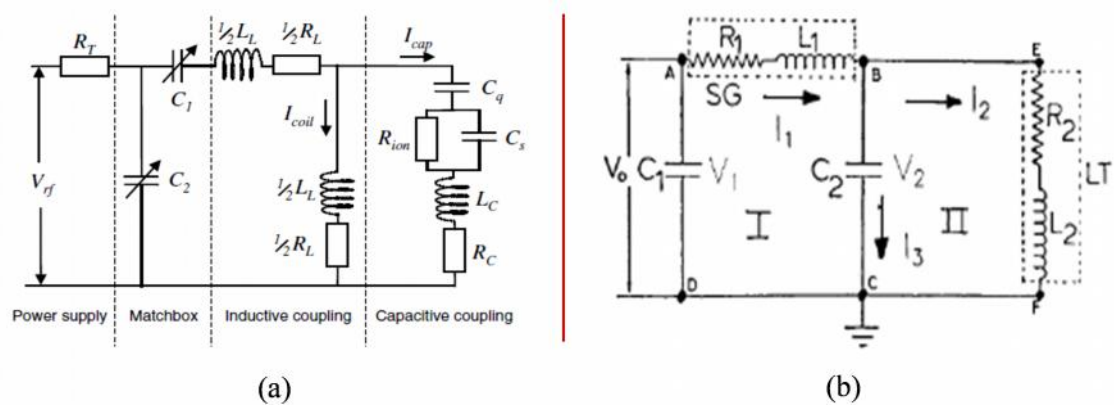


Figure 4.35: Examples of different complex models used in Refs [13] (a), and [14] (b) to model discharge phenomena in different situations.

In this work, I will not adapt any of these complex models to explain our observations, but on the contrary, I will adopt the stance of searching for the simplest model able to describe my set of experimental measurements, in particular, the voltage response observed by oscilloscope.

When interpreting the voltage traces observed by oscilloscope, probably the most unambiguous situation is that described previously as ‘region C’ in Figure 4.33, corresponding to the recharge of the residual tip-plane capacitor,  $C_f$ , after the spark extinction. The discharge interruption is attributed to the moment when the crater boundary gets too far to hold the discharge current. Next, the external voltage source provides the necessary current to recharge  $C_f$ , which circulates through the external resistances of the circuit. When plotting the trace in logarithmic scale, this region exhibits the typical linear behavior of an exponential decay (inset of Figure 4.33), with a RC time-constant that can be easily measured. Notice that this stage takes place in a straightforward circuit, where just a few components are involved ( $C_f$ , the test resistance  $R_t$  and, possibly, certain access resistance,  $R_{ac}$ , to the target layer which forms the ground contact), so their value may be easily estimated.

In Figure 4.36, traces of sparks at the same operating voltage are recorded from the same sample but using different test resistors  $R_t$ . The larger the  $R_t$  the longer the RC

time-constant, as expected. In this case  $R = R_t + R_{ac}$  and  $C = C_f$ . So with these three curves we can derive the corresponding values, resulting  $C_f$  in the order of tens pF, and  $R_t \gg R_{ac}$  ohm.

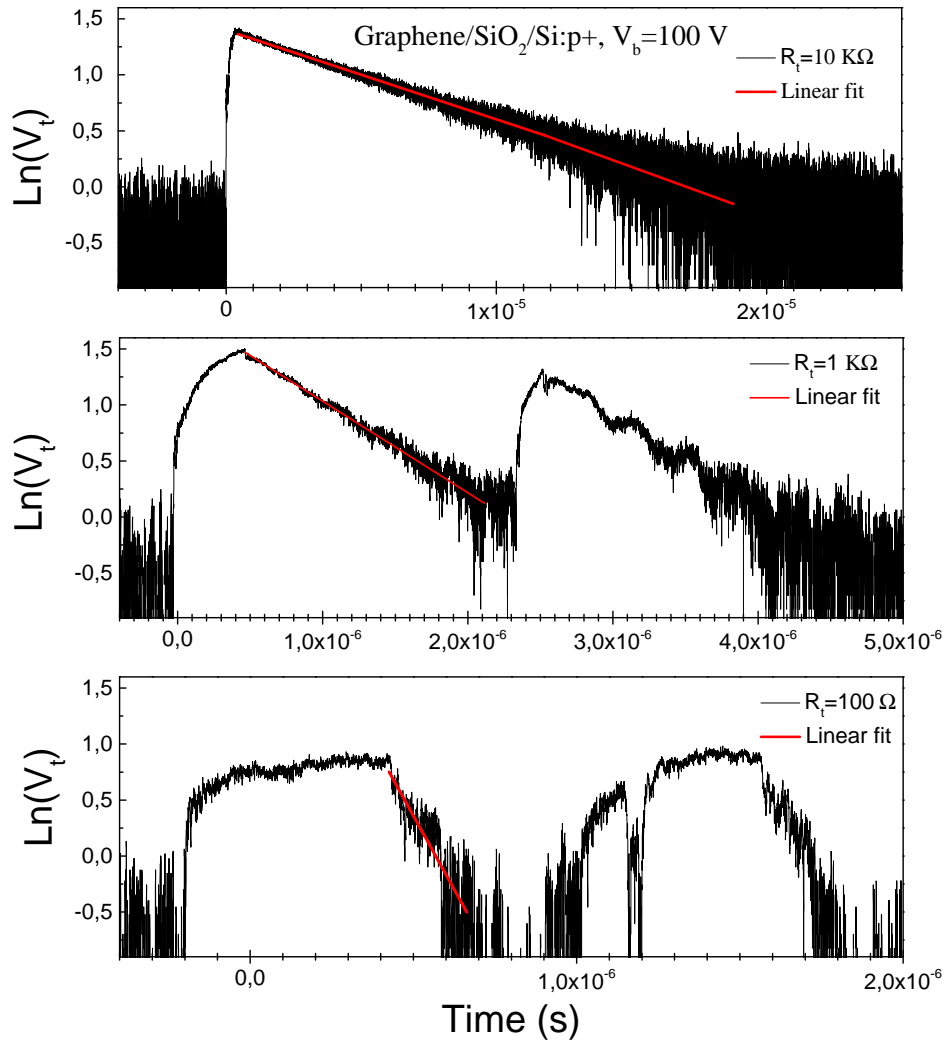


Figure 4.36: traces of sparks at the same operating from the same sample, using three different test resistors  $R_t$

The capacitance  $C_f$  of spots performed on graphene/quartz at different voltages – and consequently with different effective crater radius- are plotted in Figure 4.37. The slight reduction of  $C_f$  with increasing voltage is consistent with the larger size of the craters around the tip produced at higher voltages, a tendency already described in Figure 4.7, Figure 4.16 and Figure 4.29.

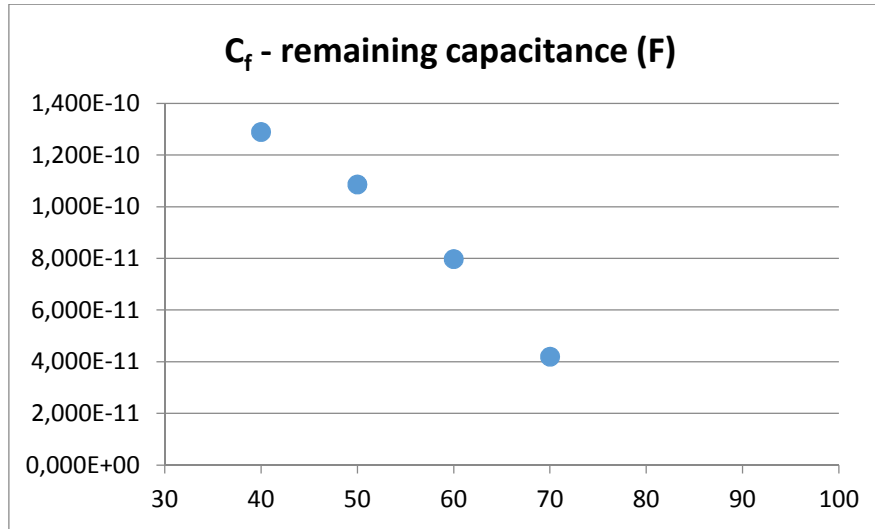


Figure 4.37: The capacitance  $C_f$  of spots performed on graphene/quartz at different voltages –and consequently with different effective crater radius

For voltages above the threshold for crater expansion ( $> 30$  V in graphene, 6 V in gold of 50 nm or 11 V in ITO of 100 nm), the voltage ramp  $V_t(t)$  tends to stabilize at a maximum value  $V_{t-max}$  (Region B) in a small time interval, from  $t_s$  to  $t_{max}$ . This steady value is a result of the negative feedback exerted by  $C_b$  and the series  $R_t$  on the short-circuit current, labelled  $I_{fe}$  from now on. When  $I_{fe}$  increases it leads to a higher voltage drop at  $R_t$ , which in turn reduces the voltage  $V_C(t)$  at  $C_b$ , slowing down  $I_{fe}$ . Due to this mechanism,  $V_C(t)$  eventually adopts a constant value just to hold the persistence of the current through the tip-plane gap, and consequently a constant current circulates across the whole circuit. This steady situation makes easier the electrical analysis and helps to derive some properties of the system. In steady state, the short-circuited tip-layer system is equivalent to the aforementioned resistor  $R_g$  (material resistance in the path from the tip to the external contacts). In this case,  $V_{t-max}$  should coincide with the value obtained by the voltage divider circuit formed by  $R_g$  and  $R_t$ . In this way,  $R_g$  can be easily determined by the expression.

$$V_{t-m} = V_b \frac{R_t}{R_t + R_g} \quad (\text{for } t > t_s) \quad (4-5)$$

Where  $V_b$  is the applied external voltage. Values obtained for  $R_g$  are in general quite close to the resistance measured from tip to contact in a static way (between 1 – 2 kohm for our commercial single-layer graphene on SiO<sub>2</sub>/Si, about 30 - 40 ohms for ITO

layers 100 nm thick, and about 2 – 3 ohms for gold layers 50 nm thick. The latter value is in agreement with the expected sheet resistance for gold of such a thickness [18].

In region A, the voltage onset  $V_t(t)$  measured in  $R_t$  is linked to the initial short-circuit of the tip-graphene capacitor,  $C_b$ . However, the correct interpretation of the function  $V_t(t)$  is not easy. We can speculate that just before the spark initiation at  $t = 0^-$ , the circuit conditions are such that  $C_b$  bears  $V_b$  and there is not voltage drop in  $R_t$ . Immediately after, in  $t = 0^+$ , the capacitor discharge current is equal to the breakdown current which, as proposed in Chapter 1, can be considered a field effect current  $I_f$ , of the Fowler-Nordheim type for tunnel current across a triangular barrier [19]. Then we can formulate:

$$C_b \frac{dV_C(t)}{dt} = -I_f (V_b) \quad (t = 0^+) \quad (4-6)$$

The discharge of  $C_b$  immediately leads to a voltage drop in  $V_c(t)$  which attracts current from the voltage source in order to verify the mesh rule. Then, the initial ramp  $dV_t(t)/dt$  of the measured voltage trace at  $R_t$ , can be derived as

$$\frac{dV_t(t)}{dt} = -\frac{dV_C(t)}{dt} \left[ \frac{R_t}{R_t + R_g} \right] = \frac{I_f (V_g)}{C_b} \left[ \frac{R_t}{R_t + R_g} \right] \quad (t = 0) \quad (4-7)$$

However, several effects obscure and modify this approach: on one hand, the bypass capacitor at the output of the voltage source shows non-ideal behavior under fast-switching, introducing a distorted response (including oscillations) and preventing an accurate measurement of the initial ramp  $dV_t(0)/dt$  along 40 - 50 ns. Unfortunately this would be the range where a field effect current could have significant effect. On the other hand, we experimentally confirm that, for operating  $V_b$  above threshold for crater expansion, the fact of increasing the test resistor  $R_t$  implies a faster initial ramp. This can be observed in Figure 4.38 for a gold layer, and is in no way compatible with just a capacitive-driven process. In Figure 4.38 initial ramps (so called region A) of discharges on a gold layer 50 nm thick at 16 V, recorded with different  $R_t$  in the range 10 – 1000 ohm are shown to confirm this observation. This finding reveals that inductive effects -

which can be tentatively attributed to self-inductance in the conductive target layer, as well as to plasma generation-, accompany this stage of the discharge.

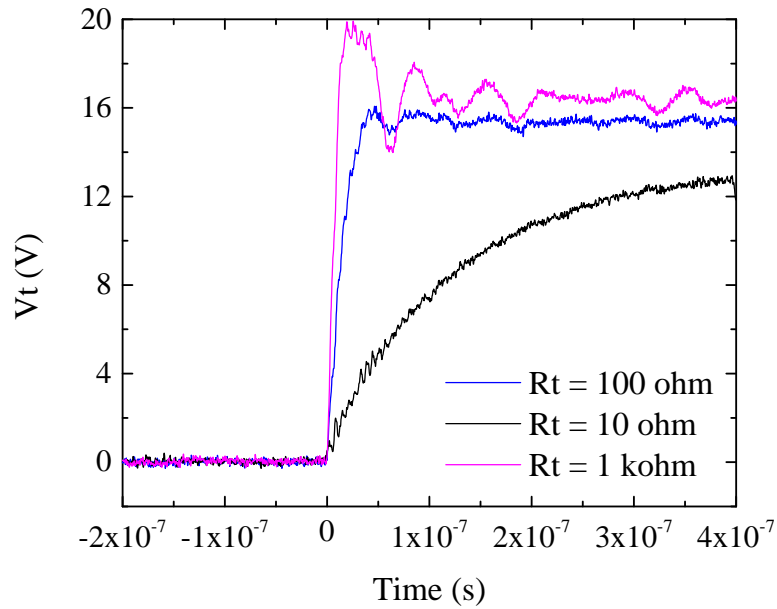


Figure 4.38: Traces  $V_t(t)$  for three discharges in a gold sample 50 nm thick, at operating voltage  $V_b = 16$  V, using three different test resistors with  $R_t = 10$ , 100 and 1 kohm.

A feature also confirming the existence of certain RLC circuit in the discharge process is the appearance of long-period damped oscillations just after the onset of  $V_t$  (t). These oscillations depend on the material and  $R_t$ , and cannot be considered a spurious inductive effect due to the external circuit.

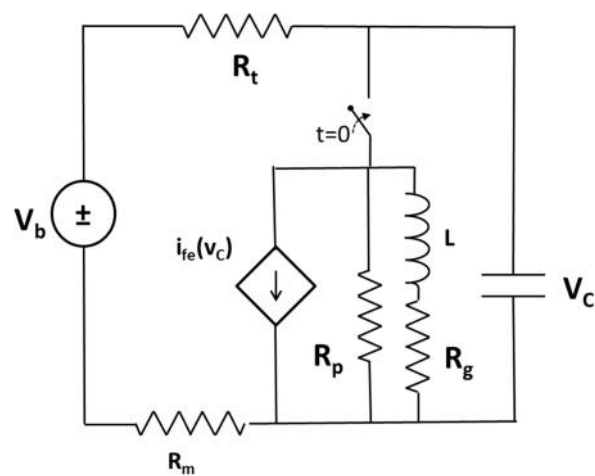


Figure 4.39: Circuitual model according to our strategy, including a coil integration

According to our strategy, the simplest component to justify such observation is a coil with resistive effects. The integration of this component together with the previously cited components results in the circuitual model of Figure 4.39.

In this plot, I have included, as a token feature, what should be a field effect current in the way of a voltage-dependent current source bypassing the tip-to-layer gap.  $R_m$  is a resistor to include effects of circuitual elements.

In order to perform simulations, the switch to be ON at  $t = 0$ , will come back OFF after  $t_{max}$ , according to our notation. In Figure 4.40 the OrCAD-PSPICE model which reproduces the circuit drafted in Figure 4.39, used for simulating the voltage traces shape, is shown. The number of switches is a must for the software in order to handle the voltage-dependent current source in the context of connection-disconnection. The time for ON-OFF in every switch must be set manually, according to the  $t_0$  and  $t_{max}$  values observed experimentally. Note that the tip-plane capacitor is split in two parameters,  $C_b$  and  $C_f$ , in order to simulate its value before and after the switching that represents  $t_{max}$ .

Neglecting the effect of the dependent current source, the unknown parameters are  $C_b$ ,  $R_p$ , and  $L$ . By solving analytically the circuit for  $V_t(t)$ , some boundary conditions may be established for  $dV_t(0)/dt$  and  $V_t(t_{max})$  from the experimental trace. With the help of this information, the final determination of the three parameters may be easily performed using OrCAD PSPICE simulator. In Figure 4.41, we can observe the result of adjusting the modeled  $V_t(t)$  to an experimental trace recorded from a spark in graphene at  $V_b = 70$  V, showing a reasonable agreement.

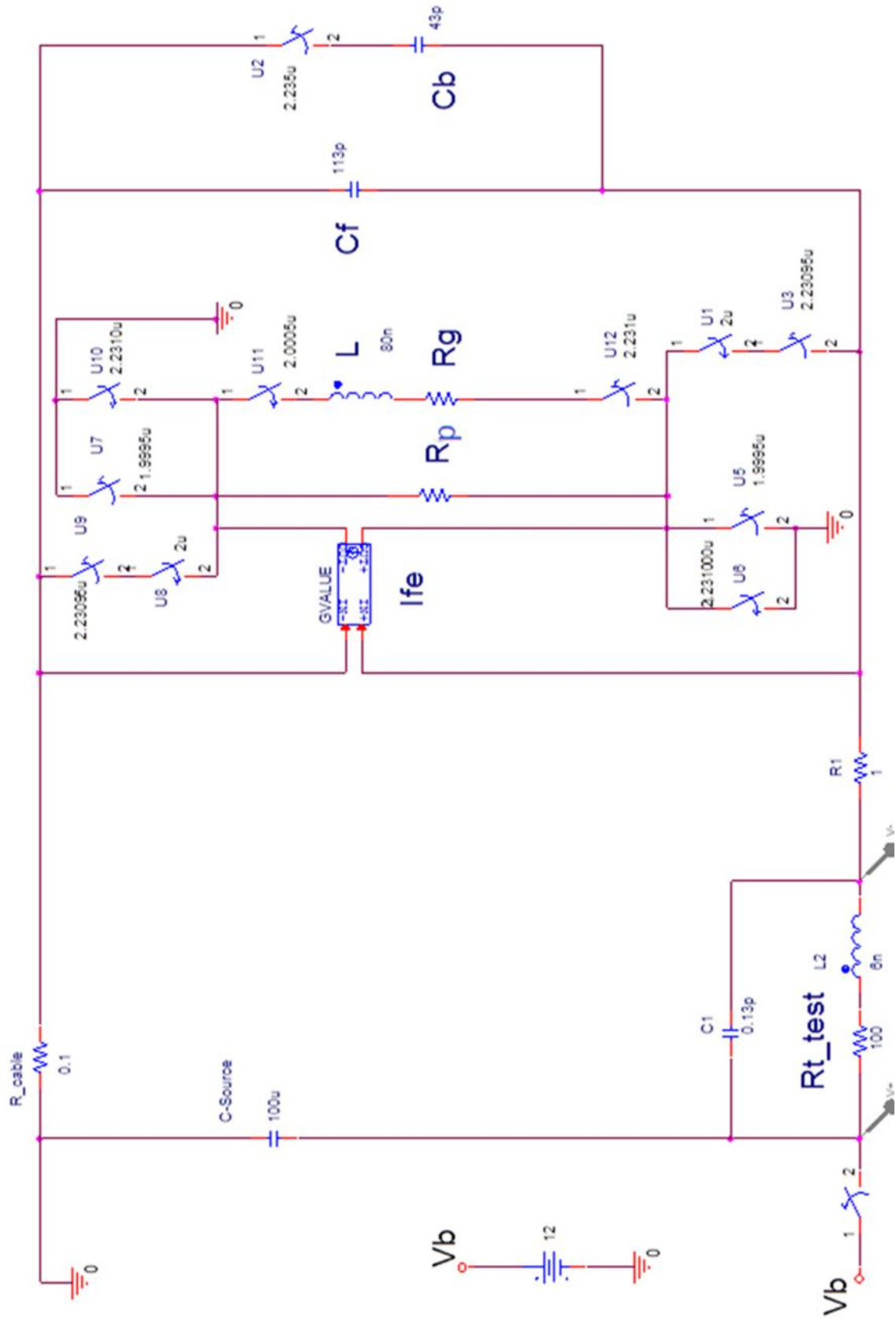


Figure 4.40: OrCAD-PSPICE circuit model used to simulate the line shape of the voltage traces recorded during discharges.

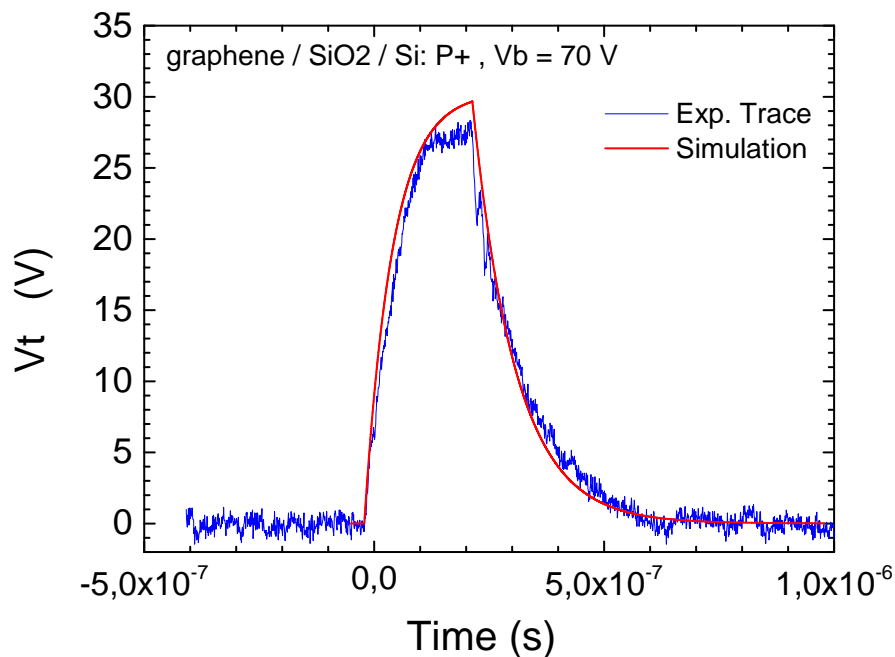


Figure 4.41: Experimental trace  $V_t(t)$  recorded from a spark in graphene (blue curve) and result of simulation (red curve) performed with the PSPICE model proposed in Figure 4. 40

#### 4.6 FINITE ELEMENT ANALYSIS FOR PHYSICAL SYSTEM SIMULATION

Whatever the process causing a discharge (field effect current, streamer propagation or dielectric breakdown), it will be triggered in those regions where the electric field is higher, so the knowledge of the field distribution in our system is of major interest. Using the COMSOL Multiphysics software for finite element analysis described in section 3.5 [20], simulations of the electrostatic properties in the tridimensional tip-to-plane system has been performed. In this case, the ‘plane’ is substituted by ITO (a semiconductor, from the point of view of the simulation software), pure metals or a combination of metal/dielectric layers as target material. We will pay specific attention to the field distribution at the edge regions, where the field lines are more densely packed and the field norm is maximum.

Two moments are important during the discharge process: the approach of the probe to the sample, and the landing of the tip on the insulating region (crater). Both situations correspond with two different geometries. In accordance, all our performed

simulations can be classified in two general groups upon the arranged geometry: (a) computational experiments in non-contact situation (keeping a distance  $d$  between tip and sample). In this case we analyze electrical magnitudes (fields, potentials and charge distribution) varying the tip angle, tip-sample distance, and charge doping of the target material, and (b) experimental simulations once the contact tip-surface has been verified ( $d = 0$ ).

Below, experiments with different geometries will be discussed. The general model is displayed in Figure 4.42. It consists of a system with cylindrical symmetry including a truncated cone-shaped tip of  $10\ \mu\text{m}$  radius, which is located  $1\ \mu\text{m}$  above a target layer (grounded) on a dielectric (glass) substrate. The system axis coincides with that of the cylindrical probe. The standard tip angle (in the Figure 4.42) is  $22.5$  degrees, since this is the sharpness of our commercial spring probes.

#### 4.6.1. Influence of the tip sharpness, separation tip-sample, and doping of the target layer on the electrostatic properties

Series of computational simulations of the electrostatic magnitudes (electric field and potential, together with charge distribution) were carried out using different tip angles:  $0^\circ$ ,  $22.5^\circ$  (the standard one)  $35^\circ$ ,  $45^\circ$ ,  $60^\circ$  and  $80^\circ$ . Simulations carried out are referred to the Tip-Glass/ITO model previously described in section 3.4.1 and displayed in Figure 4.42. The ITO layer thickness in this initial test is  $100\ \text{nm}$ , typical of commercial samples. Here, ITO is considered a “n-type semiconductor” from the software point of view, namely, a volume with free electron density (“doping” from now on) established by the user. Related to the scheme shown below, distance  $d$  ( $1\ \mu\text{m}$ ) and voltage bias ( $V_b = -10\text{V}$ ) are kept constant for all tests.

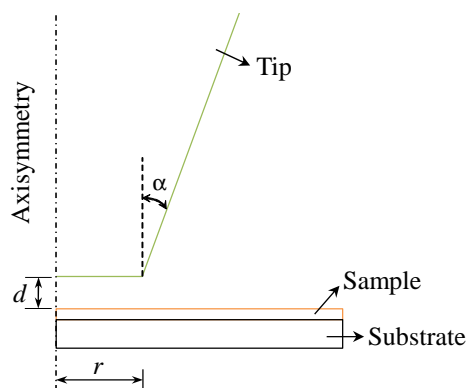


Figure 4.42: Geometrical scheme for tip angle variation simulations using Comsol Multiphysics.

Due to the high complexity of calculations involved in the *semiconductor module* of the software (since it implies a self-consistent solution of the stationary free charge density), a stepped method had to be implemented to reach numerical convergence when working with the high doping levels (free carrier density) typical of commercial ITO, which are over  $10^{25} - 10^{26} \text{ m}^{-3}$  ( $10^{19} - 10^{20} \text{ cm}^{-3}$ ) [21, 22]. In this case, the final solution is apparently so far from the simple initial conditions, that the solver algorithm is unable to manage it. For this reason, we adopted the following procedure.

All simulations begun with a non-doping value for the ITO, just considered as an insulator (no free charge) of dielectric constant  $\epsilon = 9$  [23]. Once the solution converged, the software is prompted to take this last result as an initial boundary condition for the next simulation. Then a new and very low value for ITO doping is set (usually  $1 \times 10^{17} \text{ m}^{-3}$ ). By converging and from that point, this doping value is being increased by one magnitude order, making sure that the new calculation start from the previous solution, and so on until the doping value reaches  $1 \times 10^{25} \text{ m}^{-3}$  and a convergent solution is achieved.

This stepped experiment reveals how the electric field is gradually shielded and rejected from inside the conductive layer by the free charge, as the material doping increases. A comparison between an initial no-doped ITO and  $1 \times 10^{25} \text{ m}^{-3}$  ITO doping simulation is shown in Figure 4.43, using a standard 22.5 degree tip. In this graph, the probe axis coincides with that of the cylindrical geometry (on the left side). Finite element modelling of the electric potential is shown, where blue regions correspond to -10 V and brown regions to 0 V (ground).

In absence of doping, the equipotential lines penetrate the sample, so the potential gradient is smooth, and consequently the electric fields at the tip are not very high. In the opposite case, at very high doping, free carriers are able to screen electric field lines out the doped layer, so equipotential lines get densely packed in the volume between tip and sample. The potential gradient is consequently high and the electric field at the tip is large. This is the main explanation why you need lower voltages to create a discharge when working with materials with free charge.

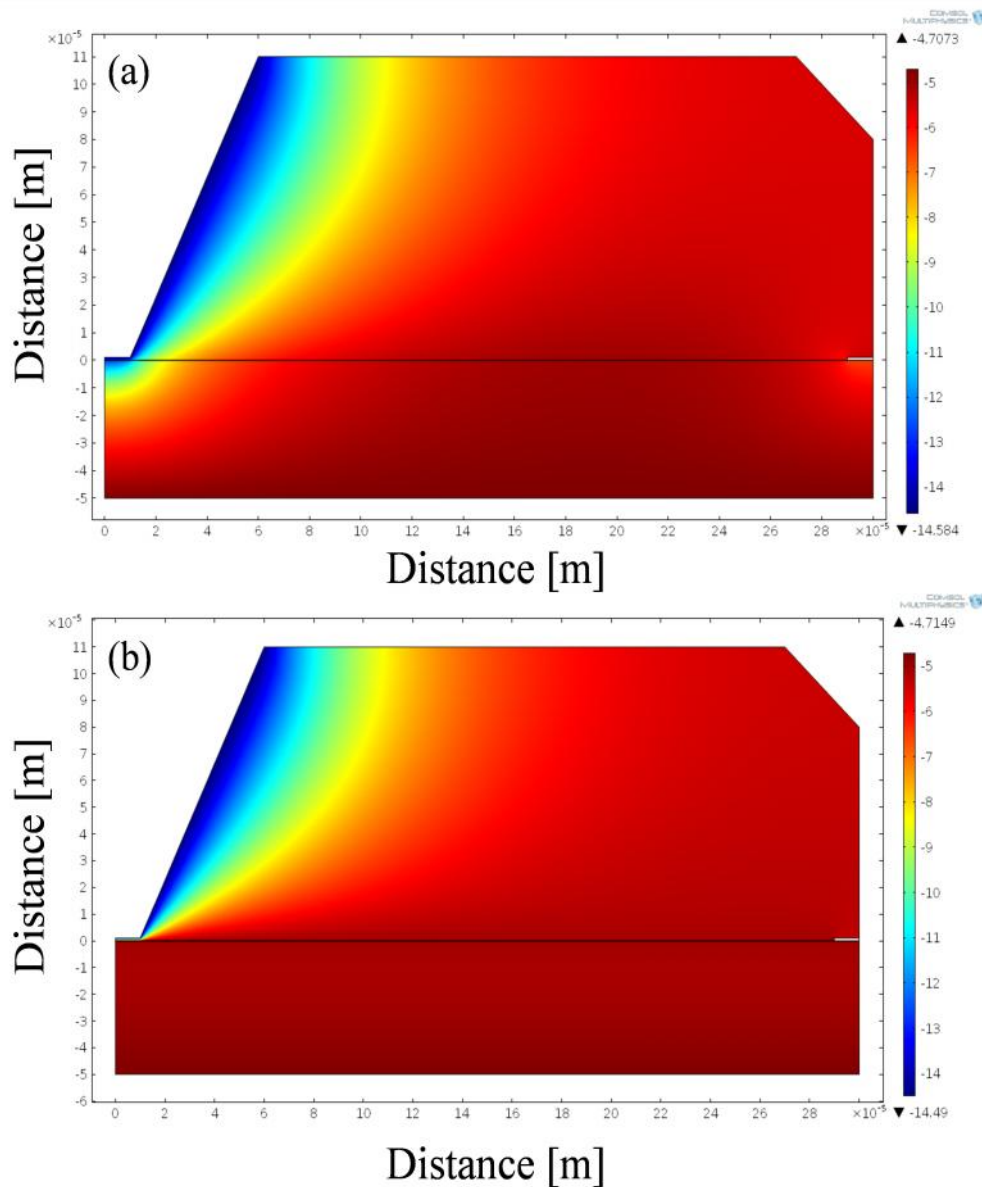


Figure 4.43: Axial view (cylindrical geometry) of a system consisting of a truncated cone-shaped tip of 10  $\mu\text{m}$  radius (biased at  $-10$  V), 1  $\mu\text{m}$  above an ITO (grounded)/Glass substrate. The probe axis coincides with that of the cylindrical geometry. Finite element modelling of the electric potential is shown where blue regions correspond to  $-10$  V and brown regions to 0 V (ground) (a) not doped ITO, and (b)  $1 \times 10^{25} \text{ m}^{-3}$  doped ITO models.

This procedure has been applied to geometries where the tip angle is varied. Final simulations involving  $1 \times 10^{25} \text{ m}^{-3}$  doped ITO are shown below in Figure 4.44. These results correspond to a tip angle ( $\alpha$ ) of 0 degrees (Figure 4.44a), 45 degrees (Figure 4.44b) and 80 degrees (Figure 4.44c), note how the electric potential lines accommodate according to the tip geometry.

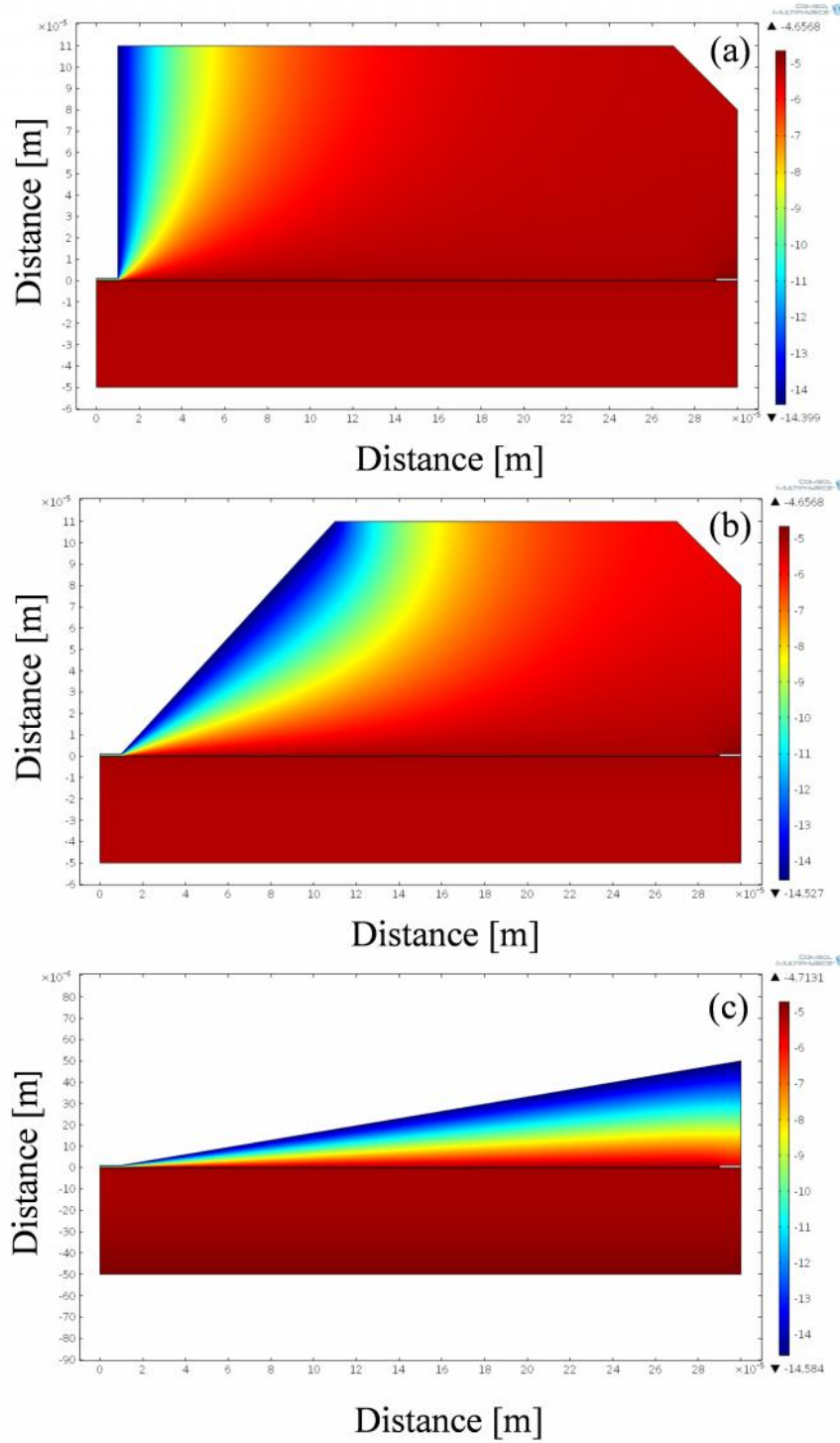


Figure 4.44: Glass/ITO finite element electric potential modelling at  $V = -10\text{V}$  and  $d = 1 \text{ }\mu\text{m}$ ; (a) 0 degrees, (b) 45 degrees and (c) 80 degrees with  $1 \times 10^{25} \text{ m}^{-3}$  doped ITO.

In the metal tip-to-plane geometries, the electric field is maximum at the tip apex. For a pure cone shape the dependence of this maximum electric field on the tip-plane distance is reported, for example, in [24]. Our simulation software allows determining

the electric field modulus along the profile of our truncated cone tip in different conditions. Figure 4.45 plots, for different tip angles, the evolution of the electric field modulus normalized to  $V_b/d$  along a radial path included into the tip surface (green line shown in the inset b of Figure 4.45). The simulation confirms the maximum field value at the edge of the truncated cone ( $10 \mu\text{m}$  far from the probe axis). The electric field remains rather constant in the blunt zone of the tip (for  $r < 10 \mu\text{m}$ ) with a value lower than  $V_b/d$ . The peak at the edge  $r = 10 \mu\text{m}$  decreases in height as the tip angle increases (inset (a) in Figure 4.45 for more details), as expected. After the overshoot at the edge, the electric field damps very quickly as the evaluation point ascends over the lateral side of the tip. This damping is sharper when the tip angle  $\alpha$  is lower.

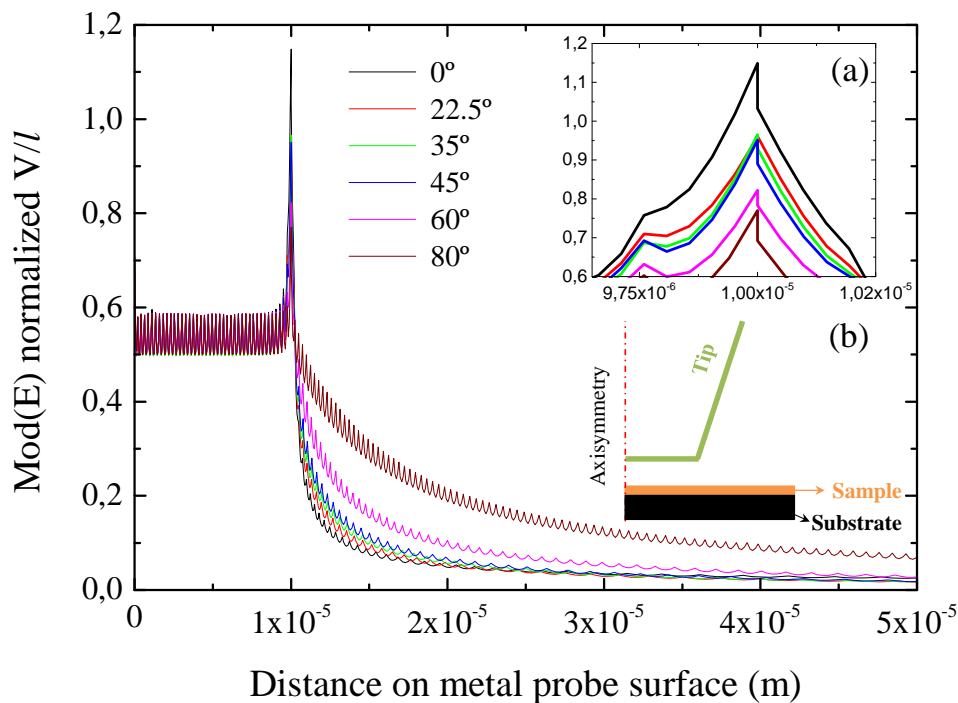


Figure 4.45: Variation of field module normalized to  $V/l$  along a path included into the metal probe surface (green line in the inset), calculated for  $V = -10 \text{ V}$ ,  $l = 1 \mu\text{m}$ , and heavily doped ITO ( $1 \times 10^{25} \text{ m}^{-3}$ ). Curves obtained from  $0^\circ$  to  $80^\circ$  different tip angles.

Numerical simulation may also prove that the field at the blunt zone tends to  $V_b/d$  as  $d$  becomes lower, in agreement with intuition [24]. At the same time, the overshoot of the field just at the edge, normalized to  $V_b/d$ , tends to reduce as  $d$  is lower.

Figure 4.46 illustrates the evolution of the electric field modulus,  $\text{Mod}(E)$ , evaluated at the probe axis ( $r = 0$ ), with the free electron charge of the target layer, for a set of tip-plane separations,  $d$ , from  $0.5$  to  $10 \mu\text{m}$ .  $\text{Mod}(E)$  is normalized to  $V_b/d$ . It is

noticed that from at certain electron density ( $10^{20}$  to  $10^{22}$   $\text{m}^{-3}$ ) there is a fairly steep transition where the electric field is eventually screened inside the conductive layer, and subsequently  $\text{Mod}(E)$  at the tip tends to stabilize at values close to 1. When  $d$  is shortened, this onset shifts to higher carrier density values, because a larger density of free carriers is necessary to screen the field.

Once the free carriers are able to reject the electric field from inside the conductor,  $\text{Mod}(E)$  approaches  $V_b/d$ , although the cone geometry prevents to reach that limit particularly at long distances. In the opposite side, when carrier density is null or very low, the electric equipotential lines extend over a larger volume, penetrating the layer and substrate, as illustrated in Figure 4.43a. Note that a dielectric permittivity  $\epsilon = 9$ , is not sufficiently efficient screening fields. In this situation, we observe a higher dispersion in the values of the normalized  $\text{Mod}(E)$  with distance and doping. This result is mainly due to the normalization of  $\text{Mod}(E)$  to  $V_b/d$ , which obscures the absolute value of the electric field. For lower  $d$ , the absolute value of  $\text{Mod}(E)$  is higher at the tip, but the normalization is performed to a much higher field ( $V_b/d$ ), resulting a lower ratio, as observed.

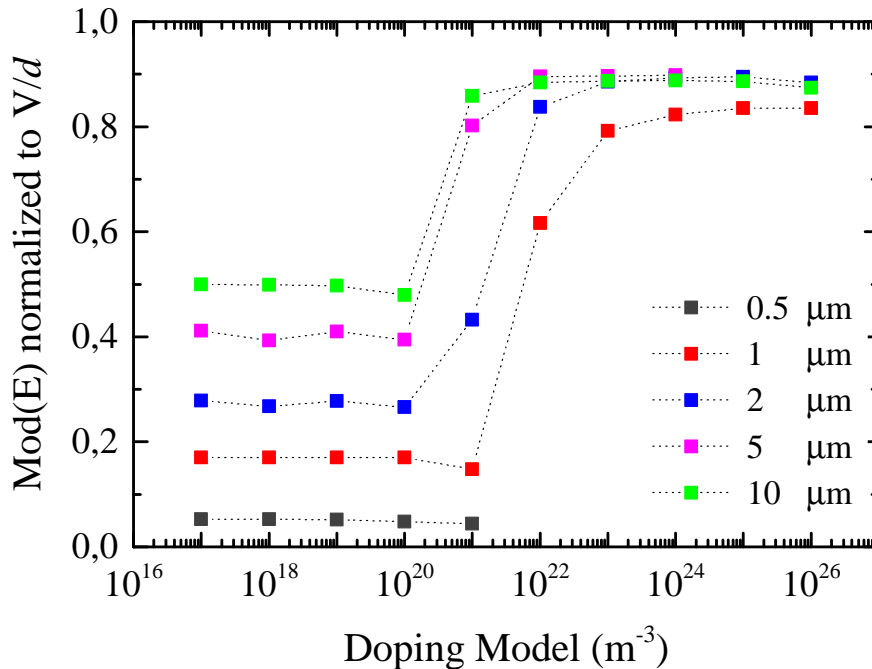


Figure 4.46: Electric field normalized to  $V/l$  at  $r = 0$ , using a  $22.5^\circ$  standard probe and different vertical distances. For low doping, the  $V/l$  law is not fulfilled.

Figure 4.47 shows the evolution of the electric field modulus,  $\text{Mod}(E)$ , normalized to  $V_b/d$  (where  $d = 1 \mu\text{m}$  and  $V_b = -10 \text{ V}$ ) at the tip axis as the free electron density in the ITO is increasing, for a set of tip angles (from  $0^\circ$  to  $80^\circ$ ). At high doping, the saturated value of  $\text{Mod}(E)$  tends to be closer to  $V_b/d$  for larger tip angles ( $\theta = 80^\circ$ ), when the tip tends to resemble a parallel plate geometry.

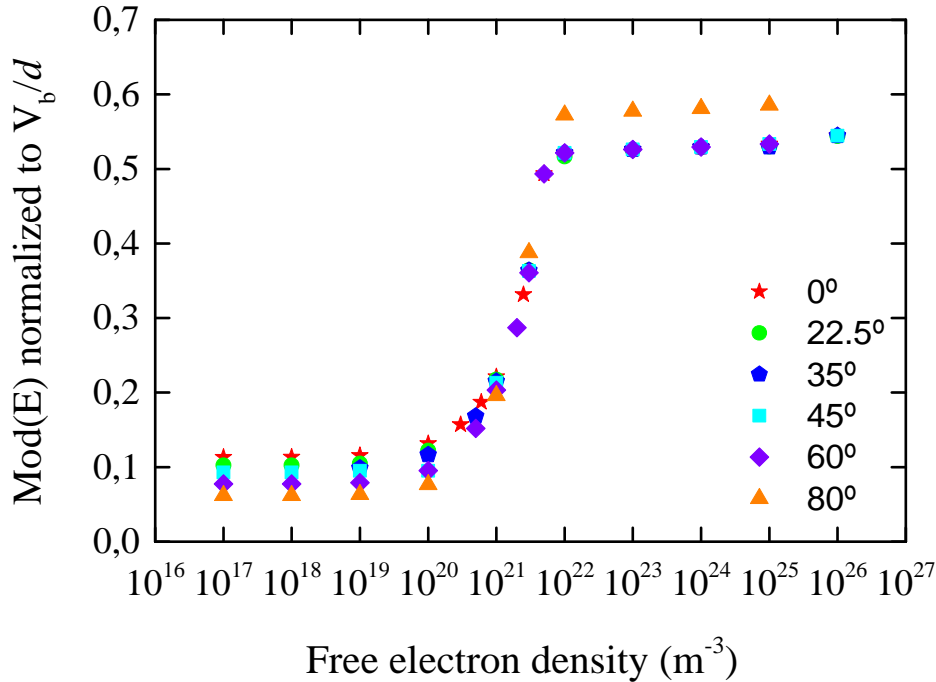


Figure 4.47: Field module shielding plot just below the tip ( $r = 0$ ) for all ITO doping cases at a different value.

#### 4.6.2. Simulation of electrostatic magnitudes in case of contact between tip and sample, for different crater radius and layer thicknesses.

When the tip lands on the conductive layer after a discharge detected by the oscilloscope, it appears surrounded by an insulating dot or crater formed by material removed or degraded. Our geometrical model was then modified in accordance with the new situation. The new geometry is shown in Figure 4.48. In this case, the tip-sample separation is vanished ( $d = 0$ ) so the tip is in contact with the layer, the tip radius ( $r_0$ ) is fixed to  $5 \mu\text{m}$ , and the target layer is decomposed in two different regions: an inner insulating circle of radius  $r'$  (shady region in Figure 4.48), which conserves the same dielectric permittivity, and the outer layer which, for simplicity, is considered a pure metal (surface component of the electric field is null).

It is noticeable that the boundary between both regions forms by itself a new edge, where electric field lines concentrate, and result in an enhancement of the field modulus. This new effect is dependent on the crater radius ( $r'$ ), as well as on the target layer thickness ( $e$ ). Subsequent simulations are directly concerned with both parameters and their influence on the crater expansion.

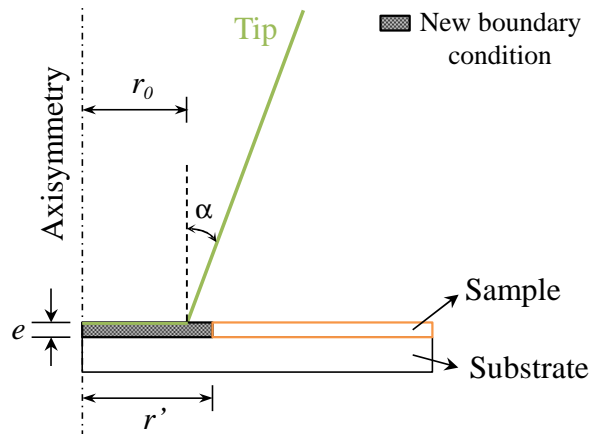


Figure 4.48: COMSOL Multiphysics modelling scheme for the tip-sample contact. Additional variable  $r'$  (crater radius) and a new boundary condition are included for simulation.

An extremely dense finite element mesh is used in order to ensure an optimal degree of accuracy in our simulations. In this case it was not possible to use the *semiconductor module* of COMSOL because of inconveniences in finding a coherent solution, with erratic behavior and subsequent non-convergence. It was then decided to perform all simulations using the *electrostatic module* in order to simplify the model, although we are obliged to work with pure insulators and metals (not semiconductors).

As an example, Figure 4.49 shows final simulated solutions of the system consisting of a tip biased at  $V_b = -15$  V, respect to the outer region of the metallic target layer (grounded). The layer thickness is 100 nm. The tip is in contact with an insulating circle (crater) of  $\epsilon = 9$ , with radius  $r' = 6$   $\mu\text{m}$  (a and b) or radius  $r' = 12$   $\mu\text{m}$  (c and d). These plots display the colored equipotential lines (blue being -15 V and brown 0 V) for both craters (a and c), as well as the electric field vectors just at the surfaces (b and d). The white arrow in a and c marks the edge of the crater. Note the high potential lines concentration at this point. On the right hand plots, red field vectors in c and d are

represented proportionally to their value, giving an idea of how large these electric fields can become.

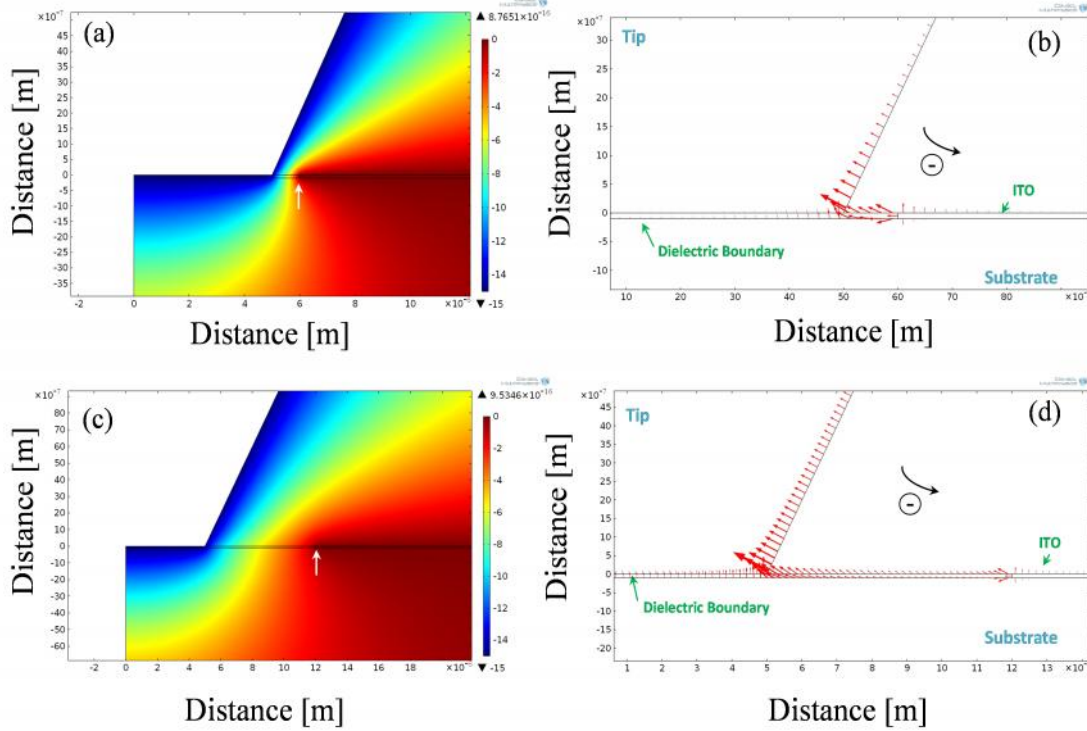


Figure 4.49: Simulation results for a tip of radius  $5 \mu\text{m}$  biased at  $V_b = -15 \text{ V}$ : (a) equipotential colors for  $6 \mu\text{m}$  crater radius and (c) Idem for  $12 \mu\text{m}$  crater radius. Electric field vector plot for: (b)  $6 \mu\text{m}$  crater radius and (d)  $12 \mu\text{m}$  crater radius ( $r'$ ). Black arrows in both plots are the electron ( $e^-$ ) current direction.

Geometrically, the edge of this boundary between the conductive and the insulator zones is much sharper than that of the cone-shaped tip. As we will check, the expected enhancement of the electric field at this edge may so high that it could trigger some of the typical phenomena producing sparks.

The dependence of the electric field modulus at the crater edge,  $|E_{edge}|$ , on the inverse of the crater radius  $r'$  (from  $r' = 6 \mu\text{m}$  to  $r' = 60 \mu\text{m}$ ), is plotted in Figure 4.50. The X axis represents  $1/(r' - r_0)$  in  $\mu\text{m}^{-1}$ , where  $r_0$  is the tip radius. In this case, the electric field values are not normalized but measured in V/m. Each colored curve corresponds to a different thickness of the target layer, from 10 nm to 300 nm. A decrease of the electric field modulus is observed for higher  $r'$  values (towards the left hand side), as expected. A detailed numerical analysis of the dependence of  $|E_{edge}|$  on  $(r' - r_0)$  for the layer thicknesses studied reveals an inverse power law,  $|E_{edge}| \approx (r' - r_0)^{-\gamma}$ , with  $\gamma$  in the range  $\frac{3}{4} < \gamma < 1$ . In this case,  $\gamma$  is close to  $\frac{3}{4}$  for thin layers (10 - 20 nm),

close to 0.85 for thick layers (300 nm) and tends to 1 for even thicker layers. So, for a given thickness  $e$ , we can propose the following law:

$$|E_e| \propto \frac{1}{\left(\frac{r'}{r_0}-1\right)^{\gamma}} \quad (r' > r_0) \quad (4-1)$$

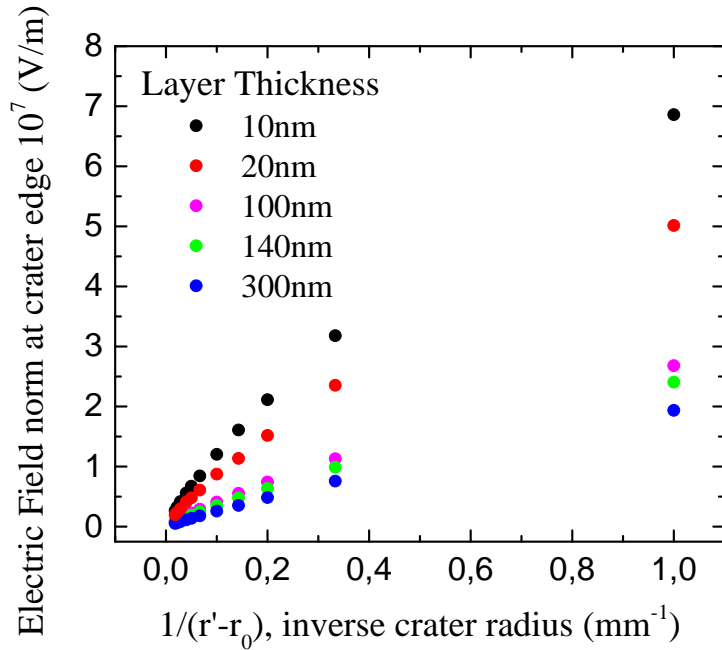


Figure 4.50: Maximum electric field value at the edge of the crater for thickness variations.

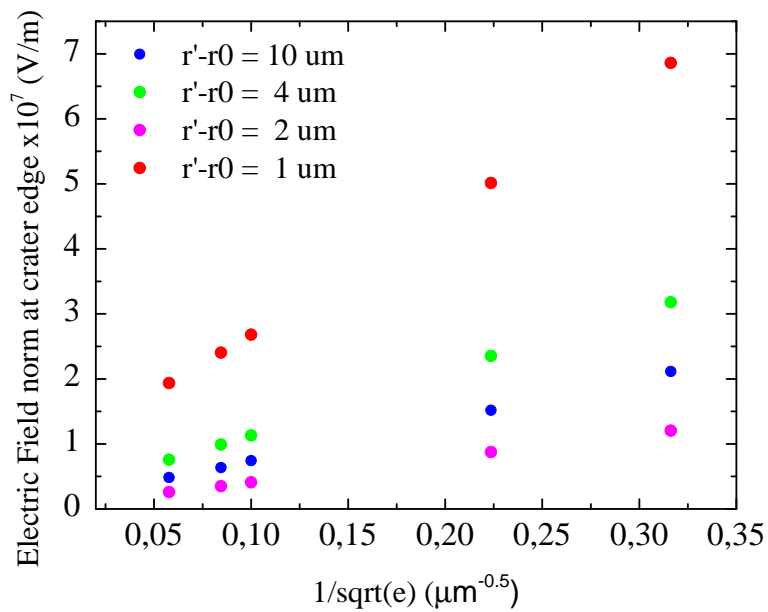


Figure 4.51: Electric field at the crater edge vs  $\frac{1}{\sqrt{e}}$  for different  $(r' - r_0)$  values

On the other hand, fixing a crater radius  $r'$ , we can plot the electric field modulus  $|E_{edge}|$  as a function of the target layer thickness ( $e$ ). Figure 4.51 displays the dependence of  $|E_{edge}|$  on the inverse of the square root of the layer thickness for a set of fixed incremental radius, from  $(r' - r_0) = 1 \mu\text{m}$  to  $(r' - r_0) = 10 \mu\text{m}$ .

For any specific crater radius ( $r'$ ) the plot 4.42 reveals a linear dependence of  $|E_{edge}|$  on the inverse square root of the layer thickness. Notice the non-zero value of  $|E_{edge}|$  for infinite  $e$  thickness (left hand region), which is attributed to a geometrical effect when the ratio of thickness to crater radius,  $e/(r' - r_0)$ , is not very small. This value will be labelled as  $|E_{e \rightarrow \infty}|$  and tends to zero when  $e/(r' - r_0) \approx 0$ . This behavior can be generalized as:

$$|E_e| = |E_{e \rightarrow \infty}| \left( \frac{\varphi(V_0)}{e} + 1 \right) \quad (4-2)$$

Where  $\varphi(V_0)$  is a phenomenological constant measured in  $\text{m}^{1/2}$  and evaluated at a certain operating voltage  $V_0$

On the other hand, as dictated by Maxwell equations, the electric field norm at the edge,  $|E_{edge}|$ , scales linearly with the *nominal value*  $V_b$  of the applied external voltage between tip and layer. Using the previously cited equations (4-1 and 4-2) derived from the experience with simulations, a general phenomenological law for the field norm at the edge of a circular crater,  $|E_{edge}|$ , can be proposed, involving its dependence on the layer thickness ( $e$ ), crater and physical tip radius ( $r'$  and  $r_0$ ) and applied external voltage ( $V_b$ ), as follows:

$$|E_e| = |E_{e \rightarrow \infty}| \left( \frac{\varphi(V_0)}{e} + 1 \right) \frac{(V_b - V_{th})}{V_0 \left( \frac{r'}{r_0} - 1 \right)^\gamma} \quad \text{For } V_b > V_{th} \quad (4-3)$$

$V_0$  is the voltage at which the constants  $|E_{e \rightarrow \infty}|$ ,  $\varphi$  and  $\gamma$  were evaluated by the model.  $V_{th}$  value adjusts the expression to the fact that, below a certain threshold voltage, experiments shown in previous subsections indicate  $r' = r_0$  (no crater expansion) and the shape is just the tip projection. This expression is valid for a system consisting of pure metals (both tip and target layer) and a perfect circular crater. If one solves 4-3 for  $V_b$ , approaching  $\gamma \approx 1$ , we can approach:

$$(V_b - V_{th}) \approx |E_e| \left[ \left( \frac{1.2}{e} + 0.053 \right)^{-1} (r' - r_0) \right] \quad (4-4)$$

Where  $r'$  and  $r_0$  are given in  $\mu\text{m}$ ,  $e$  in nm,  $|E_{edge}|$  in  $10^8$  V/m and  $V_b$  and  $V_{th}$  result in volts.

This empirical law can be used to interpret plots where crater radius generated by sparks are plotted versus the applied voltage, like those in Figure 4.7, Figure 4.16 and Figure 4.29. Among those, the most relevant plots are presented below, in Figure 4.52 and Figure 4.53, where the increment of the crater radius ( $r' - r_0$ ) is plotted versus the applied external voltage,  $V_b$ , for craters performed on ITO and gold, on layers with different thicknesses. Experimentally, a linear dependence of the increment ( $r' - r_0$ ) on  $V_b$  may be approximately observed for a significant voltage range. Dotted lines represent linear fits to these intervals. Linearity of ( $r' - r_0$ ) over  $V_b$  is a very relevant result because, according to expression 4-4, it indicates that  $|E_{edge}|$  likely holds constant along all the experiments, in other words, craters interrupt always at a constant value of  $|E_{edge}|$ . In most cases,  $|E_{edge}|$  results close to  $(3 - 5) \times 10^6$  V/m. Since this value is close or in the order of that for dielectrical breakdown of air, this results suggest that probably the field at the edge plays an important role during the crater expansion.

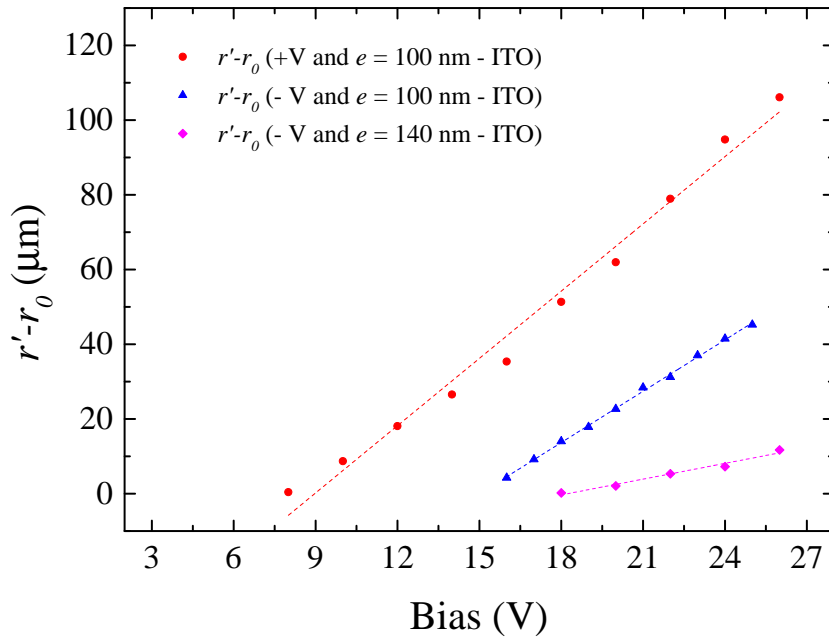


Figure 4.52: Crater radius ( $r' - r_0$ ) plotted versus the external applied voltage for several ITO thicknesses (100 nm and 140 nm), with negative (diamonds and triangles) and positive polarity (red circles). Dotted lines are linear fits to the curves.

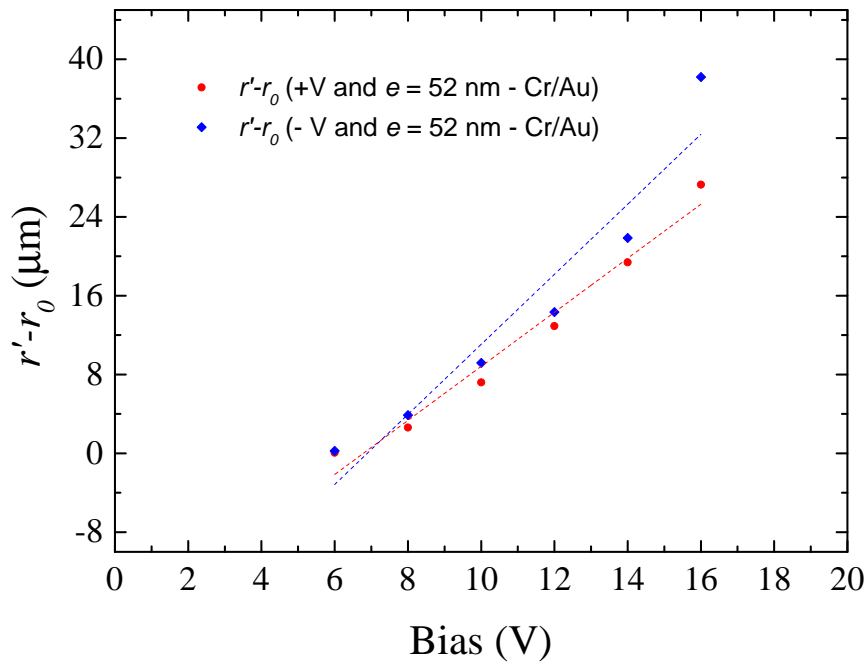


Figure 4.53: Crater radius ( $r'-r_0$ ) plotted versus the external applied voltage for 52 nm thickness Cr/Au sample. Dotted line belongs to the respective linear fit curves.

The slope values extracted from the linear fittings, together with the  $|E_{\text{edge}}|$  derived in each case by equation (4-4) are summarized in Table 4.4. For being so different materials and operating voltages, the dispersion in the  $|E_{\text{edge}}|$  is not that large. It is noticeable that values for the field at the edge of the crater in the moment of its quenching are quite close to that of the dielectric breakdown of air in room conditions.

	ITO 100 nm Polarization +V	ITO 100 nm Polarization -V	ITO 140 nm Polarization -V	Gold 50 nm Polarization +V	Gold 50 nm Polarization +V
( $r' - r_0$ ) vs V slope ( $\mu\text{m}/\text{V}$ )	6,0	4,6	1,4	2,75	3,6
Calculate d " $E_{\text{edge}}$ " $\hat{=} 10^6$ V/m	3,0	3,9	11	8,4	6,4

Table 4.4. Slope values in  $\mu\text{m}/\text{V}$  for the linear fittings in Figures 4.46 and 4.47, together with the  $|E_{\text{edge}}|$  in  $10^6$  V/m units derived in each case by equation (4-4)

In conclusion, with the support of numerical simulations we have been able to propose a phenomenological model to explain the expansion of the crater radius with applied external voltage during a spark process, involving the effect of the layer thickness ( $e$ ), tip radius ( $r_0$ ) and threshold voltage ( $V_{th}$ ). The analysis of the experimental results allows concluding that crater expansion during the erosion process is interrupted at a point where  $|E_{edge}|$  goes down to a certain critical value. This deduction suggests that the in-plane component of the electric field at the crater edge,  $|E_{edge}|$ , plays an important role in the physical process of crater progress. One can imagine that, when crater starts to progress,  $|E_{edge}|$  is sufficiently high to drive the process. Then, as crater radius increases  $|E_{edge}|$  goes down to certain value where it is no more enough to drive the process, and the expansion stops. We find this value is generally very close to that of the dielectric breakdown of air at room conditions.

## 4.7 REFERENCES

- [1] C. García-Núñez, J. Jiménez-Trillo, M. García-Vélez, J. Piqueras, J. Pau, C. Coya and A. Álvarez, “Sub-micron ZnO:N particles fabricated by low voltage electrical discharge lithography on Zn<sub>3</sub>N<sub>2</sub> sputtered films,” *Applied Surface Science*, vol. 285P, pp. 783-788, 2013.
- [2] A. Moezzi, A. McDonagh and M. Cortie, “Zinc oxide particles: Synthesis, properties and applications,” *Chemical Engineering Journal*, Vols. 185-186, pp. 1-22, 2012.
- [3] T.-H. Tsai and Y.-F. Wu, “Wet Etching mechanisms of ITO films in oxalic acid,” *Microelectronic Engineering*, vol. 83, no. 3, pp. 536-541, 2006.
- [4] D.-S. Leem, T. Lee and T.-Y. Seong, “Enhancement of the light output of GaN-based light-emitting diodes with surface-patterned ITO electrodes by maskless wet-etching,” *Solid State Electronics*, vol. 51, no. 5, pp. 793-797, 2007.
- [5] D. Hohnholz, K.-H. Schweikart and M. Hanack, “A simple method for the subdivision of ITO glass substrates,” *Adv Materials*, vol. 11, no. 8, pp. 646-649, 1999.
- [6] E. Jiménez-González, J. Soto Urueta and R. Suárez-Parra, “Optical and electrical characteristics of aluminum-doped ZnO thin films prepared by solgel technique,” *Journal of Crystal Growth*, vol. 192, no. 3-4, pp. 430-438, 1998.
- [7] X. Díez-Betriu, R. Jiménez-Rioboo, J. Sánchez-Marcos, E. Céspedes, A. Espinosa and A. de Andrés, “Amorphous-nanocrystalline Al doped ZnO transparent conducting thin films,” *Journal of Alloys and Compounds*, vol. 536, no. Supplement 1, pp. S445-S449, 2012.
- [8] C. Coya, A. Álvarez, W. Yoon and S. Park, “Influence of the 1, 2, 4-linking hyperbranched poly(arylenevinylene) structure on organic light emitting diode performance as compared to conventional 1,3,5-linking one,” *J. Appl. Phys.*,

- vol. 109, p. 094507, 2011.
- [9] W. Wang, Q. Feng, K. Jiang, J. Huang, X. Zhang, W. Song and R. Tan, “Dependence of Aluminum-doped Zinc Oxide work function on surface cleaning method as studied by ultraviolet and X-ray photoelectron spectroscopies,” *Appl. Surface Science*, vol. 257, pp. 3884-3887, 2011.
- [10] R. Juza and H. Hahn, “Über die Kristallstrukturen von  $Zn_3N_2$ ,  $Cd_3N_2$  und  $Ge_3N_4$ . Metallamide un Metallnitride. IX. Mitteilung,,” *Zeitschrift anorganische und allgemeine*, vol. 244, no. 2, pp. 125-132, 1940.
- [11] K. Kuriyama, Y. Takahashi y F. Sunohara, «Optical band gap of  $Zn_3N_2$  films,» *Phys. Rev. B*, vol. 48, n° 4, pp. 2781-2782, 1993.
- [12] J. Jiménez-Trillo, A. Álvarez, C. Coya, E. Céspedes and A. Espinosa, “The use of arc-erosion as a patterning technique for transparent conductive materials,” *Thin Solid Films*, vol. 520, no. 4, p. 1318, 2011.
- [13] N. Khusayfan and M. El-Nahass, “Study of Structure and Electro-Optical Characteristics of Indium Tin Oxide Thin Films,” *Adv Cond Matter Physics* , p. 408182, 2013.
- [14] F. Chowdhury, S. Chowdhury, F. Hasan and T. Begum, “Optical properties of Undoped and Indium-doped Tin Oxide Thin Films,” *Journal of Bangladesh Academy of Sciences*, vol. 35, no. 11, pp. 99-111, 2011.
- [15] K. Ellmer and R. Mientus, "Carrier transport in polycrystalline transparent conductive oxides: A comparative study of zinc oxide and indium oxide," *Thin Solid Films*, vol. 516, no. 14, p. 4620–4627, 2008.
- [16] P. Slade y E. Taylor, «Electrical breakdown in atmospheric air between closely spaced (0.2  $\mu\text{m}$ -40  $\mu\text{m}$ ) electrical contacts,» *IEEE Transactions onComponents and Packaging Technologies*, vol. 25, n° 3, 2002.
- [17] “Comsol Multiphysics - General Finite Element Analysis Software Suite Description, under license N° 1026943,” [Online]. Available:

- <http://www.comsol.com/products>. [Accessed 2013].
- [18] P. Chabert, A. J. Lichtenberg, M. Lieberman and A. Marakhtanov, "Instabilities in low-pressure electronegative inductive discharges," *Plasma Sources Sci. Technol.*, vol. 10, no. 478, pp. 478-489, 2001.
- [19] P. Persephonis, V. Giannetas, A. Ioannou, J. Parthenios and C. Georgiades, "The time dependent resistance and inductance of the electric discharges in pulsed gas lasers," *IEEE J. Quantum Electron.*, vol. 31, no. 10, pp. 1779-1784, 1995.
- [20] A. Phelps, Z. L. Petrovi and B. Jelenkovi, "Oscillations of low-current electrical discharges between parallel-plane electrodes. III. Models," *Physical Review E*, vol. 47, no. 4, pp. 2825-2838, 1993.
- [21] Y. Akishev, G. Aponin, A. Balakirev, M. Grushin, V. Karalnik, A. Petryakov and N. Trushkin, "DBD surface streamer expansion described using nonlinear diffusion of the electric potential over the barrier," *J. Phys. D: Appl. Phys.*, vol. 46, no. 464014, 2013.
- [22] U. Kogelschatz, B. Eliasson and W. Egli, "Dielectric-Barrier Discharges. Principle and Applications," *J. Phys. IV France*, vol. 7, pp. C4-47 - C4-66, 1997.
- [23] N. Xu, The physical origin of prebreakdown electron 'Pin-Holes', in High voltage insulation, R. Latham, Chapter 4, pp. 115-164, San Diego, CA: Academic, 1995.
- [24] S. Enderling, C. Brown, III, S. Smith, M. Dicks, J. Stevenson, M. Mitkova, M. Kozicki and A. Walton, "Sheet Resistance Measurement of Non-Standard Cleanroom Materials Using Suspended Greek Cross Test Structures," *IEEE Trans. Semicond. Manufact*, vol. 19, no. 1, pp. 2-9, 2006.

## **CHAPTER 5 . ARC-EROSION PATTERNING IN GRAPHENE AND RELATED MATERIALS**

All work related with graphene oxide (GO), reduced graphene oxide (rGO) and graphene layers is discussed in this chapter. Obtaining the adequate patterning conditions is the main objective given the great interest that these materials have been aroused in recent years. The experiments are focused in commercial graphene whose characteristics will be exhibited later on, supplied by graphene Supermarket and Graphenea. The experiments included here can be summarized in two groups: a) experiments associated to obtain well-defined and good quality straight patterns and b) experiments consisting of successive single touches, creating spot arrangements in order to study the involved physical phenomena.

As an added value, graphene oxide and reduced graphene oxide (rGO) patterning tests are included, in order to establish the conditions to obtain well defined patterns also on these strategic materials.

### **5.1 GRAPHENE OXIDE PATTERNING**

In conjunction with Instituto de Ciencia de Materiales de Madrid (ICMM, CSIC), it was possible to work in GO patterning. GO layers are obtained by collaborators at ICMM from aqueous suspensions diluted with ethanol, deposited on glass by a two-stage spin coating procedure, and then annealed at 80 °C for two hours. Thus, very

uniform layers with thickness of about 8 nm [1] were achieved. Long distance groove patterns (straight lines) have been done on this GO samples, varying the arc-erosion conditions: dry (in air at room conditions, 20 °C and RH = 30%) and wet (with mediation of water).

First test done on GO was to depict groove patterns varying the operation voltage from one to the other: 0 V, 25 V, 50 V and 60 V. As in previous cases, polarity is negative (probe negative respect to sample). The processed sample is attached to the Hera XY piezoelectric positioner by a four hook mechanism that fulfils two functions: first, to properly secure the sample avoiding unwanted movements, and second, to work as a four tip electrode contact, equalizing electrical ground on the sample. Dry conditions were used throughout this test. High speed was used for tip vertical motion (10 mm/s) and slow speeds for horizontal movements in both directions (X & Y), in a range of 0.05 to 0.3 mm/s. Tip compression was set on 50  $\mu\text{m}$  for this test.

Figure 5.1 displays arc-erosion grooves performed in dry conditions. For 0 V, the tip just leaves a subtle mark upon the layer surface which is attributed to simple mechanical friction between tip and surface. When voltage is applied, boundaries demarcating the groove boundaries become more evident. There is also some material accumulation at the edges of each groove, increasingly as the voltage increases.

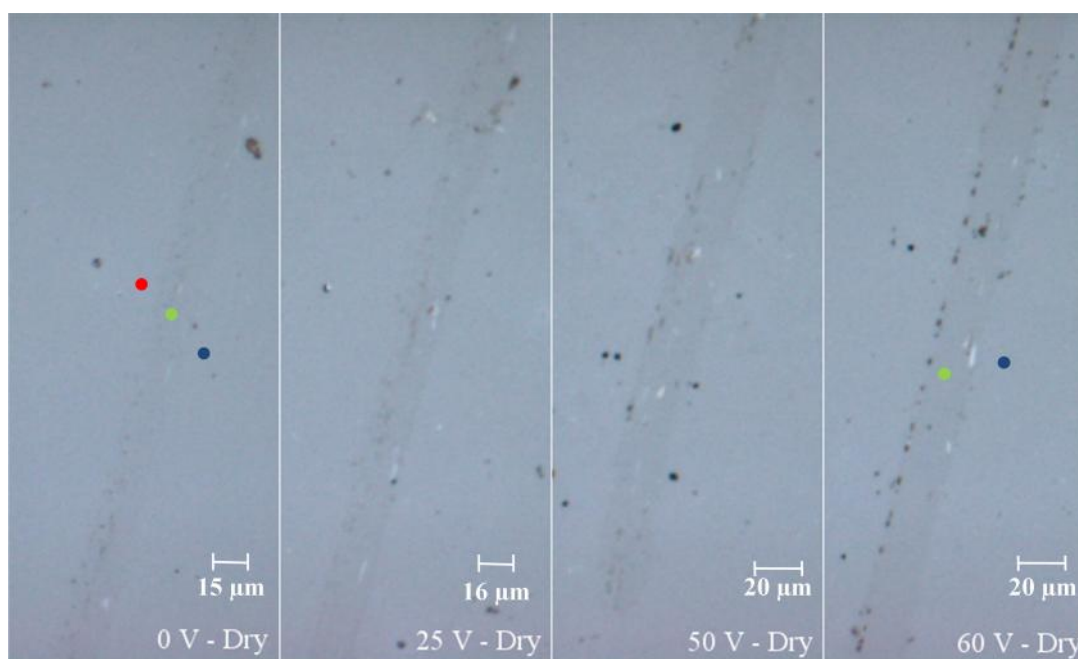


Figure 5.1: graphene oxide dry patterning optical view. Colored dots belong to measured Raman spectra, shown in Figure 5.2.

In Figure 5.2 two plots of Raman spectroscopy are shown in order to verify the removal of GO. In plot (a), Raman spectra recorded in three points of the 0 V groove are displayed, whereas plot (b) shows spectra taken from two points in a 60 V groove. Both grooves were performed in dry conditions. Green lines correspond to spectra recorded inside the grooves, while blue and red lines are from measurements taken outside the groove, where the presence of GO (broadened D and G modes) is clearly evidenced. Raman spectroscopy proves that in the groove performed at 0 V there is still a lot of GO remaining inside, what confirms that this groove originates from a simply mechanical scratching (Figure 5.2a). In contrast, operating at 60 V guarantees that all material has been almost removed (Figure 5.2b), confirming the relevance of the voltage application in order to perform GO lithography.

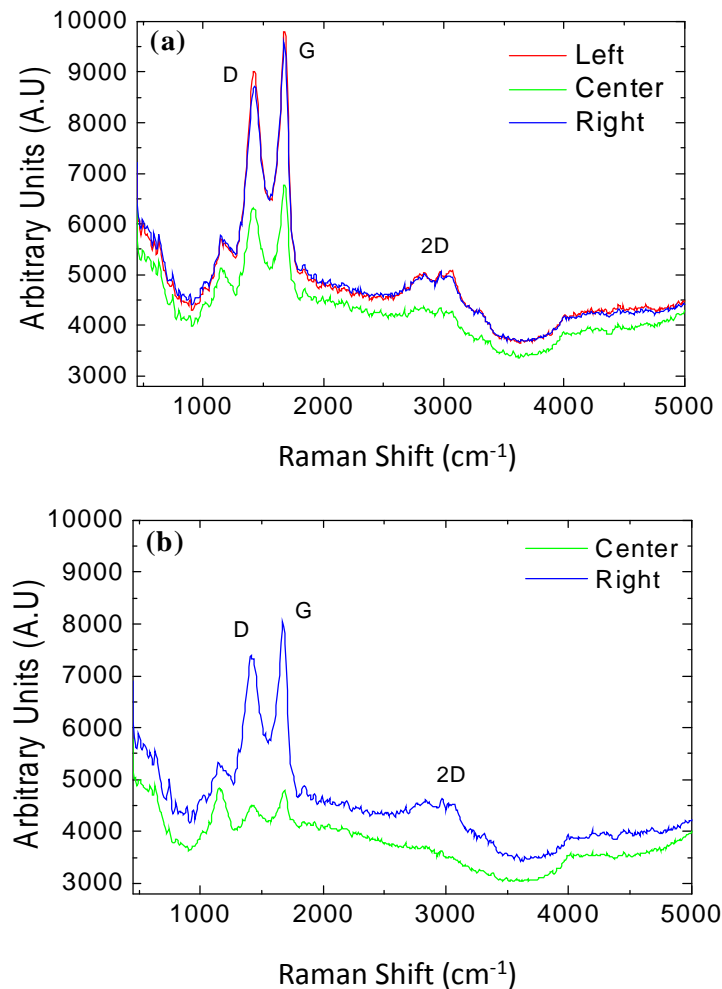


Figure 5.2: Raman Spectrum for (a) 0 V and (b) 60 V processed grooves in dry conditions.

Following trends used in those techniques based on electrochemical discharge micromachining [8] and due to the low electrical conductivity and hardness of GO, next experiment was carried out with the aid of distilled and acidulated water. It was believed that adding a moist environment would help to soften the surface, reduce mechanical friction working as a lubrication mechanism, and also enhance the electrical conductivity of the medium between probe and sample. On the other hand, it is well known that water may act as a catalyst for the interaction of carbon with electrons [3, 4, 5]. The way how this moist was added to the procedure was by solution droplets deposited on the sample surface.

For this purpose, acidulated water solutions were prepared with different acid concentration rates (Hydrochloric Acid ACS reagent 37%, Sigma Aldrich reference 320331): 0.01 ml/ml and 0.03 ml/ml. Free-acid distilled water was also used in the experiment. Straight patterns were performed using the previous voltage range: 0 V, 25 V, 50 V and 60 V, following the scheme shown in Figure 5.3

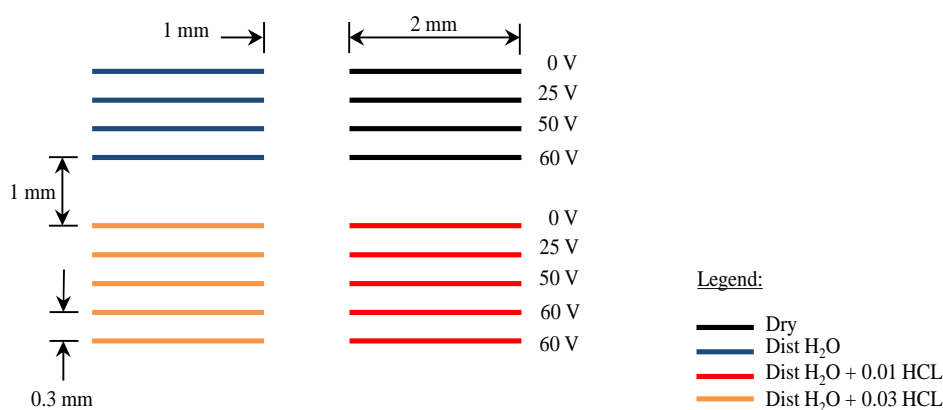


Figure 5.3: Scheme for dry and moist patterning conditions.

The conditions for patterning are the same listed at the beginning of this section. To make this pattern, an algorithm is written containing all the specific routines (speed and acceleration variables, coordinates X, Y and Z) for tip movements. To guarantee the accuracy, all beginning and finishing points were calibrated before. Contingencies such as sample tilt were corrected using this calibration method that consists to determine the height corrections (Z) from a previously pre-set zero. All this gathered height levels are then used to calculate final routine vectors.

All this previous work makes the patterning process easier, allowing the operator to focus only in voltage control. Final patterned grooves are shown in Figure 5.4. Bottom images (at 0.01 ml and 0.03 ml of HCl) have an additional 60 V groove in order to check reproducibility.

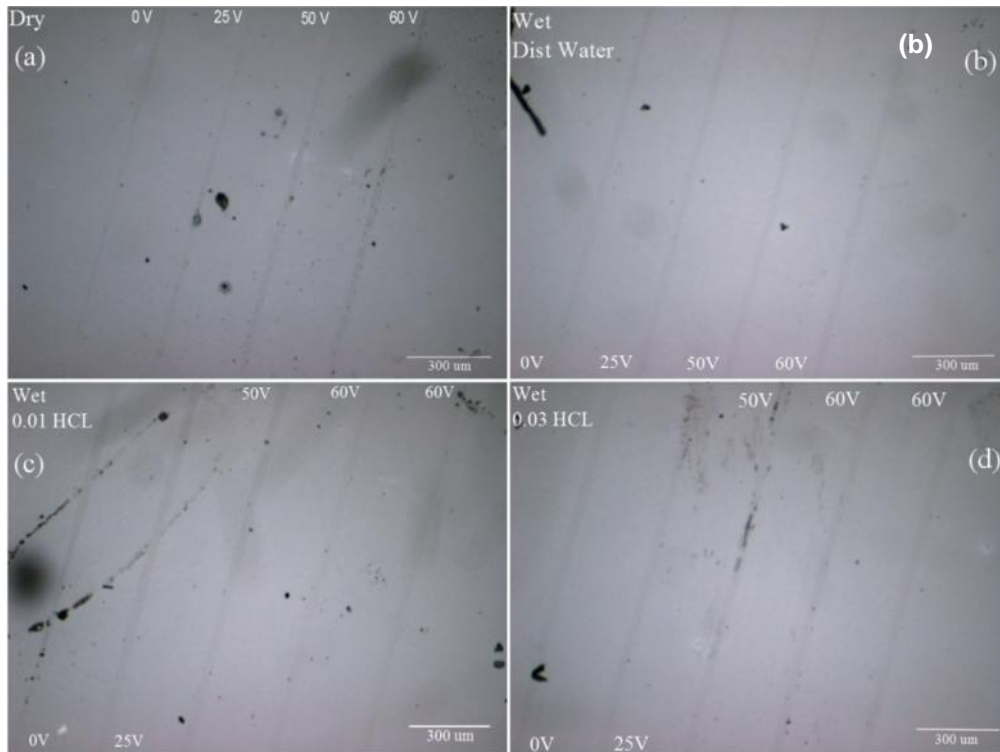


Figure 5.4: Experimental pattern at different moist conditions: a) Dry (no water), b) Distilled water, c) 0.01 ml of HCl d) 0.03 ml of HCl.

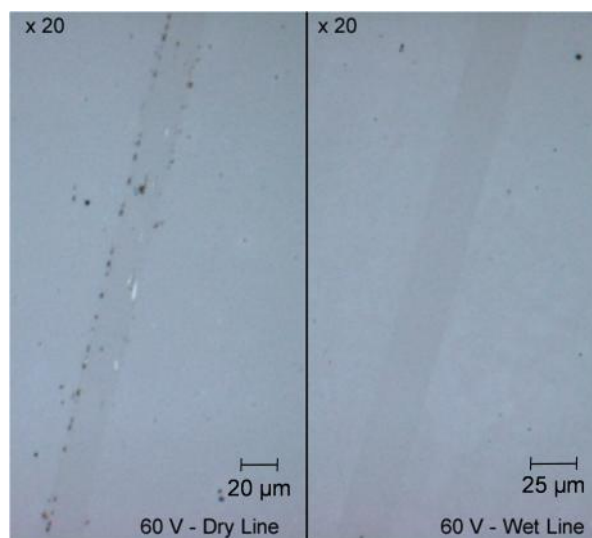


Figure 5.5: 60 V groove comparison at dry and wet (distilled water) conditions.

First comparison is between a groove patterned at dry and wet (distilled water only, no acidic agents) conditions, see a detail in Figure 5.5. Differences between dry and wet processed patterns are clear. At dry conditions, despite the groove is clearly defined and GO removal is almost complete, a fair amount of particles remains at the groove edge, attributed to deposition of residual material from the erosion (notice that GO thickness is 5-8 nm, at least 15 times larger than a single layer) graphene oxide. In moist presence, under the addition of distilled water drops, these particles have disappeared.

Figure 5.6 shows a comparison of patterns processed in the presence of moisture, specifically at the extreme voltage values, namely 0 V and 60 V. (a) shows final grooves achieved using only distilled water drops in the procedure; (b) grooves performed using a 0.01 ml HCl concentration in 1 ml distilled water and (c) increasing to 0.03 ml HCl in 1 ml H<sub>2</sub>O concentration. A common characteristic in all these grooves is the absence of residual particles either inside or at the edge grooves. Also, comparing 60 V grooves for acid concentrations (Figure 5.6b and c) no difference could be established between them.

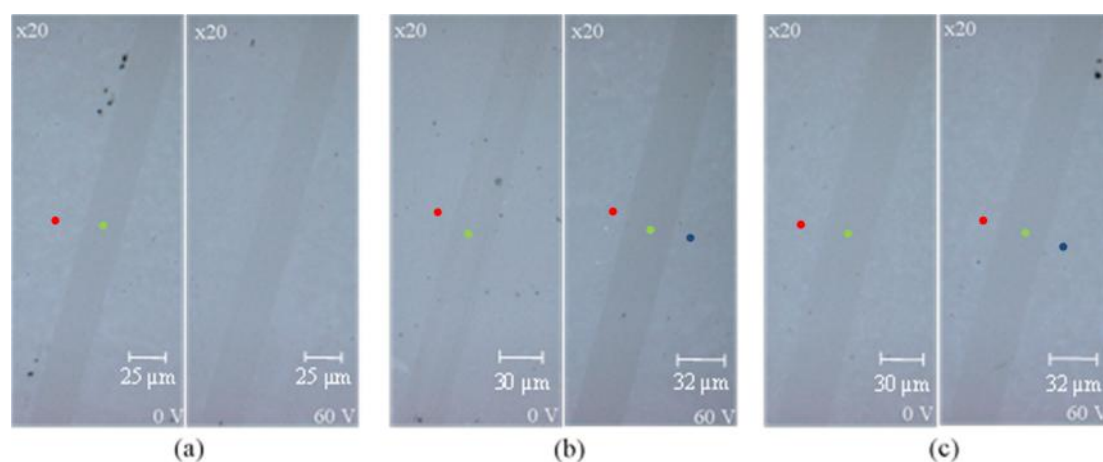


Figure 5.6: Comparison between patterns processed in the presence of moisture: (a) distilled water, (b) distilled water + 0.01 ml HCl per H<sub>2</sub>O ml concentration and (c) distilled water + 0.03 ml HCl concentration per H<sub>2</sub>O ml. The colored dots belong to the measured Raman spectra available in Figure 5.7.

Raman spectroscopy recorded from different points in these patterns reveals that for a 0 V groove (Figure 5.7a) and using distilled water droplets, graphene oxide (GO) is already fully removed; green plot belongs to a measure done inside the groove and red outside it.

The same applies when acid is added to the distilled water, final Raman spectra show the same behavior regardless of the applied voltage. Spectra involved in this experimental phase are shown in Figure 5.7: (b) and (c) are from tests performed using 0.01 ml HCl in 1 ml H<sub>2</sub>O for 0 V, and a 60 V grooves; (d) and (e) to 1 ml distilled water plus 0.03 ml HCl for the same voltages.

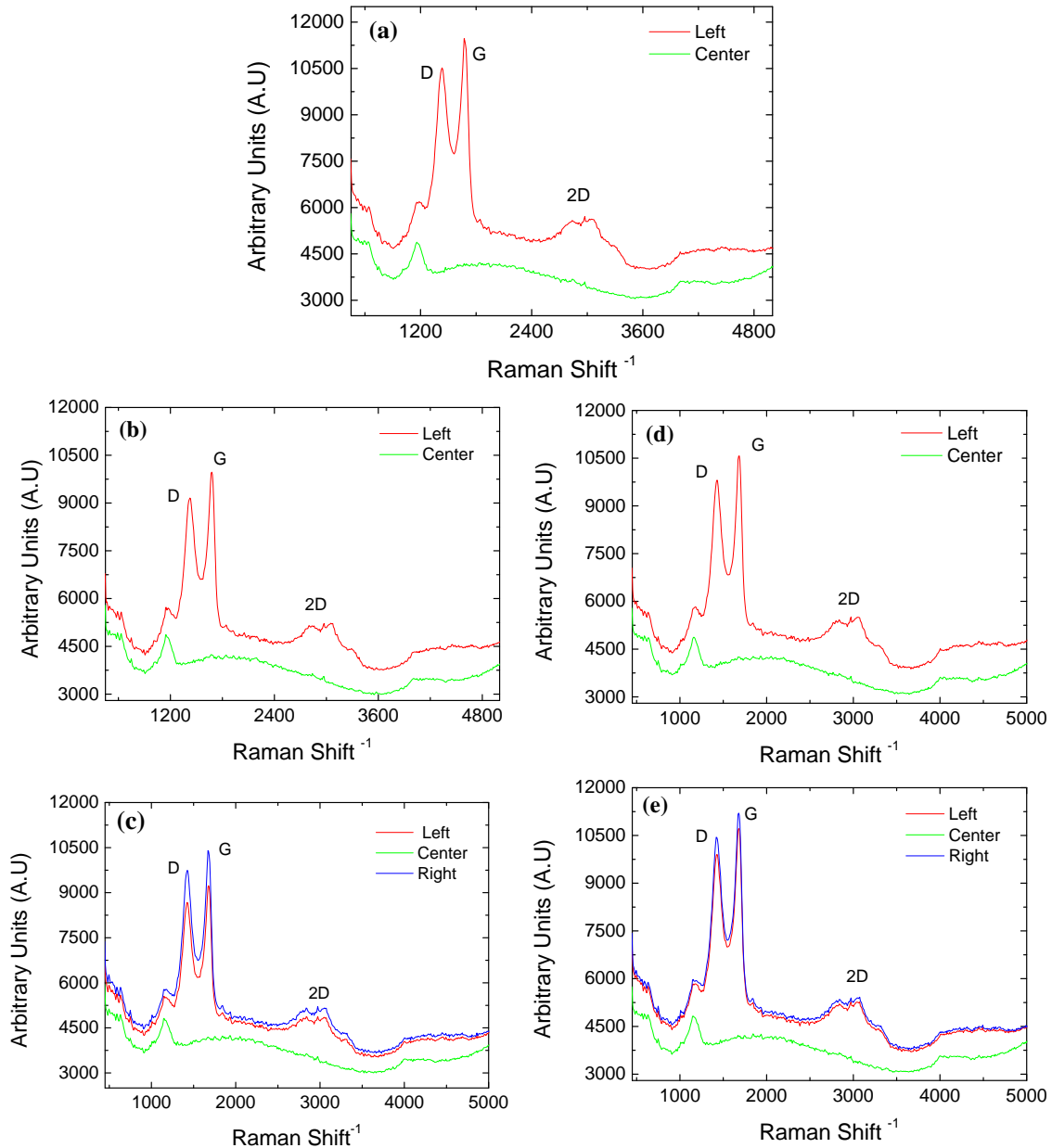


Figure 5.7: Raman Spectrum comparison: (a) Raman spectrum for 0 V groove at wet conditions (distilled water); (b) and (c) grooves processed with distilled water + 0.01 ml HCl at 0 V and 60 V; (d) and (e) finished grooves done with distilled water +0.03 ml HCl at 0 V and 60 V.

In conclusion, grooves have been performed at dry and wet conditions using the following voltage range: 0, -25, -50 and -60 V. First test in dry conditions shows that there is incomplete erosion just by mechanical interaction, without voltage application.

Raman spectroscopy proves that only a small amount of GO is removed by this mechanism. When voltage is applied, groove quality and definition are improved, but the result is not free of waste accumulation at the edges, and also inside the grooves. In dry conditions, the best results are obtained at -60 V, for which almost all material is removed, as evidenced by Raman measurements.

Alternative wet experiments have been carried out to counteract the low electrical conductivity and high stiffness of GO. For this purpose, distilled water with different acidic concentrations has been used. Clear differences can be observed between patterns performed in dry and wet conditions; in fact, all residues within the grooves and at the edges disappear with the water interaction. Besides, GO has been removed completely, according to Raman spectroscopy, for all the voltages used. On the other hand, same results are obtained regardless of the acid concentration, so grooves are excellently defined and have high quality, allowing concluding that the addition of acidulated water on the surface favors etching of the layers regardless the operating voltage. However, since acidulated water ends up reacting with the tip metal, a final recommendation is to use distilled water instead of water with acidic concentrations in order to preserve the tip life time.

## 5.2 REDUCED GRAPHENE OXIDE PATTERNING

Thanks to the collaboration with ICMM-CSIC arc-erosion was also tested on reduced graphene oxide (rGO) samples. The process to obtain these layers is equal to the previously set forth in GO patterning, but adding a second stage to obtain the chemical and thermal reduction. This latter stage consists of immersion in hydrazine monohydrate atmosphere maintaining an 80 °C temperature during 2 hours, and a final 300 °C annealing for 1 hour [1].

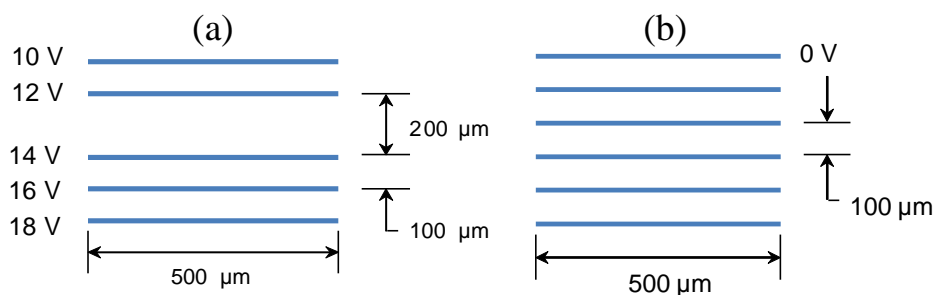


Figure 5.8: Patterning schemes for: (a) rGO arc-erosion and (b) rGO mechanical tests.

In these samples, groove patterns were carried out using a voltage range from 10 V to 18 V with a 2 V increment, following the scheme shown in Figure 5.8a. Also, another six groove pattern was performed with the aim of testing if material is removed mechanically, without applying any voltage, as scheduled in Figure 5.8b.

In terms of processing, speed and acceleration, values are kept constant for both patterning tests: horizontal speed was set at 0.1 mm/s. In relation to the acceleration value, it was set on  $100 \text{ mm/s}^2$ , in order to shorten any motor transient behavior. Patterns were processed with the spring probe previously described in section 3.1.4, with a measured diameter about  $30 \pm 2 \mu\text{m}$ .

Optical inspection of the groove test performed without voltage is shown in Figure 5.9. Six lines were patterned under conditions above described: all lines are identical, and no change is perceived at a glance in terms of width. The patterns confirm a reproducible situation where rGO is significantly removed by mechanical friction, as evidenced by profilometry shown in Figure 5.9.

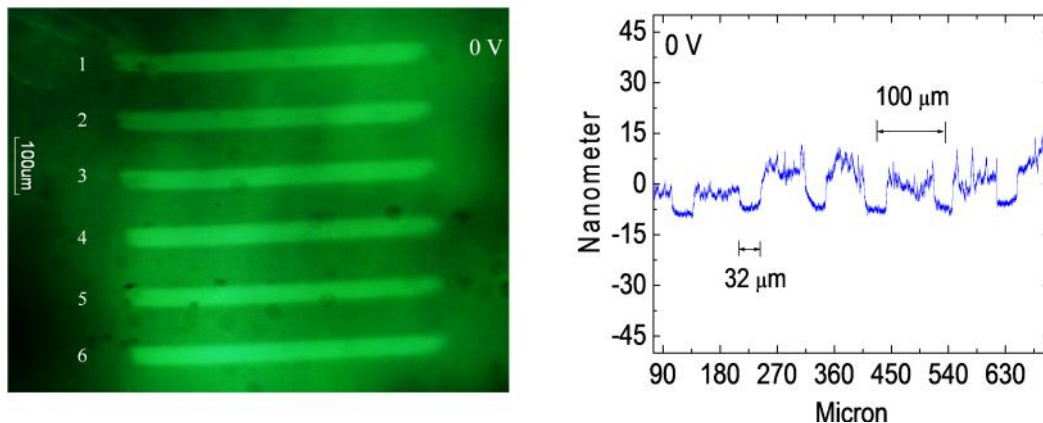


Figure 5.9: Final 0 V patterning (left) and profilometry demonstrating mechanical rGO removal (right).

Final pattern for the test at different voltages is shown in Figure 5.10. It is clearly seen that there are not significant changes, grooves are identical. The width of the grooves remains constant as evidenced by detailed profilometry characterization of each groove, attached below in Figure 5.11.

A negligible dispersion in relation to the width of the grooves is observed, not enough to confirm that there is a significant lateral progress as the voltage increases. The obtained width corresponds to the initial tip diameter measured in the spring probe. On the other hand, the profiles of Figure 5.11 also allow estimating the rGO thickness.

Thickness ranges from 5 nm to 8 nm in all performed patterns, not being possible to establish a more accurate value, due to the material inhomogeneous surface.

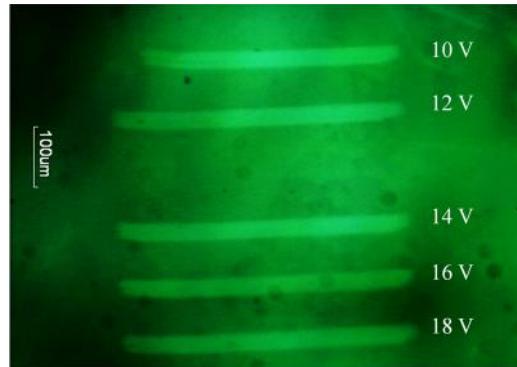


Figure 5.10: Final rGO patterning with applied range voltage (10-18V), with 2 V steps.

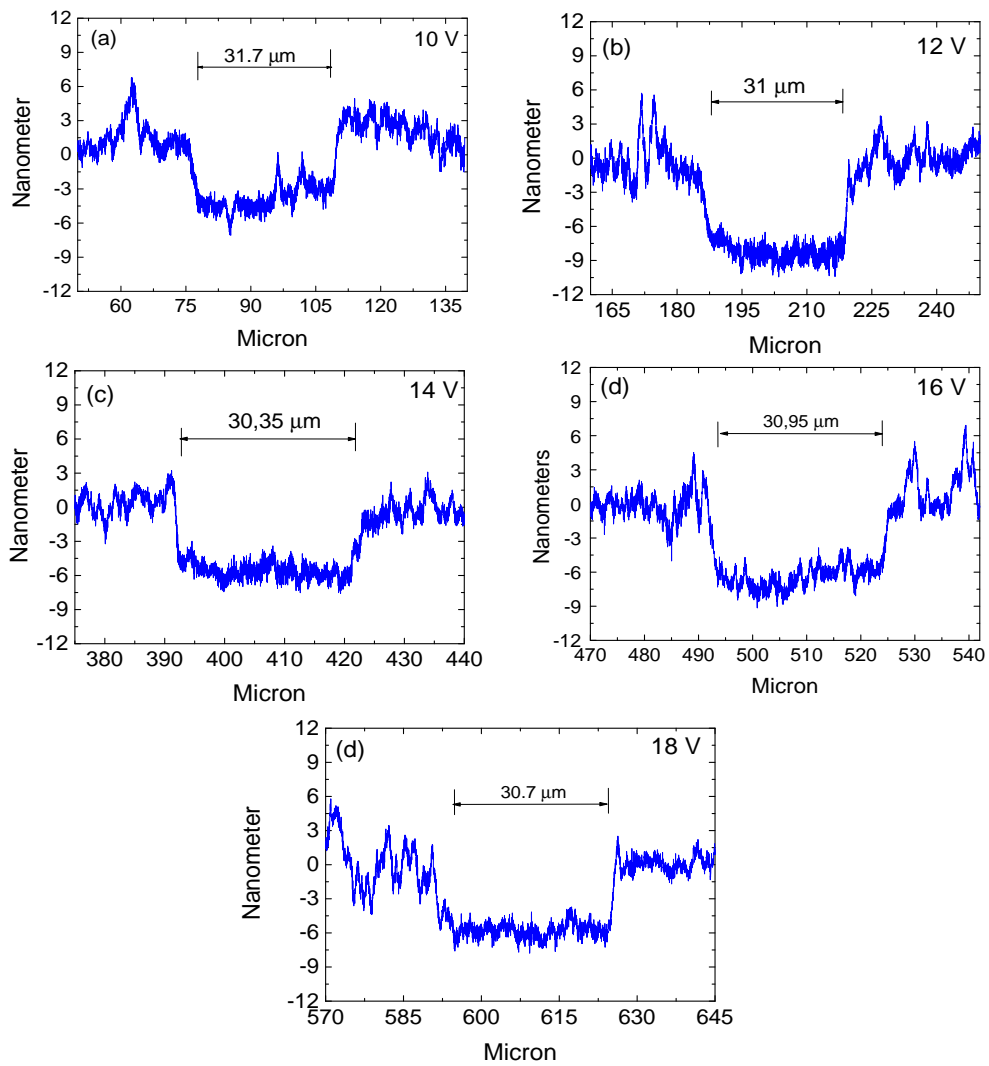


Figure 5.11: Pattern profilometry for rGO applied voltage test: (a) 10 V, (b) 12 V, (c) 14 V, (d) 16 V and (e) 18 V.

Other experiments were designed with the aim to observe and register sparks in rGO samples. For this purpose some dotted patterns were planned, but it was not possible to extract concluding results since rGO did not presented enough conductivity. The high electrical resistance, measured between  $10 \text{ M}\Omega$  and  $12 \text{ M}\Omega$ , did not allow it.

In conclusion, the work related with reduced graphene oxide (rGO) patterning may be summarized as follows: due to the soft consistency of the reduced layers and their insufficient conductance, groove patterning at different voltages from 10 to 20 V resulted in no detectable changes. No significant difference between grooves performed with an applied voltage is observed. The measured width in each groove corresponds to the tip diameter measured at the beginning of the experimentation. There is also no significant lateral progress with increasing voltage. Material removal takes place even at 0 V.

### 5.3 SINGLE-LAYER GRAPHENE PATTERNING

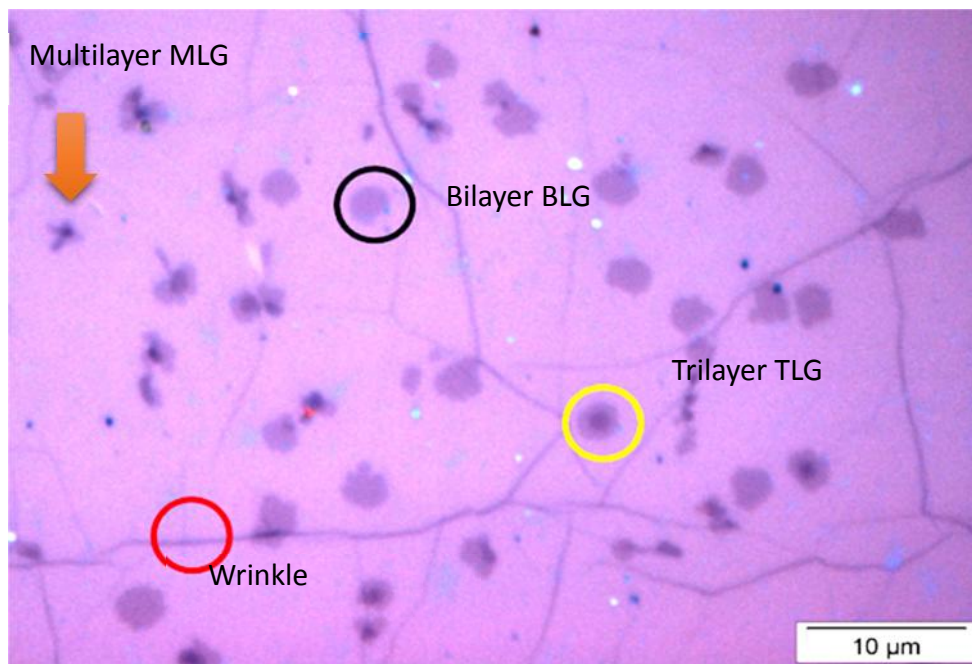


Figure 5.12: Optical image of the as received CVD-grown graphene film transferred onto SiO<sub>2</sub>/Si (90 nm-thick oxide layer) showing wrinkles (red open circle), as well as two-layer (black open circle) and three-layer graphene (yellow open circle) 1-2 μm size regions. Available in support information of [8].

After the experience with graphene-derivatives deposited in solution, in this section patterning of graphene single layers is faced. Commercial single-layer graphene on a SiO<sub>2</sub> (90 nm) / Si: p<sup>+</sup> wafer, as well as on quartz, were used for these tests, purchased directly to Graphenea, and Graphene Supermarket [6] as a 10 sample pack with 1 cm side each one. According to the manufacturer, graphene is grown on copper substrates by Chemical Vapor Deposition (CVD) following Li *et al* method [7]. Final films are predominantly single-layer graphene with 10 - 30% coverage of bilayer graphene islands (with a size of about 2 μm). It is worth noticing that these product samples have occasional holes and wrinkles in its extent, as shown in Figure 5.12, and graphene coverage is about 95%.

Once grown, graphene is transferred by an improved method described by Li *et al* [9] wherein Polymethylmethacrylate (PMMA) has a fundamental role in the transfer procedure. Figure 5.12 shows an optical image of the as received CVD-grown graphene, highlighting aforementioned features.

In the following section, experiments related to the achievement of well-defined, good quality groove patterns are discussed in first place. Next, experiments related to the study of the involved physical phenomena are discussed in depth.

### 5.3.1. Grooves in graphene

In this section, experiments aimed to derive conditions for well-defined and good quality groove patterns are performed and discussed. Aspects related to geometry, spring probe compression and variables such voltage, electrical resistances, axis movements (speed and acceleration) among others will be pooled to show the way how a straight pattern is obtained with optimum characteristics.

Samples were used as received, cleaning them with blown Nitrogen (N<sub>2</sub>) to remove unwanted particles. The sample preparation includes a conductive paint deposit in droplets near to the corners of the sample, far enough from the edges. Once the silver paint has dried the sample is secured onto the HERA XY piezoelectric stage for processing.

The patterning procedure begins with the operating parameters lay down, such acceleration, speed, spring compression and applied DC voltage. For all experiments included in this section, acceleration remains fixed at 100 mm/s<sup>2</sup>, the maximum allowed

by the electrical steppers in our homemade setup. The purpose is to avoid or shorten any slow transient behavior and to guarantee full axis motor synchronization under established conditions. The speed set for all experiments was 0.1-1 mm/s, kept constant through all the procedure.

All the experiments are performed in contact mode, i.e., the tip slides softly on the sample surface. The effects of either the applied pressure with the tip or the bias voltage are studied. In order to test mechanical effects due to the exerted force by the probe on the sample, experiments were performed without any applied voltage (0 V) by varying the spring probe compression. Table 5.1 summarizes the used compression distances, including its equivalence in force and pressure. Although, motor accuracy exceeds the minimum compression distance (0.3  $\mu\text{m}$ ) selected for patterning, this give a safety margin compatible with the tilt calibration procedure mentioned in Appendix A, section A.4.3.

Compression Dist. [ $\mu\text{m}$ ]	Force [mN]	Pressure x $10^6$ [Pa]
0.3	0.09	0.127
0.5	0.150	0.212
1	0.300	0.424
5	1.5	2.12
10	3	4.24
20	6	8.49
100	30	42.4

Table 5.1: Compression distances ( $\mu\text{m}$ ) list, applied force (mN) and pressure (Pa) for a standard tip with a 15  $\mu\text{m}$  radius for groove patterning. Additional data for stronger compressions are given to serve as a reference for the reader.

Optical images are shown in Figure 5.13, for 0.3  $\mu\text{m}$ , 0.5  $\mu\text{m}$  and 1  $\mu\text{m}$  compressing distance. Indicated white dots correspond to the Raman Spectroscopy test points, latter discussed.

No apparent changes were observed for compression distances in the range from 0.3 to 1  $\mu\text{m}$  ( $0.127 \times 10^6 - 0.424 \times 10^6$  Pa). These grooves are easily distinguishable and it is also noticeable that scratching is taking place; grooves have been clearly defined although far from an optimal quality.

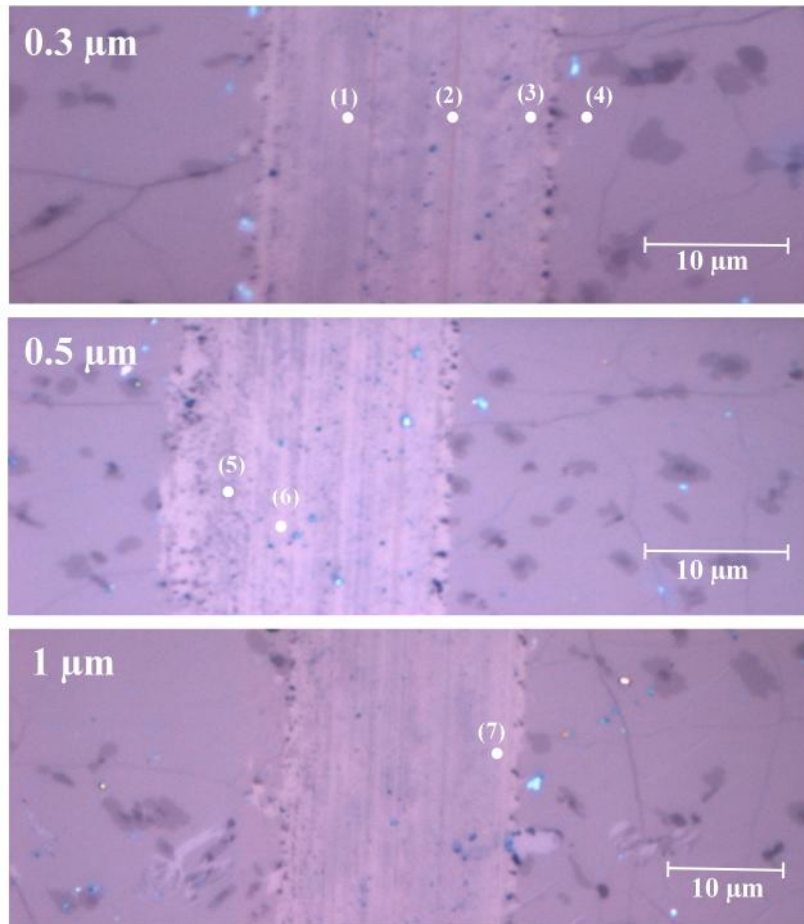


Figure 5.13: Optical images for compression distances: 0.3  $\mu\text{m}$  ( $0.127 \times 10^6$  Pa), 0.5  $\mu\text{m}$  ( $0.212 \times 10^6$  Pa) and 1  $\mu\text{m}$  ( $0.424 \times 10^6$  Pa) at 0 V tests.

Raman Spectroscopy recorded in different points inside the grooves proves that graphene is far from being completely removed. Scratching without applied voltage does not eliminate suitably the graphene layer. Figure 5.14 summarizes the obtained spectra for 0.3  $\mu\text{m}$  ( $0.127 \times 10^6$  Pa), 0.5  $\mu\text{m}$  ( $0.212 \times 10^6$  Pa) and 1  $\mu\text{m}$  ( $0.424 \times 10^6$  Pa) spring compression distances; where (4) is the typical graphene Raman spectrum obtained in a pristine region, for comparison.

Raman measurements within the groove are recorded from points (1), (2) and (3) as shown in Figure 5.13. By comparing with the reference spectrum (4) – pristine zone –, notorious differences can be appreciated (Figure 5.14): First, there is a great increase in peak D, denoting a higher amount of defects. Meanwhile, peak G undergoes significant changes compared with the pristine spectrum (4): its height is reduced in (2) and (3), hinting that some graphene has been removed.

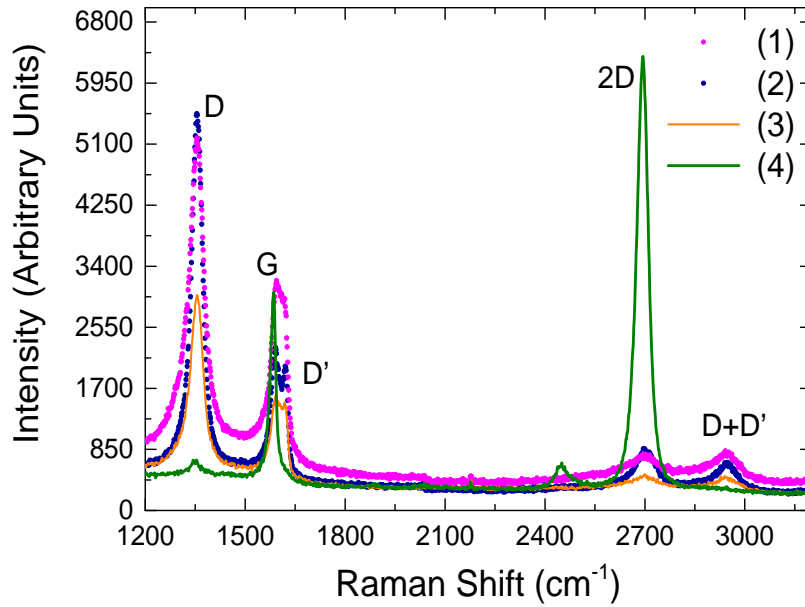


Figure 5.14: Raman Spectroscopy measurements for a  $0.3 \mu\text{m}$  compression distance ( $0.127 \times 10^6 \text{ Pa}$ ).

Furthermore, peak 2D has considerably reduced its intensity to an amount virtually negligible. This peak, as commented in section 3.5.3, is related to the graphene quality (material). A large amount (high intensity) of defects (D mode) means that the layer quality has been reduced considerably.

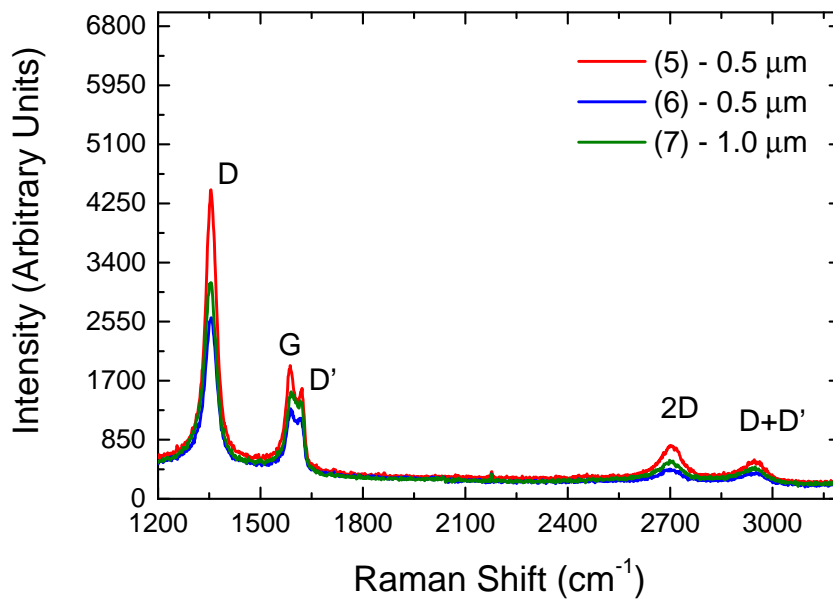


Figure 5.15: Raman Spectroscopy measurements for  $0.5 \mu\text{m}$  ( $0.212 \times 10^6 \text{ Pa}$ ) and  $1 \mu\text{m}$  ( $0.424 \times 10^6 \text{ Pa}$ ) compression distance.

The same situation can be seen for the spectra measured in the grooves with  $0.5\ \mu\text{m}$  ( $0.212 \times 10^6\ \text{Pa}$ ), (labels 5 and 6), and  $1\ \mu\text{m}$  ( $0.424 \times 10^6\ \text{Pa}$ ) (7) spring compression. These Raman spectra are shown in Figure 5.15. In all cases we can conclude that remaining graphene is cracked to a nanoscopic scale.

In order to analyze the influence of voltage, another set of straight patterns was performed at a fixed probe compression distance of  $0.3\ \mu\text{m}$  ( $0.127 \times 10^6\ \text{Pa}$  equivalent pressure), but using an operating voltage from 0 V to 60 V. This pattern consists of seven straight lines with a length of  $250\ \mu\text{m}$  and  $200\ \mu\text{m}$  separation between them. In this case, significant differences can be seen in Figure 5.16, where pictures of the different grooves are shown. The pictures show a clear optical contrast between pristine and eroded regions, this contrast being poorer in the 10 V feature. This result supports optical inspection as an interesting tool to obtain useful and preliminary information on the patterns quality.

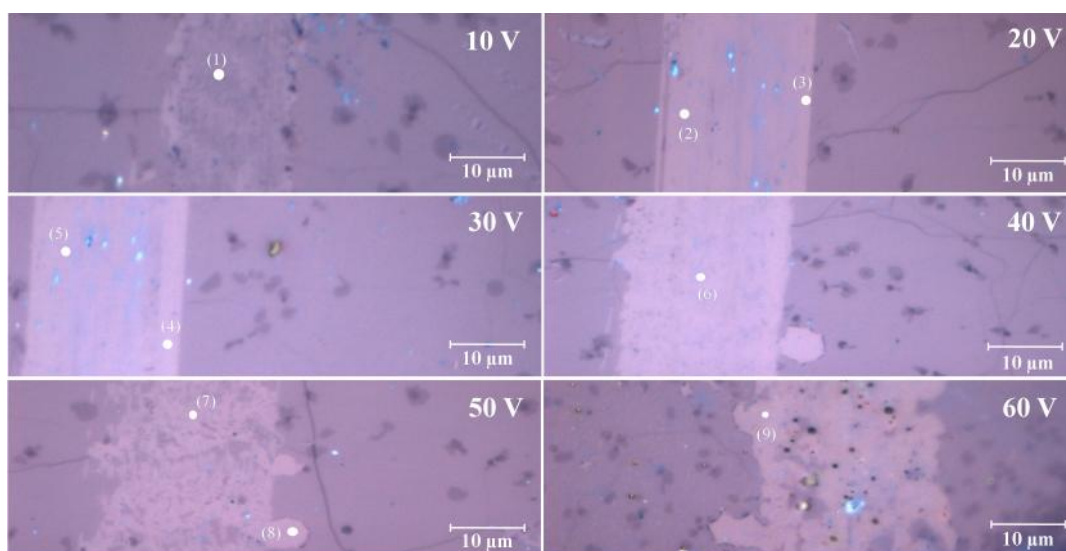


Figure 5.16: graphene straight patterns using a voltage range from 10 to 60 V at  $0.3\ \mu\text{m}$  as tip compression distance ( $0.127 \times 10^6\ \text{Pa}$ ). White dots refer to points where Raman measurements are recorded.

Next, some measured Raman spectra recorded from the white points marked in Figure 5.16, which belong to patterns performed at different voltages range from 10 to 60 V, are shown in Figure 5.17. A pristine graphene spectrum (dotted black line) is also shown for comparison. Raman spectrum (1) confirms, beyond the mere optical inspection, that 10 V is not an adequate bias voltage for arc-erosion, the spectrum being similar to those obtained from patterns at 0 V, previously commented. In contrast, for 20 V, the absence of G mode in Raman spectra (2) and (3) confirms an extensive

graphene removal, so we are able to establish a threshold voltage for this procedure between 10 and 20 V, also supported by the optical images in Figure 5.16.

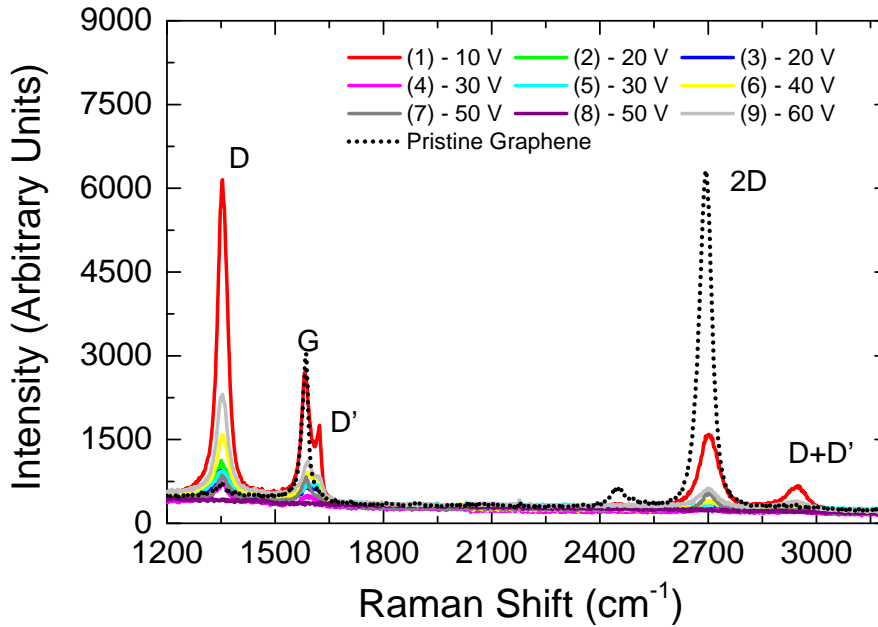


Figure 5.17: Comparison of Raman spectra recorded from points marked in Figure 5.17, which belong to patterns performed at different voltages range from 10 to 60 V.

When 30 V is applied, groove quality is considerably improved and graphene removal is virtually complete; (4) and (5) show fairly very low G peak intensities. Also defects peak (D) demonstrates a low intensity. Line patterning is more irregular when voltage increases even more. From 40 V onwards (till 60 V) the groove appearance shows new features. Groove edge definition and quality worsens. Graphene removal inside the groove may turn to be incomplete again, and lobe-like areas close to the edges are randomly removed, their density increasing with voltage. Possible mechanisms for these features will be discussed later in the text.

More detailed tests were performed increasing the applied force exerted by the probe on the surface: 5  $\mu\text{m}$  ( $2.12 \times 10^6$  Pa) and 10  $\mu\text{m}$  ( $4.24 \times 10^6$  Pa) compression lengths, applying for each case three different operation voltages: 0 V, 10 V and 20 V. Grooves carried out without voltage have been included to verify any apparent change different from that seen in Figure 5.13, discussed above. Pictures resulting from optical inspection of the patterns can be seen below in Figure 5.18.

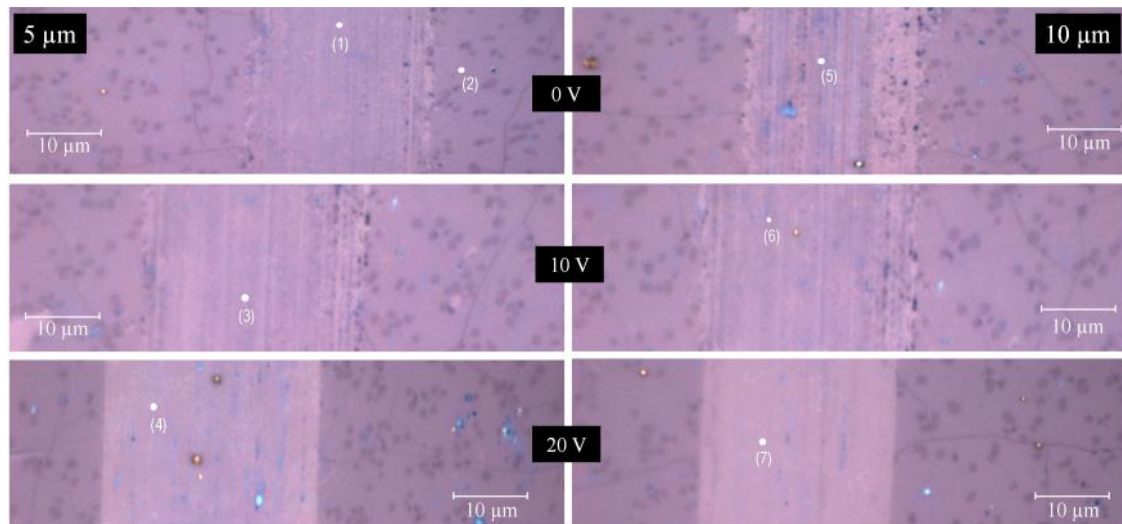


Figure 5.18: Optical comparison of straight patterns performed at 5  $\mu\text{m}$  spring compression ( $2.12 \times 10^6$  Pa), on the left hand side, and at 10  $\mu\text{m}$  compression length ( $4.24 \times 10^6$  Pa) on the right hand side. Three operating voltages 0 V, 10 V and 20 V have been used from up to down respectively. White dots labelled (1) - (7) refer to points where Raman measurements are recorded.

It is again confirmed that the threshold voltage for complete erosion is close to 20 V. It may also be discarded that the increase in the applied force could play a significant role in this process until 3 mN (10  $\mu\text{m}$  compression). In fact, it can be appreciated that there are not apparent differences in grooves when using high spring probe compressions or less applied forces, either in non – voltage tests (Figure 5.13) or at 20 V (Figure 5.16).

Figure 5.19 shows Raman spectra taken from the white dots identified in Figure 5.18. In those points from features eroded at 20 V (spectra labelled 4 and 7), G peak intensity is drastically reduced, indicating a clear graphene removal. By contrast, it is evident that material is not removed entirely with 10 V or 0 V.

Optical images previously displayed together with Raman measurements reveal that voltage plays the most relevant role in the patterning procedure. Non-voltage scratching is in general not enough for graphene removal in the pressure range from 0.127 to  $4.24 \times 10^6$  Pa (0.3 to 10  $\mu\text{m}$  spring compression lengths). For low operating voltages, say between 10 V – 20 V, a successful graphene removal may be accomplished with an adequate combination of scratching and bias voltage, but in the range 20 V – 30 V, scratching may be reduced as much as possible without loss of quality in the erosion.

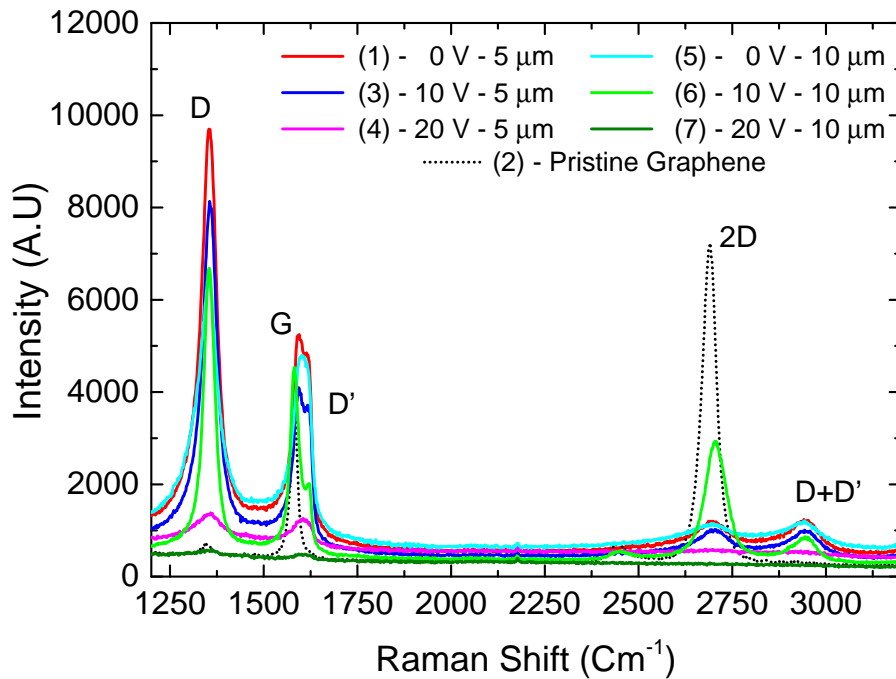


Figure 5.19: Raman spectroscopy comparison for grooves performed from 0 to 20 V at 5  $\mu\text{m}$  ( $2.12 \times 10^6$  Pa) and 10  $\mu\text{m}$  ( $4.24 \times 10^6$  Pa).

Actually, it has been found that low voltage patterns ( $< 20$  V) produce graphene flakes with pristine  $\text{C sp}^2$  structure inside the patterns. Figure 5.20 shows a detailed study of the morphology inside a 0 V groove. In Figure 5.20a, optical pictures of a 0 V groove (above) and a 20 V groove (below) are compared. The optical contrast between pristine and eroded zones appears to be poorer in the 0 V features, as expected. On the right hand, Figure 5.20c shows an optical zoom of a region in the 0 V feature. It can be observed that optical picture shows higher contrast than that of a simple AFM topographic view of the same zone -later on it will be shown that phase mode is more appropriate to get contrast in AFM pictures on these samples-. Raman mapping has been performed to go in depth the morphology of these features (Figure 5.20d). Raman single spectra in Figure 5.20-2b are extracted from those points marked on the right hand side. Raman 2D maps reveal that the intensity of the G peak ( $I_G$ ) in these flakes is maintained close to the value of the pristine single-layer graphene<sup>4</sup>, but peak D attains its maximum value ( $I_D/I_G \sim 3$ ) and the 2D mode falls ( $I_{2D}/I_G \sim 0.5$ ), as shown in single spectra of Figure 5.20b. This situation is maintained through the whole groove as

<sup>4</sup> Graphene pristine layer with the following reference values:  $I_G = 300$  cps,  $I_{2D}/I_G > 2$  and  $I_D/I_G < 0.1$ .

evidenced in the Raman 2D maps (Figure 5.20c) which indicate that it is layer fragmentation rather than graphene removal what we are producing.

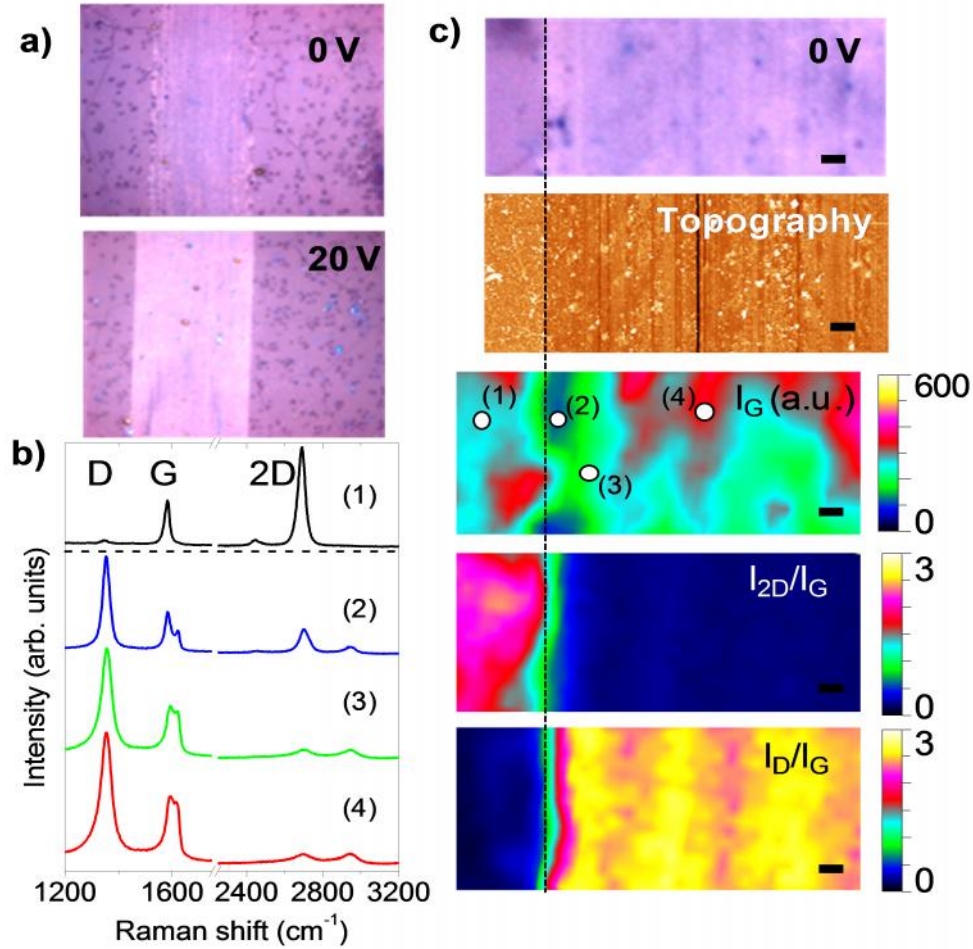


Figure 5.20: (a) Optical picture of a 0 V groove (above) and, for comparison, a 20 V groove (below). (b) Characteristic Raman spectra from the marked points in the Raman two-dimensional maps, at the right side. (c) Zoom details of the optical picture for the groove at 0 V – 0.1 mN. Together with AFM topography of the same region (below). (d) Raman two-dimensional maps of the I<sub>G</sub> mode intensity, as well as I<sub>2D</sub>/I<sub>G</sub> and I<sub>D</sub>/I<sub>G</sub> relative intensities. Black bars correspond to 1 μm. White dots labelled (1) - (4) refer to points where Raman single spectra are displayed at the left hand side.

The nanographene size,  $L_a$ , may be calculated using the expression (5-1), [10]:

$$L_a(n) = \frac{5}{E_l^4} \left( \frac{I_D}{I_G} \right)^{-1} \quad (5-1)$$

Where,  $L_a$  is the nano-graphene size,  $E_l$  is the excitation laser energy used in Raman experiment, quantified in eV [10]  $I_D$  and  $I_G$  are the measured intensities in peak D and G respectively. This equation considers the dependence on the excitation energy and is adequate for graphene size with  $L_a \geq 4$  nm. This equation considers the disorder mainly given by one-dimensional defects, among which are graphene edges and grain boundaries, against other empiric formulae which essentially consider distances

between zero-dimensional point-like defects [11]. In our case, substituting our data in the previous expression, the nanographene size is approximately 7 nm.

Raman 2D maps in grooves performed at 20 V (Figure 5.21b) show a reduced G peak intensity confirming almost complete graphene elimination, as expected (spectra 2 and 3 in Figure 5.21b). The relative  $I_{2D}/I_G$  two dimensional images reveal the groove edge sharpness, within the probe resolution (around 0.7  $\mu\text{m}$ ), also shown in detail in Figure 5.21d. So far, we can verify that high resolution optical images as those shown in Figure 5.20 and Figure 5.21 reveal clearly whether graphene is eliminated or not, and also how the groove edges are totally different by operating with and without applied voltage. These features, as well as imperfect edges and double layers, are properly confirmed by Raman maps.

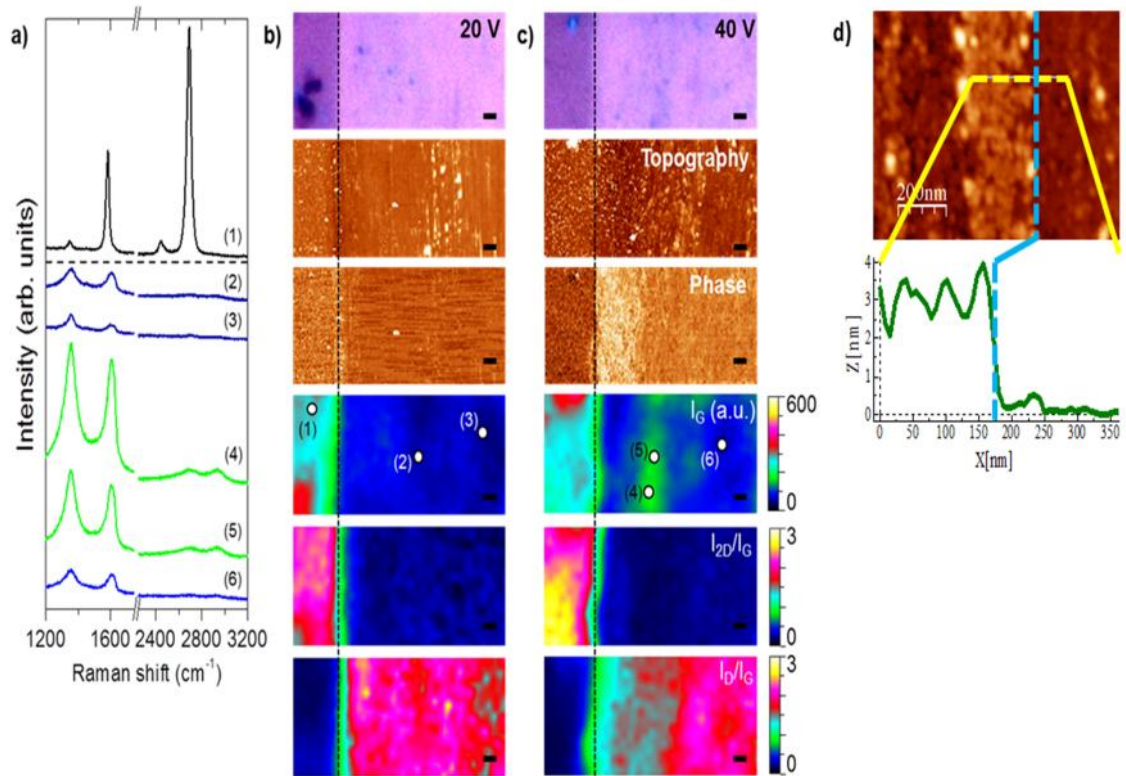


Figure 5.21: Raman spectra from the indicated points on maps at the right hand. (b) and (c) Optical, topography and phase AFM images, together with Raman maps for the  $I_G$ ,  $I_{2D}/I_G$  and  $I_D/I_G$  modes and ratios of the grooves performed at 20 V and 40 V with 0.1 mN in graphene/ $\text{SiO}_2/\text{Si}$ . The scale bar represents 1  $\mu\text{m}$ . The vertical dashed lines indicate the edge of the grooves in (b) and (c). In (a) spectrum 1 corresponds to a pristine layer with the following reference values:  $I_G = 300$  cps,  $I_{2D}/I_G > 2$  and  $I_D/I_G < 0.1$ . (d) Groove edge profilometry.

In our room conditions (20  $^\circ\text{C}$  and 30% RH), for voltages equal or above 40 V, two additional phenomena take place. First, definition of the groove boundaries worsens (Figure 5.20a): lobe-like areas of the graphene layer close to the edge are randomly

eliminated. The density of these lobes or fingers increases for higher voltages, the possible mechanisms will be discussed in a subsequent section. Also, extended regions with different Raman characteristics are formed inside the grooves. In these regions (green zones inside the groove for the  $I_G$  Raman image in Figure 5.21c, graphene is not eliminated and the width of D and G peaks increase significantly. In fact D' peak is not resolved contrary to what is observed in 0 V grooves (spectra # 2-4 in Figure 5.20b) and the 2D peak has almost disappeared. An increase of the width of the peaks, and in particular of D peak, is related to presence of defects inside the nanographene similarly to graphene oxide [12]. The observed spectra match those of typical graphene oxide. At these voltages, it is possible that the residual adsorbed water at the graphene surface may promote the oxidation of graphene instead of its elimination [3]. Alternatively, although less likely, surface of the SiO<sub>2</sub> buffer layer can be modified and also contribute to this phenomenon. In any case, we can conclude that by adequately tuning the bias voltage it is also possible to oxidize the graphene layer, in particular if certain environment conditions such as relative humidity are appropriate. This will be the subject of more experiments in the next subsection.

Next, I will focus on the edge quality. A slight contrast is detected just at the boundary between the groove and pristine graphene in large area AFM topography images (Figure 5.20 and Figure 5.20-3) and has been characterized in detail in Figure 5.20-4. AFM in phase detection mode does reveal much more contrast and seems to be a much more powerful tool for this purpose. Phase contrast is generally ascribed to differences in local energy dissipation and can, e.g. reveal different local mechanical and/or electrical properties [13, 14].

Figure 5.22 shows high resolution AFM images (topographic and phase) of a large scale area in a 0 V - 0.3  $\mu\text{m}$  ( $0.127 \times 10^6$  Pa) compression performed groove. The groove edge can be identified in the overlapped topographic profile where the measured step height yields an average value of approximately 1 nm. Unfortunately the value error is considerably high due to the large surface roughness, especially in the groove area, ascribed to scratches and debris material produced by the fabrication process. The final groove patterning is better identified in the corresponding phase image (Figure 5.22a), due to an enhanced contrast measured at the edges.

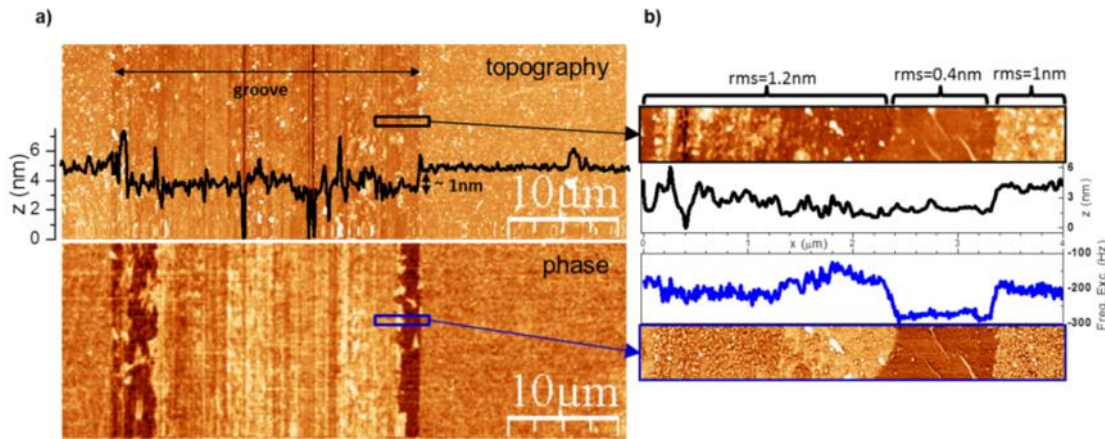


Figure 5.22: (a) Simultaneous topographic (top) and phase (bottom) images of the groove patterned with  $0.3 \mu\text{m}$  compression distance ( $0.127 \times 10^6 \text{ Pa}$ ) at  $0 \text{ V}$ . The inset in the topographic image is the average height profile along the groove. (b) High resolution topographic (top) and phase (bottom) images at the groove boundaries with their corresponding average profiles (middle). The darkest area in phase image matches with a smoother graphene layer observed at the groove edge (see text).

For the understanding the origin of this contrast observed in AFM phase images, smaller areas were scanned at high resolution close to the edge of the groove in Figure 5.22b, and compared to areas of pristine graphene Figure 5.22. The overall roughness of the as-received graphene is influenced by the PMMA transfer process residues ( $\sim 2 \text{ nm}$  height). Graphene wrinkles are also observed (bright contrast in Figure 5.22,  $\sim 6 \text{ nm}$  height). On the other hand, from the simultaneous topographic and phase images, and their corresponding average profiles shown in Figure 5.22, it is clear that the observed darkest phase contrast at the edge corresponds with a topographic smoother area. Although presenting the typical wrinkles of a graphene layer, it exhibits a considerably lower rms value compared with the pristine graphene beyond the groove limits ( $0.4 \text{ nm}$  vs  $1 \text{ nm}$  for  $0.75 \mu\text{m}^2$  areas). It is remarkable that the reported graphene – substrate distance by AFM, either in CVD transferred graphene or in mechanically exfoliated graphene (scotch tape method) is around  $1 \text{ nm}$ . So the measured heights of the grooves (between  $1$  and  $1.9 \text{ nm}$ , see Table 5.2 ) are consistent with these characteristics.

At the boundaries, the contact pressure applied by the tip might be enough to remove those residues which are observed on the as-received graphene surface (Figure 5.23), but still low to a complete graphene layer removal, thus leaving a cleaner and smoother graphene stripe along the edges. A similar effect was reported in friction tests performed on graphene/SiO<sub>2</sub>/Si with a microtribometer [15]. The differences in energy dissipation (due to different hydrophilicity, viscosity, mechanical properties...) between as-received graphene (with adsorbates) and clean graphene are likely the reason for this

contrast emphasized in the phase images of Figure 5.22. On the other hand, the electrical properties inherent to the sharp edges, where field force lines accumulate, could also contribute in some way to this contrast.

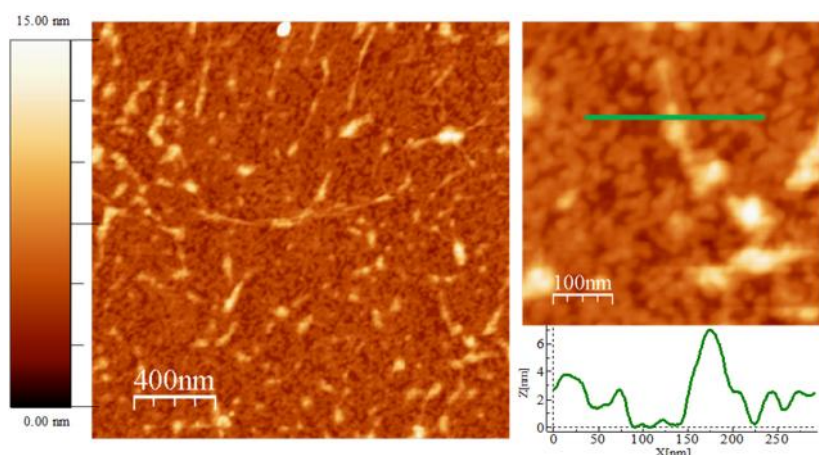


Figure 5.23: AFM topographic image of the pristine CVD-grown graphene film transferred onto SiO<sub>2</sub>/Si. The height profile corresponds to the highlighted line in AFM image. The overall roughness of the as-received graphene is dominated by the PMMA transfer process residues (~ 2 nm in height). Graphene wrinkles are also observed (~ 6 nm in height).

Parameters		Groove depth	rms	
Force	voltage		as-received graphene	groove
0.1 mN	0V	1nm	1.7nm (1 nm)	1.2nm
0.33 mN	0V	1.5nm	1.7nm (1.1 nm)	0.8nm
0.33 mN	20V	1.9nm	1.5nm (1.2 nm)	0.5nm
0.33 mN	30V	1.5nm	1.4nm (0.9 nm)	0.7nm
0.33 mN	40V	1.9nm	1.9nm (1.3 nm)	0.5nm

Table 5.2: Parameters of the morphological characterization (depth and rms values for different areas) derived from AFM images of the grooves patterned under different conditions of bias voltage and applied force. In parenthesis the rms values of the images after filtering the PMMA residues and graphene wrinkles. Available in supporting information of [9].

In Figure 5.24a and Figure 5.24c, 0 V and 30 V grooves AFM topography images, obtained with  $0.424 \times 10^6$  Pa applied pressure (1  $\mu\text{m}$  compression) are presented together. The profiles evidence differences in the sharpness of the edges with and without applied voltage. The edges are clear and sharp when voltage is applied, what is of great relevance for technological applications.

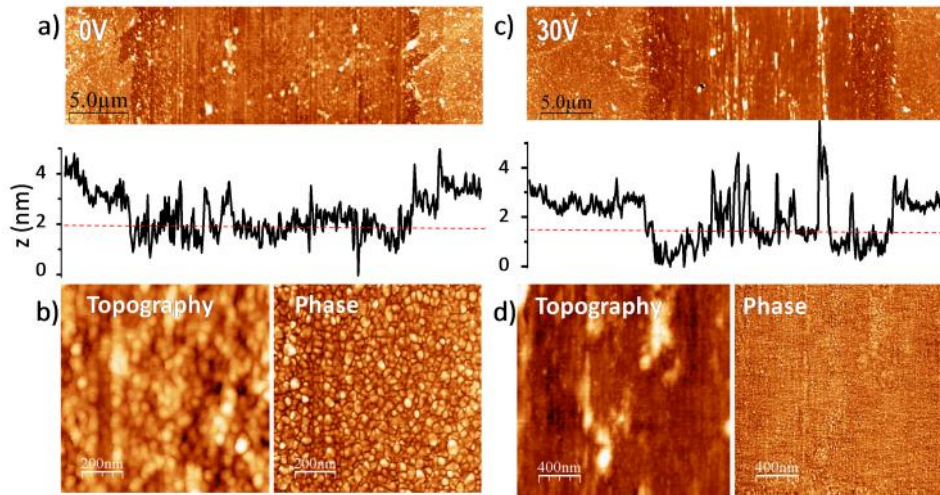


Figure 5.24: Topographic AFM images and average height profile along the groove patterned with a tip compression of  $1\ \mu\text{m}$  ( $0.424 \times 10^6\ \text{Pa}$ ) and 0V (a) and 30V (b); 0V (c) and 30V (d), high resolution topography and phase images within grooves.

In Figure 5.24b and Figure 5.24d, higher resolution AFM images of areas well inside of grooves at 0 V and 30 V are shown. Inside the grooves patterned with an applied voltage, the topography is visibly different and its roughness is reduced down to 0.5-0.7 nm when looking at small areas. The roughness of the 0 V grooves is larger (around 1 nm), of granular appearance, and particles of diameters in the range of 20-50 nm and 1-2 nm height can be identified. These features are especially well resolved in the phase image (Figure 5.24b). This is consistent with nanographene with average size of 7 nm detected by Raman mapping, taking into account that the lateral resolution in AFM is limited by the tip diameter (around 20-30 nm). As was previously stated, these particles are not seen in the grooves performed with applied voltage (Figure 5.24d) and Raman images indicate that, in this case, graphene has been almost completely eliminated. Other features with 5-8 nm height (bright areas in the images) are related to accumulation of debris material. Moreover, Figure 5.24b shows that the profile of the groove is deeper (around 1 nm) at the edges than at the central parts. Therefore, it is speculated that, at groove edges, where the electric fields around the tip are maximum, the  $\text{SiO}_2$  layer is slightly eroded and ejected producing the clusters inside the groove.

According to the previous discussion, attending to the edge quality as well as graphene removal efficiency within a groove, the optimum voltage range for graphene patterning is considered to fall within 20 to 30 V. In these conditions, as a matter of proof, a set of graphene micro-ribbons,  $1\ \mu\text{m}$  wide and up to 1.2 millimeter long, separated by stripes or removed material  $11\ \mu\text{m}$  wide, has been patterned. The diameter

of the tip was accurately measured resulting  $11\ \mu\text{m}$ , so the stepper displacement was arranged to obtain such high aspect ratio of about 1200:1. Final results can be observed in Figure 5.25.

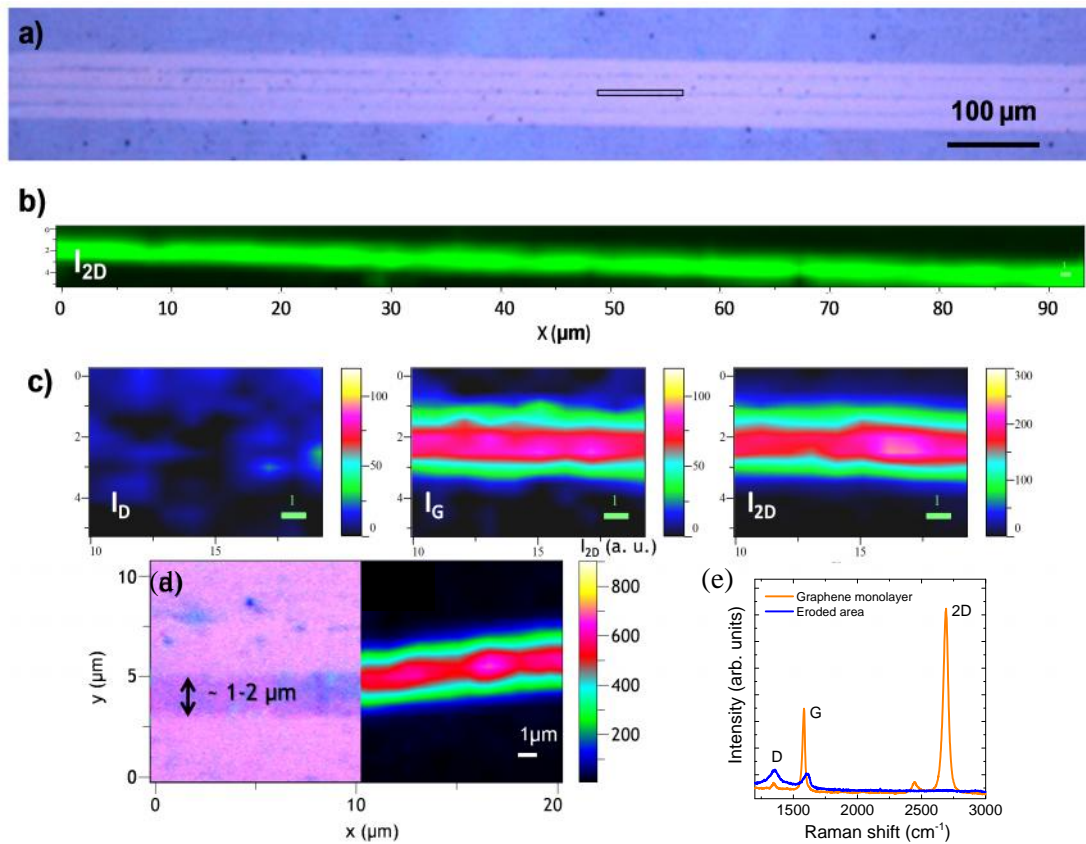


Figure 5.25: (a) Optical image of graphene micro-ribbons ( $1\ \mu\text{m} \times 1200\ \mu\text{m}$ , separated by  $11\ \mu\text{m}$ ), and (b)  $I_{2D}$  Raman image corresponding to the rectangular marked area,  $5 \times 95\ \mu\text{m}^2$ , in (a). (c) Details of the  $I_D$ ,  $I_G$  and  $I_{2D}$  Raman images in a  $5 \times 10\ \mu\text{m}^2$  area. The green bar corresponds to  $1\ \mu\text{m}$ . (d) Magnified optical image of a micro-ribbon, together with the corresponding  $I_{2D}$  Raman map. (e) Raman spectra recorded inside and outside the graphene ribbon.

A zoom corresponding to the marked rectangle ( $5 \times 95\ \mu\text{m}^2$ ), shows details of a micro-ribbon  $1-2\ \mu\text{m}$  wide. The intensity of the 2D peak along the ribbon, which is the most sensitive feature to characterize the graphene quality, corresponds exactly to that of pristine single-layer CVD graphene on  $\text{SiO}_2/\text{Si}$  (Figure 5.265b). Details of the  $I_D$ ,  $I_G$  and  $I_{2D}$  Raman maps in  $5 \times 10\ \mu\text{m}^2$  areas are observed in Figure 5.265c. Note that the resolution of Raman images is lower than the theoretical diffraction-limited spatial resolution achievable using an optical microscope and is estimated to be around  $0.7\ \mu\text{m}$ . A magnified optical image of a micro-ribbon segment, together with the corresponding  $I_{2D}$  Raman map are shown in Figure 5.265d. Figure 5.265e shows an example of Raman spectra recorded in points from the inner and outer regions of the micro-ribbon. The spectrum inside the ribbon corresponds to that of pristine single-layer CVD graphene on

SiO<sub>2</sub>/Si, confirming the quality of the graphene, as well as its absence beyond the ribbon

In conclusion, conditions for an optimum graphene patterning in terms of edge quality, material removal and minimization of residues have been derived from a set of tests. Using our direct approach, one can in principle form graphene patterns and micro-ribbons of any arbitrary size and geometry, with a resolution and quality limited by the probe diameter and roughness, as well as by precision of the steppers motion.

The versatility and precision of this technique has allowed obtaining an array of graphene micro-ribbons with an excellent aspect ratio ( $1\ \mu\text{m} \times 1200\ \mu\text{m}$ ), which is very promising for terahertz plasmonic applications [16]. It allows for a feasible methodology towards a better integration with semiconductor materials for interconnect electronics and scalable production of graphene based electronic and optoelectronic applications where the electrical gating is the key enabling factor.

### 5.3.2. Spots or craters in graphene

In this subsection, experiments related to single electrical discharges on localized regions just below the tip are faced in order to analyze more in depth the physical mechanisms governing the electrical erosion process. In practice, the electrical discharge is produced during vertical approach of the probe to the surface, presumably just before the mechanical touch. Since these discharges are transient phenomena involving a wide range of currents depending on the measurement configuration, I will adopt the general term *spark* when speaking about the brief short-circuit of the tip-to-plane capacitor, detected by oscilloscope as a short electrical trace (typically  $< 2\ \mu\text{s}$ ) during the approach of the probe to the graphene.

The spring probe damps the contact of the probe after landing on the surface and minimizes mechanical damage. Unlike the experiments involving tip dragging, when contacting only in vertical direction, defects due to erosion appear to be negligible for spring compressions  $< 1\ \mu\text{m}$  at 0 V.

The experiments are performed in successive ‘touches’, creating spot arrangements in which different operating parameters are changed. This pattern type avoids scratching effects and allows a better assessment for the involved mechanism in

graphene patterning. A particular geometry recorded on G/SiO<sub>2</sub> (90 nm)/Si: p<sup>+</sup> is displayed in Figure 5.26.

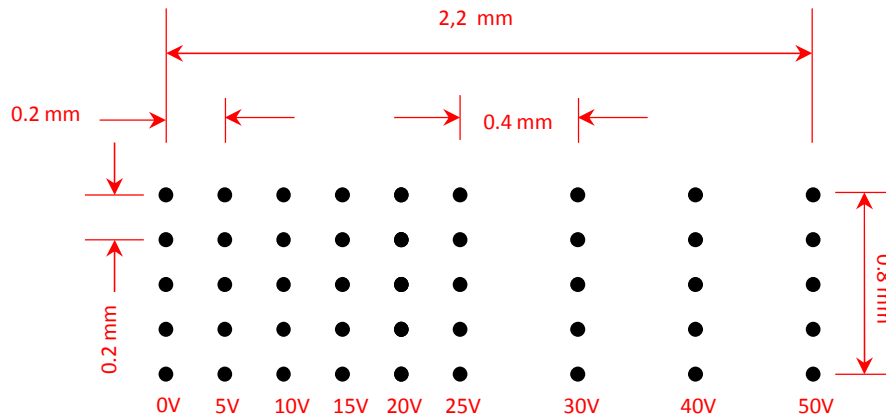


Figure 5.26: graphene tap/touches patterning scheme for a particular voltage range from 0 to 50 V.

Doted patterns here discussed consist of columns with five taps/touches performed at the same conditions in order to check the variability and reproducibility of our results, which will be delivered as an average for the five points. Next, voltage is increased from one column to each other, from 0 to 100 V and the probe is left to land on the surface a fixed applied force (1  $\mu\text{m}$  spring compression or 0.4 MPa equivalent pressure). Experiments have included points in graphene on different substrates, either SiO<sub>2</sub> (90 nm) / Si: p<sup>+</sup>, or quartz (crystalline SiO<sub>2</sub>) at low relative humidity (RH = 30%). Moreover, experiments in graphene on quartz at RH = 50%, and on SiO<sub>2</sub> (90 nm) / Si: p<sup>+</sup> at saturated RH = 84% have also been carried out to test the role of the moisture on this phenomenon.

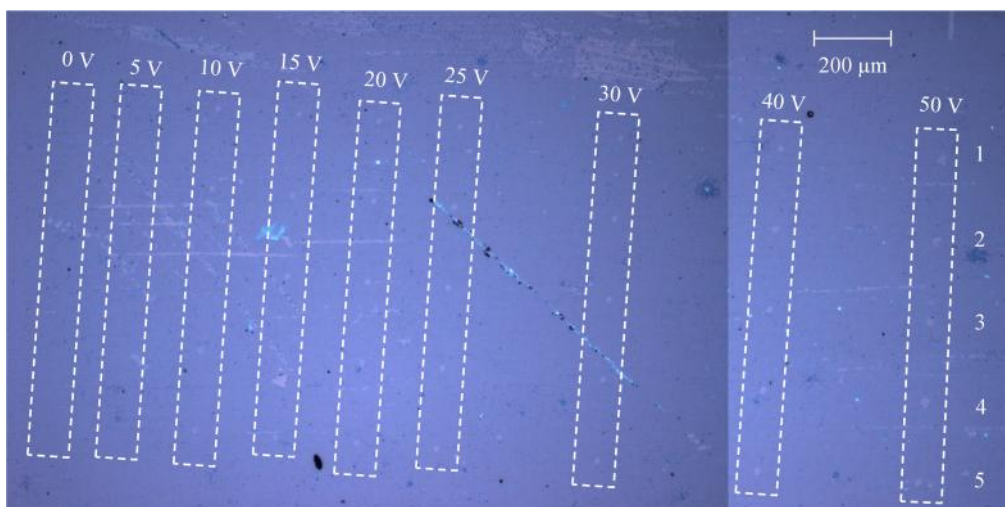


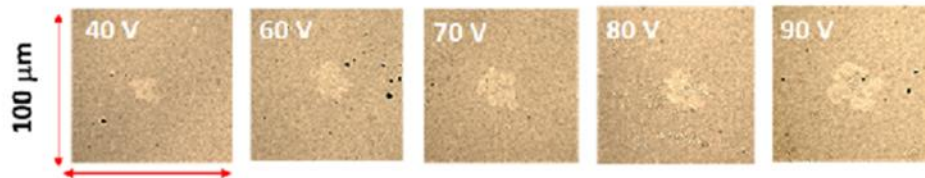
Figure 5.27: Two optical images composition for 0.3 mN pressure doted patterning in a voltage range from 0 to 50V.

Figure 5.27 shows two-optical image composition from the resulting dotted pattern from 0 V up to 50 V sketched in Figure 5.27. White dashed rectangles serve as a guide to find final spots. It is observed that 10 V is the value from which dot patterning gets visible. In agreement with results of the previous section, for voltage values below 10 V (1<sup>st</sup> column on the left) no visual features are distinguished, so mechanical damage is considered negligible. From 10 V and beyond, dots can be observed in the entire range.

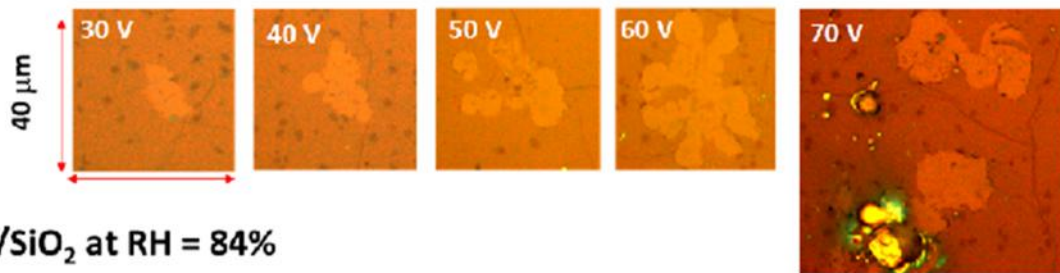
Optical and Raman images demonstrate that tip indentation, biased with voltages below 15 V at low applied force, is yet not harmful to graphene layer. This is consistent with the applied pressure range in this case ( $10^5$  to  $10^7$  Pa), much lower than the reported intrinsic graphene strength whose value is estimated at 130 GPa [17].

Figure 5.28 shows a collection of characteristic graphene craters generated by sparks at different voltages, from 30 V to 90 V, either on quartz or SiO<sub>2</sub>/Si: p<sup>+</sup> substrates. In the latter case, craters generated at two humidity conditions, 30% and 84%, are also shown.

#### G/Quartz at RH = 30%



#### G/SiO<sub>2</sub> at RH = 30%



#### G/SiO<sub>2</sub> at RH = 84%

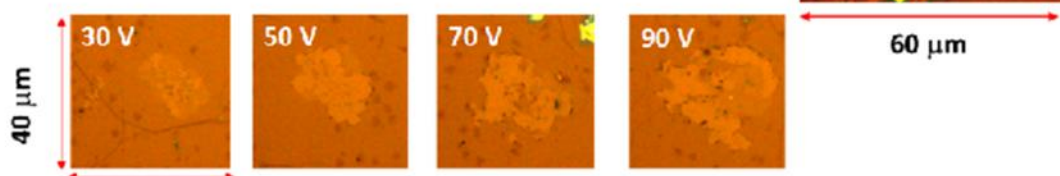


Figure 5.28: Optical images of the craters obtained for applied voltages from 30 V to 90 V by arc erosion on (a) graphene/Quartz sample at RH=30% (b) graphene/SiO<sub>2</sub>/Si: p<sup>+</sup> at RH= 30% and (c) same sample for RH= 84%

The observed features may be summarized as follows:

- a) Above a certain threshold voltage, there is a general increase of the crater area with increasing applied voltage.
- b) The crater front is irregular. In specific cases, it progresses in terms of lobes or fingers.
- c) The lobe-like progress of the front is less pronounced in craters performed at high relative humidity.
- d) The inside of the craters use to exhibit graphene nano-flakes, like those detected in patterned straight lines at low voltages ( $< 10$  V).
- e) Working in high RH, the inner region of craters shows large uniform areas of graphene oxide. In certain operating conditions, the GO dominates entirely the generated spot.

From now on, I will describe these observations in detail.

a) Above a certain threshold voltage, there is a general increase of the crater area with increasing applied voltage. In Figure 5.29, the average effective radius  $R_{ef}$  of craters has been plotted versus applied voltage. Here  $R_{ef}$  is defined as that of the circle having the same area, which was determined using specific image-treatment software. The  $R_{ef}$  plotted value is result the average for several craters performed at the same voltage, and the error bars reflect the standard deviation around this average. Figure 5.29 shows the evolution of the crater effective radius in three cases: a graphene/SiO<sub>2</sub>/Si: p+ sample worked at RH=30% (open squares), an identical sample but worked at RH=84% (bold red squares) and finally a graphene/quartz sample performed at RH=30% (blue rhombus).

In general, these plots share a common behavior also observed in other materials, as commented in Chapter 4: a flattened zone for the lowest voltages  $< 30$  V, followed by an ascending tendency at higher voltages. In the flat zone the spot coincides with the tip projection and means that there is no progress of the spot border at the lowest voltages used. The positive slope at voltages higher than a threshold ( $V_{th} \approx 30$  V), slightly depends on the substrate below graphene and, in a greater proportion, on ambient conditions. The slight differences between spots on quartz and on amorphous SiO<sub>2</sub> are not significant, probably because the residual water coming from the transfer

process softens differences. In any case, smaller spots observed for graphene on quartz may suggest a higher bonding with the crystalline substrate.

It can be verified that, for the same sample (G/SiO<sub>2</sub>/Si: p<sup>+</sup>), the increase of effective radius is lower in high humidity conditions than in dry ambient. This effect may be correlated to some features observed in the spot edge progress, commented below. On the other hand, the slight tendency to saturation observed in samples G/SiO<sub>2</sub>/Si: p<sup>+</sup> is an artifact due to the dielectric breakdown of the thin SiO<sub>2</sub> layer at high voltages. This electrical breakdown short-cuts graphene with the doped Si substrate and interrupts the process. Electrical breakdown of a SiO<sub>2</sub> layer of 90 nm depends on many factors, but statistically it is likely expected at fields over  $6 \times 10^8$  V/m of the order of those used here for 60 - 70 V [18].

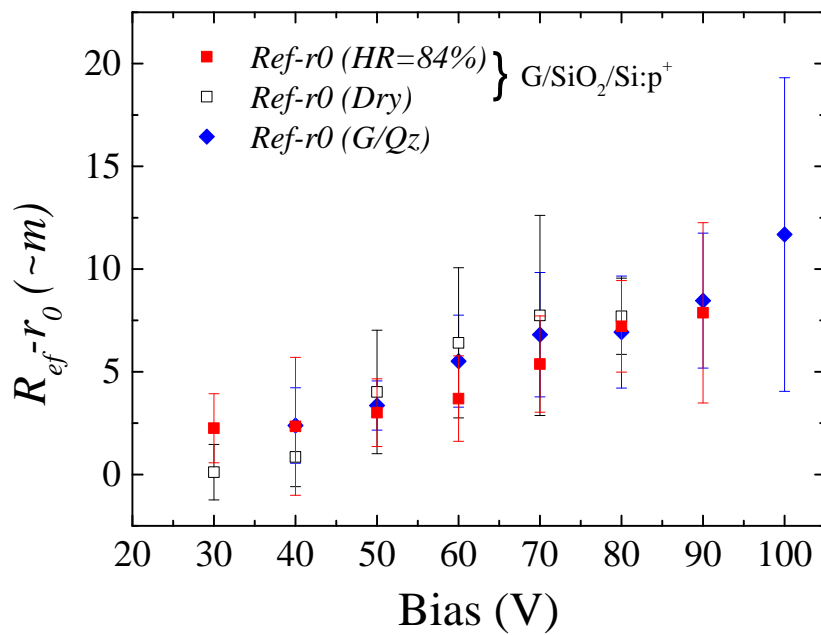


Figure 5.29: Evolution of the crater effective radius in three cases: a graphene/SiO<sub>2</sub>/Si:p+ sample worked at RH=30% (open squares), an identical sample but worked at RH=84% (bold squares) and finally a graphene/quartz sample performed at RH=30% (blue dots).

b) The crater front is irregular. At low voltages the shape appears to reflect the tip fingerprint, but above 40 - 50 V, the crater front progress by means of lobes or fingers. This irregular progress could be associated in part with the occasional evidence of multiple sparks in the electrical traces recorded by the oscilloscope, which would lead to a stepped progress, in sequential times. On the other hand, the finger-like progress

resembles that observed in gold, although in that case it was even more chaotic. Other physical systems behave similarly, for example, the surface charge distribution on insulators resulted after a high-voltage electrical discharge [19, 20]. In that case, it was proven that the progress of the lateral front of the accumulated charge is driven by the horizontal in-plane component of the electric field. This progress is irregular according to the inherent instability of the radial electric field under small perturbations of the charge density. I believe, and to some extent it has been justified in section 4.5, that at high voltages the progress of craters is also driven by the horizontal in-plane component of the electric field at the edge, which is tremendously enhanced, in a way explained in Chapter 4 (section 4.5). This field component can also be subjected to instabilities under perturbations of the front curvature, which would justify its irregular progress in way of lobes. In contrast, hard oxides like ITO, where material is not completely removed during electrical erosion, exhibit a more circular and uniform progress of the craters.

c) The lobe-like progress of the front is less pronounced in craters performed at high relative humidity. This may be co-related to the lower increment of the spot radius with increasing voltage under high ambient humidity. In this case, the dielectric character of the adsorbed water layer seems to prevail and play an important role. With reference to this, it will be shown that large areas of GO are generated when the operation is performed at high humidity conditions.

d) The inside of the craters use to exhibit graphene nano-flakes, like those detected in patterned straight lines at low voltages ( $< 10$  V) or very high voltages ( $> 50$  V) (Figure 5.30). In contrast, it is worth remembering that the inner region of straight grooves performed at voltages  $V = 30$  V was quite clean and empty of nano-flakes (Figure 5.30b). The movement of the tip allows the elimination process to be more homogeneous since several parts of the tip are in contact with the same area. This plays for the pattern quality and means a nice point for this technique.

Coming back to spots or craters, it is also remarkable that nano-graphene flakes spread along the inner region are however absent in specific zones such as those lobes appearing at the crater borders for voltages  $> 40$  V. This suggests that the erosion mechanism responsible for the appearance and progress of the lobe border is different to that removing graphene during the vertical approaching of the tip. In next subsection the size and distribution of these nanographenes will be studied in detail.

e) For high RH (84%), the inner region of craters shows large uniform areas which appear under optical inspection with two different contrasts. These regions have been highlighted in Figure 5.30b (yellow and green dashed circles). Raman spectroscopy confirms that in the higher contrast zones (green circle) graphene has been removed, as happened in craters performed at low RH, whereas in the shady or darker regions (yellow circle), a noticeable oxidation of graphene, instead of removal, has been achieved.

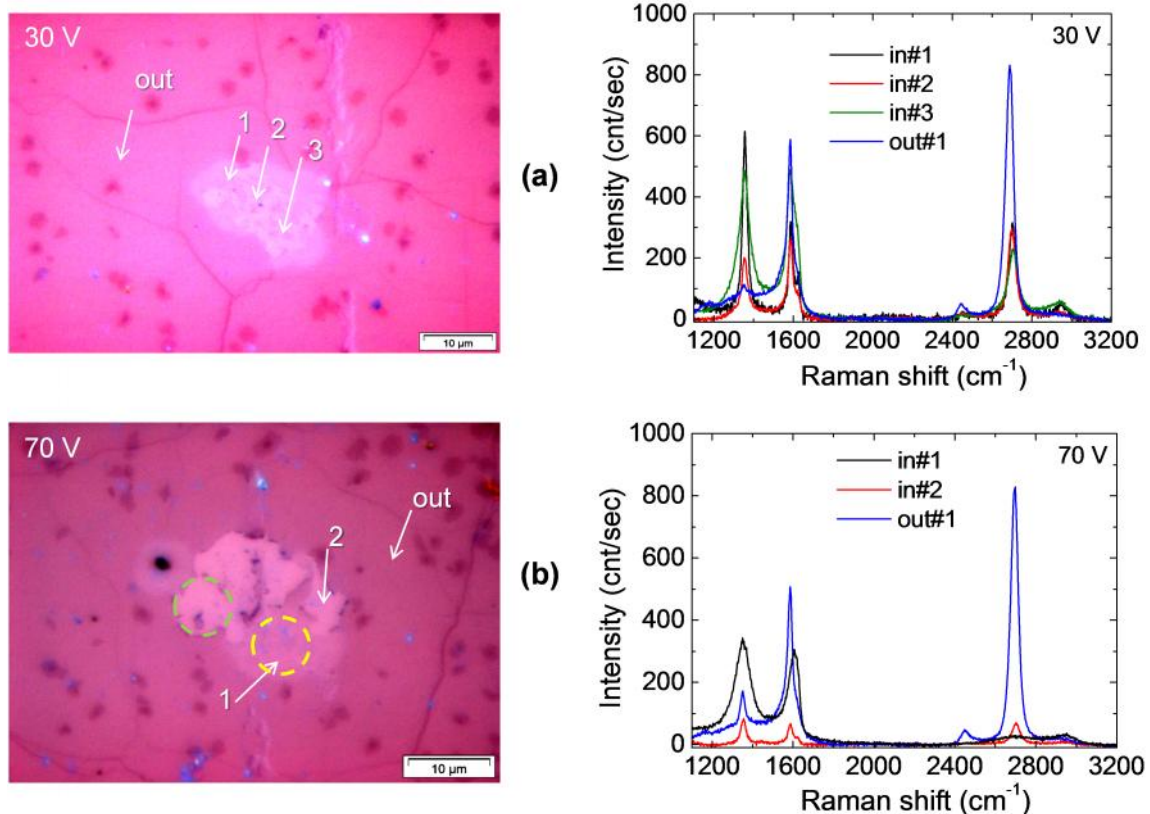


Figure 5.30: (a) Optical image of the the crater performed on G/SiO<sub>2</sub>p+ at 30 V, together with Raman spectra recorded from the marked points. (b) Optical image of the the crater performed on the same sample at 70 V, together with Raman spectra recorded from the marked points.

At lower voltages (< 30 V) domains of both regions appear, but are smaller and mixed together, spread across the whole area, in terms of micro or nano-domains (Figure 5.30a). But as increasing voltage, GO domains become larger and easily distinguished from those with absence of graphene, as shown in Figure 5.30b (yellow dashed circle and region around).

It is of major interest the discovering that under appropriate conditions, a large and complete oxidation of the whole area may be achieved. In this case, graphene removal is not accomplished, but roughly substituted by oxidation. Figure 5.31 shows

the optical image of a crater obtained at 50 V with a series resistance of 1 kOhm, where the whole area is dominated by GO.

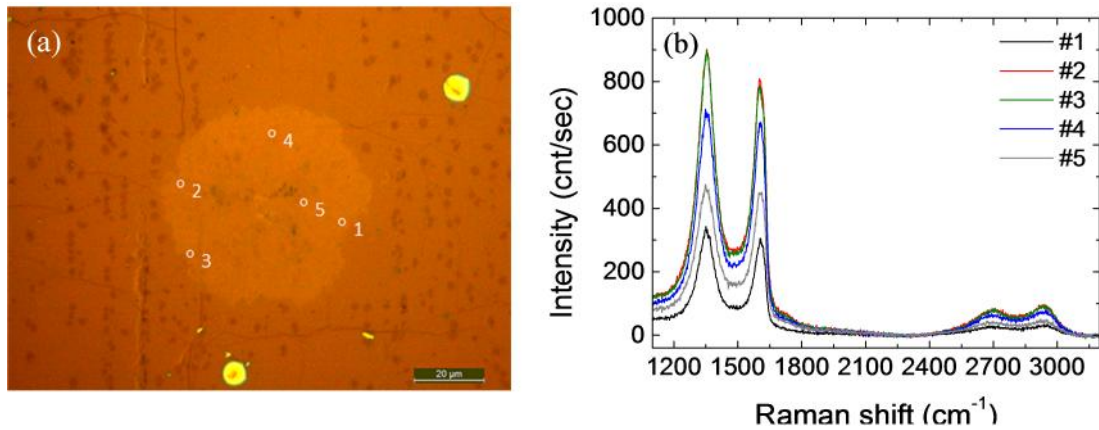


Figure 5.31: (a) Optical image of the the crater performed on G/SiO<sub>2</sub> p<sup>+</sup> at 50 V and 1 kOhm series resistance. (b) Raman spectra recorded from the marked points revealing the constant presence of GO.

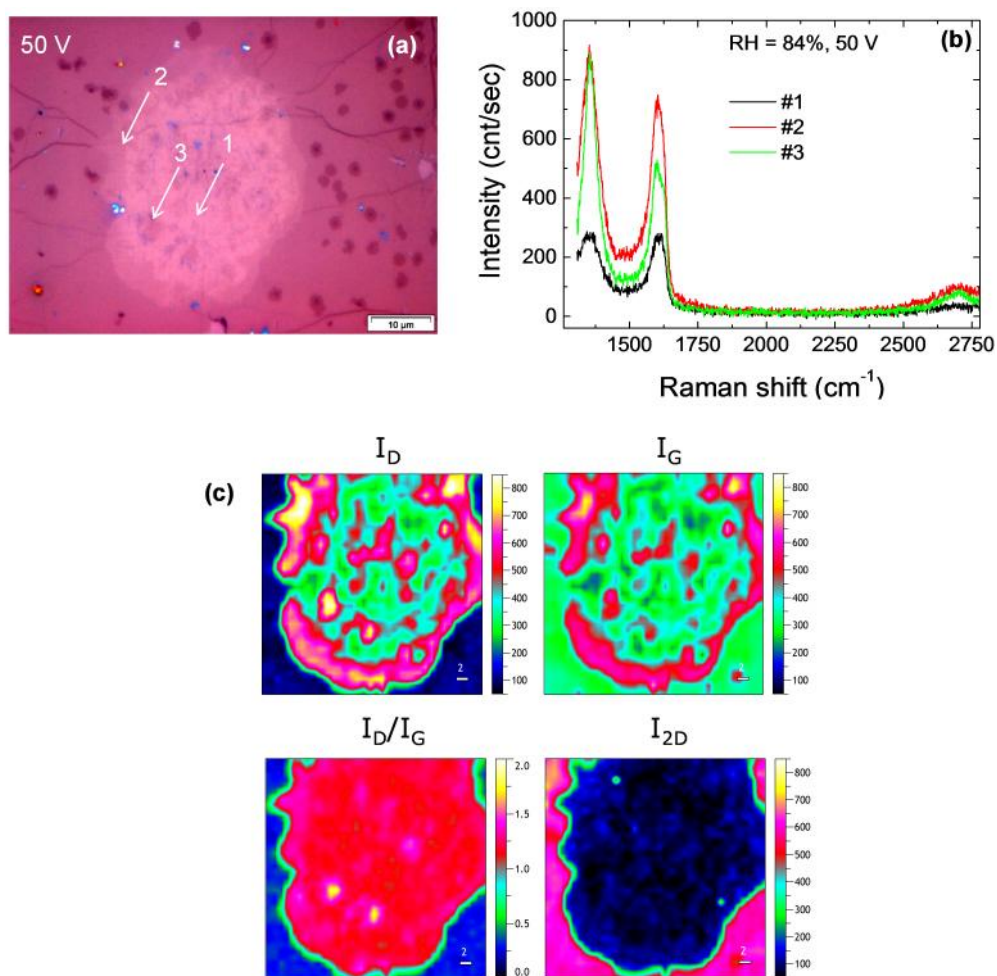


Figure 5.32: Crater performed on G/SiO<sub>2</sub>p<sup>+</sup> at 50 V: (a) Optical image, (b) Raman spectra of the indicated points and (c) Raman mapping of the crater, for the I<sub>G</sub>, I<sub>D</sub>, I<sub>2D</sub> and I<sub>D</sub>/I<sub>G</sub> ratio.

It is also noticeable that those craters where we have achieved oxidation instead of removal, are significantly larger, as large as twice, than those mainly consisting of absence of graphene. So oxidation progresses better than removal of graphene, or presumably, requires lower energy. In Figure 5.32a, we can observe a similar crater obtained under same conditions, where graphene oxide appears in all analyzed points but with different intensities (Figure 5.32b). This may indicate material elimination to some extent, in a random way. Raman mapping of this crater for the  $I_G$ ,  $I_D$ , and  $I_{2D}$  modes, together with  $I_D/I_G$  ratio is shown in Figure 5.32c. Again, the reddish area in map for ( $I_D/I_G$ ), and blue zone in map for  $I_{2D}$  mode indicate that graphene oxide is present in the whole crater area, quite uniformly.

At present, we have not been able to reproduce this type of oxidized spots in a systematic way. Despite reproducing all the operating conditions and procedures, the appearance of these fully oxidized regions depends on the material point, so we attribute this randomness to defects in the graphene layer or non-uniformity of the adsorbed water layer. Defects use to create sharp edges where electric field lines get more concentrated and promote erosion more easily, so defective or imperfect layers are probably not adequate. We believe that creation of the oxidized spots is linked to the high quality of the target region, together with specific conditions of humidity and applied voltage.

### 5.3.3. Nano-flakes in graphene

For spots obtained at -20 V and -30 V (below threshold voltage for crater expansion), optical images of repetitive spots indicate that their shape corresponds to the tip fingerprint (Figure 5.33). Raman spectroscopy inside the spots confirms that it is possible to partially eliminate the graphene layer and to obtain nano-graphene only with the tip contact and some applied force and voltage (Figure 5.33). Nano-graphene quality is clearly evidenced by the Raman maps of the  $I_{2D}/I_G$  ratio which is above 1 (Figure 5.33c, upper panel). The  $I_D/I_G$  ratio allows estimating the nano-graphene size (by using expression 5-1), and the  $I_G$  intensity the material remaining fraction in the spot. As also noticed in the previous section for straight line patterning, edge progress in the way of lobe-like areas is seen from 40 V onwards around the tip crater. An abrupt  $I_G$  intensity drop confirms the complete graphene elimination in these lobes (spectrum of Figure 5.33c lower panel, corresponding to point (2) in picture b) of the figure).

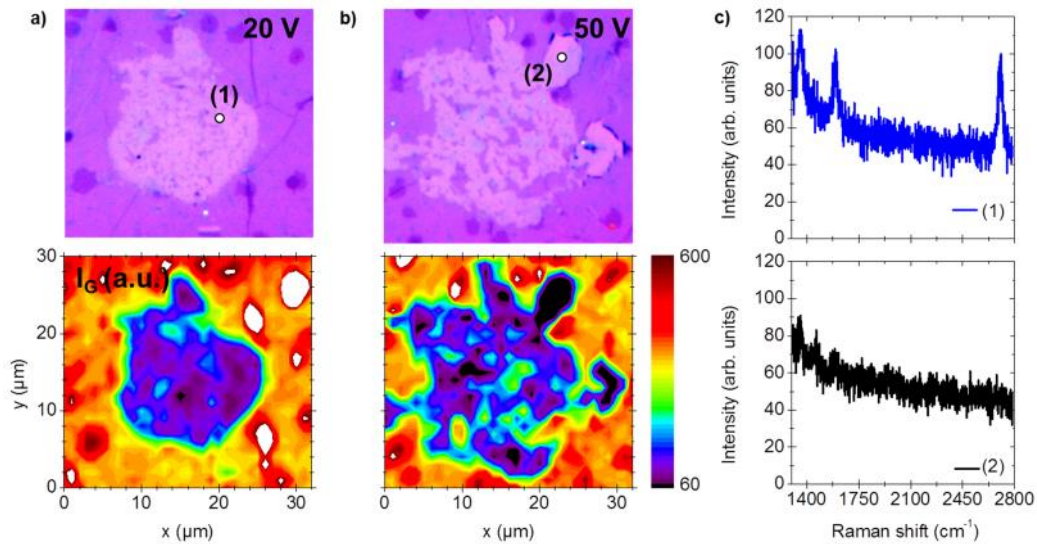


Figure 5.33: Optical image and I<sub>G</sub> Raman image from the dots performed at 20 V (a) and 50 V (b) with 0.3 mN in graphene/SiO<sub>2</sub>/Si; (c) Raman spectra corresponding to the marked points in (a) and (b).

A statistical analysis of the eliminated graphene fraction, as well as the nano-graphene size distribution within the crater, may be performed as a function of the applied voltage by means of Raman mapping. In Figure 5.34, results processed by micro-Raman performed on spots at 20 V, 30 V and 50 V are compared. The Raman maps cover  $31 \times 33 \mu\text{m}^2$  involving 1023 micro-Raman spectra, each one taken from an area  $\varnothing \approx 0.7 \mu\text{m}$ .

Histograms in Figure 5.34a, describe the percentage of Raman spectra (Y axis), or number of events over the total, corresponding to a percentage of I<sub>G</sub> intensity (X axis) for patterning at 20, 30 and 50 V. In this case, 100% of I<sub>G</sub> means an equivalent intensity to that of pristine graphene outside the spot. So this histogram describes the fraction of graphene remaining at each measured point. For example, at 20 V only 20% of the points contained 100% graphene. This refers to points likely located outside the crater. At 50 V, where the crater is higher and covers most of the area, this fraction is reduced to 15%. Then again, at 20 V, 5% of the 1023 spectra present an I<sub>G</sub> value within 19-25% of that of pristine graphene, so that the remaining graphene fraction is in the range 19-25%, while at 30 V up to 9% is in this range. Most of the points indicated a clear lack of graphene, although it is always present.

Figure 5.34b shows Raman maps of the ratio (I<sub>G</sub>/I<sub>D</sub>) for the three voltages. According to expression 5-1, this ratio gives an idea of the nano-graphene size ( $L_a$ ) in the scanned area (valid for  $L_a \geq 4 \text{ nm}$ ). There is certain uniformity inside the craters.

The information recorded in these maps can be converted into a new histogram revealing a nanographene size distribution. The vertical axes in Figure 5.34c indicate the number of points with an average nanographene size, for example, 8% of the 1023 spectra of the spot done at 20 V correspond to graphene with an average size in the range of 12 to 16 nm.

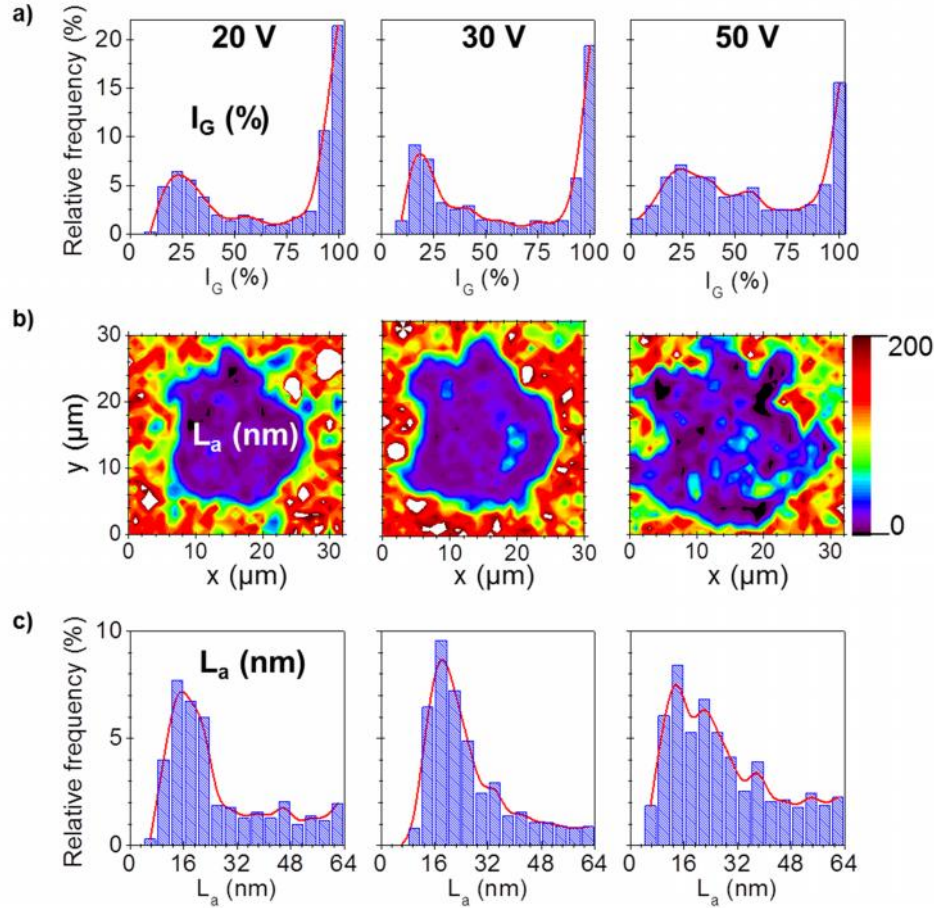


Figure 5.34: (a) Histogram distributions for graphene remaining fractions, (b)  $L_a$  images and (c) histogram distribution for  $L_a$  from the dots performed at 20, 30 and 50 V with a force of 0.3 mN in graphene/SiO<sub>2</sub>/Si. Red solid lines are guides to the eye.

Integrating the data for the three spots and operating voltages, we derive that the remaining fraction of graphene is around 23% for 20 V and decreases to 19% for 30 V inside the spot. In the latter case, showing a narrower distribution, with mean size of 19 nm and a full width at half maximum of 11 nm, indicating that the homogeneity inside the spot has increased. For higher voltages, when the edge progress by lobes, the distribution is much wider (Figure 5.34a). The average size of the remaining graphene inside the craters is around 18-19 nm in all cases. We find also that the graphene fraction with sizes below 25 nm is constant. It is important to note that the presence of a large density of bi- and multi-layered regions in the sample (Figure 5.34) may have a

negative influence in the homogeneity of the patterning. We also highlight that processing results recorded from a technique with a resolution of about 1  $\mu\text{m}$ , we have been able to derive information on features of a few nm.

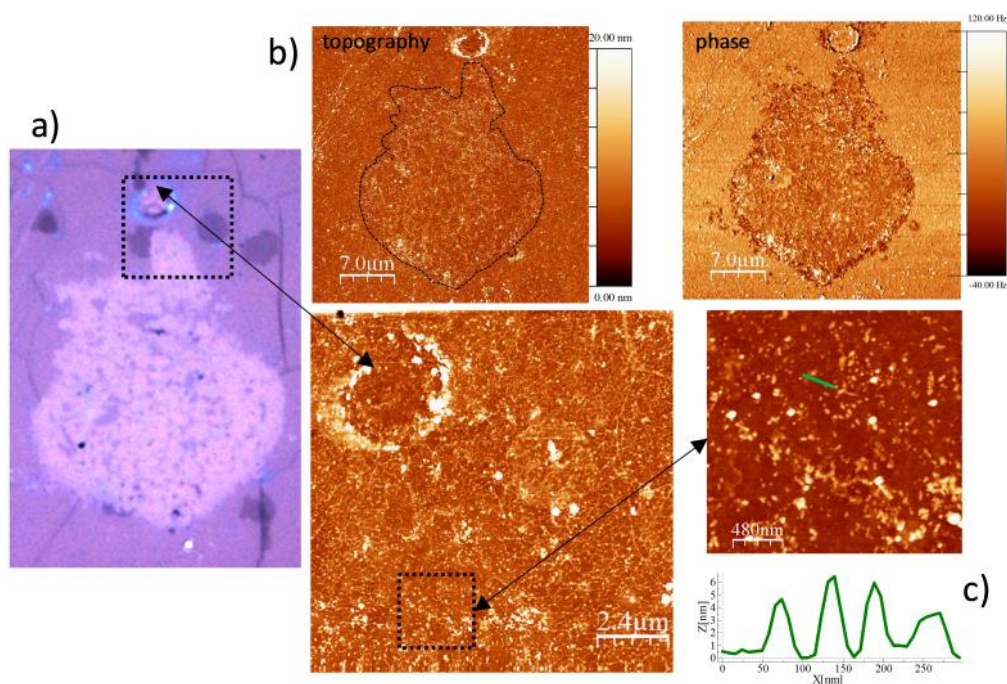


Figure 5.35: Optical (a), AFM topographic and phase images (b) 20 V performed dot images. The dashed line inserted in the topographic image of (b) corresponds to the perimeter of the darker area observed in the phase image. Higher resolution topographic AFM images of the indicated areas are also included in (b). (c) Height profile corresponding to the green line marked in the AFM image.

Figure 5.35 shows the optical picture and AFM images (topography and phase) at different magnifications of the 20 V crater. The spot is hardly visible in the topographic image (Figure 5.35b). On the contrary, phase image yields a clear contrast between the patterned spot and the pristine graphene that has been used to delimitate the crater boundaries, marked by the dashed line, in the topographic image. The origin of the phase contrast cannot be unambiguously determined. Difference in electrostatic properties between the inner (graphene absent or cracked) and outer region (pristine graphene) might be a plausible cause supported by the close correlation with optical images, where the observed contrast is due to the different reflectivity (and therefore dielectric constant) of the insulating  $\text{SiO}_2$  substrate and the graphene areas. The Raman images corresponding to this pattern indicate a graphene removal of about 77% within the spot, and its transformation to nano-graphene of 18 nm in average of the remaining fraction (Figure 5.34 and Figure 5.35).

The morphological characteristics measured in high resolution AFM images are shown in Figure 5.35b and Figure 5.35c. Defects as the one marked on the top part of the optical image in Figure 5.36a serve as guides to correlate AFM and Raman images. The topographic image of the selected area and the profile show the presence of clusters 5-7 nm high and small flakes  $\sim 2$  nm high scattered all over the surface. The rms value calculated for the image shown in Figure 5.35 is 2 nm. A similar morphology is observed for the dot performed at 40 V. For increasing applied voltages lobe-like regions at the crater edge are observed (Figure 5.36). Raman signal of the 50 V patterned crater confirms that inside these lobe-like regions graphene is completely eliminated (black in Figure 5.36c). AFM topographic images of that area (Figure 5.36c and d) show similar clusters 5-7 nm high as those observed in the regions with nanographene of Figure 5.36. Since these clusters cannot be nano-graphene according to Raman information, these rounded features are most probably originated by the substrate erosion.

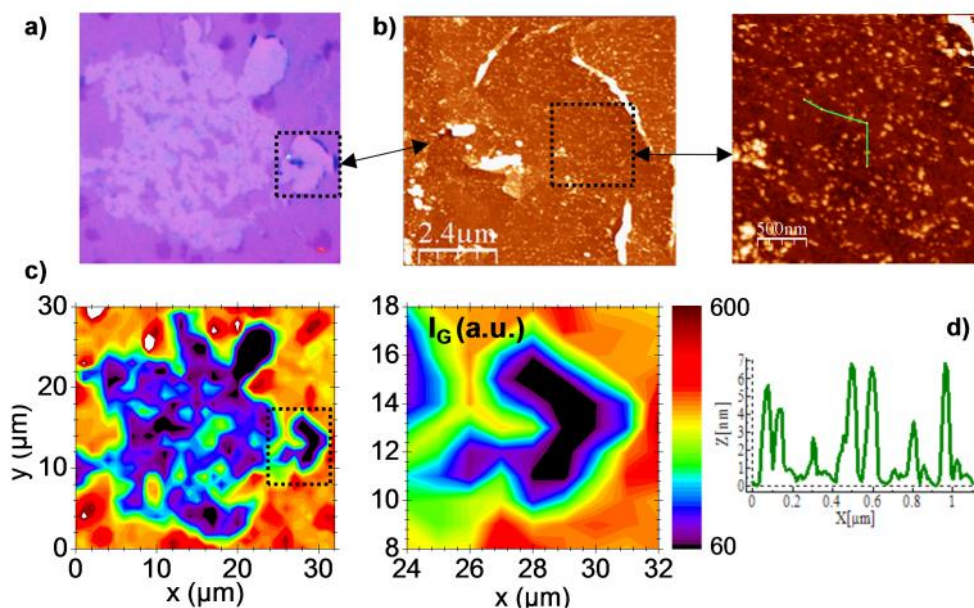


Figure 5.36: Optical (a) and AFM images (b) at the location where a 50 V lobe-like area has been formed. Raman images (c) of  $I_G$  of the whole dot and a zoom of the indicated area. The height profile (d) corresponds to the line marked in AFM image.

#### 5.3.4. Discussion on the mechanisms

There is a consensus on the electrochemical origin of the mechanism for graphene etching performed with AFM and STM. The presence of adsorbed water favors any of the observed processes, either elimination or oxidation of graphene, or even reduction of

graphene oxide, as detailed in the subsection 1.4.2. The absence of water use to result in the need of much higher voltages to attain the same effect.

We have proven that touching the surface with the tip in absence of applied voltage does not remove graphene on amorphous or crystalline SiO<sub>2</sub> substrates. Actually, high electric fields are required to trigger the etching. In fact, if the tip is in contact with the sample surface at 0 V, and the voltage is subsequently increased an electric current is established but no etching is produced.

In the present case our estimations indicate that field effects can be sufficient for graphene elimination. For a fixed external voltage ( $V_b$ ), as the metal probe approaches the conductive layer, the density of electric field lines grows particularly at the tip apex with a spatial distribution that depends on the tip geometry. Calculations indicate that the electric field at the tip edge converges to  $V_b/L$  for  $L$  around 30 – 40 nm and therefore, at smaller distances, electron tunneling across the metal-air potential barrier can be induced by the high local fields  $> 10^9$  V/m. This field effect current (measured up to tens of mA), where electrons are pulled out of the probe metal and impinge on the graphene surface (according to the negative polarity), effectively short-circuits the tip-graphene gap and may deliver the required energy density to trigger the reaction. Obviously, thermal Joule-effect in such a small and localized region may be involved, and cannot be discarded, but experiments point out the relevance of water. The final process has been tentatively explained by electron-assisted water decomposition which in turn promotes breakdown of those weakened C bonds in the vicinity of the H<sub>2</sub>O molecules [21]. Eventually many C atoms are removed by forming gaseous species such as CO, and others remain into flakes.

The dots presented in Figure 5.33 Figure 5.36 are done by approaching the tip to the graphene/SiO<sub>2</sub>/Si surface and pressing it for a short time. Graphene removal and nanographene formation due to the current discharge creates a dot or crater below the probe and leads the tip to settle on an insulating region. We observe that features are not completely homogeneous under the tip due to inhomogeneities of different nature: the mentioned PMMA residues, the graphene wrinkles, the multilayer regions, and the microscopic shape of the tip. Besides to tip-substrate distance, tunnel currents are extremely sensitive to shape and size of the tip. The morphology of our tips (a few tens micron in diameter) are far from being flat at the nanoscale and therefore is expected to produce non-uniform distributions of the electric fields.

Above the threshold voltage for crater expansion (30 - 40 V), the lobe-like regions have different Raman characteristics (there is strictly no graphene residues) compared to the region directly under the tip, indicating a different driving mechanism. We remark that distances from the tip to the crater edge are here very large (tens of  $\mu\text{m}$ ) so a strong attenuation of the electric fields should be expected at such long distances. We can speculate that formation of these lobes may have direct relation with the evaporation of the water layer existing between the graphene and the Si/SiO<sub>2</sub> substrate, as a consequence of the wet transfer process. During the violent current pulse, the dissociation of water may reach regions beyond the tip, and the generated gas pressure could be enough to overcome the weak graphene-SiO<sub>2</sub> interaction.

However, in section 4.5, I have proposed a mechanism which justifies a strong enhancement of the electric fields, able to compensate the attenuation at long distances from the tip. The edges created at the crater border are much sharper than the tip apex, and consequently promote an intense concentration of electric field lines even at long distances. We have estimated that such local fields are well above  $10^6$  V/m in craters performed on ITO (which results very uniform and circular-shape). In fact, and surprisingly, the field at the edge of craters performed at different voltages (up to 25 V), and hence with different sizes ( $r'$  up to 60  $\mu\text{m}$ ), were all very close to  $3 - 5 \times 10^6$  V/m just at the interruption. Since the distances from the probe are large, and a significant air mass is present, the fields should be able to provoke the electrical breakdown of air, involving plasmas in this phenomenon. If something similar operates in graphene crater lobes, it is then understandable the efficiency to remove completely the material, in agreement with Raman observations.

The fact that many sparks are visually accompanied by flashing glints in many materials tested supports this explanation. Also, a process driven by an in-plane electrical component should be subjected to instabilities depending on the edge geometry, so a progress in the way of lobes or fingers observed in materials which are easily removed, like gold, aluminum or graphene makes sense. Otherwise, hard materials, like ITO and amorphous oxides, which are difficultly removed, should behave more regularly against crater progress, as observed.

On the other hand, coming back to graphene, when the relative humidity is high and the adsorbed water layer is presumably extensive, the erosion mechanisms are affected and modified. Under electrical discharge, the creation of GO is favored instead

of carbon removal. Below the threshold voltage, micro-domains with either GO or lack of graphene, coexist. The progress of the crater expansion above the threshold voltage slows down as compared to the process in dry conditions, likely due to the dielectric character of the wetting layer. But, under certain conditions, a whole oxidation instead of carbon removal can be achieved. There is some competition between both phenomena, obeying to different mechanisms, probably determined by defects in the graphene layer. A defective layer would enhance crater formation by graphene removal, whereas in pristine layers with a uniform adsorbed water film, oxidation may prevail. In electrochemical etching by AFM, the formation of graphene oxide is usually reported, though it is not always possible to check the presence of graphene oxide using Raman spectroscopy for such nanoscale sized patterns. In the present case, Raman spectroscopy has evidenced the transformation to GO assisted by electrical discharge at large scales (hundreds of  $\mu\text{m}^2$ ).

## 5.4 REFERENCES

- [1] X. Díez-Betriu, S. Álvarez-García, C. Botas, P. Álvarez, J. Sánchez-Marcos, C. Prieto, R. Menéndez and A. de Andrés, "Raman spectroscopy for the study of reduction mechanisms and optimization of conductivity in graphene oxide films," *J. Mater. Chem C*, vol. 1, pp. 6905-6912, 2013.
- [2] R. Wüthrich, *Micro & Nano Technologies: Micromachining Using Electrochemical Discharge Phenomenon: fundamentals and application of spark assisted chemical engraving*, William Andrew - Elsevier, 2009.
- [3] R. McCarley, S. Hendricks and A. Bard, "Controlled nanofabrication of highly oriented pyrolytic graphite with the scanning tunneling microscope," *J. Phys. Chem.*, vol. 96, no. 25, p. 10089–10092, 1992.
- [4] J. M. Mativetsky, E. Treossi, E. Orgiu, M. Melucci, G. Veronese, P. Samorì and V. Palermo, "Local current mapping and patterning of reduced graphene oxide," *J. Am. Chem. Soc.*, vol. 132, no. 40, p. 14130–14136, 2010.
- [5] J. Gardener and J. and Golovchenko, "Ice-assisted electron beam lithography of graphene," *Nanotechnology*, vol. 23, no. 18, p. 185302, 2013.
- [6] "Graphene Supermarket - Single/Double layer Graphene on 90 nm Silicon Dioxide Wafer - 10 pack," [Online]. Available: <http://graphene-supermarket.com>. [Accessed 2013].
- [7] X. Li, W. Cai, J. An, S. Kim, J. Nah, D. Yang, R. Piner, A. Velamakanni, I. Jung, E. Tutuc, S. Banerjee, L. Colombo and R. Ruoff, "Large-area synthesis of high-quality and uniform Graphene films on copper foils," *Science*, vol. 324, no. 5932, pp. 1312-1314, 2009.
- [8] E. Climent-Pascual, M. García-Vélez, Á. L. Álvarez, C. Coya, C. Munuera, X. Díez-Betriu, M. García-Hernández and A. de Andrés, "Large area graphene and graphene oxide patterning and nanographene fabrication by one-step lithography," *Carbon*, 2015, In press.

- [9] X. Li, Y. Zhu, W. Cai, M. Borysiak, B. Han, D. Chen, R. Piner, L. Colombo and R. Ruoff, "Transfer of Large-Area Graphene films for high-performance transparent conductive electrodes," *Nano Lett.*, vol. 12, no. 9, pp. 4359-4363, 2009.
- [10] M. Pimienta, G. Dresselhaus, M. Dresselhaus, L. Cançado, A. Jorio and R. Saitoe, "Studying disorder in graphite-based systems by Raman spectroscopy," *Physical Chemistry Chemical Physics*, vol. 9, no. 11, pp. 1276-1290, 2007.
- [11] L. Cançado, A. Jorio, E. Martins Ferreira, F. Stavale, C. Achete, R. Capaz, M. Moutinho, A. Lombardo, T. Kulmala and A. Ferrari, "Quantifying defects in graphene via Raman spectroscopy at different excitation energies," *AC Nano Lett*, vol. 11, no. 8, pp. 3190-3196, 2011.
- [12] M. Currie, J. Caldwell, F. Bezares, J. Robinson, T. Anderson, H. Chun and M. Tadjer, "Quantifying pulsed laser induced damage to graphene," *Appl. Phys Lett*, vol. 99, p. 211909, 2011.
- [13] J. Tamayo and R. García, "Effects of elastic and inelastic interactions on phase contrast images in tapping-mode scanning force microscopy," *Appl. Phys. Lett*, vol. 71, p. 2394, 1997.
- [14] R. García, R. Magerle and R. Perez, "Nanoscale compositional mapping with gentle forces," *Nature Materials*, vol. 6, pp. 405-411, 2007.
- [15] H.-J. Lee, K.-S. Kim, C. Lee, S.-K. Lee, H. Jang, J.-H. Ahn, J.-H. Kim y H.-J. Lee, «Chemical Vapor Deposition-Grown Graphene: The Thinnest Solid Lubricant,» *ACS Nano*, vol. 6, pp. 5107-5114, 2011.
- [16] L. Ju, B. Geng, J. Horng, C. Girit, M. Martin, Z. Hao, H. A. Bechtel, X. Liang, A. Zettl, Y. R. Shen and F. Wang, "Graphene plasmonics for tunable terahertz metamaterials," *Nature Nanotechnology*, vol. 6, p. 630-634, 2011.
- [17] C. Lee, X. Wei, J. Kysar and J. Hone, "Measurement of the elastic properties and intrinsic strength of monolayer graphene," *Science*, vol. 321, no. 5887, pp. 385-

388, 2008.

- [18] C. M. Osburn and D. W. Ormond, "Dielectric Breakdown in Silicon Dioxide films on Silicon. II. Influence of Processing and Material," *J. Electrochem. Soc.*, vol. 119, no. 5, pp. 597-603, 1972.
- [19] M. Arrayás, M. Fontelos and J. Trueba, "Photoionization effects in ionization fronts," *Journal of Physics D: Applied Physics*, vol. 39, p. 5176–5182, 2006.
- [20] U. Ebert, W. van Saarloos and C. Caroli, "Propagation and structure of planar streamer fronts," *Phys. Rev. E.*, vol. 55, no. 2, pp. 1530-1549, 1997.
- [21] M. Kostov, E. E. Santiso, A. M. George, K. E. Gubbins and M. Buongiorno Nardelli, "Dissociation of Water on Defective Carbon Substrates," *Phys. Rev. Lett*, vol. 95, no. 136105, 2005.

## CHAPTER 6 . CONCLUSIONS

- It has been developed a lithography system based on electrical erosion, consisting of a three independent Z-axis and XY-axes piezo stages attached to long trip electromechanical steppers. The trip can be up to 3 cm in vertical and 10 cm in horizontal directions, both with a 0.1  $\mu\text{m}$  resolution and 1  $\mu\text{m}$  of reproducibility. The implemented piezo stages guarantee an accurate motion with resolution of 0.05 nm and a 38  $\mu\text{m}$  in vertical trip. A resolution of 0.4 nm is achieved for a 100  $\mu\text{m}$  horizontal displacements. The probe is biased with a DC voltage (0 –  $\pm 100$  V) respect to ground. With this system the possibility to perform patterns over 10 x 10  $\text{cm}^2$  areas at 15 mm/s is ensured.
- It has been implemented an effective tilt correction method, which has allowed scaling complete patterns up to millimeters in length. In addition, the design of an approaching protocol valid for any type of tip (commercial spring probes or home-made cantilevers) has been also established, in order to guarantee safety of the sample being processed and, ultimately, of the main prototype components.
- It has been obtained the optimal conditions for correct arc-erosion lithography on materials used in optoelectronic devices like ITO, AZO and Au. It has been remarkable as a general result that just mechanical erosion is not enough for quality performance, but an applied bias is required to achieve and adequate arc-erosion

lithography. Also, it is observed an increase in the pattern width for higher operating voltages, which adds a new control parameter to the system. It is also observed a wavy edge at higher operating voltages, more pronounced depending on the material. Excellent results have been obtained in flexible substrates using rigid tips (acupuncture type) as well as home-made cantilever probes. Also, it has been proposed a new working mode, tapping-like, by an inherent functionality implementation included in the piezo stage controller.

Precise conclusions for ITO, AZO,  $Zn_3N_2$  and Au, thoroughly studied materials in this thesis work, are outlined below:

### **Indium Tin Oxide (ITO)**

- Good quality patterns can be achieved in the 11-12 V, with negative or positive tip polarization, respect to the ITO surface. Electrical isolation can be achieved for both polarities.
- Greater amount of waste is obtained when the procedure is carried out with negative polarization, which appears to be more aggressive than the positive one. Chemical etching is used to guarantee an excellent finishing and a clear edge definition. A suitable chemical etching consists of a (1:1) HCl: distilled water solution, preheated to 20 °C for 10 s. The waste generated by using the positive polarity is removed easier. However, working in these conditions implies increasing tip wear.
- ITO micro-ribbon patterns with 2.5 - 3  $\mu\text{m}$  in width and 7  $\mu\text{m}$  spaced (250 x 100  $\mu\text{m}$ ) were obtained on PET using -12 V as applied bias and a rigid acupuncture needle. Despite the magnificent result in patterning terms, the problem is now focused on finding a suitable etching method to remove the residual waste on edges, in order to avoid subsequent manufacturing problems

### **Aluminum doped Zinc Oxide (AZO)**

- Well-defined patterns are obtained in a wide voltage range: from -30 to -45 V. AZO electrical patterning can be performed using voltages above this range but final product will be inadequate due to its irregularity and poorer definition. For voltages lower than -30 V, although there is evidence of material erosion, results do not fulfil the final pad isolation needed for devices.
- Highly amorphous AZO layers have been integrated into a bulk heterojunction organic solar cell, instead of ITO, using electrical erosion as lithography method to define the anode electrodes. The fabrication conditions and specially the ozone treatment are critical for charge injection, efficiency and the overall device performance.

### **Zinc Nitride ( $Zn_3N_2$ )**

- Several interesting effects have been found in  $Zn_3N_2$  electrical erosion. At low voltages ( $< 15V$ ), the eroded areas present a lower resistivity due to the removal of the native oxide. At larger voltages (15 - 17 V), the electric arc discharge produces high electrical resistance properties that allows their use as lithography method. At the same time, Zn-rich micro-droplets are obtained at the scan edges as residues of the sublimation process. The electric arc process also induces strong compositional changes at the central part of the scan, yielding ZnO: N submicron structures from the Zn crystal grains.

These properties make the technique a useful tool for the reduction of the contact resistivity in  $Zn_3N_2$  surfaces, the insulation of  $Zn_3N_2$  TFTs in two-dimensional arrays, and its use in the preparation of advanced ZnO nanostructures for optoelectronic applications. From the optical point of view, the transformation process is also attractive as optical data storage technique since it enables the definition of visible transparent ZnO windows in opaque  $Zn_3N_2$  layers.

## Gold (Au)

- Patterning of gold (Au) layers with different thicknesses has been performed. For the three analyzed cases (15, 52 and 100 nm), the threshold voltage decreases with the layer thickness, as also the material amount to be removed.
- Patterns done using the voltage range from -16 to -20 V have irregular finished edges far from a good resolution and quality pattern.
- For 15 nm thin layers, conditions for excellent results have been obtained. These grooves are the best defined so far. Threshold voltage is found at -3 V, and good quality electrical erosion can be performed in a wider voltage range (-3 to -14 V) compared to above tests. Pure mechanical erosion takes place at -2 V.
- It has been demonstrated a sweeping method to reduce waste accumulation at the edges from hundreds to tens nanometers in height. It is also demonstrated that the accumulated material is not melted or adhered to the surface, enhancing the possibility to remove it through repetitive movement cycles avoiding the use of chemical or wet methods
- COMSOL Multiphysics software for finite element analysis has been successfully used to simulate electrostatic characteristics of the tip-layer system. With the aid of the results from simulations a phenomenological model to explain the expansion of the crater radius with an applied external voltage during a spark process has been proposed.
- The analysis of the experimental results allows concluding that crater expansion is interrupted at a point where the in-plane component of the electric field at the crater edge,  $|E_{\text{edge}}|$ , goes down to a certain critical value. This value is common whatever the voltage used for a fixed layer thickness. We find this value is generally very close to that of the dielectric breakdown of air at room conditions. This deduction suggests that  $|E_{\text{edge}}|$  is related to plasmas in air, and plays an important role in the physical process of crater progress.

- It has been proposed a simple circuital model that explains the dynamics of the discharges during the erosion process.

The arc-erosion lithography system has also been tested for graphene and 2D related materials (graphene oxide and reduced graphene oxide). Below, conclusions related to graphene patterning are summarized:

### **Graphene Oxide (GO)**

- Satisfactory grooves on GO have been performed at dry and wet conditions using the following voltage range from -25 to -60 V. In dry conditions there is incomplete erosion just by mechanical scratching, without voltage application. In dry conditions, the best results are obtained at -60 V, for which almost all material is removed, as evidenced by Raman measurements.
- Alternative wet experiments using different acidic concentrations, resembling electrochemical etching, resulted in excellently defined patterns (all residues within the grooves and at the edges disappear), whatever the voltage used, with a large margin in the acid concentration. However, since acidulated water ends up reacting with the tip metal, a final recommendation is to use distilled water instead, to preserve the tip life time.

### **Reduced graphene oxide (rGO)**

- Due to the soft consistency and poor conductivity of the reduced layers, groove patterning at different voltages from -10 to -20 V resulted in no detectable changes. No significant difference between grooves performed with an applied voltage is observed. The measured width in each groove corresponded to the tip diameter. There is also no significant lateral progress with increasing voltage. Material removal takes place even at 0 V.

## Graphene

- The optimum voltage range for graphene patterning is considered to fall within 20 to 30 V. Using our direct approach, it can be done graphene patterns and micro-ribbons of any arbitrary size and geometry, with a resolution and quality limited by the probe diameter and roughness, as well as by precision of the steppers motion. No waste is observed on the edges.
- The versatility and precision of this technique and the operation voltage optimization has allowed obtaining an array of graphene micro-ribbons with an excellent aspect ratio ( $1\ \mu\text{m} \times 1200\ \mu\text{m}$ ), which is very promising for terahertz plasmonic applications.
- Raman spectroscopy and AFM performed inside patterned spots confirm that it is possible to partially eliminate the graphene layer and to obtain uniform distributions of graphene nano-flakes under certain operating conditions.
- Taking advantage of the capability to perform Raman mapping in large areas, a method to determine the average size of graphene nano-flakes inside a pattern has been proposed. This method has been successfully used to determine the average size of the remaining nano-graphene inside the craters to be around 18-19 nm. This result is in agreement with AFM measurements.
- The inner region of craters may exhibit large uniform areas of graphene oxide when working at high relative humidity. In certain operating conditions, the GO dominates entirely the generated spot. Oxidized circular areas of more than  $100\ \mu\text{m}$  radius have been obtained at once, with a simple discharge.



# APPENDIX A.

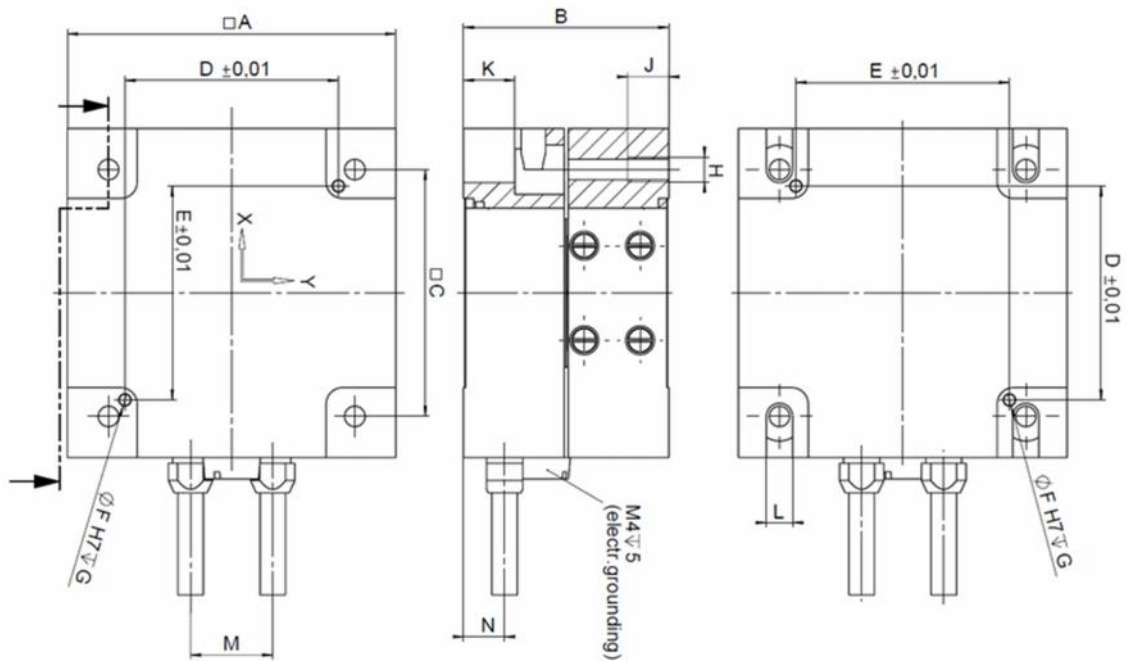


## A.1. P-621.2 CD PIHERA XY PIEZO STAGE: SPECIFICATIONS

General information for PIHERA XY piezo stage by Physik Instrumente.

Model	P-621.2CD	Units	Tolerance
Active axes	X, Y		
<b>Motion and positioning</b>			
Integrated sensor	Capacitive		
Open-loop travel X, Y, -20 to +120 V	120	μm	min. (+20%/-0%)
Closed-loop travel	100	μm	
Open-loop resolution	0.2	nm	typ.
Closed-loop resolution	0.4	nm	typ.
Linearity	0.02	%	typ.
Repeatability	±2	nm	typ.
Pitch / yaw	±3	μrad	typ.
<b>Mechanical properties</b>			
Stiffness	0.25	N/μm	±20%
Unloaded resonant frequency in X,	420	Hz	±20%
Unloaded resonant frequency in Y	535	Hz	±20%
Resonant frequency in X @ 50 g/100 g	285/220	Hz	±20%
Resonant frequency in Y @ 50 g/100 g	365/285	Hz	±20%
Push/pull force capacity in motion direction	10/2	N	Max.
Load capacity	10	N	Max.
Lateral Force	10	N	Max.
<b>Drive properties</b>			
Ceramic type	PICMA P-885		
Electrical Capacitance	1.5	μF	±20%
Dynamic operating current coefficient	1.9	μA/(Hz μm)	±20%
<b>Miscellaneous</b>			
Operating temperature range	-20 to 80	°C	
Material	Aluminium		
Mass	0.295	kg	±5%

P-621.2 CD PIHera XY Piezo Stage drawings (in mm): selected device is highlighted by the red box.



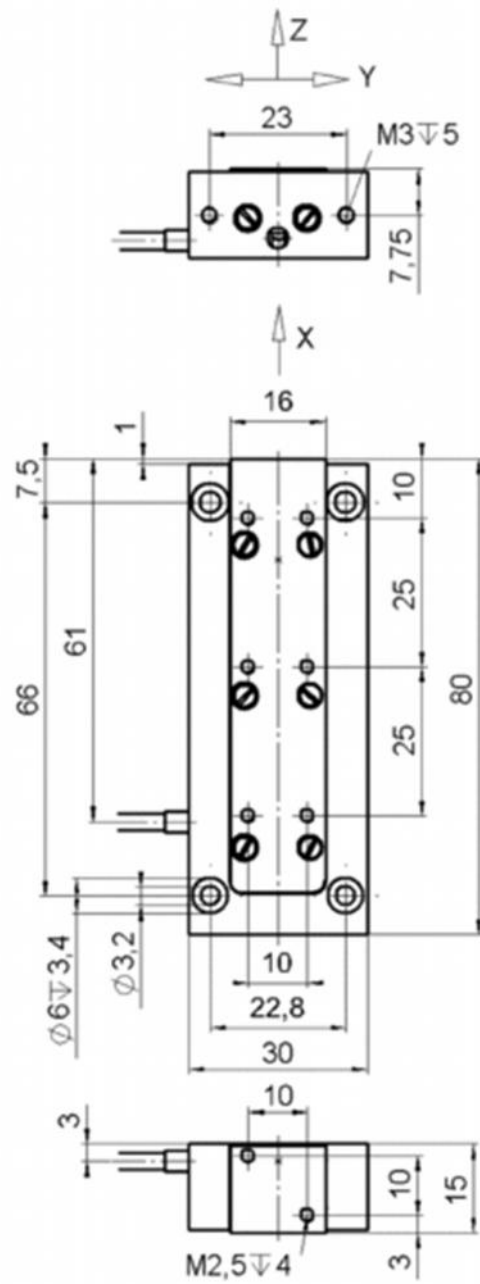
	A	B	C	D	E	$\varnothing F$	G	H	J	K	L	M	N
P-620.2CD / 20L	30	21,5	24	24	19	1,01	1,5	M2	3,5	5,1	2,2	9	6
P-621.2CD / 20L	40	25	30	26	26	1,51	2,5	M3	5	6,25	3,2	10	5
P-622.2CD / 20L	50	25	40	35	35	1,51	2,5	M3	5	6,25	3,2	11	5
P-625.2CD / 20L	60	25	50	46	46	1,51	2,5	M3	6	6,75	3,2	11	5
P-628.2CD / 20L	80	30	70	66	66	1,51	2,5	M3	6	6,75	3,2	11	5
P-629.2CD / 20L	100	40	90	82	82	2,01	3,5	M4	7	9,75	4,3	16	7,5

## A.2. P-753.31 C LISA LINEAR ACTUATOR & STAGE: SPECIFICATIONS

General information for LISA linear actuator by Physik Instrumente.

Model	P-753.31C	Units	Tolerance
Active axes	X		
<b>Motion and positioning</b>			
Integrated sensor	Capacitive		
Closed-loop travel	38	μm	calibrated
Closed-loop / open-loop resolution	0.2	nm	typ., full travel
Linearity, closed-loop	0.03	%	typ.
Repeatability	±3	nm	typ.
Pitch / yaw	±10	μrad	typ.
<b>Mechanical properties</b>			
Stiffness in motion direction	16	N/μm	±20%
Unloaded resonant frequency	2.9	kHz	±20%
Resonant frequency @ 200 g	1.4	kHz	±20%
Push/pull force capacity in motion direction	100 / 20	N	Max.
Load capacity (vertical/horizontal mounting)	10/2	kg	Max.
<b>Drive properties</b>			
Ceramic type	PICMA P-885		
Electrical capacitance	4.6	μF	±20%
Dynamic operating current coefficient	15	μA/(Hz μm)	±20%
<b>Miscellaneous</b>			
Operating temperature range	-20 to 80	°C	
Material	Stainless steel		
Dimensions	44 x 30 x 80	mm	
Mass	0.25	kg	±5%

P-753.31 C LISA Linear Actuator & Stage drawings (in mm): selected piezoelectric device measurements.





## **A.4. ARC EROSION PROCEDURE**

### **A.4.1. General Procedure: description**

Once all components and supporting equipment is ready, it is time to introduce a general procedure valid for any sample, independent of material and substrate characteristics. This process can be summarized in five main items:

1. The tip to use will depend of the type of test to perform. There are two possibilities: a spring probe or a rigid tip: the selection will depend of the case. Also is very important to clean it at the beginning of or even during any procedure.
2. Sample preparation and location over piezoelectric surface. Before placing the sample over PI Hera's surface, is necessary to clean it with a nitrogen gun and then conductive paint must be added (on each corner of the sample) to ensure electrical contact between the sample and positive electrode. Once conductive paint has dried, sample must be secured on PI Hera's surface by using four clamps available in each corner to guarantee electrical conduction and also to avoid any unwanted movement during arc erosion process.
3. Once this is done, begins tip's approach to the sample using Corvus controller. The sample is placed under the tip performing X and Y-axis movements to reach an approximate centered location. Using Z-axis step by step approach (Corvus controller) a first point is located (with micron precision), engaging the tip over the sample in a well know height, e.g. 0.1 mm. The real reference will be chosen immediately, moving the X and Y axis to a pre-specified point and making the appropriate approximation for establishing an "origin coordinate". This step may vary depending of the case; more details will be given in the approach protocol section.

4. A method has been implemented to correct tilt issues. Besides “origin coordinate”, three additional points must be taken. The purpose is to know the point’s Z-axis differences with the origin coordinate in order to deliver the correct compensation instructions to XY and Z unit, to guarantee a full and well done patterning procedure. These Z-axis coordinates are introduced in a spreadsheet, yielding final values ready to introduce them by code or manually on the machine. More detailed information in the next section.
  
5. Finally, arc erosion takes place automatically (using a final file with all the routines) or manually, introducing each routine by the operator.

#### **A.4.2. Tip Approaching Protocol**

Approaching is a very crucial step, must be carried out carefully during the arc erosion procedure. Corvus electrical motors are very powerful and if there is no a suitable protocol, damage could happen, affecting process safety. The purpose is merely to protect the sample in process and the main components of the machine.

One of the main concerns is the possibility to hit the sample and the piezoelectric device (PI Hera) with the vertical Z-axis unit making some abrupt vertical movements at high speed. Here is where the selection of the tip becomes relevant. Spring probe tips give a damping margin when the tip touches the sample surface.

The established approach protocol is as follows: when tip is located above (e.g. 0.1 mm) the final original coordinate, approach begins with a precise descent, varying electrical motor’s step (0.01 mm), until the tip reaches 10  $\mu\text{m}$  above the sample (software distance marker shows 0.01 mm). Then motor’s step is changed to 0.001 mm and begins to go down micron by micron until the tip touches.

The method used to know in which moment the tip touch the surface is with an oscilloscope connected to a high resistor (10 k  $\Omega$ ). The power supply is current limited, so when the tip touch with a small amount of potential, will need more current to guarantee the conduction, the signal in the oscilloscope will drop down. This is the way how it is known that touch exist. For patterning, the resistor is changed for a lower one.

Up here, the approach protocol is valid for wide area patterns. At the time of making even smaller patterns, the Corvus Z-axis is disabled and the relief is handed to piezoelectric Lisa for subsequent calibration heights using the above protocol stated. The main difference is that now the final approach is made in nanometers. Using Lisa actuator, final point can be achieved with a 10 nm height precision.

#### A.4.3. Tilt Correction

During the first arc erosion patterning test procedures, after making the appropriate modifications to the machine, final result was not the expected one: incomplete sections were obtained and sometimes even a single groove. No arc erosion occur because the tip did not touch the surface in an appropriately way. To ensure a full and good quality patterning a calibration method has been implemented.

As stated in item 4 of the approaching protocol at the beginning of this section, this method uses a Microsoft Excel spreadsheet to make calculations depending of the Z-axis coordinate previously measured. As mentioned, this spreadsheet needs four points, one of them is the origin coordinate already established and the other three are selected depending of the final patterning geometry.

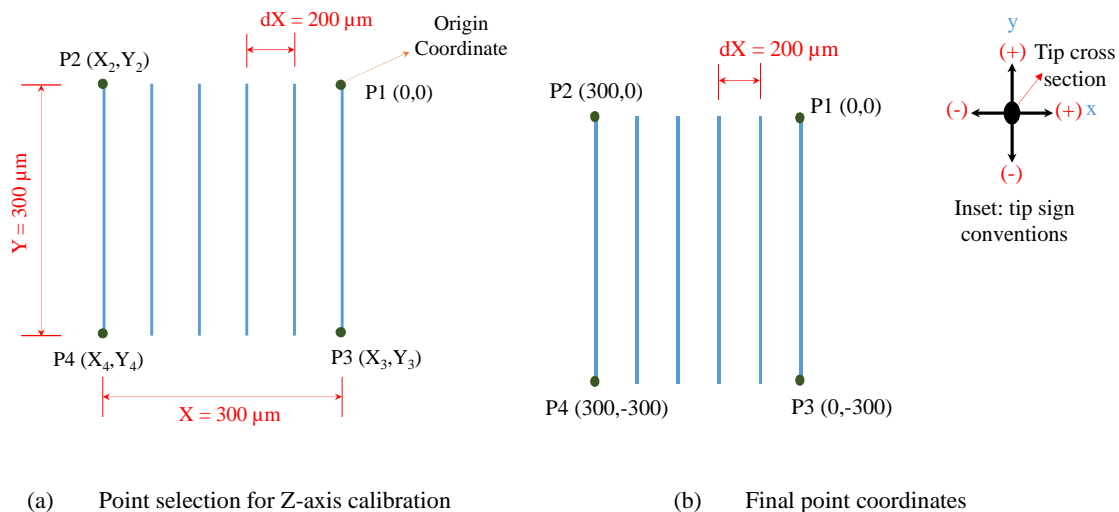


Figure A.1: Example patterning – point selection

One of the patterning model designed for experimentation is showed in Figure A.1a. Is a six vertical line pattern, values are assigned for explanation. P1 is the origin coordinate point, relative to this point others will be measured, tip is over this point 0.1

mm above. Patterning geometry has been set in advance, so final coordinate points are showed in Figure A1.b. The signs of each coordinate are considered in relation to the tip's movement, important to consider when general routines are established for a final automatic process file, as can be seen in inset of Figure A.1b.

Using the approach protocol, Z-axis difference between origin coordinate and measuring point is defined. This approach should be made for the three points remaining, in this case the surrounding square that contains the pattern. Once heights calibrated, these data is introduced in the spreadsheet together with four pair X & Y coordinates.

For more precise results, using Microsoft Excel's solver adds in, approximation to a plane containing these points was made. Plane is defined by a point P ( $P_x, P_y, P_z$ ) and two vectors:  $u (u_x, u_y, u_z)$  and  $v (v_x, v_y, v_z)$ . Usually, plane equation is obtained solving the determinant formed by this variables, and the equalize it to zero, as seen in (A-1).

$$\begin{vmatrix} X - P \\ u \\ v \end{vmatrix} = \begin{vmatrix} x - P_x & y - P_y & z - P_z \\ u_x & u_y & u_z \\ v_x & v_y & v_z \end{vmatrix} = 0 \quad (\text{A-1})$$

$$A + B + C + D = 0$$

$$A = (u_y v_z - u_z v_y), B = (u_z v_x - u_x v_z), C = (u_x v_y - u_y v_x) \quad (\text{A-2})$$

$$D = P_x(u_z v_y - u_y v_z) + P_y(u_x v_z - u_z v_x) + P_z(u_y v_x - u_x v_y)$$

The main idea is to minimize the distance variable, in order to obtain as close as possible a plane that contains this points with a smaller error. Variables A, B, C and D are solved, using them as initial values for solver (A-2). Finally, these optimized values and each coordinate point (belonging to each of the pattern lines) are used to calculate variable Z: to know how many units Z-axis has to go down at the beginning and then how many units has to countervail as it moves in X and Y for each of groove's patterning. To these data were added the initial tip height (0.1 mm) and tip's depth onto

the sample's surface. With these information, final patterning design file can be written as a text file for an automatically arc erosion procedure.

As a graphical example, Figure A.2 shows the calculus procedure performed by the spreadsheet. Both situations, initial and final are highlighted in green.

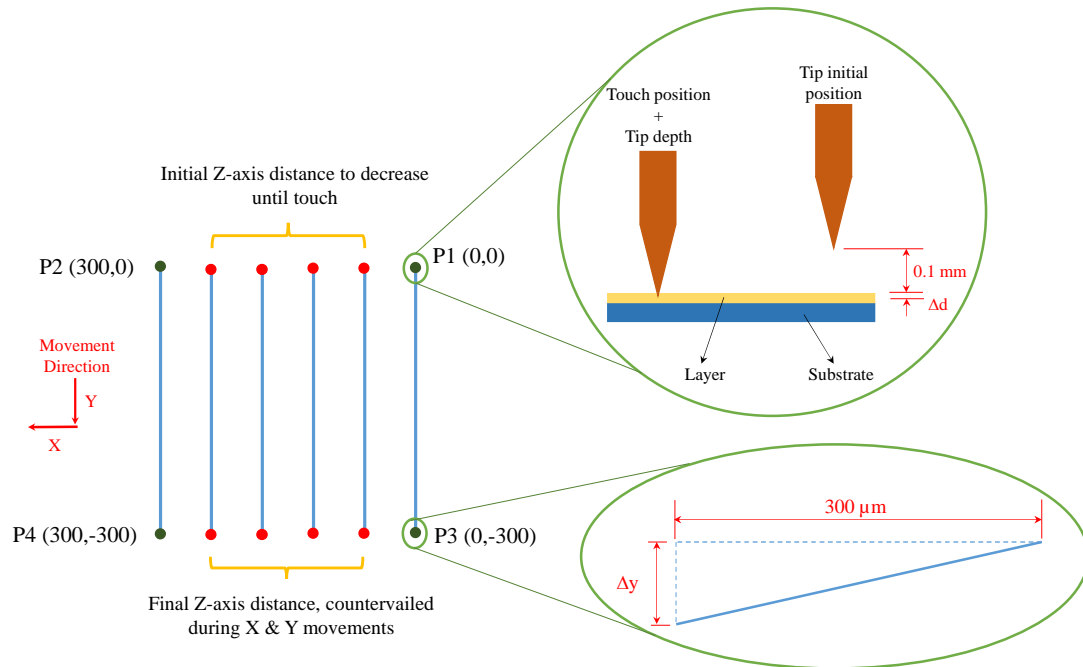


Figure A.2: Graphical summary for spreadsheet calculus.

# APPENDIX B. TECHNICAL DRAWINGS

**B.1.** GENERAL MOUNTING BASE FOR LONG RANGE PLS-85 STAGE

**B.2.** HORIZONTAL MOUNTING BASE FOR PI-HERA XY PIEZOELECTRIC

**B.3.** VERTICAL MOUNTING BASE FOR PI-LISA PIEZOELECTRIC

**B.4.** SCREW BOLT ADAPTER FOR COLLET FASTENING

**B.5.** TIP HOLDER ADAPTER

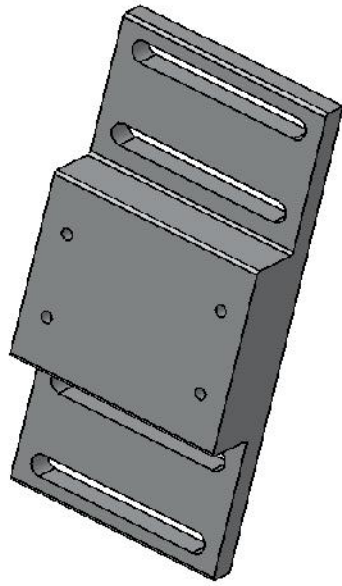
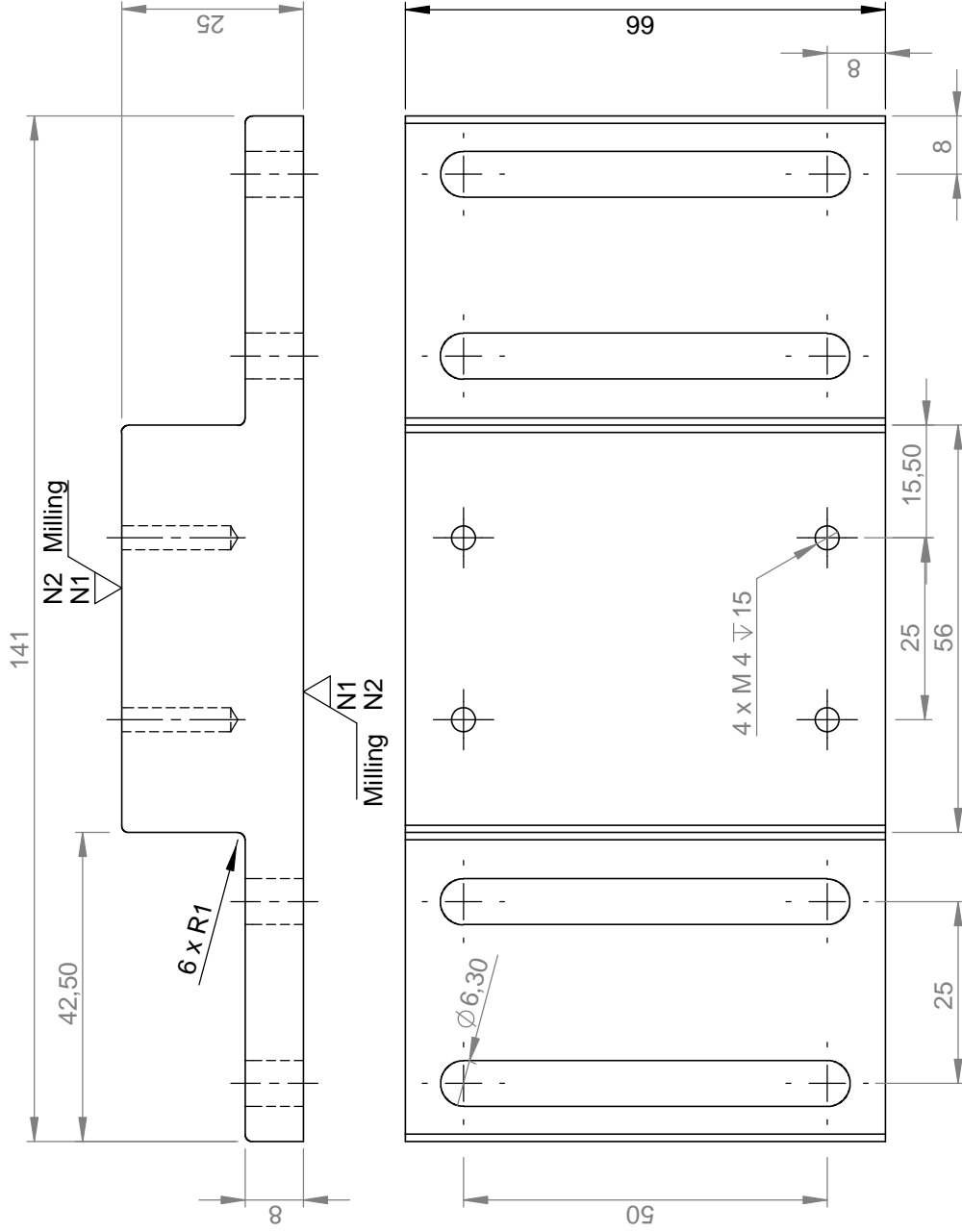


**Notes:**

Ensure maximum resolution of all dimensions.

Specular surface finish.

Material: Aluminum



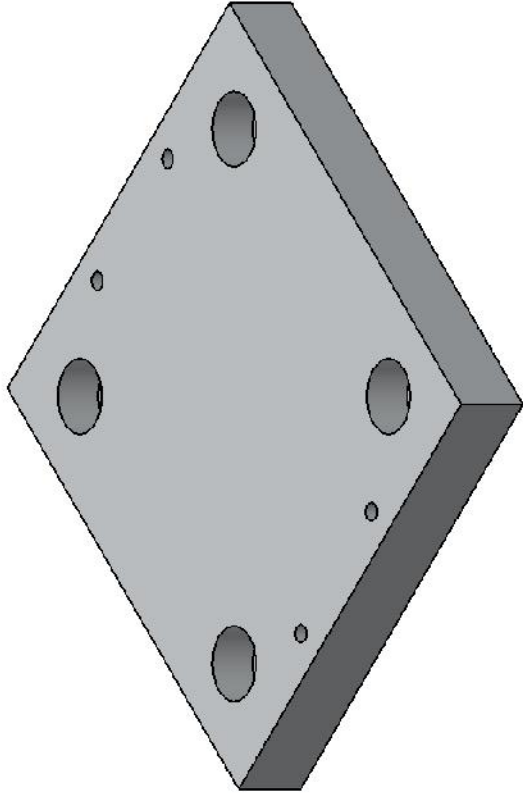
Auxiliary View  
scale: 1:2

<b>DRAWING: B1</b>	Project: Arc-erosion prototype	Date: 12/11/2012
	Part: General mounting base for PLS85	Approval date 12/11/2012
	Design: M Garcia      Format: A4	Approved: C Coya, A L Alvarez
		Scale: 1:1
	Units: mm	

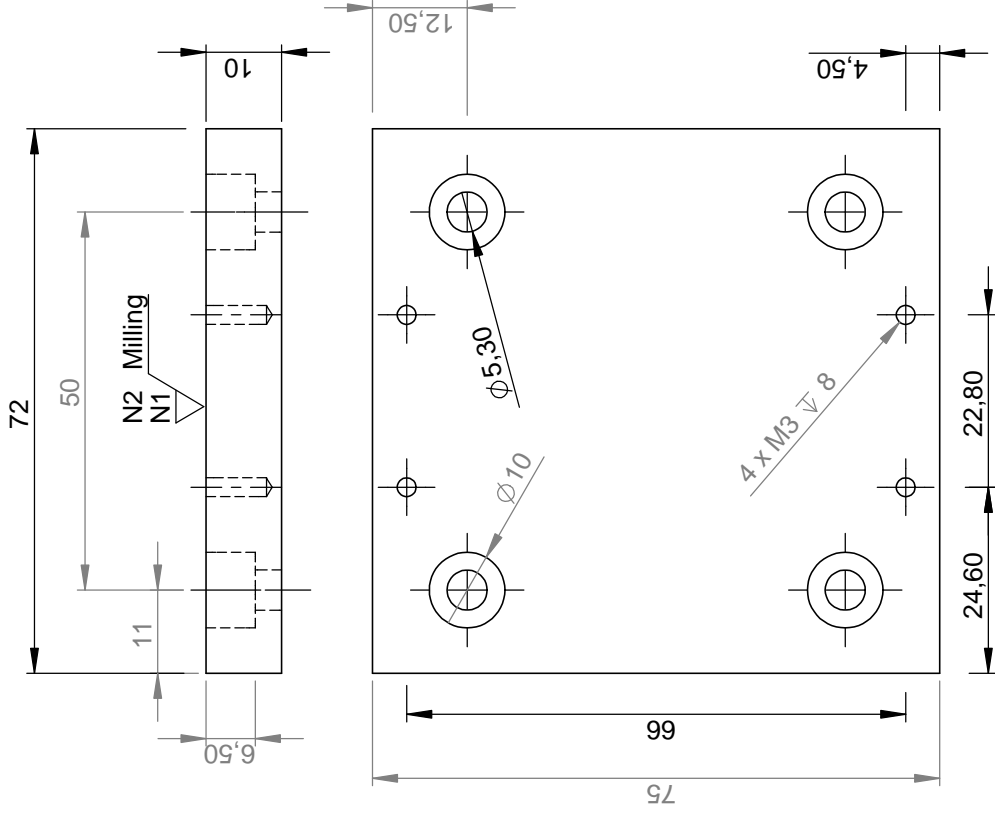






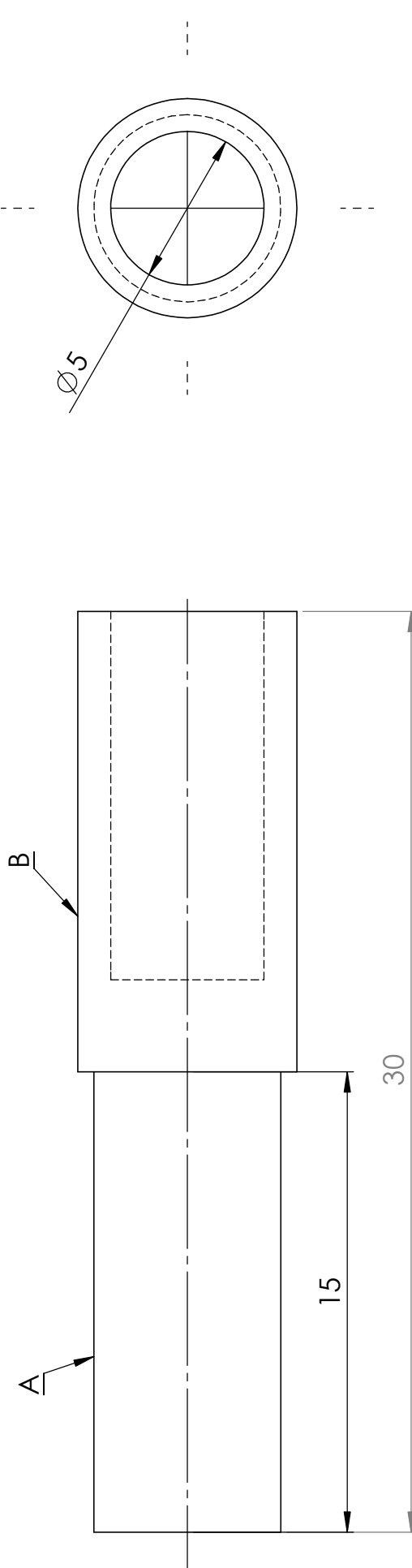


Isometric View



<p><b>DRAWING: B3</b></p>		Project: Arc-erosion prototype	Date: 19/11/2012
		Part: Vertical mounting base PI Lisa	Approval Date: 19/11/2012
Design: M. Garcia	Formato: A4	Approved: C. Coya, A. Alvarez	
		Scale: 1:1	Units: mm





**ANOTATIONS:**

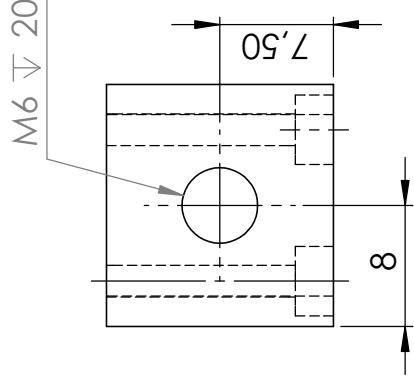
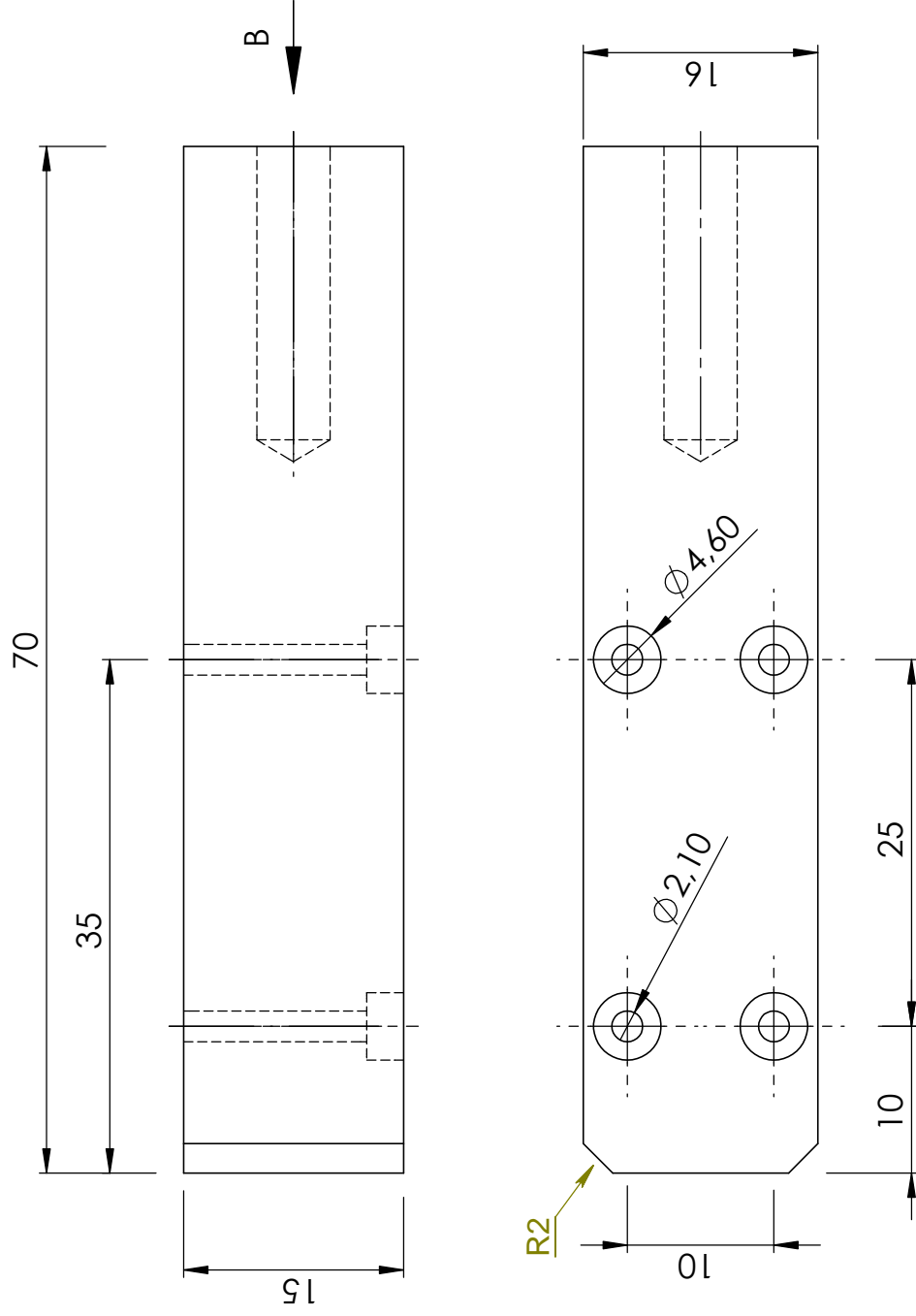
Elements	Description
A	M6, external thread
B	0.280" - 40NS - 2, external thread

**DRAWING: B4**



Project: Arc-erosion prototype	Date: 30/11/2012
Part: Screw bolt adapter for collet fastening	Approval Date: 04/12/2012
Design: M. García	Format: A4
Approved C.Coya y A.Álvarez	
	Scale: 5:1
Units: mm	





View B

Material: methacrylate

<p><b>DRAWING: B5</b></p>	Project: Arc-erosion prototype	Date: 30/11/2012
	Part: Tip holder adapter - coupling Pi Lisa	Approval Date: 03/12/2012
	Design: M. García	Format: A4
		Scale: 2:1
		Units: mm



